The Pennsylvania State University
The Graduate School
Department of Materials Science and Engineering

TEMPLATED GRAIN GROWTH OF TEXTURED STRONTIUM NIOBATE CERAMICS

A Thesis in
Materials Science and Engineering
by

Bhaskar Brahmaroutu

Submitted in Partial Fulfillment
of the Requirements
for the Degree of

Doctor of Philosophy

August 1999

UMI Number: 9940816

UMI
300 North Zeeb Road
Ann Arbor, MI 48103

We approve the thesis of Bhaskar Brahmaroutu:

Date of Signature

July 16, 1999

Gary L. Messing
Professor of Ceramic Science and Engineering
Thesis Co-Advisor
Co-Chair of Committee

Susan Trolier-McKinstry 7-16-99

Susan Trolier-McKinstry
Associate Professor of Ceramic Science and Engineering
Thesis Co-Advisor
Co-Chair of Committee

Robert E. Newnham 7-16-99

Robert E. Newnham
Professor Emeritus of Solid State Science

T. R. Shrout 7/16/99

Thomas R. Shrout
Senior Scientist and Professor of Materials

July 16, 99

Qiming Zhang
Associate Professor of Electrical Engineering

John R. Hellmann 19 July 1999

John R. Hellmann
Associate Professor of Ceramic Science and Engineering
In Charge of Ceramic Science Option

Abstract

$Sr_2Nb_2O_7$ holds the promise of high temperature piezoelectricity that can be used in high temperature sensors. Development of texture in a ceramic along the direction of spontaneous polarization (crystallographic c-axis) is a prerequisite for the use of ceramics as an alternative to single crystals due to property anisotropy in $Sr_2Nb_2O_7$. Anisotropic grain growth and its use for fabricating textured $Sr_2Nb_2O_7$ by the templated grain growth (TGG) approach was investigated.

Synthesis of large, single crystal template particles by molten salt synthesis was studied. The size and morphology of niobium precursor was found to determine the morphology and size of the template particles. Large $SrNb_2O_6$ particles synthesized in $SrCl_2$ melts were mixed with $SrCO_3$ and reacted in molten KCl to obtain $Sr_2Nb_2O_7$ templates in the 10-30 μm range. The morphology of the templates was correlated to the crystal structure and it was determined that the large rectangular face of the blade-shaped particles was parallel to the ac-plane, and the long edge was along the a-axis. Fine, submicron matrix powder used for TGG was synthesized by coprecipitation and solid state reaction.

Donor doping with lanthanum was necessary to increase electrical resistivity at high temperatures. Anisotropic grain growth in doped and undoped, randomly oriented matrix powder was studied to determine the kinetics of grain growth. Lanthanum doping was found to suppress grain growth in stoichiometric compositions. Addition of excess niobium was found to form a low melting liquid phase which enhances grain growth in this system.

Samples with fiber and sheet texture were fabricated by tapecasting slurries containing 10-40 vol% templates mixed with matrix powder. Grain growth behavior and texture development were studied by stereological measurements and X-ray diffraction. Fiber texture was obtained along the b-axis in undoped $Sr_2Nb_2O_7$, and sheet texture was obtained in La-doped samples containing 200-1000 ppm excess niobium. Sheet texture results in a greater degree of orientation along the c-direction as compared to randomly oriented or fiber texture (b-axis) samples. Texture in samples was reflected in their physical properties. The presence of sheet texture was determined by pole figure measurements. The dielectric constants showed the expected anisotropy for both fiber texture and sheet texture cases. The understanding of TGG developed in the $Sr_2Nb_2O_7$ was then used to texture $PbNb_2O_6$, another high temperature piezoelectric. A d_{33} of 120 pC/N was obtained at room temperature in poled, textured $(Pb,K)Nb_2O_6$ ceramics fabricated by TGG.

TABLE OF CONTENTS

LIST OF FIGURES

LIST OF TABLES

ACKNOWLEDGEMENTS

I am very grateful to Dr. Gary Messing and Dr. Susan Trolier-McKinstry for their guidance and patience. I thank them for not only improving my thinking, writing, and presentation skills but also for encouraging independent research. I am also grateful to my committee members for their time and interest. I would also like to thank my lifelong teachers, my parents, for their unconditional patience, guidance, and sacrifice.

I acknowledge and express my thanks to all those who have helped me in my experiments during the course of my Ph.D., in particular, Dr. Schlom, Mark Angelone, and John Cantolina for help with Pole figure measurements, Rosemary Walsh for help with EDS, Else Breval for help with TEM, Scott Atkinson with platinum sputtering, Gaylord, Joe, Tim, and the rest of the MRL staff for their help on a regular basis, and Leah Witzig for smoothing problems and patiently answering questions regarding University rules and forms.

A special thanks to all my colleagues in Dr. Messing's research group, both past and present. They have been a source of continuous support and a pleasure to work with. I would like to thank Y, Seongtae, Roger, and Scott for their help and guidance in my early years at Penn State, Matt, Ender, Akira, Paul, and Rob for their company and help through numerous discussions on both research and life. I am grateful to Ed & Mike for thought provoking questions and discussions, help with experiments on numerous occasions, extending my education to football, skiing, gardening, and cars, and above all for being good friends and maintaining my humor through tough times.

I will surely miss the company of a number of colleagues in the Department and in State College as a whole. One person who I am deeply thankful to is my wife, Nivedita, for her unconditional support and patience during my Ph.D. She made it easy for me to cope with the demands and pressures of graduate school and writing a thesis. I would also like to record my appreciation and gratitude to Cihangir, Robie, and Seyit for helping me with stereological analysis, Huseyin for help with Mathematica, and Reetinder for helping me finish writing my thesis in time.

Chapter 1

INTRODUCTION AND STATEMENT OF PROBLEM

1.1 INTRODUCTION

1.1.1 Textured Ceramics

A number of materials with useful ferroelectric, piezoelectric, optical, and superconducting properties in the single crystal form have not been exploited due to the high cost of conventional crystal growth techniques.[1,2] Some of these materials do not retain their useful properties in a randomly oriented polycrystalline ceramic form. Although most inorganic crystals exhibit anisotropy in structure, habit, and properties, the reduction in the magnitude of desired physical properties due to averaging in a randomly oriented ceramic prevents the harnessing of useful property-anisotropy. This problem is most pronounced in materials with low symmetry crystal structures.

The microstructure developed during processing determines the ultimate properties of a ceramic. Equiaxed microstructures with a narrow grain size distribution are generally preferred to obtain reproducibility, reliability, and predictability of properties in the fabrication of a large number of parts. In fact, one of the challenges of conventional ceramic processing is the inhibition of exaggerated grain growth[3,4] – the growth of a few very large grains in a homogeneous microstructure resulting from physical or chemical heterogeneities in the green body. Anisotropic grain growth or the growth of anisotropic grains in the entire microstructure has been observed in many ceramic systems,[5,6] and has been attributed either to anisotropic surface energies of different crystal planes resulting from an anisotropic crystal structure or the poisoning of a few crystallographic planes by impurities which results in anisotropic grain boundary mobilities.[7,8]

With increasing understanding of anisotropic grain growth in ceramics there has been a renewed interest in tailored microstructures for improved and optimized properties of functional ceramics. Anisotropic grain growth can be used to form microstructures with interpenetrating grains to obtain high strength and high toughness SiC and Si_3N_4 or to produce textured ceramics with anisotropic physical properties.[9-15] One method of enhancing anisotropy in polycrystalline ceramics is to enhance grain orientation along one or more directions, leading to the formation of textured ceramics which can exhibit single crystal-like properties.

Techniques of inducing texture in ceramics are largely based on alignment of anisotropically shaped particles such as plates or whiskers by the application of uniaxial pressure at high temperatures (hot forging),[16] recrystallization from a liquid phase or melt texturing,[17,18] or the use of less expensive, pressureless techniques based on orienting anisotropically shaped particles under the application of an anisotropic magnetic,[19] electrical,[20] mechanical stress, or shear field during forming.[21-23] Melt texturing requires the presence of a suitable thermal gradient during processing at the crystallization temperature. This makes it difficult to texture materials with very high melting points. A common limitation of the other processes is the use of large anisotropic particles which do not pack very well during forming, do not densify very well during heat treatment, and hinder complete alignment of particles by mutual impingement.

Templated grain growth (TGG) of textured ceramics is a relatively new, pressureless sintering technique which can overcome the limitations of the previously mentioned grain orientation techniques, and has been used to fabricate dense, grain-oriented ceramics in the presence of a liquid phase.[24-30] TGG is based on exaggerated and/or anisotropic grain growth. Texture development during TGG results from the preferential growth of large anisotropically shaped single crystal particles (templates) which are oriented in a fine-grained matrix during forming. The fine-grained matrix provides a large driving force for densification of the part and growth of oriented templates due to their size advantage. The preferential growth of large, oriented templates leads to an increase in the textured fraction during heat treatment. The requirements for successful TGG are large, anisotropic single crystal particles (templates) which can dominate grain growth, fine matrix powder which provides the driving force for densification and growth of templates, a method to orient the templates in the fine matrix powder, and finding conditions for preferential growth of templates in the densified matrix to produce large volume fractions of textured material. Figure 1.1 shows a schematic of the TGG process using tape casting as the orientation technique.

1.1.2 High Temperature Piezoelectrics

The nuclear, aerospace, automotive, oil, and geothermal industries have driven the need for electronic materials that operate at higher tempcrature. One of the needs of these industries is high temperature acoustic and vibration sensors.[31] The design of these devices is limited by the operating temperature range of the material used. The trend

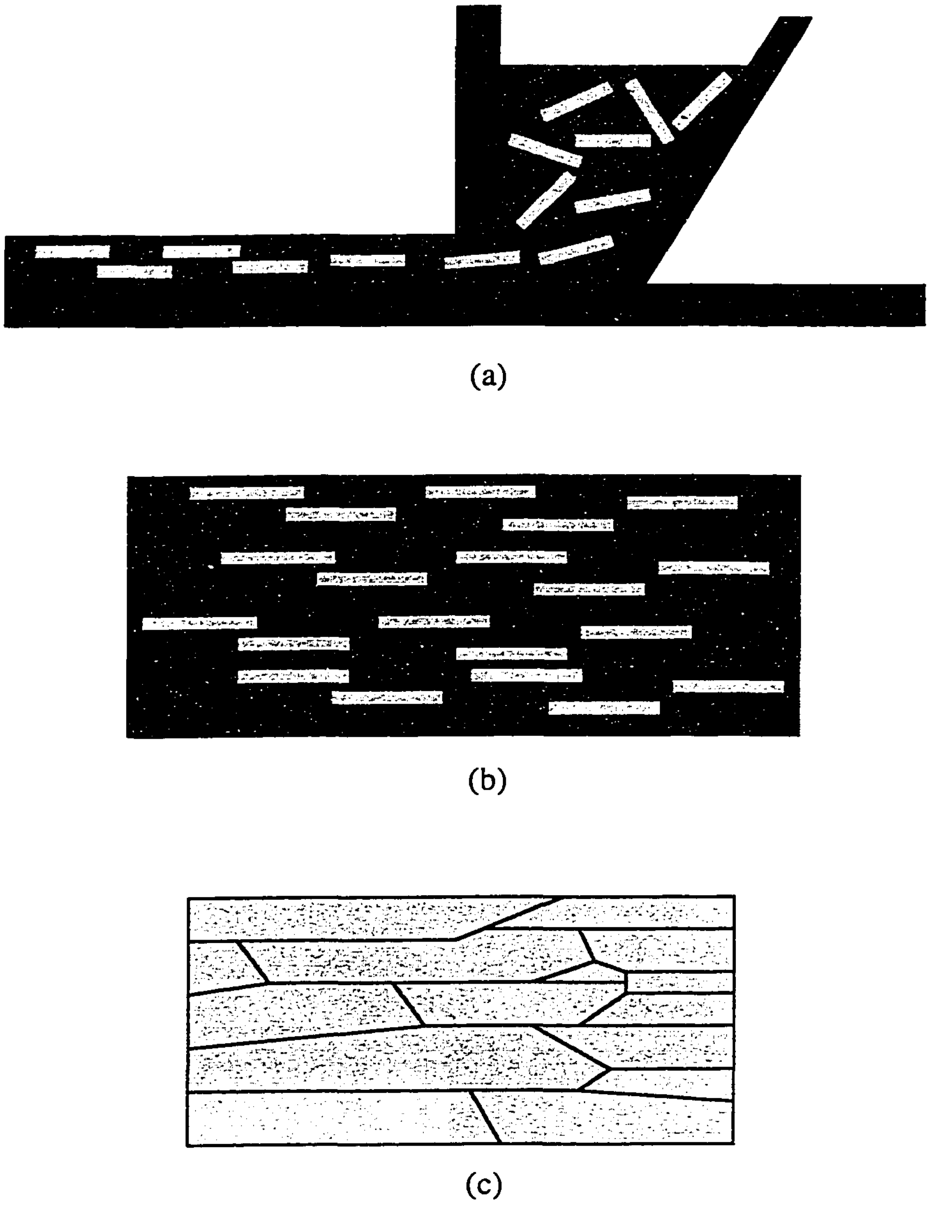

Figure 1.1 Schematic of the TGG process. (a) Orientation of templates by tape casting, (b) Laminated green sample containing oriented templates dispersed in a fine matrix, (c) Texture development due to preferential growth of templates.

towards placing sensors directly in the high temperature zones of automotive and aerospace engines due to reliability and noise considerations requires materials that can operate in the 500-1000°C temperature range with lifetimes of up to 100,000 h.[16,31] Among the different types of acoustic and vibration sensors, piezoelectric sensors are leading candidates based on sensitivity, cost, and design. Sensors based on the principle of spatial modulation in a multimode optical waveguide are also used for high temperature stress monitoring and displacement measurements.[32]

Most piezoelectric materials have an operating temperature limit of approximately half of their Curie temperatures. This precludes the use of widely used piezoelectrics such as PZT due to their relatively low Curie temperatures. The Curie temperatures, crystal structure, and properties of some piezoelectrics with high Curie temperatures are listed in Table 1.1.[16,33-37] Most piezoelectric materials that possess a high Curie temperature also possess anisotropic, low symmetry crystal structures. Texturing these materials by TGG to obtain enhanced single crystal-like properties is an alternative to growing high quality single crystals from high temperature melts. Among these materials, ferroelectrics belonging to the perovskite layer structure (PLS) family, which have the general formula $A_2B_2O_7$, have been reported to have the highest known Curie temperatures. Among the PLS compounds, lanthanum titanate, calcium niobate, and strontium niobate show high temperature ferroelectricity. Single crystals of $La_2Ti_2O_7$, $Ca_2Nb_2O_7$, and $Sr_2Nb_2O_7$ possess coercive fields of 45 kV/cm, 65 kV/cm, and 6 kV/cm at room temperature, respectively.[37] For a ceramic, grain oriented, La-modified $Sr_2Nb_2O_7$, the polarization versus applied field hysteresis was not saturated at even 100 kV/cm.[16] $Sr_2Nb_2O_7$ possesses the highest d_{33} among the PLS compounds (18 pC/N), a k_{33} of 0.29,

Table 1.1 Curie temperature and properties of selected high T_C piezoelectrics

Material	T_C(°C)	Crystal Structure	Coupling coefficients					Piezoelectric Coefficients			
			k_p	k_t	k_{33}	k_{31}	k_{15}	d_{33}	d_{31}	d_{15}	(pC/N)
PZT-5A[32]	365	Perovskite	0.6	0.49	0.70	-0.34	0.68	374	-171	584	
$PbTiO_3$[32]	470	Perovskite	0.07	0.46	0.46			51	-4.4		
$PbNb_2O_6$[32]	560	Tungsten-Bronze	0.07	0.38	0.045			85	-9.0		
$PbBi_4Ti_4O_{15}$[33]	570	Bismuth layer structure	0.005	0.07					-0.4		
$Na_{0.4}Bi_{4.5}Ti_4O_{15}$[33]	670	Bismuth layer structure	0.04	0.29	0.15	0.033	0.12	15.6	3.5	19.7	
$Bi_4Ti_3O_{12}$[16]	675	Bismuth layer structure	0.044	0.19	0.15	0.035	0.12	15.1	3.64	17.8	
AlN*[34]	1150*										
$LiNbO_3$[16]	1210							6.0	-0.85	69.2	
$Sr_2Nb_2O_7$[35]	1342	Perovskite Layer Structure			0.29	0.05	0.18	18	2.0		
$La_2Ti_2O_7$[33]	1500	Perovskite Layer Structure			0.29	0.06		16	3.0		
$Ca_2Nb_2O_7$[36]	>1500	Perovskite Layer Structure			0.30						

*Temperature at which properties were measured and not a Curie temperature as AlN is not a ferroelectric.[34]

and a Curie temperature of 1342°C. It is also chemically stable in vacuum and has moderate tolerance to neutron irradiation.[38] These factors make $Sr_2Nb_2O_7$ a leading candidate for use in sensors with a high operating temperature and good thermal stability in harsh environments.[38] Consequently, this thesis is directed towards understanding the factors controlling TGG in $Sr_2Nb_2O_7$.

1.2 RESEARCH OBJECTIVES AND THESIS ORGANIZATION

The primary objective of this study is to investigate and control the densification and grain growth processes during TGG which lead to grain orientation, and to quantify the texture of these ceramics by comparing their physical properties to those of single crystals. The material of interest is $Sr_2Nb_2O_7$ due to its potential for high temperature piezoelectric properties and its low crystal symmetry. The overall technological problem is composed of the following elements:

1.2.1 Template Particle Synthesis

A key element for successful TGG is the availability of suitable single crystal template particles. The factors which control the morphology of particles formed during Molten Salt Synthesis (MSS) are poorly understood. Consequently, a study was undertaken to determine how reaction sequence and precursor shape and size affect the final morphology of $Sr_2Nb_2O_7$ crystals. The first part of Chapter Two deals with the synthesis of $Sr_2Nb_2O_7$ templates by MSS. The reaction sequence and the effect of processing parameters on the morphology and size of $Sr_2Nb_2O_7$ single crystals will be discussed in this section. In particular the relations between the observed morphology of the templates, crystal structure, and the morphology of the precursors will be identified.

1.2.2 Synthesis of Fine Matrix Powder

The synthesis of fine, stoichiometric $Sr_2Nb_2O_7$ powder is important for providing a homogeneous and dense matrix for the growth of oriented templates. Sol-gel processing, solid state reaction, and coprecipitation were investigated for the synthesis of fine $Sr_2Nb_2O_7$ powder, and the sintered microstructures were compared to determine the suitability of the powders for TGG. This study is reported in the second half of Chapter Two.

1.2.3 Anisotropic Grain Growth in $Sr_2Nb_2O_7$

The intrinsic anisotropic grain growth in $Sr_2Nb_2O_7$ is studied in Chapter Three. The scientific objectives of this study are to understand the mechanism of grain growth, determine whether TGG can proceed in the absence of a liquid phase, and if not, to determine how much liquid phase is required for anisotropic grain growth. The densification behavior and grain growth behavior of pure and donor-doped $Sr_2Nb_2O_7$ fine powders were investigated as a function of time and temperature. An understanding of the conditions required for grain growth enables better control of TGG. The role of the strontium to niobium ratio on the degree of grain growth is also investigated in Chapter

Three. This ratio affects liquid phase formation, which has a very strong effect on grain growth. The effect of La-doping on densification and grain growth is reported. The growth of randomly oriented templates was also studied as a function of time and temperature. Dielectric measurements indicated a high dielectric loss at temperatures above 200°C in pure $Sr_2Nb_2O_7$. Donor doping either the Sr-site with La[16] or the Nb-site with W suppressed the dielectric loss at higher temperatures and the extent of grain growth. The results of this study form the basis for the TGG investigations in Chapter Four.

1.2.4 Templated Grain Growth in $Sr_2Nb_2O_7$

Orientation of template particles in a fine matrix was achieved by tape casting. Conventional tape casting yields green samples in which the $Sr_2Nb_2O_7$ templates show fiber texture along the crystallographic b-direction. These samples were studied to elucidate the effect of template size and concentration on the development of texture in pure $Sr_2Nb_2O_7$ as a function of time and temperature. Texture in undoped samples was characterized by Lotgering factor measurements.

Although there are several cases where sheet texture is desirable, it has been only recently that a technique has been devised to obtain sheet texture in superconducting thick film ceramics by the RABiTs (Rolling Assisted Biaxial Textured Substrates) technique.[39,40] This technique is based on thin film deposition of epitaxial superconducting films on a rolled, buffer oxide coated, metal substrate with sheet texture. There have been no previous reports on production of sheet texture in bulk ceramics.

Therefore, a method for preparing sheet textured bulk ceramic needs to be developed. The tape casting process was modified to produce sheet texture in La-doped $Sr_2Nb_2O_7$ templated with blade-like single crystal $Sr_2Nb_2O_7$ particles. Equations of particle motion in flowing suspensions were used as the basis for designing a gated tape casting system which could impart orientation along the long axis as well as along the normal to the flat rectangular face of the template particles. The understanding of anisotropic grain growth in La-doped $Sr_2Nb_2O_7$ developed in Chapter Three was used to promote template growth in TGG samples. In order to obtain better electrical properties, the amount of excess niobium in the system was minimized. The microstructural evolution and stereological characterization of texture is also discussed in Chapter Four.

1.2.5 Anisotropic Physical Properties in TGG samples and Crystal Symmetry

This study was required to establish relationship between pole figure measurements and property anisotropy. In order to quantify texture in a polycrystalline material, the position and orientation of every crystallite must be determined with respect to a frame of reference. Since this is practically impossible, statistics of grain orientation can only be determined by measuring properties of the ceramic in different directions and comparing them to the properties of a single crystal. The properties of a single crystal depend on the chemistry of the material and the symmetry of the crystal structure.

X-ray diffraction patterns obtained from θ-2θ scans of different cuts through the ceramic samples give an idea of the texture in the ceramic as the planes oriented parallel to the cut plane diffract X-rays, leading to an increase in the relative intensity of the diffraction peak at the corresponding Bragg angle. A more complete description of the overall orientation distribution of the crystallites in a ceramic can be determined by measuring the diffraction in a hemisphere instead of a single plane of scanning. Such a scan gives orientation information for a family of crystallographic planes within the sample in all directions. Pole figure measurements and their interpretations based on crystal symmetry and sample texture are also presented in Chapter Five.

Texture in microstructure translates to anisotropic physical properties in materials with anisotropic single crystal properties. Measurements of piezoelectric properties, dielectric constants, elastic constants, d.c. resistivity, and thermal expansion coefficients as a function of sample orientation were studied to understand the effect of texture on the properties of polycrystalline $Sr_2Nb_2O_7$.

1.2.6 Application of TGG to Other Anisotropic Piezoelectric Materials

The results from the study of TGG in $Sr_2Nb_2O_7$ can be applied to many other ceramic systems. Based on the understanding of the effect of processing parameters on TGG, texture development in $(Pb,K,Ba)Nb_2O_6$ is discussed in Chapter 6. Synthesis of large, anisotropically shaped template particles, their orientation and growth during TGG, and the piezoelectric properties of the textured samples are described.

1.3 BACKGROUND

1.3.1 Perovskite Layer Structure Family

The $A_2B_2O_7$ or $ABO_{3.5}$ type compounds have excess oxygen when compared to the ABO_3 perovskite structure. The extra oxygen atoms are incorporated at equally spaced intervals along the [110] direction in the perovskite lattice as illustrated in Figure 1.2. The excess oxygen containing compounds are members of the homologous family $A_nB_nO_{3n+2}$ ($n \geq 4$) with end members $A_2B_2O_7$ ($n=4$) and ABO_3 ($n=\infty$).[41] The integer n corresponds to the number of BO_6 octahedra in each parallel slab. The lattice parameters of $A_nB_nO_{3n+2}$, a_n, b_n, and c_n are related to the cubic perovskite lattice parameter a_p as follows:

$$a_n = a_p$$

$$b_n = n2^{0.5}a_p + 2K$$

$$c_n = 2^{0.5}a_p$$

where K is a constant. The n=4 structure compounds are referred to as the perovskite layer structure (PLS) family, and the compounds belong to either the orthorhombic or the monoclinic system. The structure field map[16] (Figure 1.3) shows that the PLS structure is confined to a relatively small region of possible A and B cation radii. A smaller B cation results in either the thortveitite structure that is made of octahedrally coordinated A atoms, with BO_4 tetrahedra, or pyrophosphate structure with the pyro-groups $(P_2O_7)^{4-}$. On the other hand, decreasing A-cation radius results in the formation of the pyrochlore structure.

Calcium niobate was the first PLS compound to be investigated. Its structure was described in detail by Brandon and Megaw.[42] In addition to calcium niobate, other compounds such as strontium niobate, strontium tantalate, lanthanum titanate, and

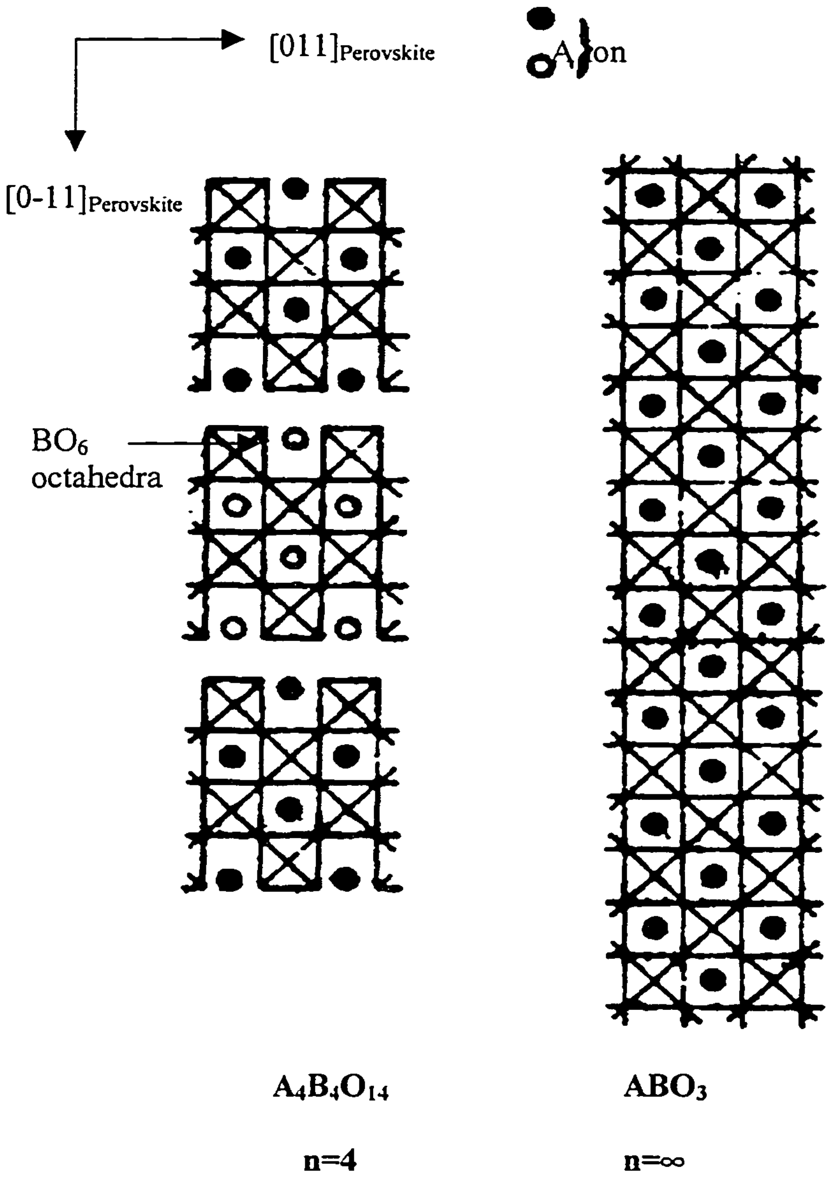

Figure 1.2 Comparison of the arrangement of BO_6 octahedra in the perovskite structure and the perovskite layer structure of $A_2B_2O_7$ compounds. Open circles represent Sr atoms which are displaced vertically from the plane of projection [41].

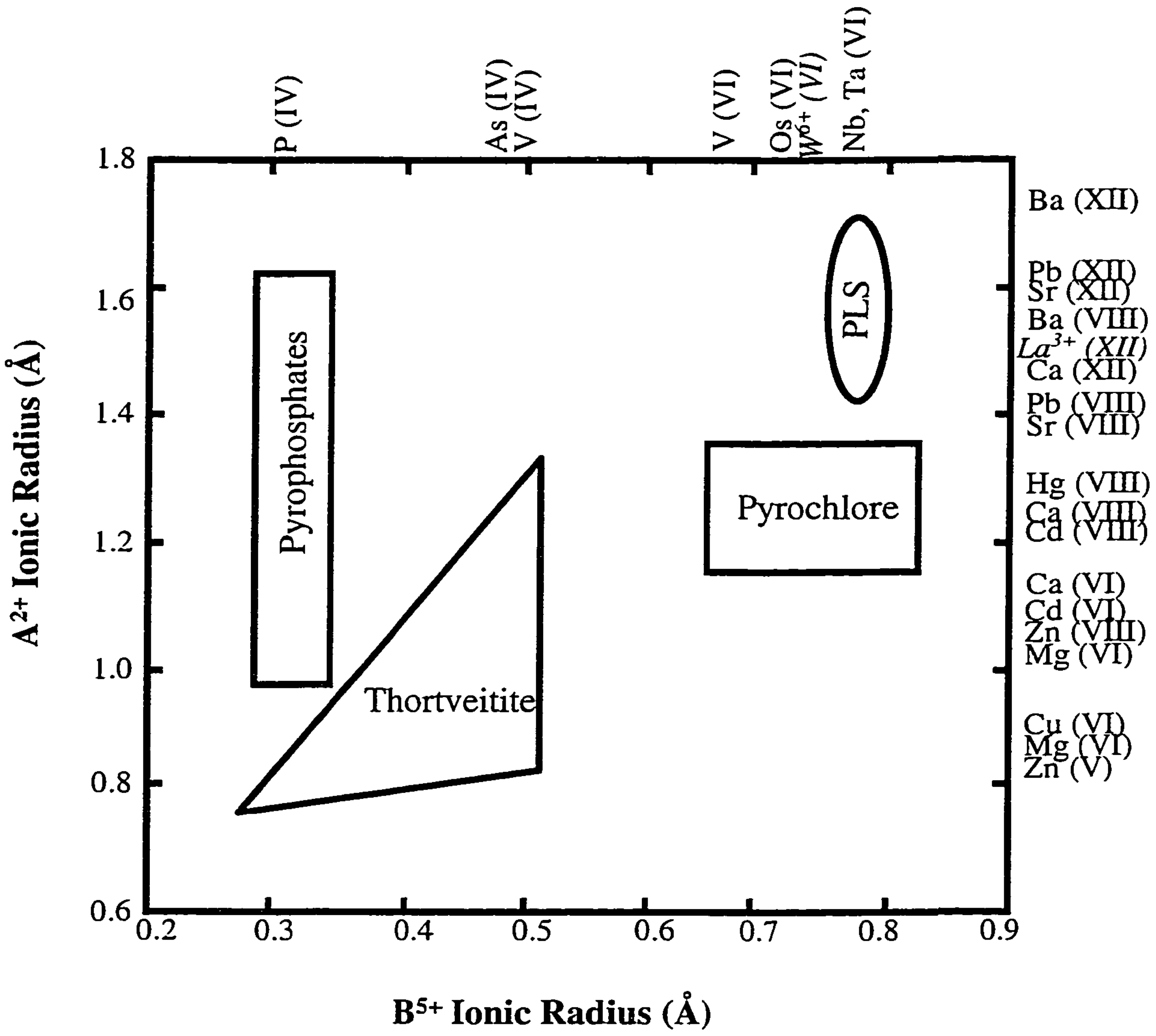

Figure 1.3 Structure field map for $(A^{2+})_2(B^{5+})_2O_7$ [16].

titanates with larger-size rare-earths in the A-site belong to the PLS family. The complicated structure and very high melting points makes crystal growth very difficult. Among the PLS compounds, lanthanum titanate, calcium niobate, and strontium niobate show high temperature ferroelectricity.[36,43] $Sr_2Nb_2O_7$ possesses the highest d_{33} among the PLS compounds (18 pC/N), a k_{33} of 0.29, and a Curie temperature of 1342°C. It is also chemically stable in vacuum and has moderate tolerance to neutron irradiation.[38] These factors make $Sr_2Nb_2O_7$ a leading candidate for use in sensors with a high operating temperature and good thermal stability in harsh environments.[38]

1.3.2 $Sr_2Nb_2O_7$

All polymorphs are characterized by stacked perovskite-type slabs containing corner-shared NbO_6 octahedra and 12 coordinated Sr cations. Figure 1.4 illustrates the crystal structure of $Sr_2Nb_2O_7$.[44] The perovskite layer slabs are four octahedra thick and are linked by Sr cations lying at their boundaries. These slabs extending in two dimensions are responsible for the micaceous cleavage observed in crystals perpendicular to the b-axis.

All the Nb atoms are octahedrally surrounded by oxygen atoms, the Nb-O distance ranging from 1.84-2.31 Å. Sr(2) is coordinated to twelve oxygen atoms. However, Sr(1), lying near the boundary of the slab, is greatly displaced towards the boundary from the center of the cube formed by atoms O(2), O(4), O(5) and O(6). As a result, the atom is surrounded by five oxygen atoms in the same slab and two oxygen atoms in the neighboring slab at distances ranging from 2.43 to 2.85 Å. Thus, the Sr(1) atoms link adjacent slabs. Two more oxygen atoms in the same slab are at a distance of 3.27 Å from Sr(1). The mean Sr(1)-O distance is 2.74 Å including these two longer bonds and that of Sr(2)-O is 2.78 Å.

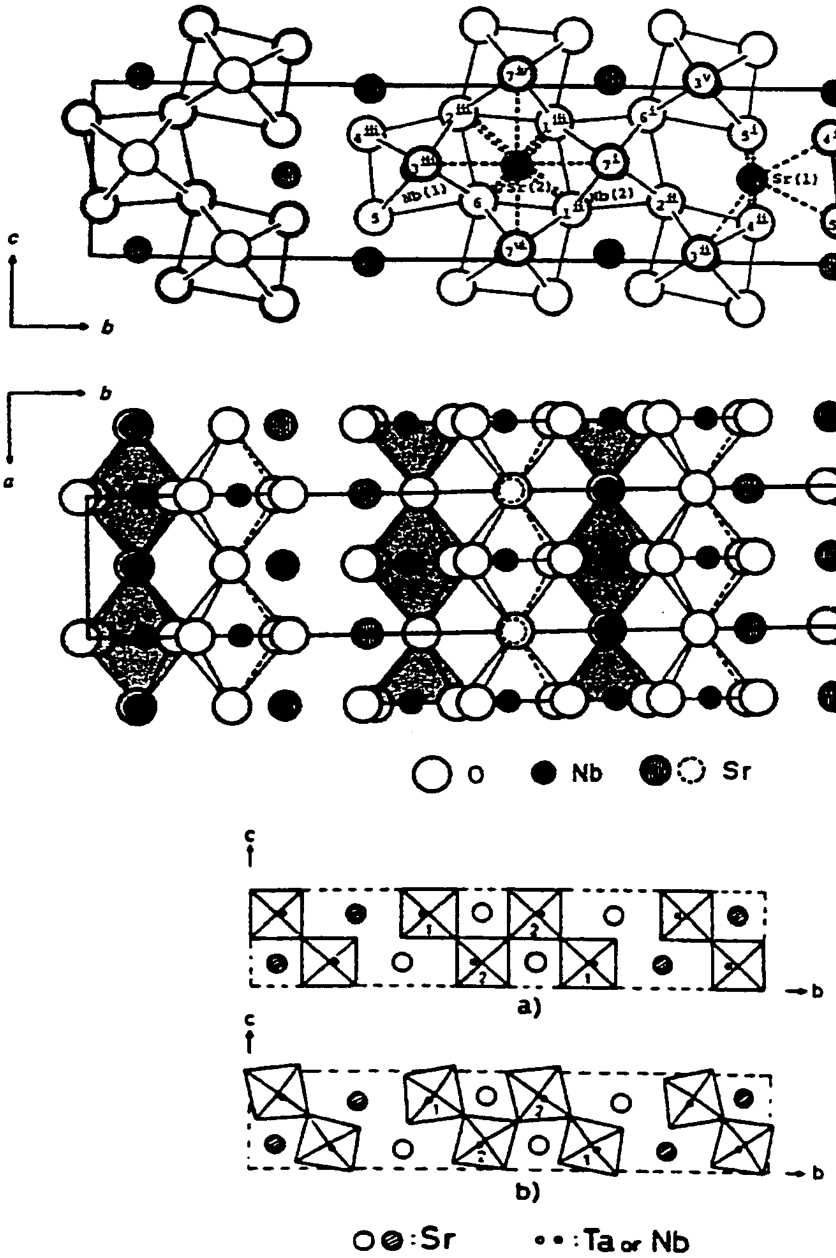

Figure 1.4 Crystal structure of $Sr_2Nb_2O_7$ and comparison of the paraelectric and ferroelectric phases, showing the distortion of the orthorhombic cell due to the rotation of NbO_6 octahedra about the a-axis [44].

1.3.3 Ferroelectricity in $Sr_2Nb_2O_7$

The possibility of ferroelectricity in $Sr_2Ta_2O_7$ was first proposed by Smolenskii et al.[45] as evidenced by hysteresis loop measurements at liquid nitrogen temperature on a polycrystalline sample.

$Sr_2Nb_2O_7$ polymorphs originate from a high temperature prototype structure belonging to the orthorhombic space group Cmcm. All polymorphs are characterized by stacked perovskite-type slabs containing corner-shared BO_6 octahedra and twelve-coordinated "A" cations.

Figure 1.4b compares the atomic positions in the high temperature paraelectric Cmcm and in the ferroelectric normal phase $Cmc2_1$. Successive phase transitions as a function of temperature are summarized in Figure 1.5. The dielectric constant follows the Curie-Weiss law above T_C.[46] The crystallographic analysis of all possible paraelectric-ferroelectric phase transitions in terms of point group symmetry shows that the mmm to mm2 transition is allowed and it is characterized by a continuous change in P_s. The transition is represented in Shuvalov notation as: mmm(1)DmFmm2. Below the ferroelectric Curie temperature T_C, there is a slight deformation of the oxygen atom framework in the perovskite-like slab which can be regarded as a small rotation of the NbO_6 octahedra around axes parallel to the a-direction. This results in a spontaneous polarization parallel to the c-axis in the ferroelectric phase. The phase transition is a second order transformation.[47]

The major structural difference between paraelectric $Sr_2Nb_2O_7$ and ferroelectric $Sr_2Nb_2O_7$ is the degree of deformation of the perovskite-type layers. In $Sr_2Nb_2O_7$, the arrangement of O atoms is largely deformed from the ideal in the ferroelectric phase, in contrast to the nearly regular arrangement in the paraelectric phase. The centrosymmetric structure of the undistorted phase results in the paraelectric character of $Sr_2Nb_2O_7$ crystals above the Curie temperature.

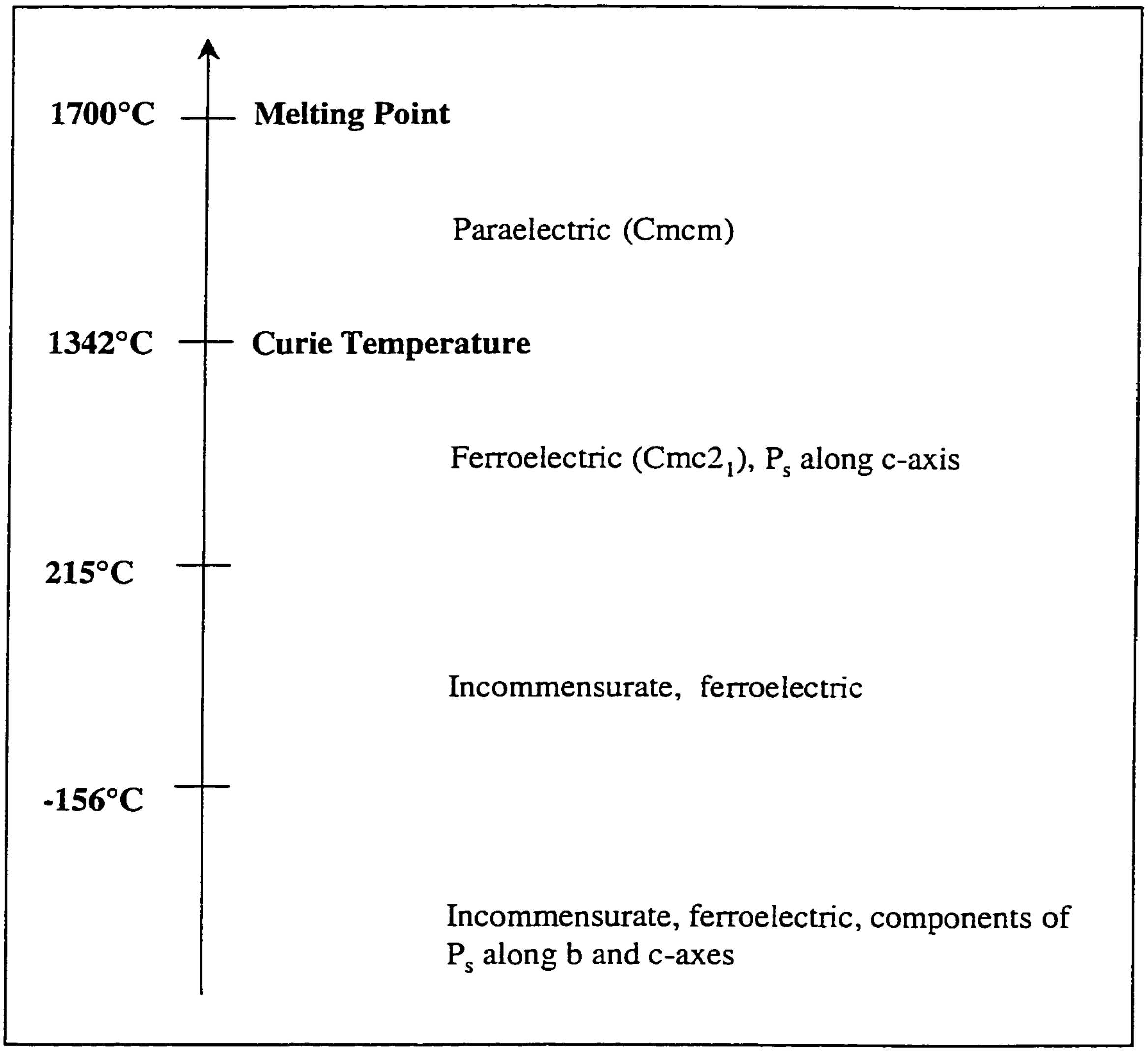

Figure 1.5 Phase transitions in $Sr_2Nb_2O_7$ as a function of temperature [47].

The dielectric behavior of single crystal $Sr_2Nb_2O_7$ is shown in Figure 1.6. There is a low temperature phase transition at about –156°C. This transition is ferroelectric and results from the tilting of the spontaneous polarization towards the b-axis at T_o. P_s is $2\mu C/cm^2$ at 4.2 K. The symmetry below T_o is point group m if the slight incommensurate nature of the structure below 215°C is neglected.

1.3.4 Effect of Substitutions on Ferroelectricity in $Sr_2Nb_2O_7$

Extensive solid solution exists among systems with the $A_2B_2O_7$ compounds as end members. Nanamatsu et al.[46] reported that the solid solution $Sr_2(Ta_{1-x}Nb_x)_2O_7$ exists over the entire composition range. The system obeys Vegard's Law for solid solutions, and the lattice parameters vary linearly with concentration of solute. The ferroelectric phase transition temperature increases non-linearly from -107°C to 1342°C with increasing x. It is assumed that this difference is due to the differences in electronic polarizability and band structure of Ta and Nb. The solid solutions of $Sr_2(Ta_{1-x}Nb_x)_2O_7$, $(Sr_{1-x}Ca_x)_2(Ta_{1-x}Nb_x)_2O_7$, $(Sr_{1-x}Ca_x)_2Nb_2O_7$, $(Sr_{1-x}La_x)_2(Ta_{1-x}Ti_x)_2O_7$ were reported to form a single phase up to x=1. Ba and Pb showed limited solubility in $Sr_2Nb_2O_7$. Replacement of Sr (A) sites by a smaller cation (Ca) increases the phase transition temperature, while partial substitution of Pb or Ba (larger cations) leads to a lowering of the transition temperature as shown in Figure 1.7. The maximum Pb solubility was found to be 25%. No morphotropic phase boundaries in these PLS systems have yet been reported.

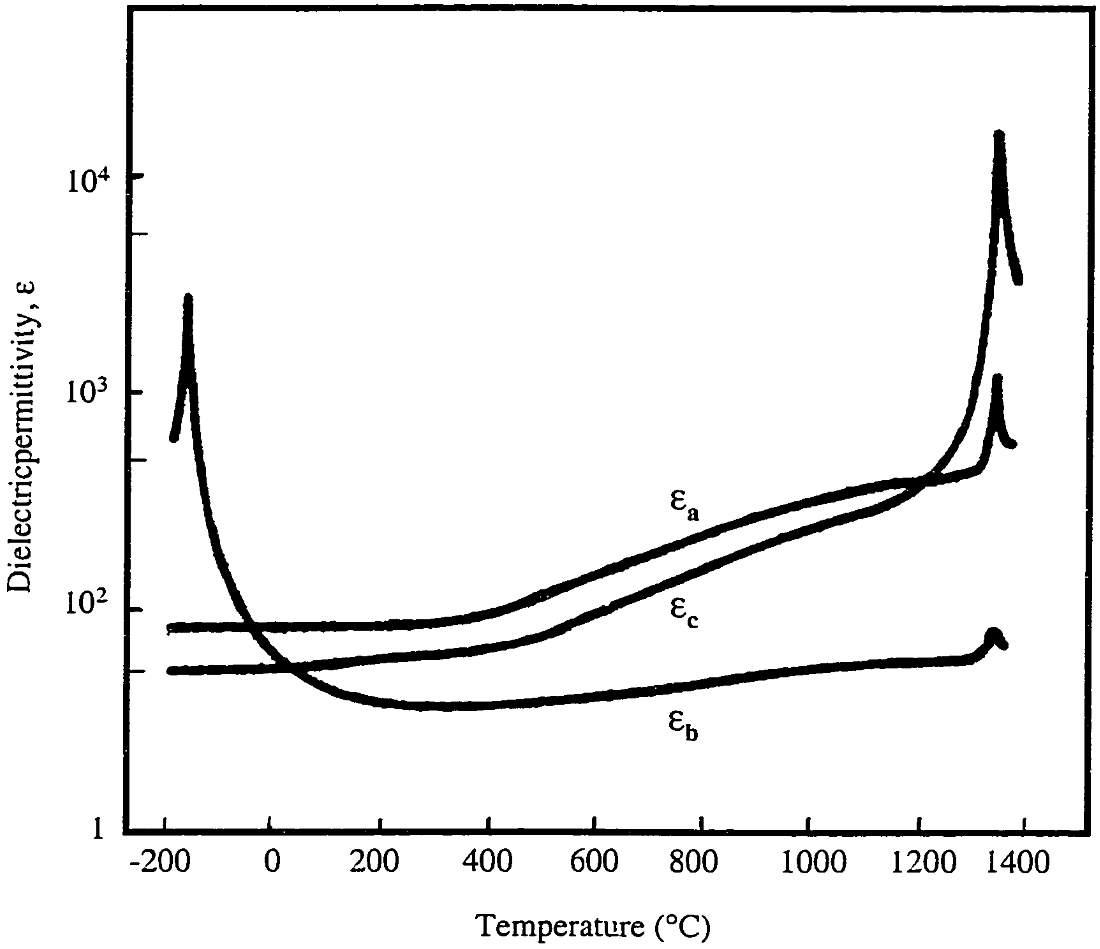

Figure 1.6 Dielectric permittivities of $Sr_2Nb_2O_7$ crystal at 1 MHz as a function of temperature [36].

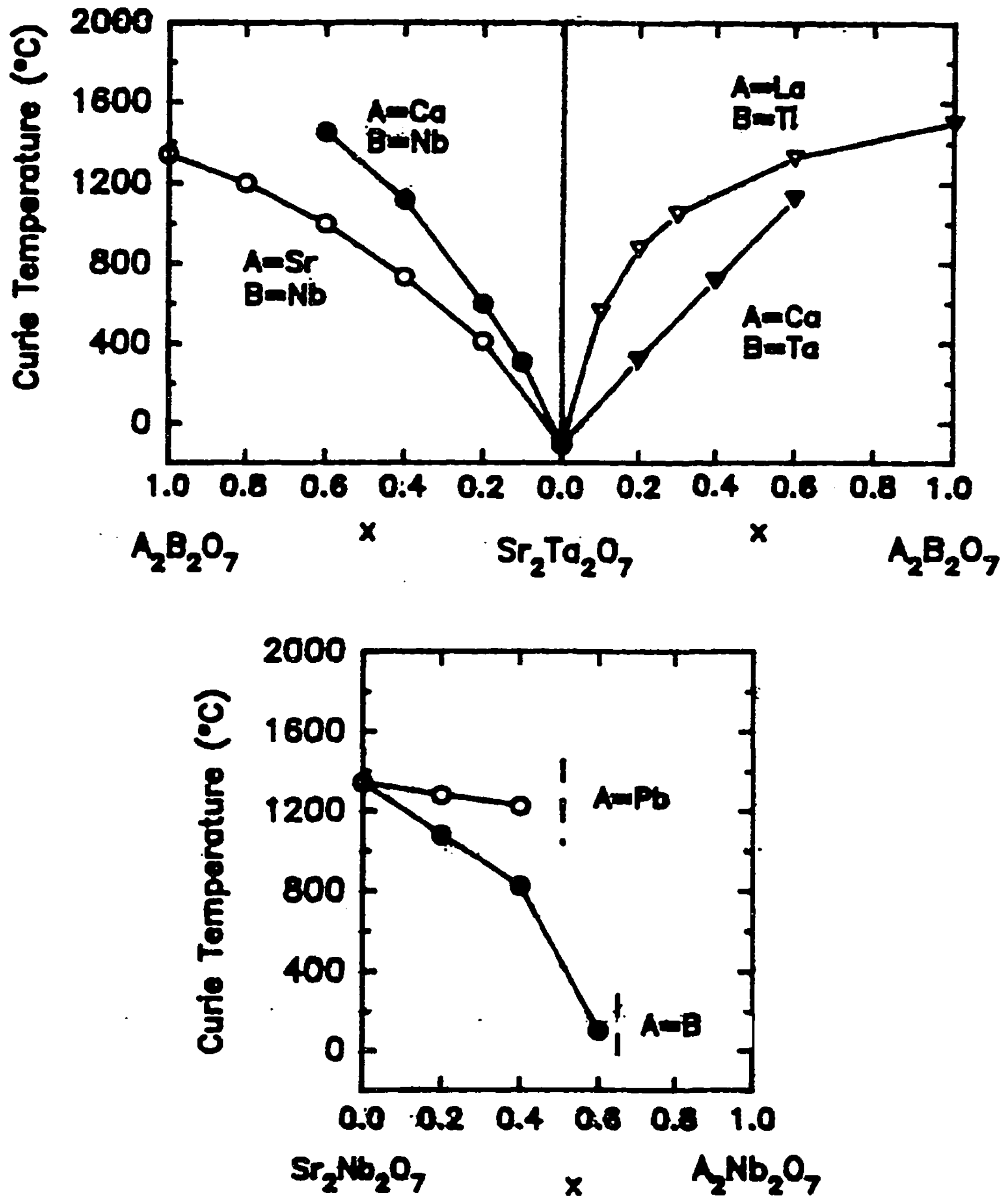

Figure 1.7 Effect of A-site substitution on Curie Temperature of $Sr_2Nb_2O_7$ and $Sr_2Ta_2O_7$ [46].

1.3.5 Textured $A_2B_2O_7$ Ceramics

There have been a number of studies[48-50] on ceramic $Sr_2Nb_2O_7$. None of these studies reported the detection of piezoelectricity in randomly oriented ceramic. Texture in ceramic $Sr_2Nb_2O_7$ and $La_2Ti_2O_7$ was induced by hot-forging, and weak piezoelectricity in modified $Sr_2Nb_2O_7$ and $La_2Ti_2O_7$ was reported by Fuierer et al.[16] Texture in thin films of $Sr_2Nb_2O_7$ has also been reported by Ishitani et al.[51] and by Okuwada et al.[52]

1.4 REFERENCES

1 D. Elwell and H. J. Scheel, Crystal Growth from High-Temperature Solutions, Academic Press, London (1975)

2 A. Linz, V. Belruss, and C. S. Naiman, "Solution-Growth Perovskites," *J. Electrochem. Soc.*, **112** [6] 60C (1965)

3 D. Kolar, "Discontinuous Grain Growth in Multiphase Ceramics," *Ceram. Trans.*, **7** 529-44 (1988)

4 F. Shimanskij, M. Drofenik, D. Kolar, "Subsolidus Grain Growth in Donor Doped Barium Titanate," *J. Mat. Sci.*, 29 [23] 6301-5 (1994)

5 S-H. Hong, W. Cermignani, and G. L. Messing, "Anisotropic Grain Growth in Seeded and B_2O_3-doped Diphasic Mullite Gels," *J. Eur. Ceram. Soc.*, **16** 133-41 (1996)

6 M. F. Yan, "Microstructural Control in the Processing of Electronic Ceramics," *Mater. Sci. Engg.*, **48** 53-72 (1981)

7 J. D. Powers and A. M. Glaeser, "Grain Boundary Migration in Ceramics," *Interface Sci.*, **6** 23-39 (1998)

8 H. Emoto and M. Mitomo, " Control and Characterization of Abnormally Grown Grains in Silicon Nitride Ceramics," *J. Eur. Ceram. Soc.*, **17** 797-804 (1997)

9 N. P. Padture, "In-situ-Toughened Silicon Carbide," *J. Am. Ceram. Soc.*, **77** [2] 519-23 (1994)

10 K. Hirao, M. Ohashi, M. Brito, and S. Kanzaki, "Processing Strategy for Producing Highly Anisotropic Silicon Nitride," *J. Am. Ceram. Soc.*, **78** [6] 687-90 (1995)

11 H. Igarashi, K. Matsunaga, T. Taniai, and K. Okazaki, "Dielectric and Piezoelectric Properties of Grain-Oriented $PbBi_2Nb_2O_9$ Ceramics," *Am. Ceram. Soc. Bull.*, **57** [9] 815-17 (1978)

12 Y. Inoue, T. Kimura, T. Yamaguchi, K. Nagata, and K. Okazaki, " Grain Orientation and Electrical Properties of Hot-Pressed Bismuth Titanate Ceramics," *Yogyo-Kyokai-Shi*, **92** [7] 416-19 (1984)

13 H. Igarashi, M. Fujii, K. Nagata, and K. Okazaki, "Mechanical Properties of Grain Oriented Piezo-Ceramics with Bismuth-Layer and Tungsten-Bronze Structures," *Ferroelectrics*, **49** 189-94 (1983)

14 K. Nagata, Y. Kawatani, and K. Okazaki, "Anisotropies of Hot-Pressed Transparent (Pb, Ba, La) Nb_2O_6 Ceramics," *Jap. J. Appl. Phys.*, **22** [9] 1353-56 (1983)

15 K. Nagata and K. Okazaki, "One-Directional Grain-Oriented Lead Metaniobate Ceramics," *Jap. J. Appl. Phys.*, **24** [7] 812-14 (1985)

16 P.A. Fuierer, "Grain Oriented Perovskite Layer Structure Ceramics for High Temperature Piezoelectric Applications," Ph.D. Thesis, The Pennsylvania State University, University Park, PA (1991)

17 T. Kokubo and N. Suzuki, "Preparation of Grain Oriented Ceramics of Layer-Structure Bi Compounds by Unidirectional Solidification of their Melts," *Yogyo-Kyokai-Shi*, **90** [11] 633-41 (1982)

18 I. Monot, J. Wang, G. Desgardin, and B. Raveau, "Crystal Chemistry of the Texture Formation in Superconductive $YBa_2Cu_3O_{7-\delta}$ Ceramics," *J. Mater. Res.*, **7** [2] 273 (1992)

19 K. Sumiya, S. Watani, F. Hayama, K. Nakamae, and T. Matsumoto, "The Orientation of Magnetic Particles for High Density Recording," *J. Magnetism and Magnetic Mater.*, **2** (1983)

20 Y. V. Pridatchenko and Z. V. Pasechnik, "Flow of Dilute Suspensions of Deformable Ellipsoidal Particles in the Presence of an Applied Electric Field, Unsteady Orientation of Particles," *Fluid Mech. Sov. Res.*, **3-4** (1991)

21 H. Watanabe, T. Kimura, and T. Yamaguchi, "Particle Orientation during Tape Casting in the Fabrication of Grain-Oriented Bismuth Titanate," *J. Am. Ceram. Soc.*, **72** [2] 289-93 (1989)

22 M. Wu and G. L. Messing, "Fabrication of Oriented SiC-Whisker-Reinforced Mullite Matrix Composites by Tape Casting," *J. Am. Ceram. Soc.*, **77** [10] 2586-92 (1994)

23 Y-S. Chou and D. J. Green, "Silicon Carbide Platelet/Alumina Composites: I, Effect of Forming Technique on Platelet Orientation," *J. Am. Ceram. Soc.*, **75** [12] 3346-52 (1992)

24 K. Hirao, T. Nagaoka, M. E. Brito, and S. Kanzaki, "Microstructure Control of Silicon Nitride by Seeding with Rodlike β-Si_3N_4 Particles," *J. Am. Ceram. Soc.*, **77** [7] 1857-62 (1994)

25 M. J. Sacks, G. W. Scheiffele, and G. A. Staab, "Fabrication of Textured Silicon Carbide via Seeded Anisotropic Grain Growth," *J. Am. Ceram. Soc.*, **79** [6] 1611-16 (1996)

26 M. M. Seabaugh, I. H. Kerscht, and G. L. Messing, "Texture Development by Templated Grain Growth in Liquid-Phase-Sintered α-Alumina," *J. Am. Ceram. Soc.*, **80** [5] 1181-88 (1997)

27 B. Brahmaroutu, G. L. Messing, S. Trolier-McKinstry, and U. Selvaraj, "Templated Grain Growth of Textured $Sr_2Nb_2O_7$," pp 883-886, *ISAF '96 Proceedings of the Tenth IEEE International Symposium on Applications of Ferroelectrics Volume II*, Edited by B. M. Kulwicki, A. Amin, and A. Safari, IEEE, Piscataway, NJ (1996)

28 S.-H. Hong and G. L. Messing, "Development of Textured Mullite by Templated Grain Growth," *J. Am. Ceram. Soc.*, **82** [4] 867-72 (1999)

29 J. A. Horn, S. C. Zhang, U. Selvaraj, G. L. Messing, and S. Trolier-McKinstry, "Templated Grain Growth of Bismuth Titanate," *J. Am. Ceram. Soc.*, **82** [4] 921-26 (1999)

30 E. Suvaci, M. M. Seabaugh and G. L. Messing, "Reaction-Based Processing of Textured Alumina by Templated Grain Growth," *J. Eur. Ceram. Soc.*, (1999) in press

31 R. C. Turner, P. A. Fuierer, R. E. Newnham, and T. R. Shrout, "Materials for High Temperature Acoustic and Vibration Sensors: A Review," *Appl. Acoustics*, **41** 299-324 (1994)

32 D. M. Gualtieri and R. C. Morris, "Epitaxial waveguides of aluminum garnet, " *J. App. Phys.*, **74** 20-3 (1993)

33 B. Jaffe, W. R. Cook, and H. Jaffe, Piezoelectric Ceramics, Academic Press, London (1971)

34 Landolt-Bornstein Numerical Data and Functional Relationships in Science and Technology, Vol 16: Ferroelectrics and Related Substances, Springer-Verlag, New York (1981)

35 P. S. Nicholson and N. D. Patel, "Development of AlN High-Temperature Piezoelectric and Use for In-situ Monitoring of Ceramic Machine Tools and HIP Processing," *Ceram. Trans.*, **75** 51-60 (1996)

36 S. Nanamatsu, M. Kimura, K. Doi, and M. Takahashi, "Ferroelectric Properties of $Sr_2Nb_2O_7$ Single Crystal," *J. Phys. Soc. Jpn*, **30** 300 (1971)

37 S. Nanamatsu and M. Kimura, "Ferroelectric Properties of $Ca_2Nb_2O_7$ Single Crystal," *J. Phys. Soc. Jpn.*, **36** 1495 (1974)

38 G. H. Broomfield, "High-Temperature and Post-Irradiation Piezoelectric Properties of Strontium Niobate," *Metall. and Mater. Technol.*, pp. 515-20 (1984)

39 A. Goyal, D. P. Norton, D. K. Christen, E. D. Specht, M. Paranthaman, D. M. Kroeger, J. D. Budai, Q. He, F. A. List, R. Feenstra, H. R. Kerchner, D. F. Lee, E. Hatfield, P. M. Martin, J. Mathis, and C. Park, "Epitaxial Superconductors on Rolling-assisted Biaxially-textured Substrates (RABiTS): A Route towards High Critical Current Density Wire," *Appl. Superconductivity*, **4** [10-11] 403-27 (1996)

40 A. Goyal, F. A. List, and J. Mathis, "High Critical Current Density $YBa_2Cu_3O_x$ Tapes Using the RABiTs Approach," *J. Superconductivity*, **11** [5] 481-87 (1998)

41 D. Liu, X. Yao, and D. M. Smyth, "Structure Intergrowth in Ceramic $SrNbO_{3.5-x}$," *Mat. Res. Bull.*, **27** 387-92 (1992)

42 J.K. Brandon and H.D. Megaw, "On the Crystal Structure and Properties of $Ca_2Nb_2O_7$, Calcium Pyroniobate," *Phil. Mag.*, **21** [8] 189 (1970)

43 W. Kinase, S. Nanamatsu, N. Ishihara, K. Hasegawa, and K. Yano, "On Ferroelectricity of $Sr_2Nb_2O_7$ and other $A_2B_2O_7$-Type Layer-Structure Crystals," *Ferroelectrics*, **38** 849-51 (1981)

44 N. Ishizawa, F. Marumo, T. Kawamura, and M. Kimura, "The Crystal Structure of $Sr_2Nb_2O_7$, a Compound with Perovskite-Type Slabs," *Acta Cryst.*, **B31** 1912-15 (1975)

45 G.A. Smolenskii, V.A. Isupov, A.I. Agranovskaya,"A New Group of Ferroelectric (With Layered Structure)," *Sov. Phys. Solid State (Eng. Transl.)*, **1** [1] 149 (1959)

46 S. Nanamatsu, M. Kimura, and T. Kawamura, "Crystallographic and Dielectric Properties of Ferroelectric $A_2B_2O_7$ (A=Sr, B=Ta, Nb) Crystals and Their Solid Solutions," *J. Phys. Soc. Jpn*, **38** [3] 81 (1975)

47 Y. Akishige, M. Kobayashi, K. Ohi and E. Sawaguchi, "Dielectric and Ferroelectric Properties in the Low Temperature Phase of Strontium Niobate," *J. Phys. Soc. Japan*, **55** [7] 2270-77 (1986)

48 M. Fukuhara, C-Y. Huang, A.S. Bhalla, R.E. Newnham,"Grain Orientation and Electrical Properties of $Sr_2Nb_2O_7$ Ceramics," *J. Mater. Sci.*, vol. **26** 61(1991)

49 V. Prasadarao, U. Selvaraj, S. Komarneni, and A.S. Bhalla, "Sol-Gel Synthesis of Strontium Pyroniobate and Calcium Pyroniobate," *J. Am. Ceram. Soc.*, **75** [10] 2697-701 (1992)

50 N.W. Thomas,"The Influence of Crystal Chemistry on The Ferroelectric and Piezoelectric Properties of Perovskite Ceramics," *Proceedings of the Condensed Matter and Materials Physics '93 Meeting*, pp 1 (1993)

51 A. Ishitani and M. Kimura, "Single-Crystal $Sr_2Nb_2O_7$ Film Optical Waveguide Deposited by rf Sputtering," *Appl. Phys. Lett.*, **29** [5] 289-91 (1976)

52 K. Okuwada, S-I. Nakamura, and H. Nozawa, "Crystal Growth of Layered Perovskite $Sr_2Nb_2O_7$ and $Sr_2Ta_2O_7$ Film by Sol-Gel Technique," *J. Mater. Res.*, **14** [3] 855-60 (1999)

CHAPTER 2

SYNTHESIS OF $Sr_2Nb_2O_7$

TEMPLATE PARTICLES

2.1 INTRODUCTION

The initial template orientation in the green ceramic and relative growth rate of templates during sintering determines the degree of texture that is developed during TGG. The degree of orientation of the templates and their relative growth rates depend on the size and morphology of the template particles. Hence, the ability to grow large single crystal particles with a well defined and anisotropic morphology is crucial for the success of templated grain growth of textured ceramics. To date, highly textured ceramics have been fabricated by TGG using high aspect ratio whiskers or platelets in the 5-50 μm size range.[1-4] Platelet or whisker shaped habits are generally preferred, as templates of these shapes can be oriented by tape casting or extrusion.[5,6] The morphology of single crystal particles (templates) and its relation to the crystal symmetry of the material determine the nature and direction of possible texture. $Sr_2Nb_2O_7$ has a perovskite layer slab structure (PLS), with a room temperature orthorhombic unit cell of a=3.97 Å, b=26.86 Å, and c=5.72 Å.[7] $Sr_2Nb_2O_7$ undergoes a series of transitions, but the crystal structure remains orthorhombic with a slight distortion in the ferroelectric phase.[8] This enables the use of orthorhombic $Sr_2Nb_2O_7$ template particles to produce texture by epitaxial growth at all temperatures up to the melting point.

By regulating the morphology of templates and suitably orienting them in a fine-grained matrix it should be possible to fabricate one dimensionally oriented (fiber texture) or even three dimensionally oriented (sheet texture) ceramics which would exhibit single-crystal-like properties. The required characteristics of potential template particles are (i) a phase that has an epitaxial relation to the matrix grains, (ii) a size that is suitable for TGG (5-50 μm), (iii) anisotropic morphology, and (iv) a relatively cheap synthesis technique to form the template particles.

There are two common methods of synthesizing single crystal particles – solution growth[9,10] and hydrothermal[11] techniques. Single crystal particles of a number of technologically important materials are routinely synthesized by crystallization from critically supersaturated solutions or their melts at high temperatures. Alternately, low temperature methods often employ a flux, such as in molten salt synthesis,[12-15] or use reactive solvents, as in hydrothermal methods. For materials which melt incongruently or exhibit low temperature phase transitions, flux growth can be very useful by effecting crystal growth at temperatures far below the melting point of the product phase.[16] Molten salt synthesis (MSS) provides an environment for enhanced reaction rate and relatively unconstrained growth in the molten flux. The low temperature growth also minimizes the thermal strain during growth and leads to the growth of discrete and faceted single crystal particles with lower defect concentrations.

A number of process parameters, and the chemical and physical properties of the reaction mixture determine the phase, morphology, and size of the final product. For successful MSS, the salt and the reactants must not form solid solutions, and the salt must be the lower melting component. The salt must not react with the reactants or the crucible material and form inseparable impurity phases. It is desirable to have a molten salt viscosity of ~ 1-100 mPa.s as a high melt viscosity can retard the growth process. The single-crystal particles must be easily and completely separable from the solidified mixture by a simple physical separation technique such as selective dissolution. The vapor pressure of the salt must be low at the reaction temperature in order to maintain a constant salt bath chemistry, and to prevent surface crystallization due to evaporation.[16]

Some of the disadvantages of molten salt synthesis are the possible inclusion of salt ions in the growing crystals, precipitation of inseparable impurity phases, and relatively slow growth rates compared to crystallization from pure melts. It is therefore advantageous to have a common cation between the salt and the solute to minimize contamination by other metal ions.

$Sr_2Nb_2O_7$ has a high melting point (~1700°C)[17] compared to alkali metal chlorides, alkali carbonates, and alkaline earth metal chlorides (<1000°C).[18] Strontium borate has been used as a flux to grow strontium niobate crystals by reacting the borate with Nb_2O_5. However, this led to the formation of reduced or strontium deficient $Sr_{0.77}NbO_3$ and $Sr_{0.83}NbO_3$ phases.[19] Therefore, alkali halides (KCl, NaCl), an alkali carbonate (K_2CO_3), and an alkaline-earth chloride ($SrCl_2$) were chosen as potential fluxes to examine the effect of solvents on the phase stability and morphology of $Sr_2Nb_2O_7$.

2.2 EXPERIMENTAL PROCEDURE

The starting materials used in the synthesis of $Sr_2Nb_2O_7$ were 0.5-2 μm sized 99.5% $SrCO_3$ (Cerac Chemicals), 0.3-1 μm sized 99.9% Nb_2O_5 (HCST Starck), and reagent grade KCl, NaCl, K_2CO_3, and $SrCl_2$ (Alfa Æsar). $SrCO_3$ and Nb_2O_5 were mixed in the desired ratio by ball milling for 12 h prior to the addition of the salt. Ball milling was carried out using 6 mm cylindrical zirconia grinding media in 2-propanol. Salt was then added and mixed for 4 h before drying, and the mixture was sealed in an alumina crucible. Alumina crucibles were chosen because they have a high melting point and low chemical reactivity with the salts used in this study. The sealed crucible was heated above the melting point of the salt. After the reaction, the crucible was cooled to room temperature at 3-5°C/min. The single crystal particles were separated from the mass of solidified salt by washing eight times in hot (~90°C) deionized water to ensure complete removal of the salt.

2.3 RESULTS AND DISCUSSION

2.3.1 Effect of Molten Salt

Stoichiometric mixtures of $SrCO_3$ and Nb_2O_5 (Sr:Nb=1) were mixed with different salts and reacted at 1100°C for 6h. The phases obtained in different salts are summarized in Table 2.1. Molten salt synthesis in K_2CO_3 leads to the formation of $Sr_5Nb_4O_{15}$ and Sr_2NbO_4. MSS in KCl and NaCl leads to formation of $Sr_2Nb_2O_7$. However, sodium is known to occasionally form water-insoluble Na-niobates in NaCl which might remain as trace impurities, and can be detrimental to the electrical properties of $Sr_2Nb_2O_7$.[20] An electron dispersive spectroscopy (EDS) scan of the washed product did not reveal residual K^+ or Cl^-. As the sensitivity of EDS is limited, we cannot preclude the possibility of trace inclusion of K^+ or Cl^- in $Sr_2Nb_2O_7$. Therefore, the possibility of using $SrCl_2$ is especially attractive as it minimizes cation-impurity incorporation in $Sr_2Nb_2O_7$. All further studies on template synthesis were carried out in KCl and $SrCl_2$.

2.3.2 Molten Salt Synthesis in $SrCl_2$

The possibility of synthesizing strontium niobate in a strontium chloride melt (melting point = 875°C) was explored by reacting mixtures of anhydrous $SrCl_2$ and Nb_2O_5. The reactions were carried out at temperatures between 900°C and 1100°C. Cuboid-shaped $Sr_2Nb_2O_7$ particles in the 50-200 μm length range were formed when a

Table 2.1 Sr-Nb-O Phase formation in different salts

Salt Used	Phase Formed	Morphology
NaCl	$Sr_2Nb_2O_7$, possible trace $Na_2Nb_8O_{21}$	Rectangular platelets
K_2CO_3	$Sr_5Nb_4O_{15} + Sr_2NbO_4$	Irregular chunky particles
KCl	$Sr_2Nb_2O_7$	Rectangular platelets
$SrCl_2$	$Sr_2Nb_2O_7$ from mixtures of $4SrCl_2 + 1Nb_2O_5$	Large cuboidal crystals

mixture containing a 4:1 molar ratio of $SrCl_2$ and Nb_2O_5 was heated to 900°C for 4h and cooled at 3°C/min to 200°C. Figure 2.1 shows an optical micrograph of these particles.

Thermogravimetry (Figure 2.2) and phase analysis (X-ray diffraction) of $SrCl_2$-Nb_2O_5 mixtures shows that $SrNb_2O_6$ is formed at about 550-570°C by the reaction :

$$SrCl_2(s) + Nb_2O_5(s) + 1/2O_2(g) \text{ ----------> } SrNb_2O_6(s) + Cl_2(g) \qquad (1)$$

The thermodynamic free energy change involved in the conversion of $SrCl_2$ to SrO by reaction with oxygen in the atmosphere is only about 60 Kcal/mole.[16] Further reaction of $SrNb_2O_6$ and $SrCl_2$ above the melting point of $SrCl_2$ (875°C) led to the formation of $Sr_2Nb_2O_7$.

$$SrNb_2O_6(s) + SrCl_2(l) + 1/2O_2(g) \text{ ----------> } Sr_2Nb_2O_7(s) + Cl_2(g) \qquad (2)$$

Observed weight loss corresponds to the change in weight expected for the above reactions.

The use of less than 4 moles of $SrCl_2$ per mole of Nb_2O_5 led to the formation of Sr-deficient $SrNb_2O_6$ and $Sr_{0.83}NbO_3$ at 900°C. For hold times greater than 4 h at 1100°C, hexagonal $Sr_5Nb_4O_{15}$ was the major phase formed in mixtures containing more than 4 moles of $SrCl_2$ per mole of Nb_2O_5. The relative thermodynamic stability of the various phases at the reaction temperature, and the kinetics of the different reactions control phase formation in the Sr-Nb-O system. The reaction between Nb_2O_5 and solid $SrCl_2$ leads to the formation of $SrNb_2O_6$. The formation of Sr-rich phases was not observed even after hold times of 6h at 850°C. However, above the melting point of

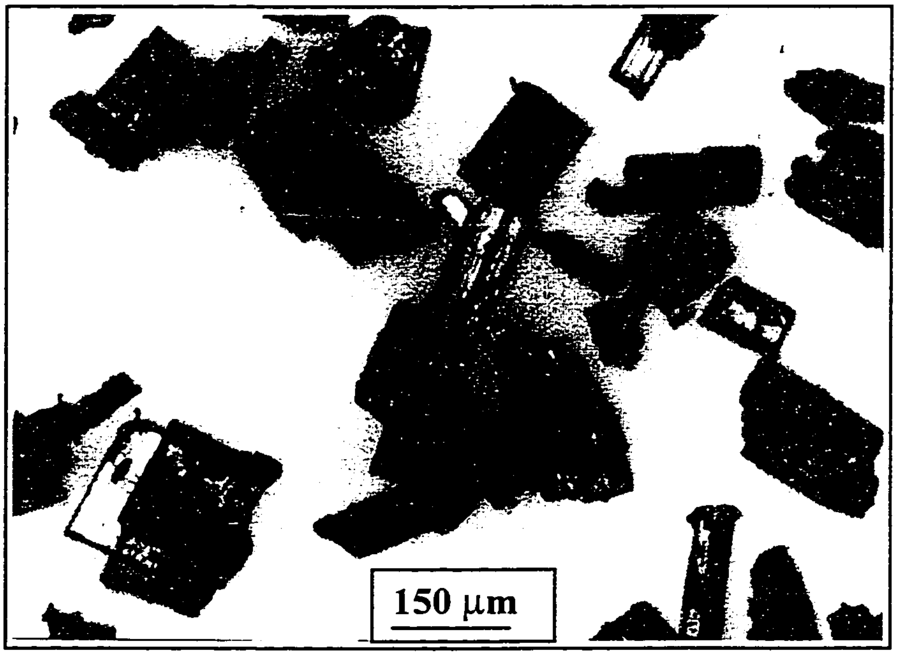

Figure 2.1 SEM micrograph of $Sr_2Nb_2O_7$ particles crystallized from $4SrCl_2$ + Nb_2O_5 mixtures heated to 900°C for 4h and cooled at 3°C/min.

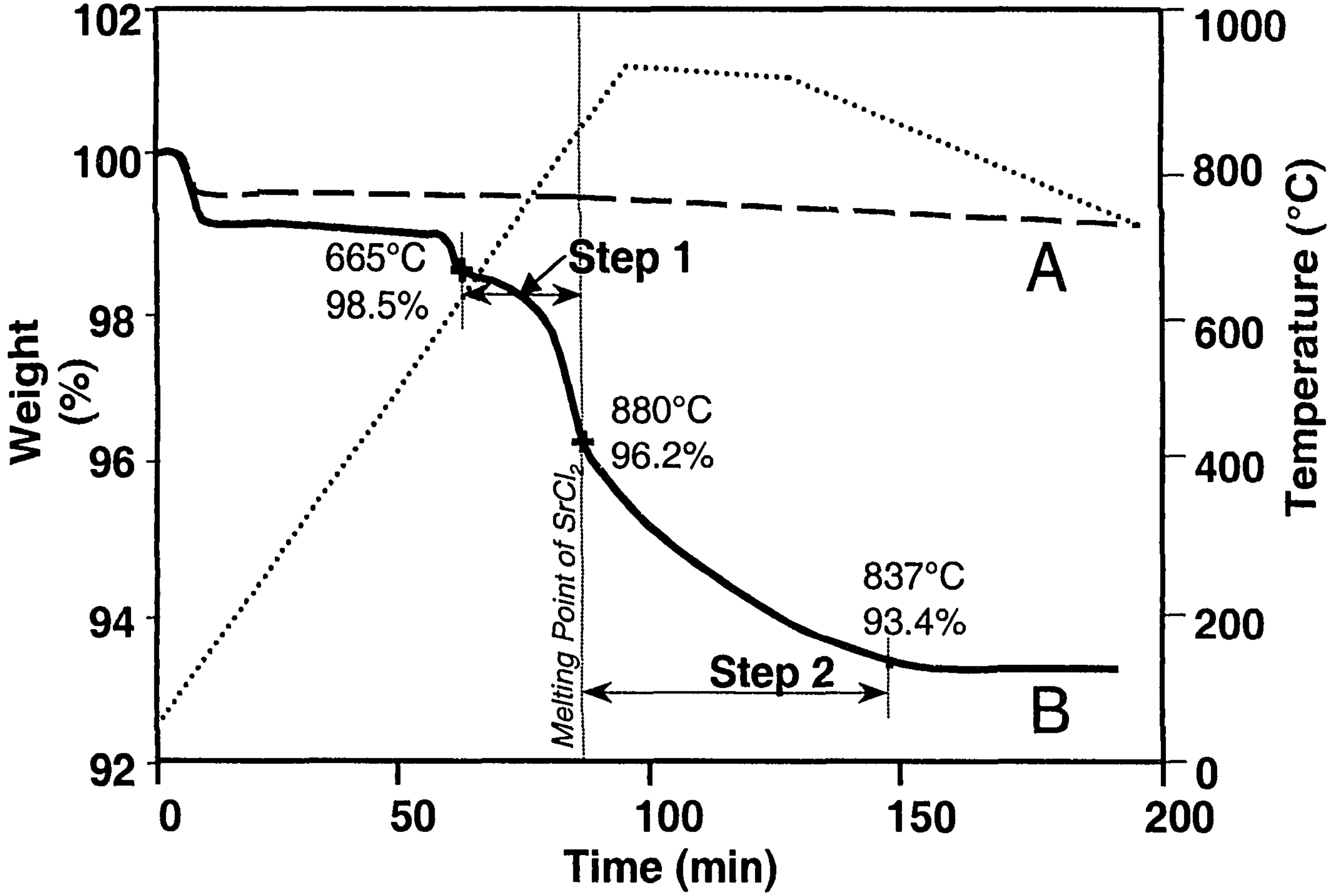

Figure 2.2 Thermogravimetry plot of : (A) $SrCl_2$ shows no significant weight loss even above the melting point, (B) $4SrCl_2 + Nb_2O_5$ mixtures show a two step decomposition. Step 1 prior to melting of $SrCl_2$ corresponds to the weight loss for the formation of $SrNb_2O_6$, and a second gradual step 2 corresponds to the formation of $Sr_2Nb_2O_7$.

$SrCl_2$, Sr-rich $Sr_2Nb_2O_7$ and $Sr_5Nb_4O_{15}$ were formed for $SrCl_2$ to Nb_2O_5 molar ratios greater than 2:1. The large product particle size of ~0.2 mm is indicative of crystallization in a melt. Although data for the solubility of strontium niobate in $SrCl_2$ has not been reported in the literature, crystallization and solubility data for other strontium-transition metal oxide compounds in $SrCl_2$[21,22] suggests these compounds have solubilities of several grams per 100 g of $SrCl_2$ above 875°C.

2.3.3 Molten Salt Synthesis in KCl

Mixtures of 33 wt% $SrCO_3$ and Nb_2O_5 (Sr:Nb=1) were combined with 67 wt% KCl (melting point = 771°C) and reacted at 900-1100°C for 6h in a sealed alumina crucible. Though the crucible was sealed, there was some weight loss (10 to 25 wt% calculated on the basis of initial KCl) due to the escape of H_2O, CO_2, and salt vapor. The amount of weight loss depended on the reaction temperature and time. Faceted $Sr_2Nb_2O_7$ was formed in KCl above its melting point. Figure 2.3 shows the phase evolution with temperature as determined by X-ray diffraction. $Sr_2Nb_2O_7$ formation was observed after 0.5 h at 750°C, below the melting point of KCl. Thermogravimetry showed that $SrCO_3$ starts decomposing at 720-750°C. Much lower $SrCO_3$ decomposition temperatures (550-650°C) and formation of intermediate Sr-Nb-O phases were reported by Neiman et al.[23]

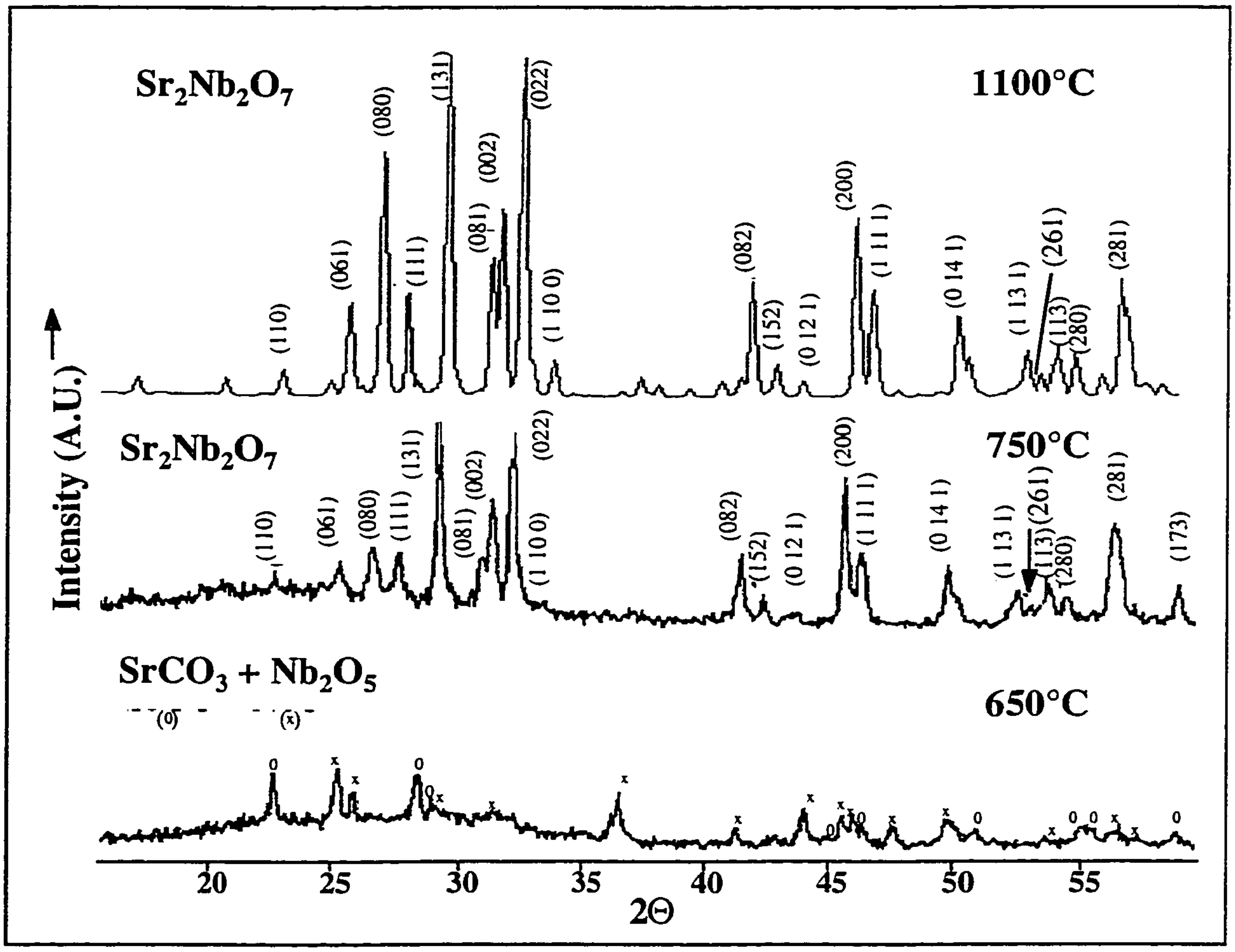

Figure 2.3 Phase evolution of particles synthesized in KCl from $2SrCO_3 + Nb_2O_5$ mixtures as a function of temperature. X-ray diffraction pattern (Cu Kα) of washed reaction products show the absence of Sr-niobates at 650°C and the formation of $Sr_2Nb_2O_7$ at 750°C (below the melting point of KCl).

in the $SrCO_3$-Nb_2O_5 solid state system. This suggests that the formation of $Sr_2Nb_2O_7$ is limited by the onset of $SrCO_3$ decomposition.

Decomposition of $SrCO_3$ leads to the formation of SrO, which has a solubility of ~0.2 g/100g of KCl at 800°C.[16] The solubility does not exceed 1g/100g of KCl even at 1100°C.[16] Nb_2O_5 is insoluble in alkali chlorides.[24] Hence, the formation of $Sr_2Nb_2O_7$ can be expected to be essentially a solid-state reaction process at the surface of the Nb_2O_5 particles. Evidence for the solubility of SrO in KCl was also observed in the formation of 100 μm $SrCO_3$ particles on cooling reaction mixtures of molten KCl and $SrCO_3$ particles with a starting size of 0.5-2 μm. The small but finite SrO solubility in KCl enhances the diffusion of Sr^{2+} and O^{2-} in the vicinity and surface of the solid Nb_2O_5 particles, and the formation of $Sr_2Nb_2O_7$ is rate-limited either by the rate of $SrCO_3$ decomposition, or the reaction of SrO and Nb_2O_5. Since diffusion coefficients in fluxed melts are typically 10^{-6} cm^2/s, which is 3-4 orders of magnitude higher than in the solid state,[25] diffusion is generally not expected to be the rate limiting factor. This is definitely true for short-range diffusion as seen by the formation of phase pure $Sr_2Nb_2O_7$ at relatively low temperatures in molten KCl. However, Sr-rich and Nb-rich phase formation in mixtures of $SrCO_3$ and Nb_2O_5 powder layers separated by an initial layer of KCl demonstrated that long range diffusion of Sr^{2+} and O^{2-} in the melt can be rate-limiting in mixtures with a low degree of mixing of the reactants and large amounts of salt. Therefore, a high degree of mixing, and proximity of the reactants is critical to the formation of the stoichiometric phase. The small solubility of SrO in KCl helps accelerate $Sr_2Nb_2O_7$ formation on the Nb_2O_5 particles, and allows for growth of faceted particles from mixtures containing well-mixed reactants. The decomposition of $SrCO_3$ seems to be the rate limiting step for well mixed compositions.

When a mixture of Nb_2O_5 and KCl was heated above the melting point of KCl, the formation of some $K_2Nb_8O_{21}$ was observed. The formation of potassium niobate is limited by the temperature and rate of conversion of KCl to K_2O. However, no potassium niobate phase was detected by XRD when $SrCO_3$ was present in the initial reaction mixture.

Particles synthesized from mixtures containing 67 wt% KCl and 33 wt% stoichiometric mixture of $SrCO_3$ and Nb_2O_5 at 1100°C for 6h, have a rectangular-platelet morphology with the rectangular face parallel to the crystallographic b-plane (Figure 2.4) which causes enhanced (080) peak intensity in the XRD pattern of platelets lying face down (Figure 2.3). Once formed, neither the size (~1-2 μm) nor the aspect ratio change significantly with reaction temperature or time. This was observed even in compositions that had enough KCl to dissolve all the initial $SrCO_3$. This suggests that once $Sr_2Nb_2O_7$ forms on the surface of Nb_2O_5 it is not very soluble in KCl. An electron dispersive spectroscopy (EDS) scan of the washed product did not reveal residual K^+ or Cl^-.

As explained above, MSS in KCl is a melt-aided reaction rather than a crystallization process. The insoluble Nb_2O_5 particles act as the reaction sites for the

Figure 2.4 SEM micrograph of $Sr_2Nb_2O_7$ particles synthesized from (($2SrCO_3$ + Nb_2O_5 by moles) + 2KCl by weight) mixtures reacted at 1100°C for 6h.

formation of $Sr_2Nb_2O_7$. Formation of strontium niobates in the solid state has been reported to involve the ambipolar diffusion of Sr^{2+} and O^{2-} ions into the Nb_2O_5 particle surface. $Sr_2Nb_2O_7$ forms as Sr^{2+} and O^{2-} diffuse into the Nb_2O_5 particle through the layer of initial reaction product.[23] Assuming a similar reaction mechanism in the melt, the $Sr_2Nb_2O_7$ particle volume was calculated to be 1.74×10^{-19} m^3, based on a one to one number correspondence of $Sr_2Nb_2O_7$ particles to initial Nb_2O_5 particles (0.6 μm spheres of 4.47 g/cm^3 density). The observed volume of a particle ~ 2 μm x 1 μm x 0.1 μm in size is ~ 2×10^{-19} m^3, which is of the same order of magnitude as the calculated value. This suggests that $Sr_2Nb_2O_7$ particle size is limited by the size of the Nb_2O_5 particles.

2.3.4 Seeded MSS in KCl

Larger and more anisotropic single-crystal particles of $Sr_2Nb_2O_7$ can be grown by changing the size and morphology of the growth sites, either by seeding or by changing the composition of the precursor mixture. The use of seeding to increase the size of $SrTiO_3$ particles was reported by Arendt and Pasco.[26]

$Sr_2Nb_2O_7$ seed particles were synthesized by reacting a stoichiometric mixture of $SrCO_3$ and Nb_2O_5 in KCl at 1100°C for 6h as described above. The 2 μm seed particles were mixed with an equal weight of $SrCO_3$ and Nb_2O_5 (in the molar ratio 2:1). The precursor mixture was mixed with KCl (1:2 by weight) and reacted at 1100°C for 6h.

Long, rectangular blade-like particles in the 5-15 μm range are observed along with a small fraction of smaller particles as seen in Figure 2.5. The aspect ratio of the rectangular faces ranges from 3 to 10.

2.3.5 MSS in KCl Melt Using $SrNb_2O_6$ as Nb-source

The above experiments showed that the particle size obtained in molten salt mixtures containing KCl depends on the size of the Nb-rich particles, availability of the Sr-rich reactant at the Nb-rich particle surface, and the reaction rate.

By modifying the reactant mixture in KCl, we can use the morphology of the Nb-rich reactant to control the final $Sr_2Nb_2O_7$ morphology. The SrO-Nb_2O_5 phase diagram[17] shows that the $Sr_2Nb_2O_7$ phase field is bounded by Sr-rich Sr_5Nb4O_{15} and Nb-rich $SrNb_2O_6$. Hence, we studied the synthesis of $Sr_2Nb_2O_7$ particles by reacting combinations of Sr-rich and Nb-rich oxides. Long, blade-like $SrNb_2O_6$ particles, crystallized from $1Nb_2O_5{:}2SrCl_2$ (by moles) mixture heated to 900°C for 4h and cooled at 3°C/min, were mixed with $SrCO_3$ in a 1:1 molar ratio. 5-15 μm long blade-like $Sr_2Nb_2O_7$ particles were obtained by reacting this mixture in KCl at 1100°C for 4 h (Figure 2.6). The highest phase purity was obtained for $SrNb_2O_6$ + $SrCO_3$ mixtures in KCl. $Sr_2Nb_2O_7$ templates synthesized by reacting $SrNb_2O_6$ + $SrCO_3$ mixtures in 67 wt% KCl at 1200°C for 4h (Figure 2.7).

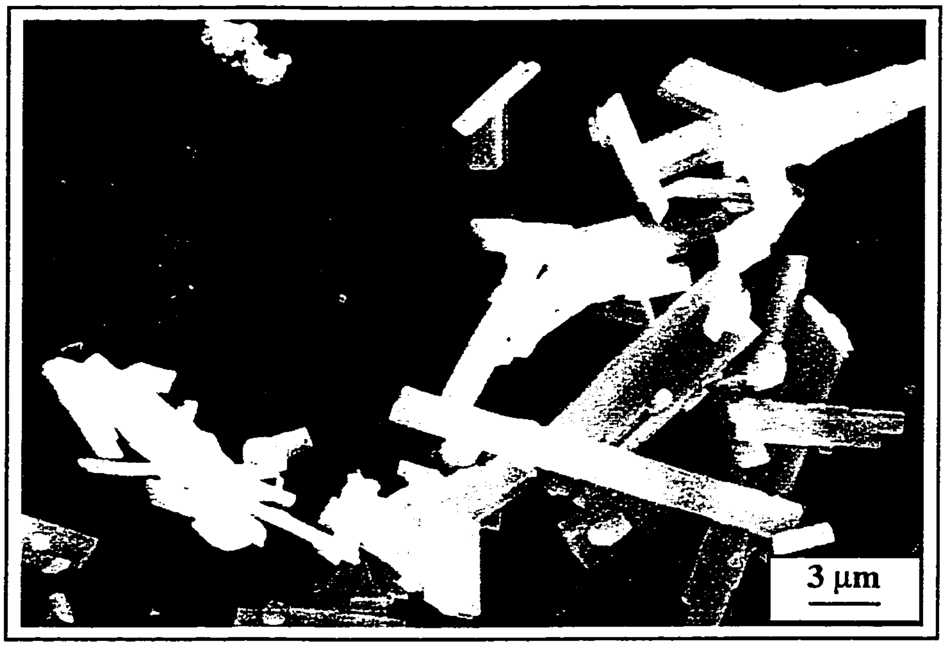

Figure 2.5 SEM micrograph of $Sr_2Nb_2O_7$ particles synthesized from $Sr_2Nb_2O_7$ seeded mixtures in KCl containing 50 wt% $Sr_2Nb_2O_7$ seeds shown in Figure 2.4 + 50 wt% $2SrCO_3 + Nb_2O_5$.

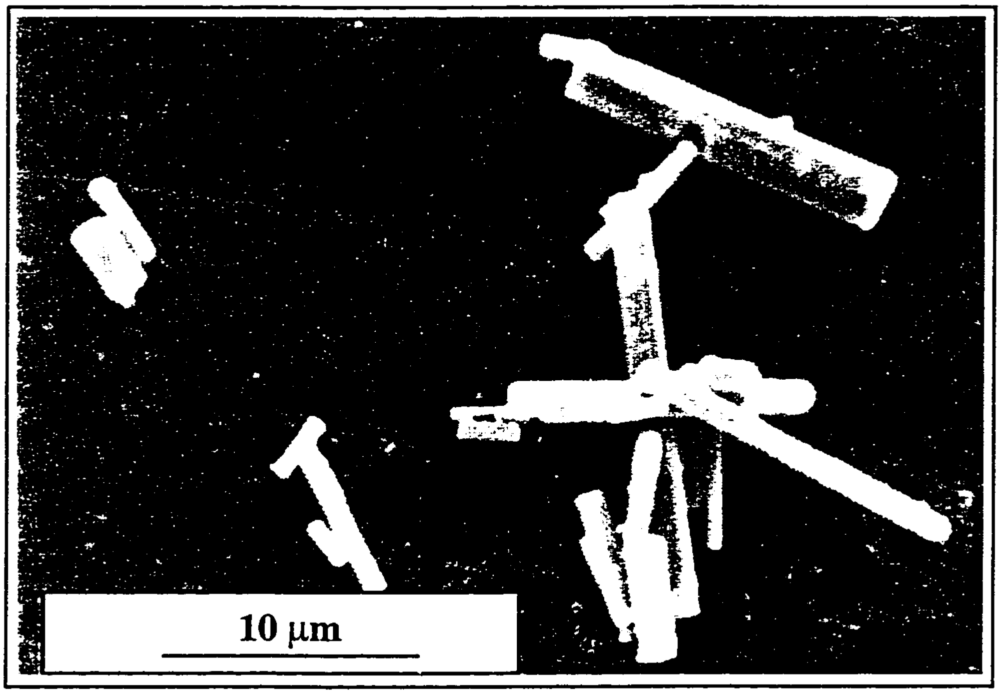

Figure 2.6 $Sr_2Nb_2O_7$ particles synthesized from a mixture of $SrNb_2O_6$, crystallized from $SrCl_2$ and $SrCO_3$ reacted in KCl at 1100°C for 4h.

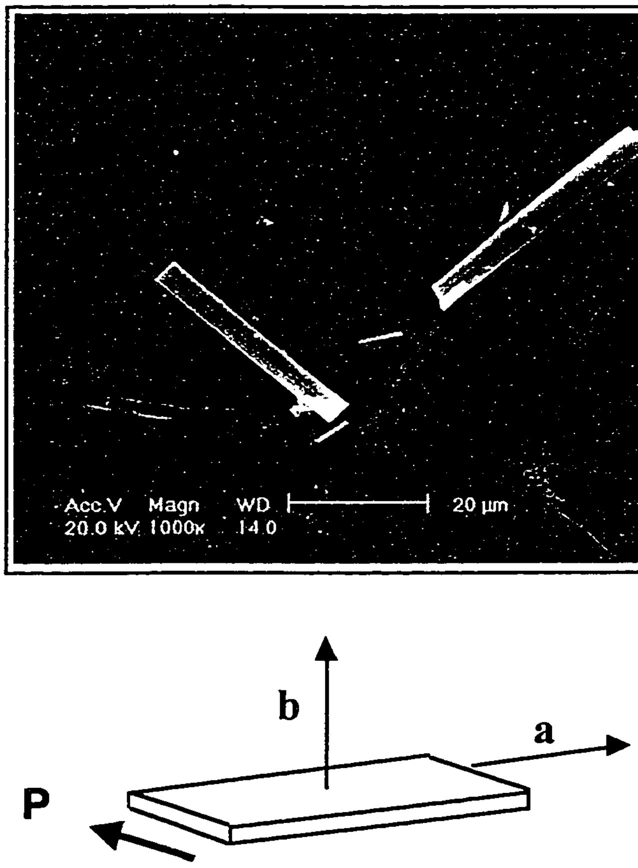

Figure 2.7 Template particles synthesized by reacting $SrNb_2O_6$+$SrCO_3$ in KCl at 1200°C for 4 h, and their relation to crystal structure

2.4 CONCLUSIONS

$Sr_2Nb_2O_7$ particles synthesized in KCl melts by reacting Nb_2O_5 and $SrCO_3$ are too small (1-2 μm) because the particle size obtained in molten KCl depends on the size of insoluble Nb_2O_5. Alternatively, $Sr_2Nb_2O_7$ single crystal particles crystallized from $SrCl_2$ melts are too large (50-200 μm), and not anisotropic enough for successful TGG. High aspect ratio $Sr_2Nb_2O_7$ single crystal particles in the 5-50 μm size range can be synthesized by seeding or by the use of $SrNb_2O_6$ + $SrCO_3$ mixtures in KCl.

FINE MATRIX POWDER

2.5 INTRODUCTION

$Sr_2Nb_2O_7$ fine powder has been synthesized by solid state reaction and sol-gel synthesis.[23,27] Some of the general disadvantages of the solid state reaction route are the contamination during comminution which might lead to degradation of dielectric properties, comparatively large particle size, a particle size distribution which is typically broader than that obtained by chemical routes, higher calcination temperatures and longer reaction times to ensure complete reaction, and the scope for formation of secondary phases due to mixing at a lower scale. On the other hand, sol-gel synthesis of $Sr_2Nb_2O_7$ provides a very high degree of control on the purity and stoichiometry of the nanosized product, and a very low calcination temperature of 700°C as compared to 1000-1200°C for solid state reacted powder.[27] However, sol gel synthesis is unsuitable for forming bulk ceramics because of the high cost of niobium ethoxide, which is one of the precursors used in the process. Another technological problem with the use of sol-gel derived powder is the inability to form a stable dispersion of the nanosized powder, and thus the propensity for exaggerated grain due to the presence of agglomerates.

An alternative to these two techniques is coprecipitation. Most coprecipitation schemes rely on the precipitation of insoluble hydroxides, carbonates, and oxalates which are calcined to obtain oxides.[28,29] The oxides further react in the solid state and form the desired phase.

$Sr(OH)_2$ begins to precipitate at a pH of 13 based on its solubility product (K_{sp}= $3.2x10^{-4}$) in aqueous solutions. On the other hand, strontium oxalate has a much lower solubility product (K_{sp}=$5.6x10^{-8}$),[18] and can be precipitated by using a mixture of oxalic acid and ammonium hydroxide at a much lower pH. Nb^{5+} is precipitated as a hydrated niobium hydroxide from a niobium oxalate solution.[30] Coprecipitation of Sr and Nb can be achieved by drop-wise addition of a solution of $Sr(NO_3)_3$ and niobium oxalate containing excess oxalic acid, to a mixture of oxalic acid and ammonium hydroxide. Coprecipitation also offers the flexibility of incorporating dopants with a high degree of mixing. The phase evolution, powder characteristics, and electrical properties of sintered polycrystalline $Sr_2Nb_2O_7$ are discussed in the following sections.

2.6 EXPERIMENTAL PROCEDURE

Solid state reactions were carried out by calcining stoichiometric mixtures of 67 mol% $SrCO_3$ (0.5-2.0 μm) and 33 mol% Nb_2O_5 (0.3-1.0 μm) at temperatures above the decomposition temperature of $SrCO_3$ (700°C-1400°C). The initial mixture was first ball-milled in 2-propanol for 12 h and dried at 80°C. The reacted powder was comminuted in a SWECO vibratory-mill for 12 h to obtain fine powder (0.6 μm average particle size). The calcined and milled powder was analyzed by X-ray diffraction to determine the phases present.

The starting materials used for coprecipitation were strontium carbonate (Alfa Aesar, 99.994%), niobium oxalate (Niobium Products Company, 20.5 wt% Nb_2O_5), lanthanum oxide (Unocal Molycorp, 99.99%), oxalic acid dihydrate (Fisher, Reagent grade), nitric acid (J.T. Baker, 70%), ammonium hydroxide (J.T. Baker, 30%), and deionized water. The starting Nb-precursor for solid state reactions was Nb_2O_5 (HCST Starck).

The steps involved in coprecipitation are outlined in Figure 2.8. The Sr^{2+} solution was prepared by dissolving a known amount of oven dried $SrCO_3$, which was thermogravimetrically assayed, in a minimum amount of nitric acid by drop-wise addition to form a $Sr(NO_3)_2$ solution. The Nb^{5+} solution was prepared by dissolving the niobium oxalate solid in water in the presence of excess oxalic acid. Since the starting material contains about 0.1% of insoluble material, the solution was filtered and cooled. The exact Nb^{5+} concentration was determined by thermogravimetry. Niobium oxalate solution was

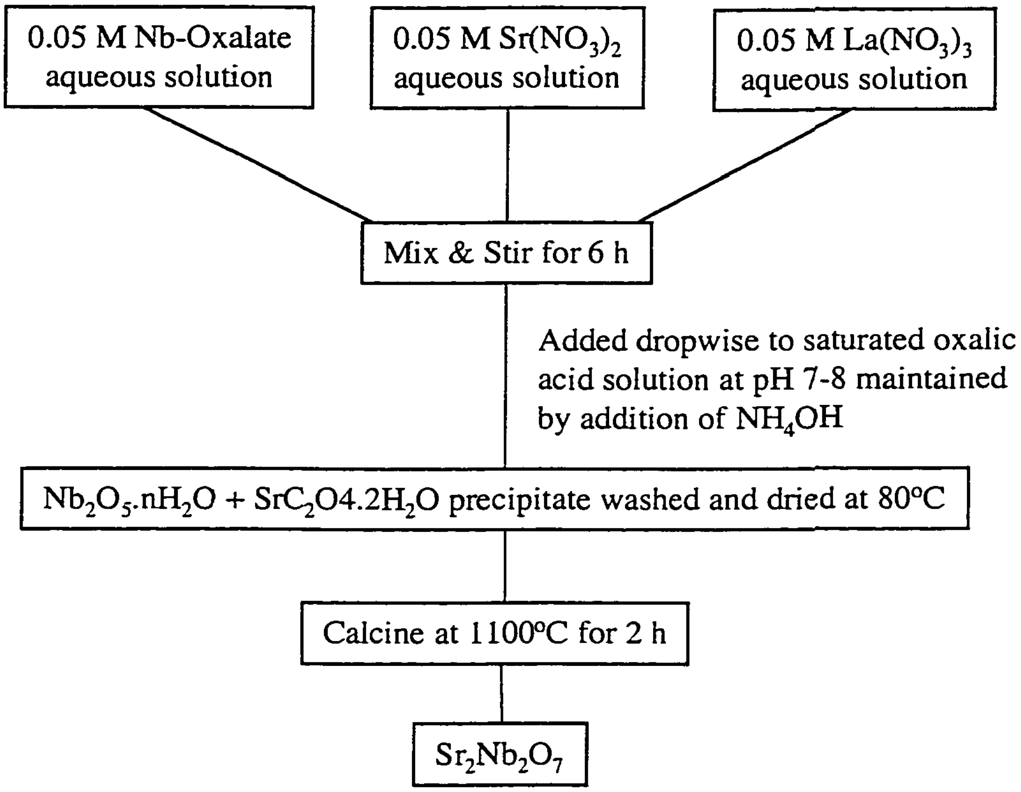

Figure 2.8 Schematic of coprecipitation process

mixed with the strontium nitrate solution to form a 0.1M solution of Nb^{5+} and Sr^{2+} in ~1.2 M oxalic acid at a solution pH of ~0.5-0.8. This solution was stirred for 6h at room temperature.

The conditions for quantitatively complete, simultaneous precipitation of both Sr^{2+} and Nb^{5+} in an ammonium hydroxide-oxalic acid solution were established as a function of pH. It was found that coprecipitation at pH of 7.0-8.5 yielded a 1:1 Sr:Nb ratio in the precipitate. Hence, the coprecipitation was conducted by drop-wise addition of the starting Sr+Nb solution to a bath of oxalic acid plus ammonium hydroxide maintained at a constant pH of 8.0 by frequent addition of NH_4OH. The precipitate was centrifuged, washed with a pH 8.5 aqueous solution of NH_4OH, and dried at 80°C in an oven.

The dried precipitate was analyzed by thermogravimetry and X-ray diffraction analysis to establish calcination conditions for the formation of $Sr_2Nb_2O_7$ powder. The powder was calcined at 1100°C for 2h. The calcined powder was redispersed in 2-propanol by ultrasonification, ball milled, and dried to obtain soft agglomerates for uniaxial pressing of pellets.

Pellets of solid state reacted powder and calcined coprecipitate were used for sintering studies. Uniaxial pressing at 40 MPa was followed by cold isostatic pressing at 275 MPa to obtain green pellets in the 55-60% theoretical density range. The pellets were sintered at temperatures between 1300 and 1550°C, and their densification behavior was studied. Sintered densities were determined by Archimedes technique.

The sintered pellets were used for evaluating dielectric properties. As discussed below, donor doping with La on the Sr site helps lower the dielectric loss at higher temperatures.[31] La-doped powder was also synthesized by the same technique by adding the required amount of La in the form of $La(NO_3)_3$ to the starting solution for coprecipitation and mixing La_2O_3 with the oxide reactants for solid state reacted powder.

2.7 RESULTS AND DISCUSSION

2.7.1 Solid State Reaction

The formation of $Sr_2Nb_2O_7$ was observed at temperatures as low as 900°C. However, the reaction was only completed at 1000°C in 2h. The completion of reaction was the point at which all other Sr-Nb-O phases disappeared, as determined by X-ray diffraction. The kinetics of $Sr_2Nb_2O_7$ formation was affected by process parameters such as bed height and crucible height, which affect the decomposition kinetics. The powder with the highest phase purity was obtained by reactions in powder beds with low heights in low walled crucibles. The powder bed was laid on a platinum foil to avoid possible contamination from the alumina crucibles. The powder used for sintering studies was calcined at 1050°C for 2 h or 1100°C for 2 h.

2.7.2 Coprecipitation

The mechanism of coprecipitation of Sr^{2+} and Nb^{5+} can be understood by considering the mechanisms of precipitation of $Sr(C_2O_4)$ and hydrated Nb_2O_5, separately. The chemistry of niobium species in aqueous solutions containing oxalic acid has been reported by Jehng et al.[32] It was found that the solubility of niobium oxalate in aqueous oxalic acid solutions could be increased to almost 30 wt% by maintaining the oxalic acid concentration at 1-1.2 M. The solubility rapidly decreases to about 1-2 wt% with the addition of excess oxalic acid. The equilibrium between stable niobium oxide complexes containing one, two, or three oxalate groups was found to depend on the solution pH, oxalic acid concentration, and the niobium concentration. The two niobium oxalate species that were found to coexist in aqueous solutions were $[NbO(C_2O_4)_2.H_2O]$ and $[NbO(C_2O_4)_3]$. With increasing pH these units start to polymerize by forming Nb-O-Nb bonds and the formation of dimeric $[Nb_2O_4(OH)_2(C_2O_4)_2]$ at $pH > 3$. Further addition of ammonium hydroxide results in hydrolysis of the dimeric species, forming hydrated Nb_2O_5 precipitate and ammonium oxalate.

SrC_2O_4 has a low solubility (K_{sp}=$5.6x10^{-8}$) and completely precipitates at pH 7. by the following reaction:

$$Sr(NO_3)_2 + H_2C_2O_4 + 2NH_4OH = SrC_2O_4 + 2\ NH_4NO_3 + 2H_2O$$

Complete precipitation of both Sr^{2+} and Nb^{5+} (Sr/Nb=1) can be obtained at a pH of 7-8.5. X-ray diffraction analysis of the oven-dried precipitate showed that the precipitate was composed of $SrC_2O_4.2.5H_2O$, $Nb_2O_5.nH_2O$, and $(NH_4)_2C_2O_4.H_2O$. The solid byproducts of precipitation in the niobium oxalate-strontium nitrate-oxalic acid-ammonium hydroxide system decompose on heating without leaving any residual impurities. This is an advantage of the process over those based on alkali hydroxide precipitants, like KOH, which require extensive washing to remove alkali metal ions.

The results of thermogravimetry and differential thermal analysis are shown in Figure 2.9. The products before and after each decomposition step, and exothermic or endothermic process were analyzed by X-ray diffraction to determine the reaction steps. The precipitate loses its water of hydration and ammonium oxalate decomposes to form gaseous ammonia and carbon dioxide below 300°C, leaving a residue of α-SrC_2O_4 and X-ray amorphous Nb_2O_5. Strontium oxalate loses carbon monoxide to form strontium carbonate, and amorphous Nb_2O_5 crystallizes to form the TT- Nb_2O_5 phase by ~600°C. The solid state reaction of $SrCO_3$ and Nb_2O_5 leads to formation of $Sr_2Nb_2O_7$ as the major phase at 900°C.

In order to ensure complete solid state reaction and a homogeneous product, the powder used for sintering studies was calcined at 1100°C for 2h. The specific area of the calcined powder was measured by a Micromeritics BET surface area analyzer. The change in specific surface area of the synthesized powder as a function of calcination

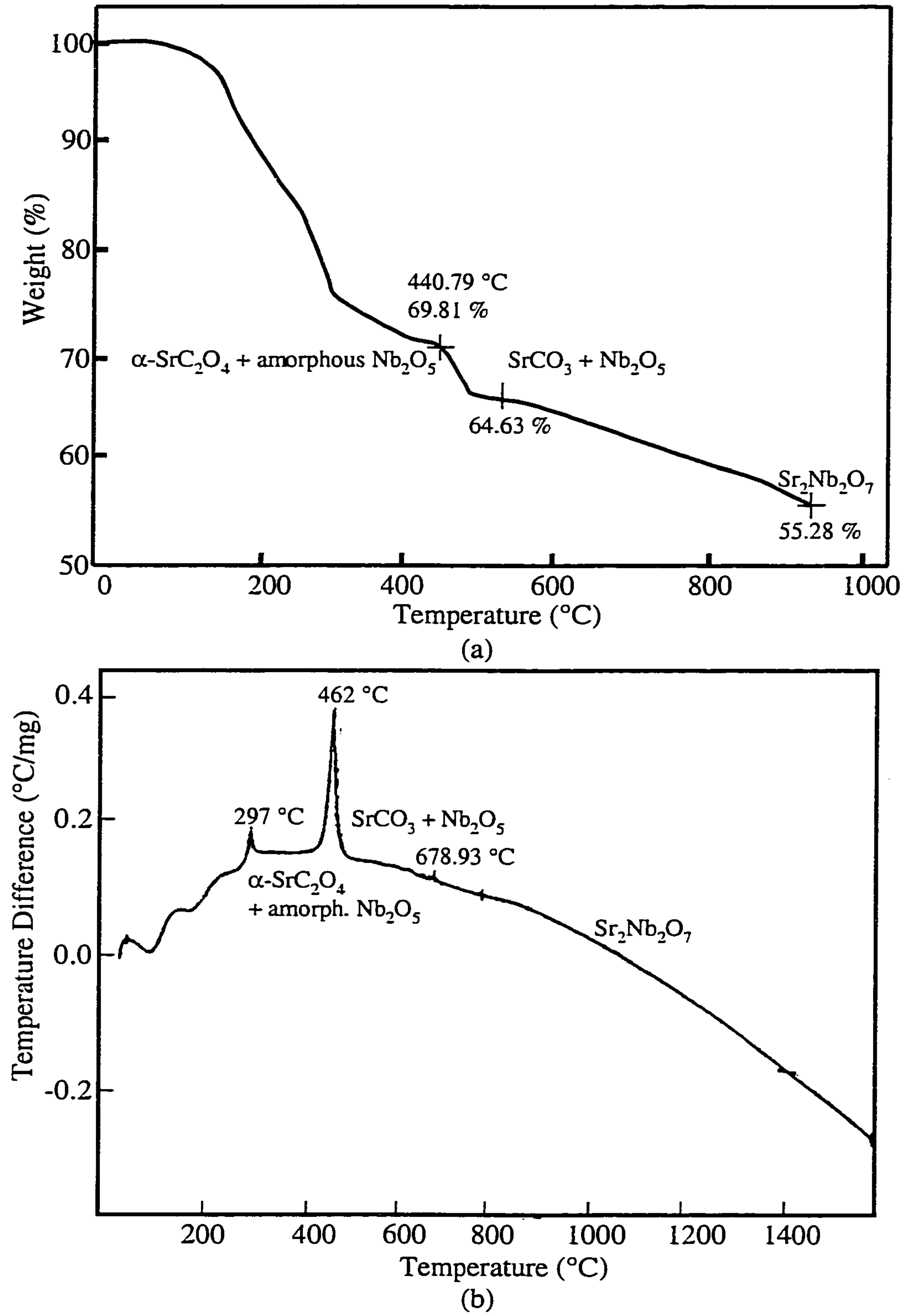

Figure 2.9 Thermal analysis of oven dried (80°C) precipitate. (a) Thermogravimetry (b) Differential thermal analysis data. The phases were identified by X-ray diffraction.

temperature is summarized in Table 2.2. Based on this measurement, the $Sr_2Nb_2O_7$ powder obtained after calcining at 1100°C for 2h has a primary particle size of ~0.25 μm, which is finer than the 0.5-1 μm size range obtained by milling calcined powder obtained by conventional solid state reaction. The X-ray diffraction pattern and the SEM micrograph of the synthesized powder are shown in Figure 2.10.

2.7.3 Sintering Studies

Pellets were sintered to >97% of theoretical density at >1400°C for 2h. Comparison of microstructures of sintered microstructures of pellets fabricated with coprecipitated $Sr_2Nb_2O_7$ and solid state reacted $Sr_2Nb_2O_7$ (Figure 2.11) shows that the powder synthesized by coprecipitation results in a more homogeneous microstructure with fewer large anisotropic grains. This is most probably due to the better mixing of Sr^{2+} and Nb^{5+} species.

2.7.4 Electrical Properties

The dielectric properties of the sintered samples were measured using a Hewlett Packard HP 4172 impedance analyzer. The relatively high dielectric loss makes it impossible to apply a large electric field in order to pole the sample. This dielectric loss has been shown to be due to p-type conduction due to the formation of oxygen vacancies

Table 2.2 Specific surface area of coprecipitated powder as a function of calcination temperature showing the rapid coarsening with temperature and reaction.

Calcination temperature (°C)	Specific Surface Area (m^2/g)
600°C	28
925°C	13
1100°C	5

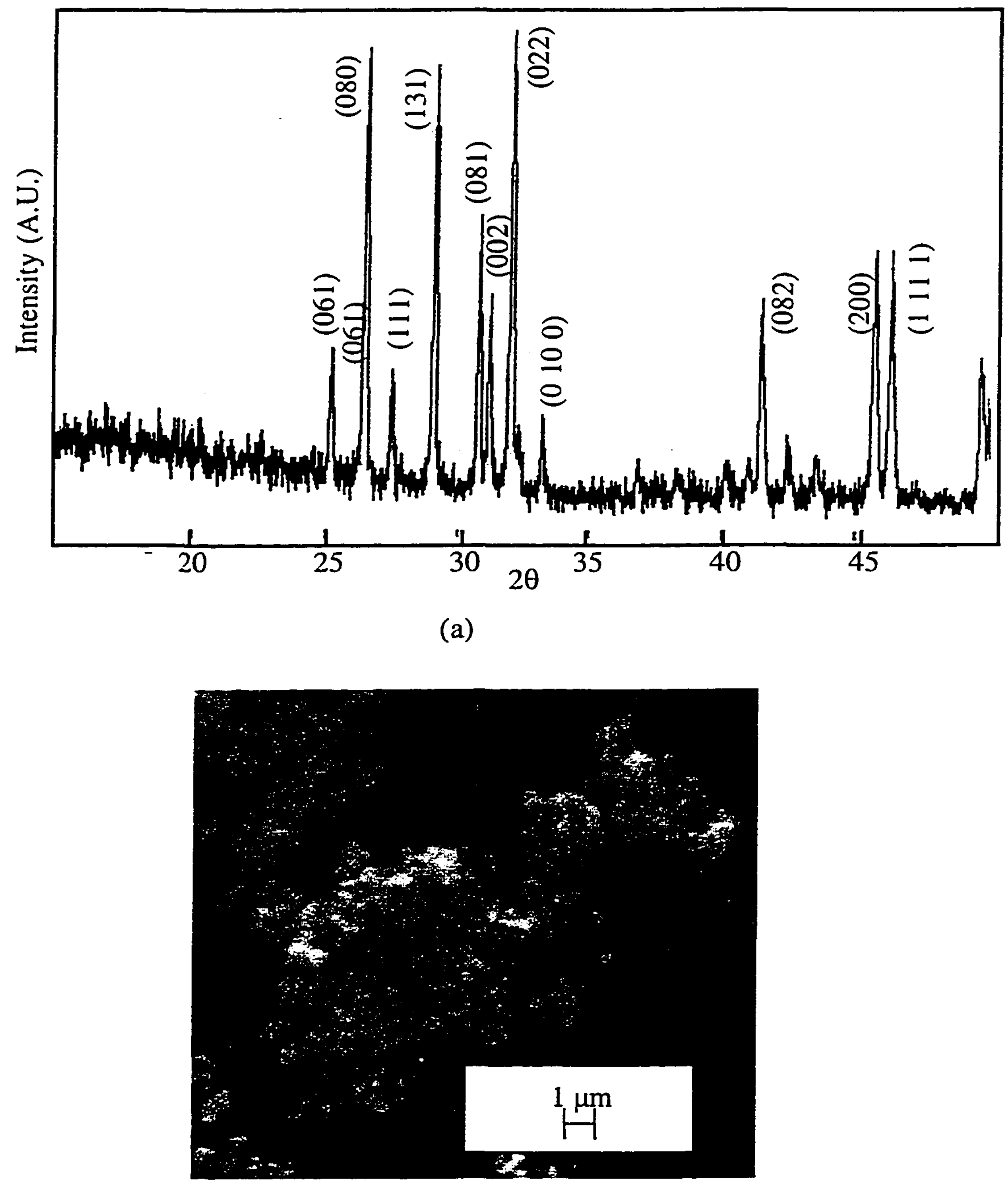

(a)

(b)

Figure 2.10 (a) X-ray diffraction pattern of calcined coprecipitate (1050°C, 2h) showing the formation of $Sr_2Nb_2O_7$, (b) SEM micrograph of calcined and milled coprecipitate (1050°C, 2h)

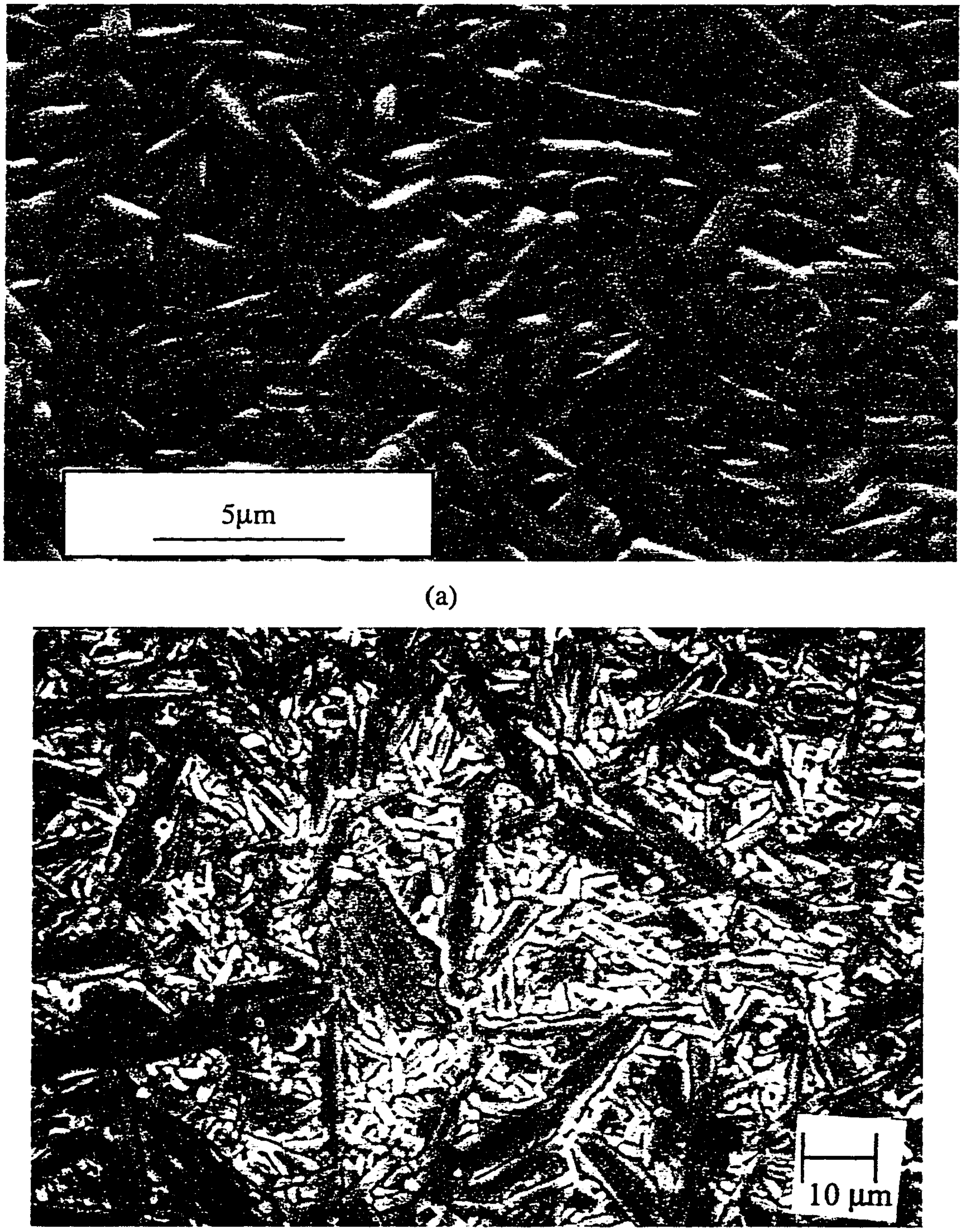

(a)

(b)

Figure 2.11 Comparison of sintered microstructures (a) Coprecipitate powder sintered at 1550°C for 3min, (b) Solid state reacted powder sintered at 1400°C for 1min or acceptor type impurities.[32] The dielectric loss can be suppressed by donor doping the Sr-site with 2 mol% lanthanum or doping the Nb-site with 2 mol% tungsten as shown in Figure 2.12. The addition of lanthanum is easily incorporated in the first step of precursor solution preparation in the form of $La(NO_3)_3$. Lanthanum doping was preferred due to the ease of homogeneous addition of lanthanum during coprecipitation, and the relatively high vapor pressure of tungsten oxides which makes control over stoichiometry difficult. A remanent polarization value of 0.5 $\mu C/cm^2$ was measured, and a partial polarization versus electric field hysteresis loop was observed as shown in Figure 2.13. Although the rounding of the loop at high fields indicates some lossy behavior, the hysteresis loop indicates the ferroelectric nature of coprecipitated $(Sr_{0.9}La_{0.1})_2Nb_2O_7$. The samples had a breakdown strength of ~70-100 kV/cm.

2.8 CONCLUSIONS

$Sr_2Nb_2O_7$ powder with a fine particle size, phase purity, and controlled Sr/Nb ratio was synthesized by calcining a mixed precipitate of strontium oxalate and hydrated niobium hydroxide. The SrC_2O_4 decomposition and TT-Nb_2O_5 crystallization were completed by ~600°C. Solid state reaction of the fine decomposition products led to the formation of the desired phase. Hence it was possible to obtain fine-grained, phase pure powder. The high density sintered microstructure demonstrates inhibition of exaggerated grain growth in the matrix as compared to solid state reacted powder. The dielectric loss

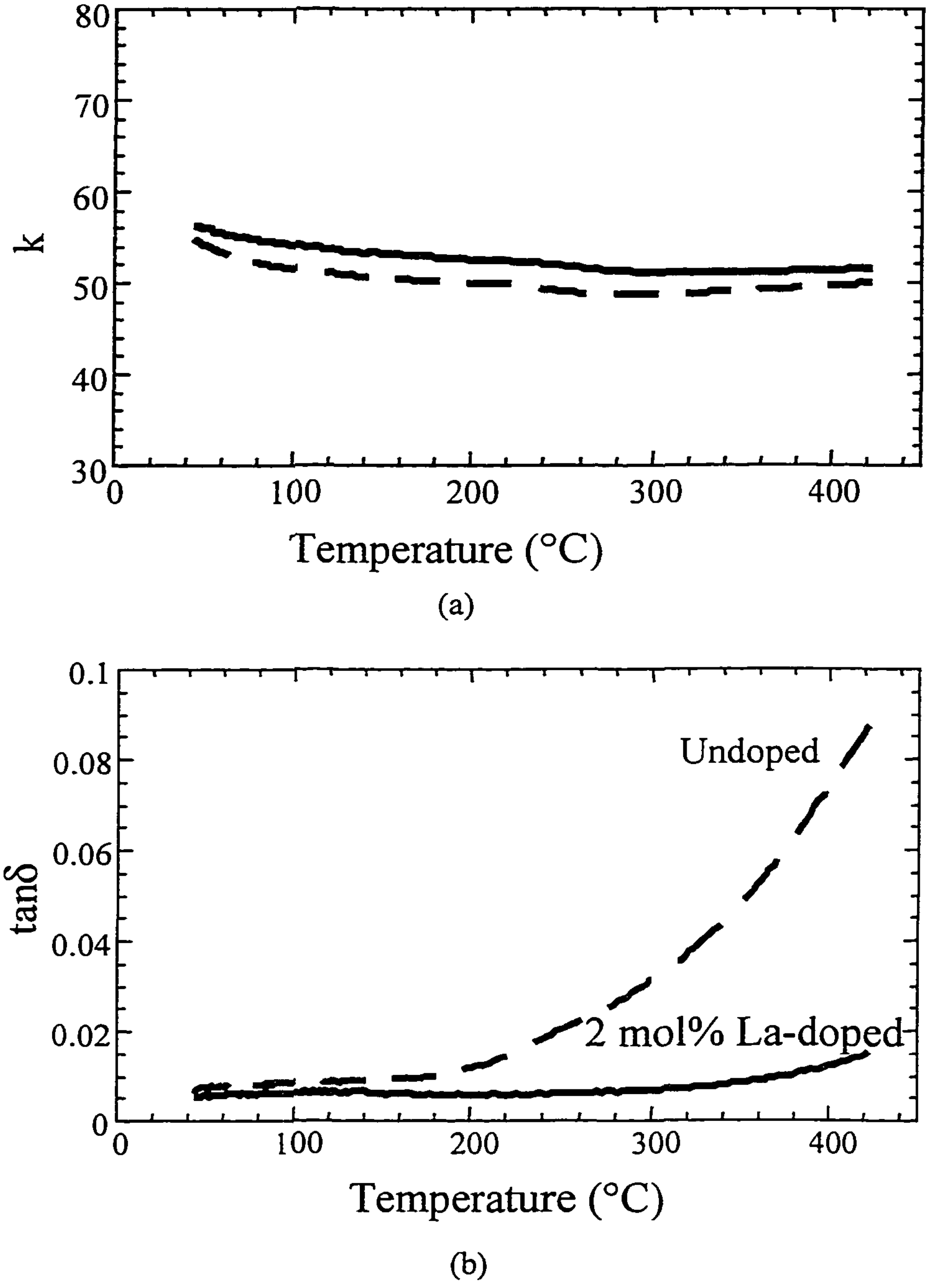

Figure 2.12 (a) Dielectric constant (k) measured as a function of temperature at 1 MHz, (b) Dielectric loss measured as a function of temperature at 1 MHz

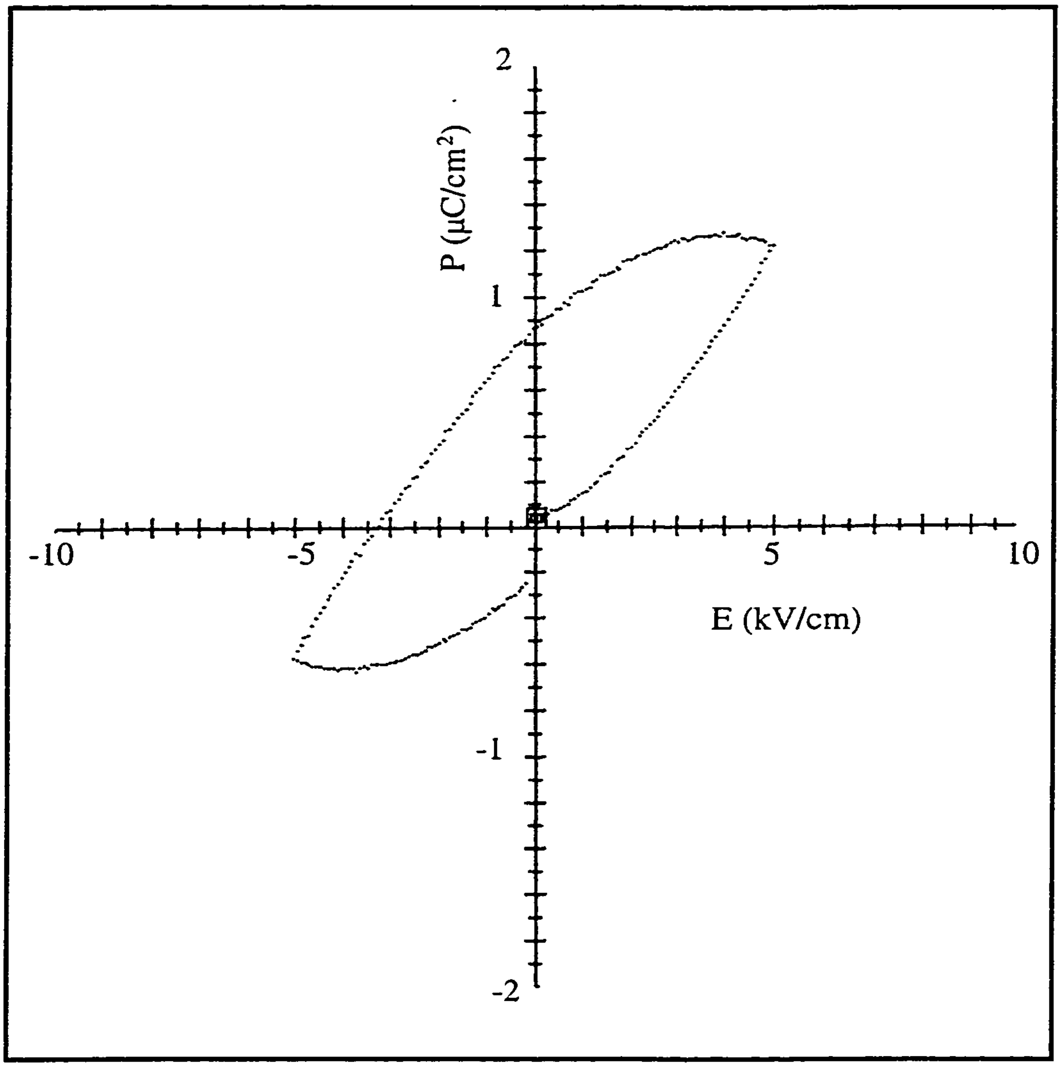

Figure 2.13 Polarization vs. applied electric field behavior for randomly oriented $(Sr_{0.99}La_{0.01})_2Nb_2O_7$ showing a P_r of 0.5 μC/cm^2

can be suppressed by donor doping with lanthanum on the strontium site. Hence coprecipitation is suitable for the production of large quantities of $Sr_2Nb_2O_7$ matrix powder with a controlled stoichiometry. Thus, coprecipitated powder was used for TGG studies of La-doped compositions.

2.9 REFERENCES

1 K. Hirao, T. Nagaoka, M. E. Brito, and S. Kanzaki, "Microstructure Control of Silicon Nitride by Seeding with Rodlike β-Si_3N_4 Particles," *J. Am. Ceram. Soc.*, **77** [7] 1857-62 (1994)

2 M. J. Sacks, G. W. Scheiffele, and G. A. Staab, "Fabrication of Textured Silicon Carbide via Seeded Anisotropic Grain Growth," *J. Am. Ceram. Soc.*, **79** [6] 1611-16 (1996)

3 M. M. Seabaugh, I. H. Kerscht, and G. L. Messing, "Texture Development by Templated Grain Growth in Liquid-Phase-Sintered α-Alumina," *J. Am. Ceram. Soc.*, **80** [5] 1181-88 (1997)

4 S.-H. Hong and G. L. Messing, "Development of Textured Mullite by Templated Grain Growth," *J. Am. Ceram. Soc.*, **82** [4] 867-72 (1999)

5 H. Watanabe, T. Kimura, and T. Yamaguchi, "Particle Orientation during Tape Casting in the Fabrication of Grain-Oriented Bismuth Titanate," *J. Am. Ceram. Soc.*, **72** [2] 289-93 (1989)

6 C. G. Kang and S. S. Kang, "Effect of Extrusion on Fiber Orientation and Breakage of Aluminar Short Fiber Composites," *J. Composite Mater.*, **28** [2] 155-66 (1994)

7 K. Scheunemann and H. Muller-Buschbaum, "Zur Kristallstruktur Von $Sr_2Nb_2O_7$," *J. Inorg. Nucl. Chem.*, **37** 1679-80 (1975)

8 Y. Akishige, M. Kobayashi, K. Ohi and E. Sawaguchi, "Dielectric and Ferroelectric Properties in the Low Temperature Phase of Strontium Niobate," *J. Phys. Soc. Jpn.*, **55** [7] 2270-77 (1986)

9 D. Elwell and H. J. Scheel, Crystal Growth from High-Temperature Solutions, Academic Press, London (1975)

10 A. Linz, V. Belruss, and C. S. Naiman, "Solution-Growth Perovskites," *J. Electrochem. Soc.*, **112** [6] 60C (1965)

11 W. J. Dawson, J. C. Preston, and S. L. Swartz, " Processing Issues of Hydrothermal Synthesis of Dielectric Powders," pp. 27-32 in Ceramic Powder Science IV, Vol. 22, American Ceramic Society, Westerville, OH (1991)

12 W. Schulze "Molten Salt Synthesis of Anisotropic Powders," US Patent # 5270293 (1993)

13 Y. Hayashi, T. Kimura, and T. Yamaguchi, "Mechanism of Flux-Aided Reaction in Ferrite Systems," *Ceram. Bull.*, **64** [9] (1985)

14 L. H. Brixner and K. Babcock, "Inorganic Single Crystals from Reactions in Fused Salts," *Mat. Res. Bull.*, **3** 817-24 (1968)

15 T. Kimura, M. Machida, T. Yamaguchi, and R. E. Newnham, "Products of Reaction Between PbO and Nb_2O_5 in Molten KCl or NaCl," *Comm. Am. Ceram. Soc.*, 195-197 (1983)

16 B. N. Roy, Crystal Growth From Melts: Applications to Growth of Groups 1 and 2 Crystals, John Wiley & Sons Ltd., New York (1992)

17 P. P. Leshchenko, A. V. Shevchenko, L. N. Lykova, L. M. Kovba, and E. A. Ippolitova, "The System SrO-Nb_2O_5," *Russ. J. Inorg. Chem.*, **18** [7] 1202-05 (1982)

18 Lange's Handbook of Chemistry (14th Ed.), Ed. J. A. Dean, McGraw-Hill Inc., New York (1992)

19 B. Hessen, S. A. Sunshine, T. Siegrist, and R. Jimenez, "Crystallization of Reduced Strontium Niobate Perovskites from Borate Fluxes," *Mat. Res. Bull.*, **26** 85-90 (1991)

20 F. Fairbrother, The Chemistry of Niobium and Tantalum, Elsevier Pub. Co., New York (1967)

21 A. Packter and B. N. Roy, "The Crystallization of Alkaline-Earth Metal Tungstates (Molybdates, Chromates, and Sulphates) from Metal Chloride Salts," *Kristall und Technik*, **6** [1] 39-51 (1971)

22 A. Packter, "The Crystallization of Alkaline-Earth Metal Oxides from Metal Chloride Melts: Solubility-Temperature Phase Diagram Analyses and Preliminary Experimental Studies," *Kristall und Technik*, **15** [4] 413-20 (1980)

23 Y. Neiman, I. P. Zapasskaya, A. L. Podkorytov, and V. M. Zhukovskii, "The Macromechanism of the Solid-phase Reactions of Alkaline Earth Metal Carbonates and Oxides with Niobium(V) and Molybdenum(VI) Oxides," *Russ. J. Inorg. Chem.*, **28** [9] 1259-63 (1983)

24 B. N. Roy, S. Appalasami, and A. Packter, "The Crystallization of Alkaline-Earth Metal Titanates from Metal Chloride Melts; Nucleation and Final Crystal Sizes," *J. Cryst. Growth*, **36** 311-18 (1976)

25 M. Blander, Molten Salt Chemistry, Interscience Publishers, New York (1963)

26 R. H. Arendt and W. D. Pasco, "The Molten Salt Synthesis of Large Crystal-Sized $SrTiO_3$," *J. Electrochem Soc.*, **134** [3] 733-736 (1987)

27 V. Prasadarao, U. Selvaraj, S. Komarneni, and A.S. Bhalla, "Sol-Gel Synthesis of Strontium Pyroniobate and Calcium Pyroniobate," *J. Am. Ceram. Soc.*, **75** [10] 2697-701 (1992)

28 J. Takahashi and T. Ohtsuka, "Vibrational Spectroscopic Study of Structural Evaluation in the Coprecipitated Precursors to $La_2Sn_2O_7$ and $La_2Ti_2O_7$," *J. Am. Ceram. Soc.*, **72** [3] 426-31 (1989)

29 N. P. Spitsyna, A. A. Fotiev, P. K. Spitsyn, and Y. A. Raikov, "Synthesis of Yttrium Barium Cuprate by Coprecipitation of Oxalates," *Inorg. Mater.*, **30** [8] 983-86 (1994)

30 L. Marta, M. Zaharescu, I. Haiduc, and C. G. Macarovici, "Synthesis of Strontium Metaniobate by a Coprecipitation Method," *Revue Roumaine de Chimie*, **28** [11-12] 957-66 (1983)

31 P.A. Fuierer,"Grain Oriented Perovskite Layer Structure Ceramics for High Temperature Piezoelectric Applications," Ph.D. Thesis, The Pennsylvania State University, University Park, PA (1991)

32 J-M. Jehng and I. E. Wachs, "Nobium Oxide Solution Chemistry," *J. Raman Spectroscopy*, **22** 83-9 (1991)

Chapter 3

ANISOTROPIC GRAIN GROWTH IN $Sr_2Nb_2O_7$ CERAMICS

3.1 INTRODUCTION

The equilibrium shape of melt grown crystals can be predicted by the Wulff plot on the basis of surface energies for the different planes of the crystal structure.[1] However, grain growth in a ceramic body is affected by a different set of factors, such as the presence of other growing grains, difference in radii of curvature of neighboring grains, impurities, secondary phases, defect chemistry, and the presence of porosity. All of these factors can significantly alter the grain growth rates.[2-6]

Since densification and grain growth during sintering are driven by the same thermodynamic requirement to reduce the total energy of the system, these are competitive processes. Once the densification rate starts to decelerate in the final stage of sintering (>92% of theoretical), coarsening leads to further reduction of the total grain boundary energy by reducing the total grain boundary area. Coarsening has been viewed as a result of mass transport from regions of high curvature which have a higher chemical potential to flatter boundaries which have a lower chemical potential due to lower curvature. The change in surface energy with radius of curvature can be calculated using Young's equation.[7] Several researchers have predicted grain growth laws to explain coarsening based on this model during sintering.[8,9]

Anisotropic grain growth can be viewed as the thermodynamic requirement to replace high surface energy grain boundaries with lower energy grain boundaries formed between low surface energy crystallographic planes. Thus it is somewhat different from curvature driven coarsening. Anisotropic grain growth results in preferential growth of certain crystallographic planes, and explains the presence of anisotropic grains in the equilibrium microstructure. The inherent crystallographic anisotropy of $Sr_2Nb_2O_7$ and the difference in unsatisfied atomic bond densities for different crystallographic planes is expected to result in anisotropic surface energies for different crystallographic planes.[10] Anisotropic grain growth has been observed in other systems possessing anisotropic crystal structures such as SiC,[11] Si_3N_4,[12] Al_2O_3,[13] $Bi_4Ti_3O_{12}$,[14] $PbNb_2O_6$,[15] Na and K β"/β-aluminate,[16] YBCO,[17] and mullite.[18]

In practice, starting powder characteristics such as stoichiometry, compositional homogeneity, particle size distribution, morphology, and degree of agglomeration have a strong influence on the microstructural evolution. Thus, the precursor chemistry and synthesis route have a strong effect on subsequent grain growth during sintering. The presence of impurities or second phases at grain boundaries can lead to a reduction of grain boundary mobility by grain boundary pinning or an equivalent increase in the resistance (or friction) to grain boundary motion.[6,19,20]

Theoretical considerations by Hillert[21] and some practical examples in the literature[9,12] have shown that normal grain growth can give way to exaggerated or discontinuous grain growth due to the presence of a few large grains which are larger than twice the average grain size (critical size for the onset of exaggerated grain growth). Alternately, exaggerated grain growth can occur in a microstructure with a narrow grain size distribution due to the rapid growth of a few grains which are "unpinned" as a result of the inhomogeneous formation and distribution of a liquid phase at certain grain boundaries.[20]

Initial particle morphology is also important as the formation of facets alters the driving force for dissolution in the matrix. The net surface energy of the system can be reduced more efficiently by replacing high- energy grain boundaries between misoriented grains with low energy grain boundaries between oriented grains. The alignment of neighboring particles might also result from grain rearrangement due to the stress imparted on the grains by the growth of neighboring grains.[22]

In multicomponent oxides such as $Sr_2Nb_2O_7$, defect chemistry plays an important role in determining the rate of mass transfer and thus the rates of densification and grain growth.[4,23,24] The defect chemistry also determines the electrical properties such as conductivity. Hence any dopant added to achieve desirable electrical properties should also be expected to alter the sintering behavior. Although isovalent dopants can inhibit grain growth by inducing lattice strain due to ionic size difference, grain growth inhibition is often observed to a greater extent in materials that are doped with aliovalent ions.[6]

In order to determine the relative importance of various phenomena in the specific system of $Sr_2Nb_2O_7$, experiments were designed to distinguish the effects of different variables. The effect of the synthesis technique on sintering behavior was determined by comparing the sintering behavior of powders made by coprecipitation, and solid state reaction as described in Chapter 2. Grain growth was tracked by stereological measurement of grain dimensions in terms of major and minor axes of growing grains. Isothermal sintering experiments at different sintering temperatures were used to determine the growth law: $G^n - G_o^n = \alpha M \gamma t$ and the constant $\alpha M \gamma$, where α is a geometric constant, M is the average boundary mobility, and γ is the grain boundary energy.[7] The mean value of grain size and the standard deviation of the grain size distribution were tracked to determine the onset and extent of exaggerated grain growth. A change in the growth law exponent-'n', or a sudden change in the extent of grain growth with temperature would be indicative of the formation of a liquid phase and the onset of solution-reprecipitation assisted growth. In order to determine the effect of particle size distribution on anisotropic grain growth, and the feasibility of using templated grain growth to produce grain-oriented $Sr_2Nb_2O_7$, the sintering of samples containing varying amounts of large molten salt synthesized template particles was also studied. Densification was followed by studying the sintering shrinkage and density as a function of initial green density, temperature and time. This study was used to determine the activation energy for densification. It also helps track the impingement of anisotropically grown grains and the subsequent desintering that was observed in $Sr_2Nb_2O_7$.[25]

Donor doping was used to increase the resistivity of $Sr_2Nb_2O_7$. This can be accomplished by doping the Sr^{2+}-site with La^{3+}.[26] The amount of dopant in solid solution and the amount of dopant at the grain boundaries was estimated by measuring the lattice parameters by powder X-ray diffraction of crushed powder from sintered samples. The observed change in lattice parameters was well above the detection limit of 10^{-4} to 10^{-5} Å for the instrument.

The understanding developed about the intrinsic sintering behavior of pure and doped $Sr_2Nb_2O_7$ was coupled with studies conducted on samples templated with large, single-crystal particles to determine the conditions required to produce textured $Sr_2Nb_2O_7$ and La^{3+} doped $Sr_2Nb_2O_7$.

3.2 EXPERIMENTAL PROCEDURE

Coprecipitated $Sr_2Nb_2O_7$ powder was prepared by the drop-wise addition of an aqueous precursor solution consisting of 0.05 M $Sr(NO_3)_3$ and 0.05 M Nb-oxalate (Niobium Products Co., Pittsburgh PA, USA) in excess oxalic acid to a solution of ammonium hydroxide and excess oxalic acid maintained at pH 8. The precipitate, composed of SrC_2O_4 and hydrated niobium oxide, was calcined at 1100°C for 2 h and ball milled for 12 h to obtain phase pure, 0.5-0.7μm $Sr_2Nb_2O_7$ as measured by light scattering by Shimadzu SALD particle size analyzer. Particle size measured by light scattering was larger than that estimated by specific surface area measurement. La-doped powder was prepared by adding $La(NO_3)_3$ to the aqueous precursor solution, with subsequent precipitation as lanthanum hydroxide.

Solid state reacted powder was prepared by calcining a ball-milled stoichiometric mixture of $SrCO_3$ (99.994%, Alfa Aesar, Ward Hill MA, USA) and Nb_2O_5 (99.9%, H. C. Starck, Berlin, Germany) at 1100°C for 2 h. The starting powder was milled for 24 h in 2-propanol with a commercial dispersant KD-2 (ICI Chemicals, Wilmington DE, USA) in a vibratory mill. The calcined powder was milled in 2-propanol for 12 h in a vibratory mill to obtain $Sr_2Nb_2O_7$ powder with an average particle size of 0.6 μm. La-doped powder was prepared by the addition of La_2O_3 (99.99%, Unocal Molycorp, White Plains NY, USA) to the starting powder. The coprecipitation and solid state reaction processes are described in detail in Chapter 2.

Samples with relative green densities of 58-60% of theoretical density were selected for sintering studies. These samples were first formed by uniaxially pressing 0.625 cm and 1.27 cm diameter pellets at ~ 70 MPa. This was followed by isostatic pressing at 250 MPa to obtain high green density samples with randomly oriented crystallites.

Samples were sintered isothermally in air from 1300°C to 1550°C for 1-100 min in a horizontal tube furnace. The typical loading and unloading times were 1-2 s, and the samples were estimated to reach the sintering temperature in ~15-20 s. After sintering, the samples were quenched in air. Therefore, the uncertainty in sintering time measurement is very low for hold times >1 min. Hence, hold times of 1, 3, 10, 30, and 100 minutes were chosen. Sintered samples were air quenched. The bulk density of sintered samples was measured by Archimedes' technique. The theoretical density of doped samples was estimated by measuring the unit cell parameters by slow scan X-ray diffraction (Scintag X-ray diffractometer, Model No. MZX 105) of powder crushed from the sintered samples using Si as the reference standard. Peaks in the 5-65° 2θ range were indexed and used for these measurements. For stereological measurements, samples were first polished with 0.1 μm diamond paste and then annealed 100-200°C below the sintering temperature. SEM micrographs with 250-1000 grains from 2-5 random cross-sections were used for stereological measurements. Grain size statistics were computed using the NIH image analysis software.[27] The feasibility of using templated grain growth in La-doped samples was studied using samples initially containing 10 vol% of oriented $Sr_2Nb_2O_7$ template particles and 90 vol% La-doped matrix powder. These samples were fabricated by a tape casting process described in Chapter 4.

3.3 RESULTS AND DISCUSSION

3.3.1 Sintering

Earlier studies on the sintering of solid state reacted $Sr_2Nb_2O_7$ reported an inability to obtain densities >95% by pressureless sintering as a result of dedensification caused by anisotropic grain growth.[26,28] Prolonged anisotropic grain growth leads to wrenching apart of grains and the creation of voids due to a combination of thermal expansion anisotropy and the large grain size, which favors fracture, in $Sr_2Nb_2O_7$. In contrast, in this work, samples of coprecipitated $Sr_2Nb_2O_7$ and solid state reacted $Sr_2Nb_2O_7$ attained a sintered density of ~97-98% after 10 min at 1500°C as seen in Figure 3.1. The presence of large anisotropic grains can be seen in the samples sintered at 1550°C (Figure 3.2). Figure 3.2 also shows the increase in porosity in the microstructure with time at 1550°C. As the increase in porosity was observed under isothermal conditions, the observed dedensification is related to stresses due to impingement of growing grains rather than to thermal expansion anisotropy.

Donor doping with La was found to decrease the dielectric loss as described in Chapter 2. Lanthanum incorporates into the $Sr_2Nb_2O_7$ lattice at a temperature >1250°C. Thus, the theoretical density was calculated for each sintering temperature using lattice parameters measured by X-ray diffraction (Table 3.1). The results of the isothermal sintering experiments are summarized in Figures 3.3 and 3.4. A density of 99% was obtained at temperatures >1400°C. From the data in Table 3.1, it is observed that for the sintering conditions used in this study, a small amount of unreacted La_2O_3 (~15% of the total available La) is present at the grain boundaries.

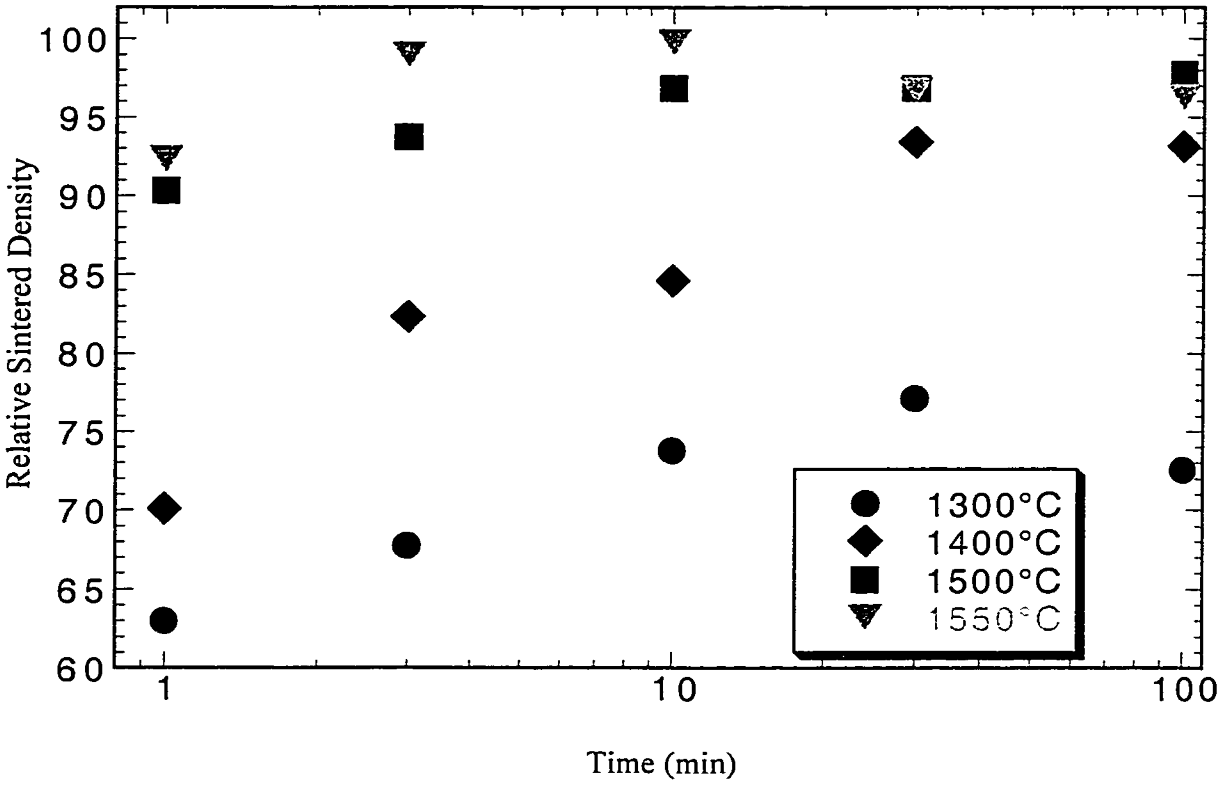

Figure 3.1 Isothermal sintered density as a function of time at different temperatures for $Sr_2Nb_2O_7$

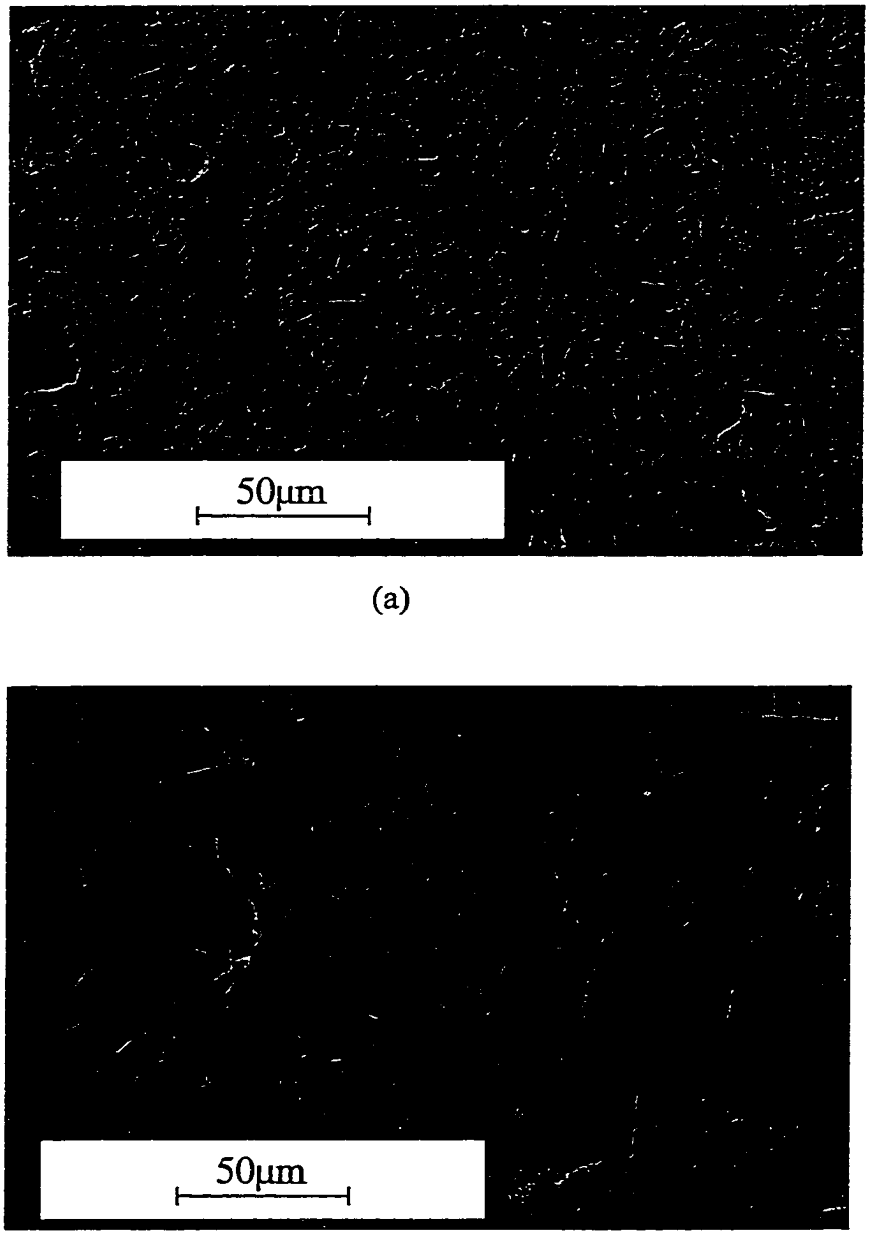

(a)

(b)

Figure 3.2 SEM micrographs of $Sr_2Nb_2O_7$ sintered at 1550°C for (a) 10 min, (b) 100 min

Table 3.1 Calculated lattice parameters and fraction of total available La (2 mol%) incorporated in to the $Sr_2Nb_2O_7$ lattice as a function of temperature.

T(°C)	t(min)	a(nm)	b(nm)	c(nm)	Fraction of La in the lattice
1250	120	0.3955	2.6770	0.5699	0
1350	120	0.3957	2.6734	0.5694	0.75
1450	120	0.3958	2.6719	0.5691	0.85
1550	1	0.3958	2.6708	0.5691	0.85
1550	120	0.3961	2.6704	0.5689	1.00

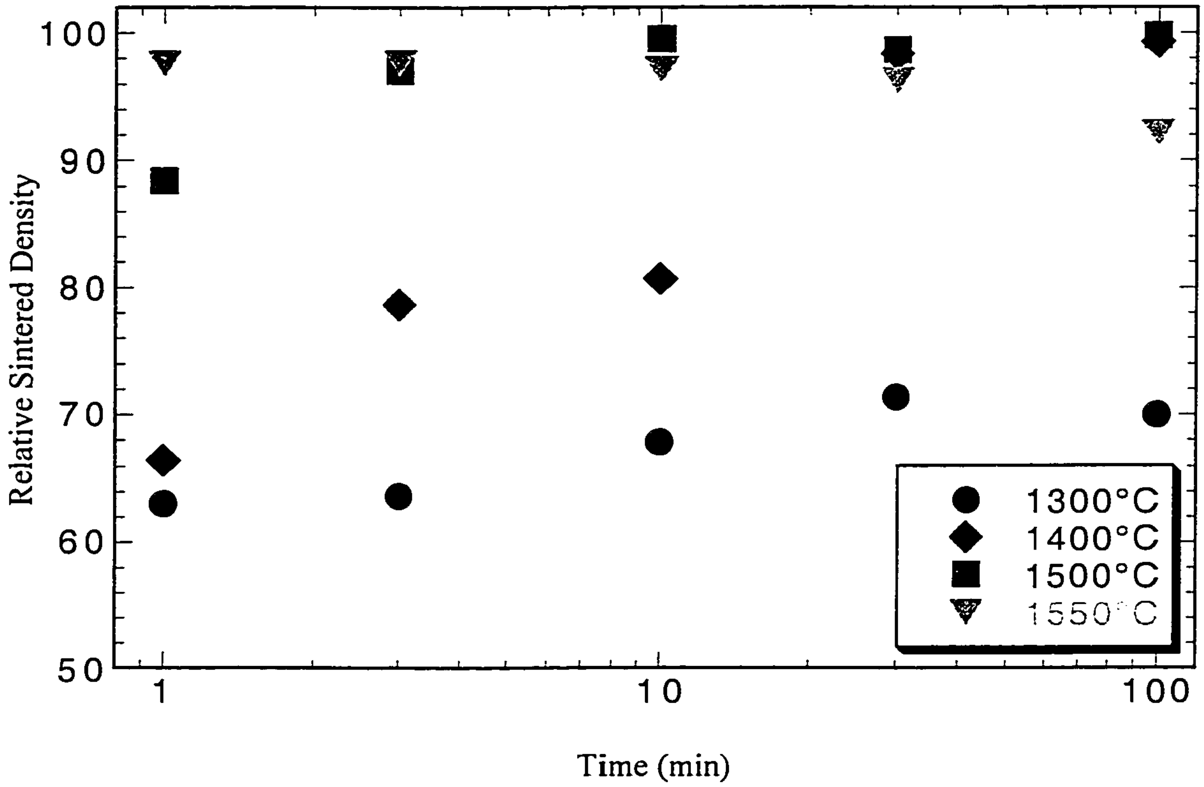

Figure 3.3 Isothermal sintered density as a function of time at different temperatures for 2 mol% La-doped $Sr_2Nb_2O_7$

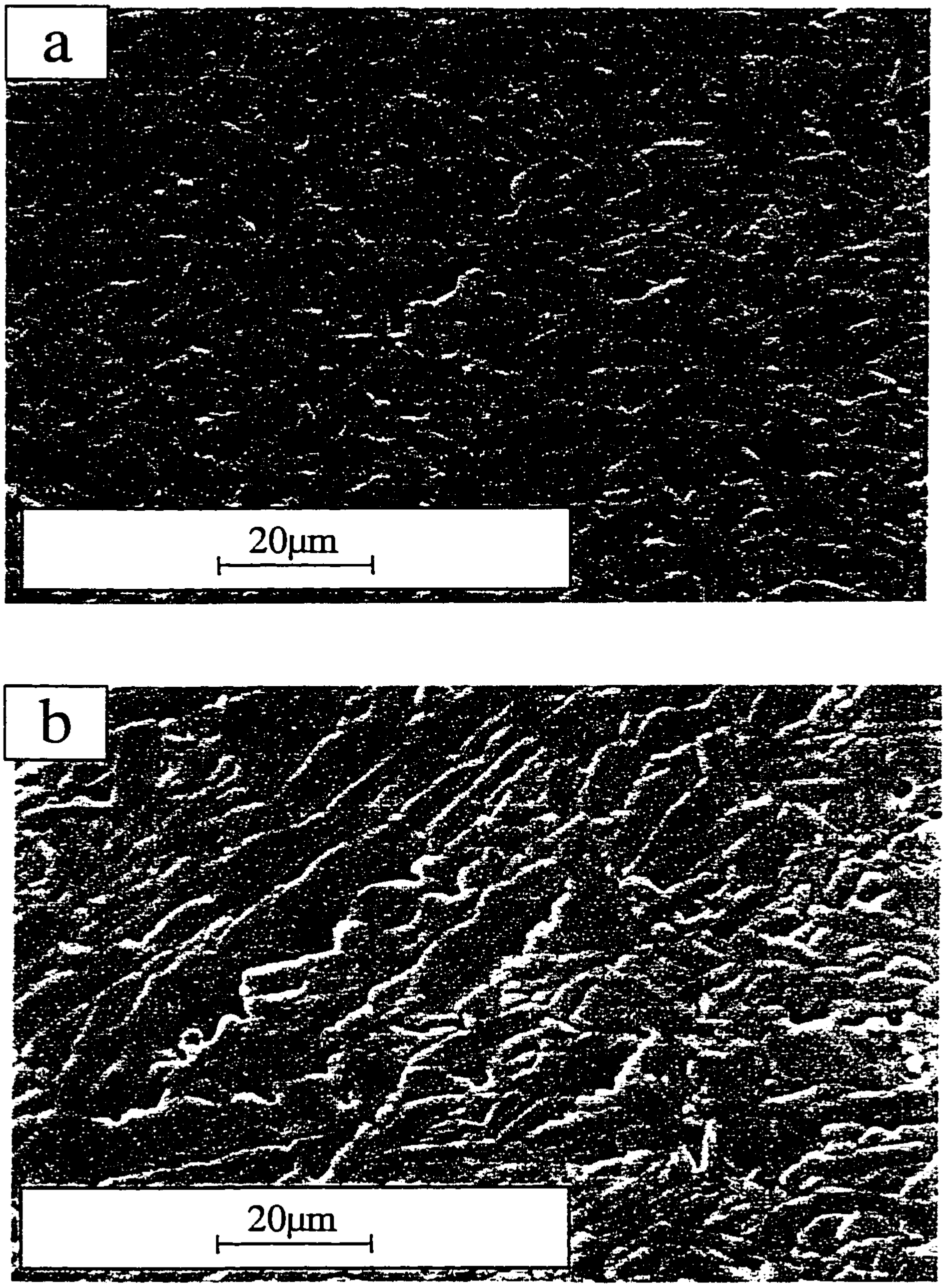

Figure 3.4 SEM micrographs of 2 mol% La-doped $Sr_2Nb_2O_7$ sintered at 1550°C for (a) 10 min, (b) 100 min

3.3.2 Grain Growth in Undoped $Sr_2Nb_2O_7$

Samples of undoped, coprecipitated powder were sintered at 1300, 1400, and 1500°C. In order to understand the effect of stoichiometry on grain growth, samples with Sr:Nb ratios of ~1.05, 1, 0.95 and 0.9 were studied. SEM micrographs of sintered microstructures obtained at 1300°C for 1 h and 1400°C for 1 h for different Sr:Nb ratios are shown in Figures 3.5 and 3.6 respectively. The extent of grain growth in compositions containing excess niobium is clearly evident from these microstructures.

The presence of a liquid layer has been reported to enhance anisotropic grain growth in other ceramic systems.[19,23] The presence of a thin liquid film increases the grain boundary mobility by providing a path for rapid diffusion. The boundary migration rate can be determined by the relative kinetics of diffusion through the liquid film and surface reaction (dissolution).

Large anisotropic grains were observed to form in Nb-rich samples heated to 1300-1400°C which were at least 90% dense. On examining the SrO-Nb_2O_5 phase diagram reported by Leschenko et al.[29] (Figure 3.7) for possible liquid phase compositions that form between 1300°C and 1400°C, it can be seen that phase pure $Sr_2Nb_2O_7$ exists only at a molar ratio of Sr:Nb = 1. For $Nb_2O_5:SrO<0.5$ no liquids form at any of the sintering temperatures in this study. The liquid responsible for grain growth does not form between $Sr_2Nb_2O_7$ and $SrNb_2O_6$ because the grain growth is observed well below their eutectic point of 1450°C. This suggests that the liquid is a result of the reaction between $SrNb_2O_6$ and $Sr_2Nb_{10}O_{27}$, or $Sr_2Nb_{10}O_{27}$ and Nb_2O_5 which form eutectic liquids at 1340°C and 1330°C, respectively. Studies on solid state reaction between SrO

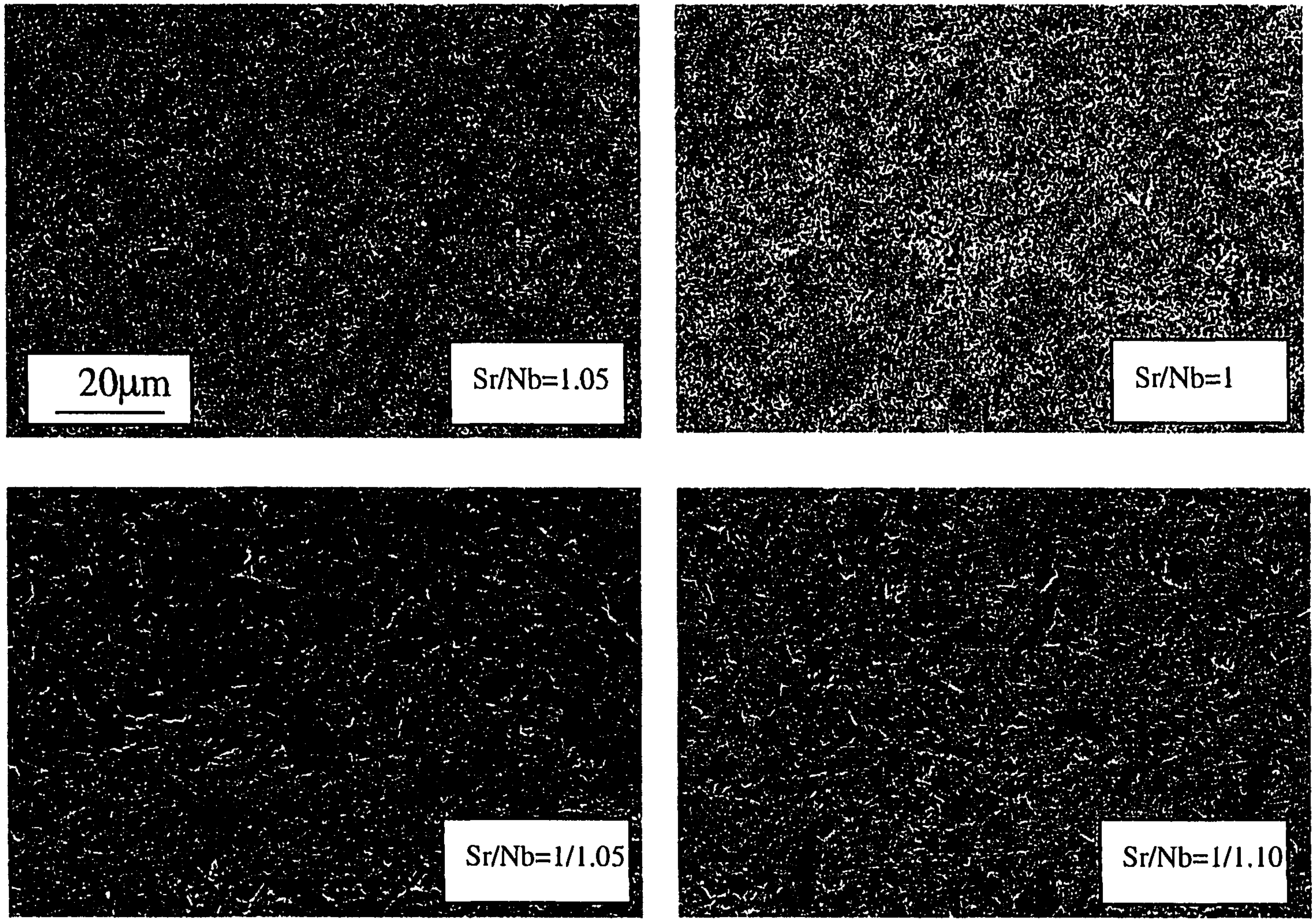

Figure 3.5 SEM micrographs of sintered microstructures obtained at 1300°C, 1h for different Sr/Nb ratios.

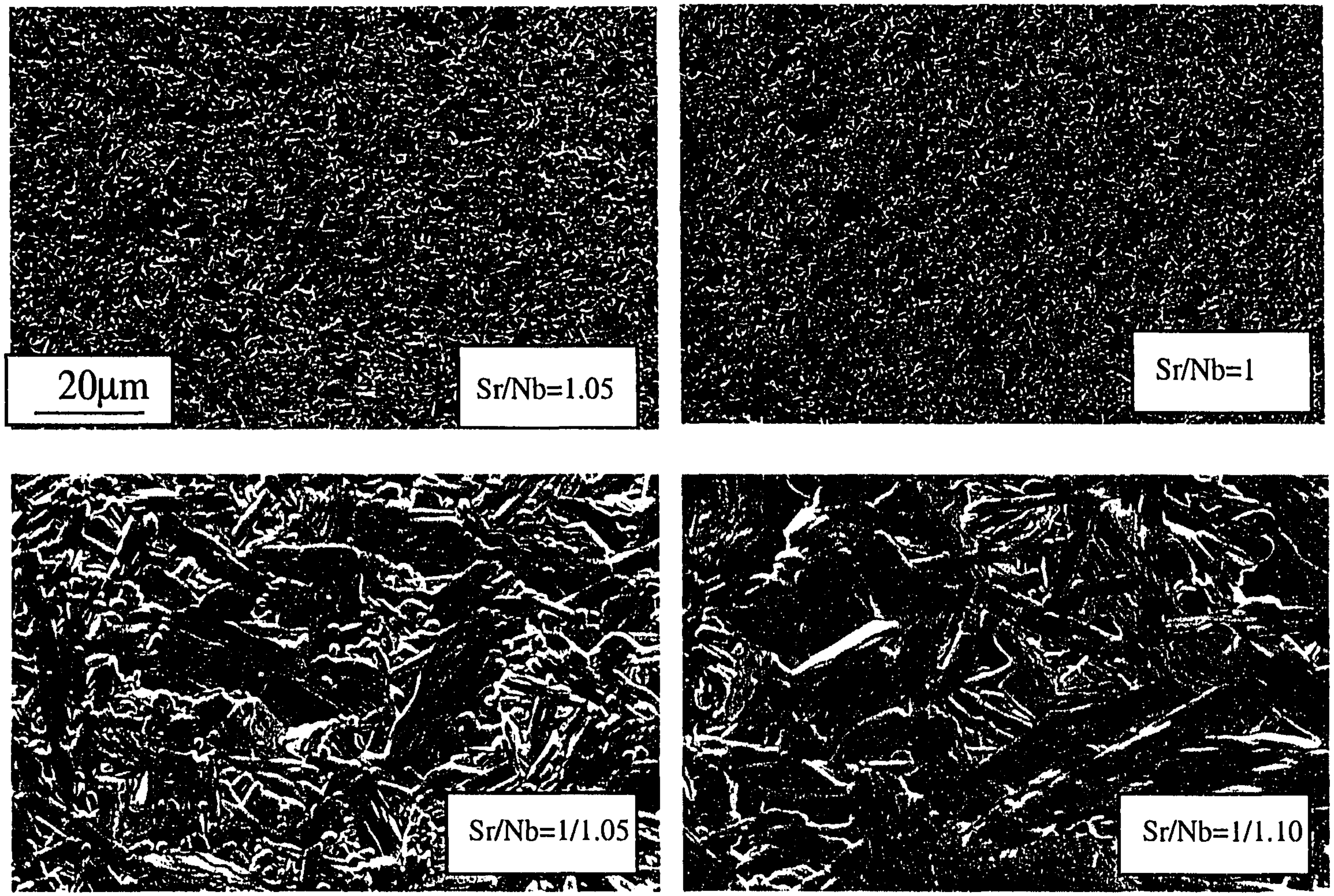

Figure 3.6 SEM micrographs of sintered microstructures obtained at 1400°C, 1h for different Sr/Nb ratios.

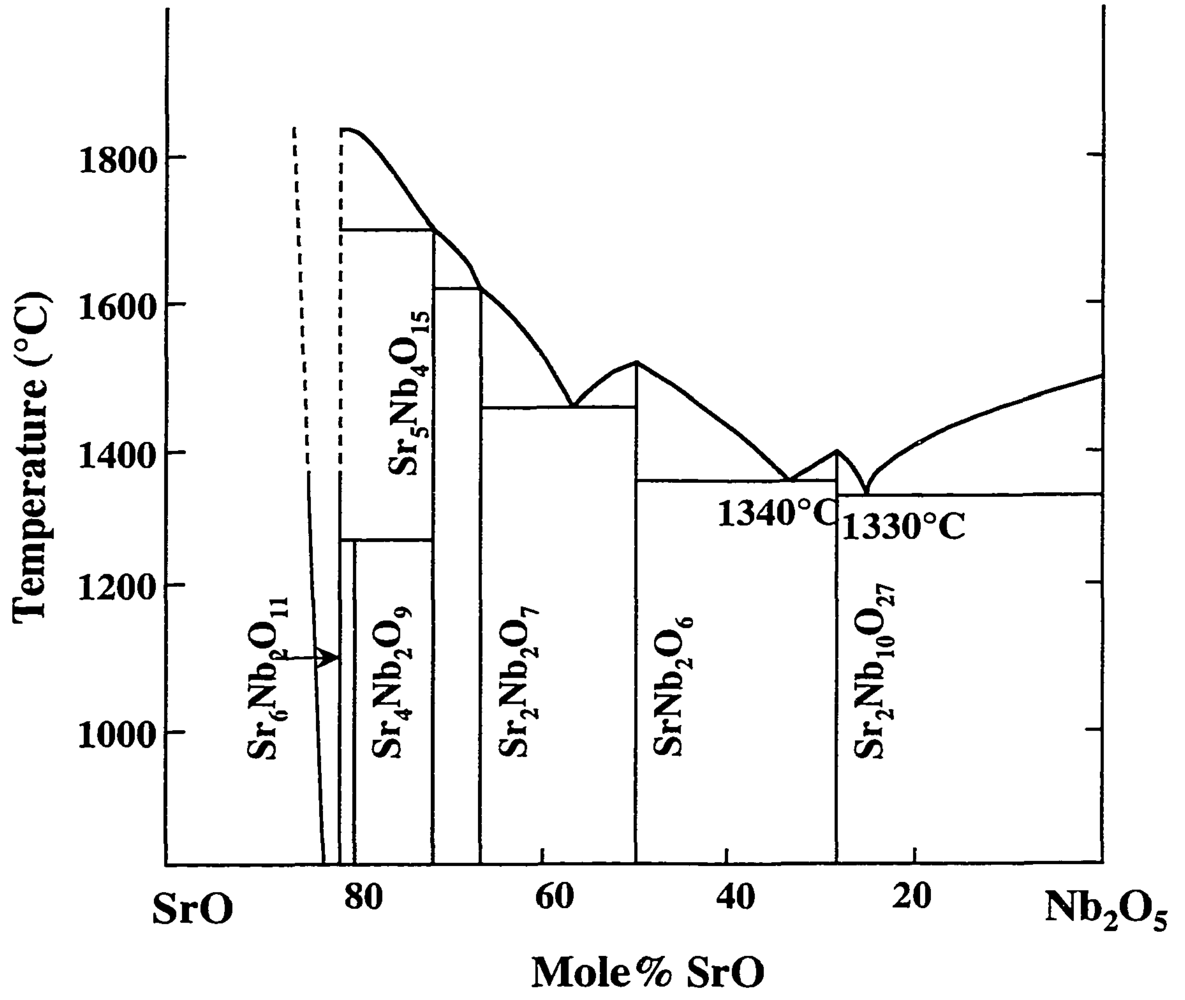

Figure 3.7. SrO-Nb_2O_5 phase diagram from Leschenko et al. [40]

and Nb_2O_5[30] and CaO and Nb_2O_5[31] have shown that the reaction proceeds by the ambipolar diffusion of Sr^{2+} and O^{2-} into the Nb_2O_5 particle. This is a result of the extremely low diffusion coefficient of Nb^{5+}. As a result of this process, a number of Sr-Nb-O phases with different Sr:Nb ratios are formed in layers between the SrO and the Nb_2O_5 particles. A $Sr_2Nb_2O_7$-Nb_2O_5 diffusion couple would behave no differently. This would lead to the formation of liquid phases above ~1330°C in Nb-rich samples as seen from the phase diagram.

The homogeneous microstructures obtained at 1300°C for different Sr/Nb ratios show a narrow grain size distribution. There were no grains larger than 2 times the average grain size. Thus, the Hillert criterion[21] for a size ratio which is required for the onset of exaggerated grain growth was not satisfied. However, the development of a bimodal grain size distribution from an initial microstructure composed of a narrow grain size distribution has been observed in other systems.[12,32]

Based on our observations, the formation of a liquid at certain grain boundaries causes the appearance of large anisotropic grains at 1400°C in $Sr_2Nb_2O_7$. This observation is consistent with the model proposed by Rios[20] as well as the explanation for exaggerated grain growth in $BaTiO_3$.[23]

3.3.3 Grain Growth in La-doped $Sr_2Nb_2O_7$

Figure 3.8 shows how the grain size distribution changes as a function of major axis length for various hold times at 1550°C. The distributions are self-similar for hold

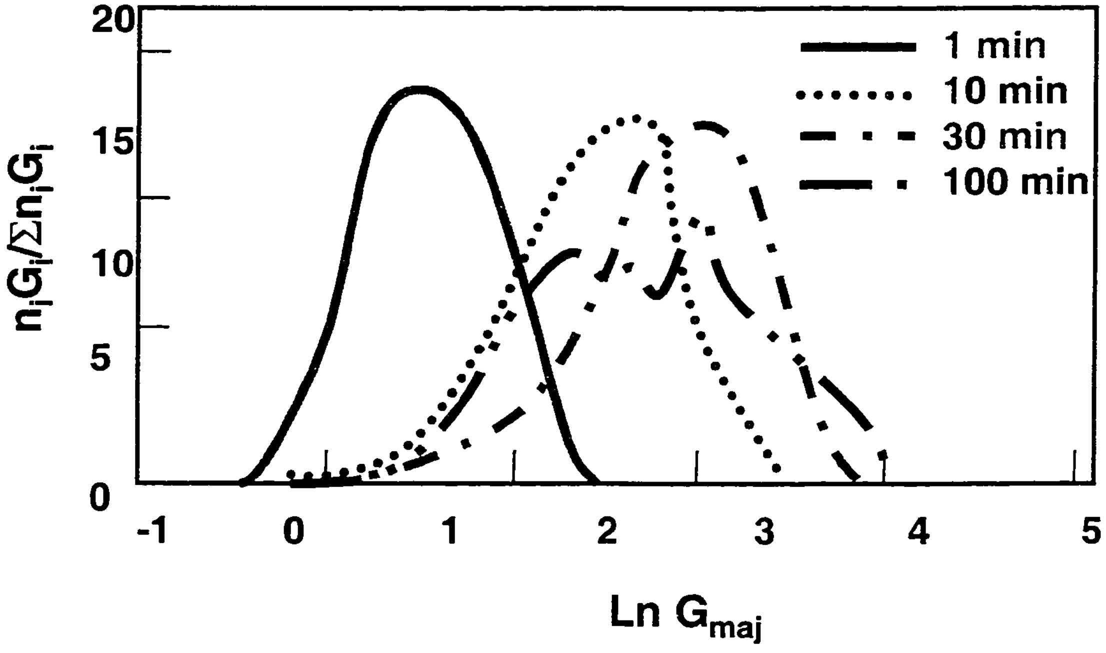

Figure 3.8 Isothermal grain growth in La-doped $Sr_2Nb_2O_7$ at 1550°C. G_{maj} is the major axis dimension in microns and n_i is the number of grains of size G_i

times ranging from 1 minute to 30 minutes. As seen in Figure 3.4, some broadening of the distribution, and growth of larger grains was observed for a hold time of 100 minutes. Interestingly, there is less anisotropic grain growth in doped samples relative to undoped $Sr_2Nb_2O_7$. Because the amount of La present in the sample is only 2 mol%, it was not possible to physically locate La_2O_3 in our samples by SEM or EDS. However, from lattice parameter measurements (Table 3.1), La incorporation was found to be incomplete until ~100 minutes at 1550°C. Therefore, La_2O_3 can exist as a separate phase, possibly on the grain boundaries, and thus suppresses anisotropic grain growth by pinning the grain boundaries.

To determine the grain growth mechanism, the average grain size from isothermal sintering experiments was fit to the general grain growth equation,

$$G_{av}(t)^n - G_{av}(0)^n = kt,$$

where k is a constant under isothermal conditions and t is the duration of sintering. The best fit to the equation was obtained for $n=3$ ($R^2=0.98$). Lower values of n yielded a R^2 parameter < 0.92. A cubic growth law is predicted for kinetics which are a result of drag-limited growth due to either a liquid or a dispersed phase.[6] We conclude that La-doping suppresses anisotropic grain growth as a result of pinning the grain boundaries. However, the effect of La_2O_3 pinning is completely offset by using Nb-rich $(Sr_{0.99}La_{0.01})_2Nb_2O_7$ as seen in Figure 3.9. Although a complete ternary phase diagram for the 1300°C-1500°C temperature range is unavailable, the observations of a large liquid phase field for low amounts of La_2O_3 in the Sr-La-Nb-O system[33] at 1500°C suggest the possibility of liquid phase formation at lower temperatures.

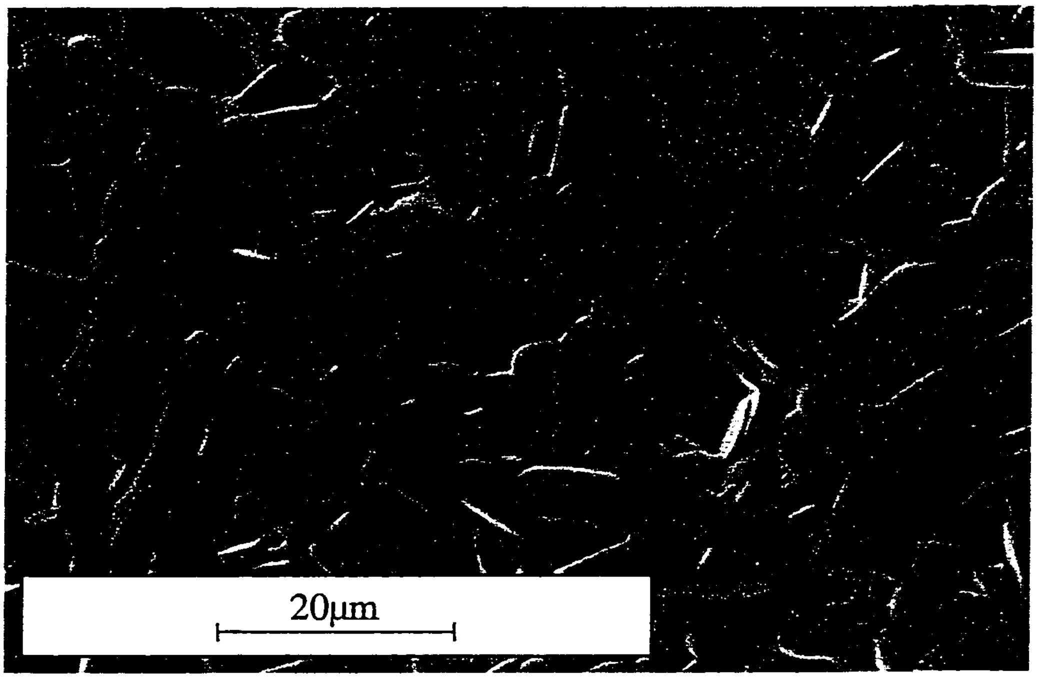

Figure 3.9. SEM micrograph of 2 mol% La-doped sample with Nb:Sr=1.1, showing larger grains in 0.5 min at 1550°C as compared to Nb:Sr=1 case at longer hold times.

3.3.4 Grain Growth in the Presence of Templates

Based on the above observations, anisotropic grain growth can be promoted in $(Sr_{0.99}La_{0.01})_2Nb_2O_7$ by using Nb-rich compositions. The grain growth behavior of samples initially containing 10 vol% oriented $Sr_2Nb_2O_7$ templates in a matrix of $(Sr_{0.99}La_{0.10})_2Nb_2O_7$ was studied to test the feasibility of using a liquid phase to accelerate template growth during TGG. Samples containing a Nb:(Sr,La) ratio of 1.0 and those containing 1 mol% excess Nb in the form of niobium oxalate coated matrix and template particles were sintered at 1275°C and 1350°C. Figure 3.10 shows the sintered microstructures of sample edges perpendicular to the tapecast plane. The Nb-rich microstructure at 1275°C does not exhibit large oriented grains. Therefore template growth has not been initiated at this stage. The Nb-rich samples show a number of very large, oriented grains at 1350°C indicating the onset of growth, and hence liquid phase formation, between 1275°C and 1350°C. The samples with a Nb:(Sr,La) ratio of 1.0 do not show extensive template growth even at 1350°C. This implies that the presence of a Nb-rich liquid phase can accelerate template growth even in La-doped samples, making it possible to fabricate dense, highly textured, insulating $Sr_2Nb_2O_7$ ceramics.

TGG in La-doped samples with excess niobium and blade-shaped templates will be discussed in detail in the following Chapter.

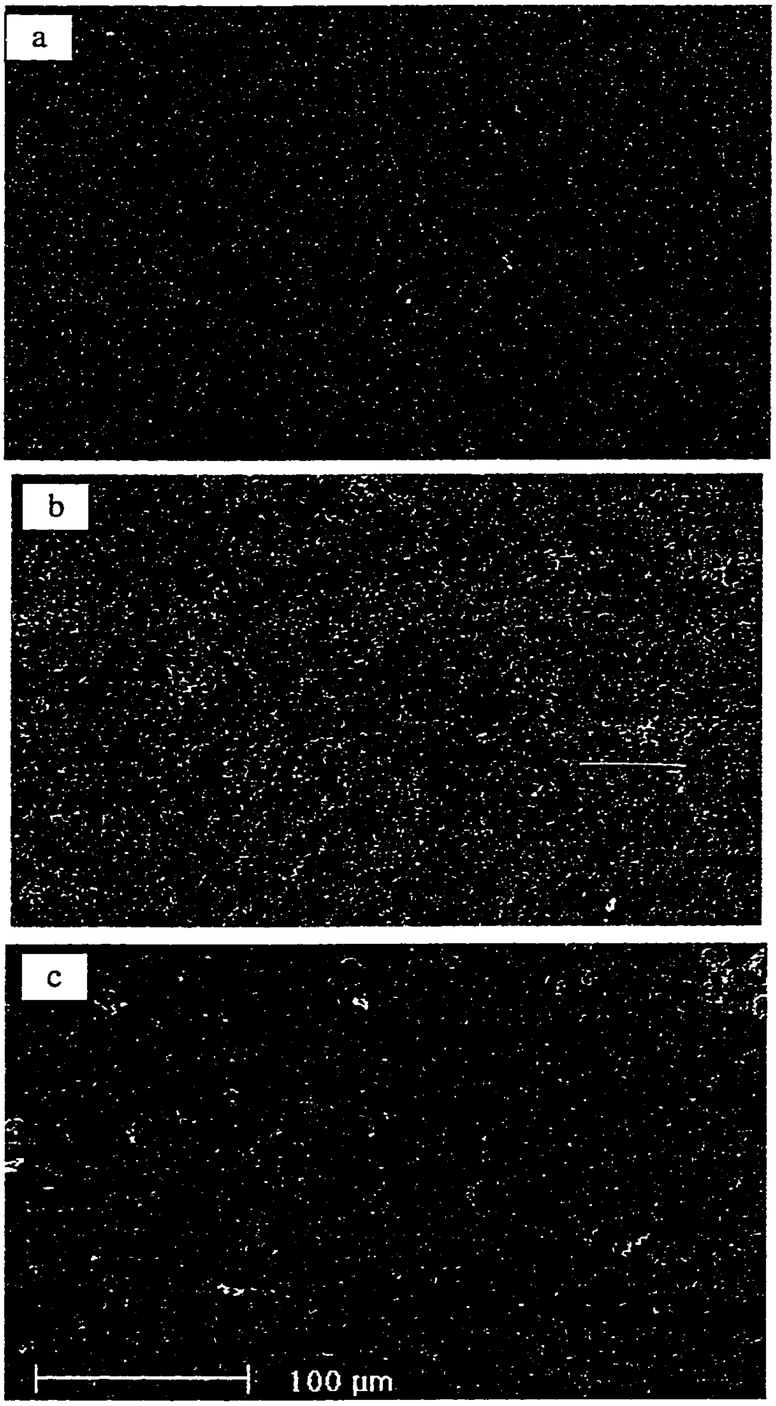

Figure 3.10 SEM micrographs of sintered edges of TGG samples containing 10 vol% initial template. (a) Nb:(Sr,La)=1.01 sintered at 1275°C, (b) Nb:(Sr,La)=1 sintered at 1350°C for 1h, (C) Nb:(Sr,La)=1.01 sintered at 1350°C for 1h

3.4 CONCLUSIONS

Growth of large anisotropic grains in a matrix of fine grains is due to the local heterogeneous formation of liquid phase at certain Nb-rich grain boundaries. The mobility difference of wetted boundaries leads to growth of large anisotropic grains. The Sr:Nb ratio in the starting material determines if the material will exhibit bimodal microstructures. Donor doping with lanthanum is effective in lowering the dielectric loss and retarding grain growth. Careful control over doping and the Sr:Nb ratio can be used to fabricate high density $Sr_2Nb_2O_7$ samples with either fine grained microstructures or a microstructure exhibiting large anisotropic grains. The preferential growth of template particles in a doped matrix can be achieved only by increasing the mobility of the template grain boundary by coating the template particles with Nb_2O_5. A higher initial volume concentration of templates results in a higher volume fraction of large anisotropic grains in the final microstructure.

3.5 REFERENCES

1 A. C. Bishop, An Outline of Crystal Morphology, Hutchinson Scientific and Technical, London (1967)

2 J. E. Burke, "Role of Grain Boundaries in Sintering," *J. Am. Ceram. Soc.*, **40** [3] 80-5 (1957)

3 C. Kooy, "Anisotropic Exaggerated Growth and Sintering in $MnFe_2O_4$ and $Y_3Fe_5O_{12}$," pp 21-34 in Science of Ceramics, Vol. 1. Edited by G. H. Stewart, Academic Press (1962)

4 G. M. Dynna and Y. –M. Chiang, "Mechanisms of Grain Growth Enhancement and Inhibition in Donor Doped Barium Titanate," *Ceram. Trans.*, **7** 547-61 (1988)

5 D. Kolar, "Discontinuous Grain Growth in Multiphase Ceramics," *Ceram. Trans.*, **7** 529-44 (1988)

6 M. F. Yan and D. W. Johnson, jr., "Impurity-Induced Exaggerated Grain Growth in Mn-Zn Ferrites," *J. Am. Ceram. Soc.*, **61** [7-8] 342-9 (1978)

7 M. N. Rahaman, Ceramic Processing and Sintering, Marcel Dekker, Inc., New York (1995)

8 C. S. Pande and S. P. Marsh, "The Analytical Modeling of Normal Grain Growth," *J. Mater.*, no. 9 (1992)

9 C. V. Thompson, H. J. Frost, and F. Spaepen, "The Relative Rates of Secondary and Normal Grain Growth," *Acta Metall.*, **35** [4] 887-90 (1987)

10 S. Nanamatsu, M. Kimura, K. Doi, and M. Takahashi, "Ferroelectric Properties of $Sr_2Nb_2O_7$ Single Crystal," *J. Phys. Soc. Jpn*, **30** 300 (1971)

11 M. J. Sacks, G. W. Scheiffele, and G. A. Staab, "Fabrication of Textured Silicon Carbide via Seeded Anisotropic Grain Growth," *J. Am. Ceram. Soc.*, **79** [6] 1611-16 (1996)

12 H. Emoto and M. Mitomo, " Control and Characterization of Abnormally Grown Grains in Silicon Nitride Ceramics," *J. Eur. Ceram. Soc.*, **17** 797-804 (1997)

13 M. Seabaugh, D. Horn, I. Kerscht, S-H. Hong, and G. L. Messing, "Anisotropic Grain Growth in Alumina Ceramics," Sintering Technology, Edited by R. M. German, G. L. Messing, and R. Cornwall, Plenum Press, NY (1996)

14 Y. Inoue, T. Kimura, T. Yamaguchi, K. Nagata, and K. Okazaki, " Grain Orientation and Electrical Properties of Hot-Pressed Bismuth Titanate Ceramics," *Yogyo-Kyokai-Shi*, **92** [7] 416-19 (1984)

15 K. Nagata and K. Okazaki, "One-Directional Grain-Oriented Lead Metaniobate Ceramics," *J. Jap. Appl. Phys.*, **24** [7] 812-14 (1985)

16 A. Tan, C. K. Kuo, and P. S. Nicholson, "Preparation and Characterization of Textured Polycrystalline Na and K-β''/β-aluminas," *Solid State Ionics*, **42** 233-41 (1990)

17 I. Monot, J. Wang, G. Desgardin, and B. Raveau, "Crystal Chemistry of the Texture Formation in Superconductive $YBa_2Cu_3O_{7-\delta}$ Ceramics," *J. Mater. Res.*, **7** [2] 273-82 (1992)

18 S-H. Hong, W. Cermignani, and G. L. Messing, "Anisotropic Grain Growth in Seeded and B_2O_3-doped Diphasic Mullite Gels," *J. Eur. Ceram. Soc.*, **16** 133-41 (1996)

19 Y-S. Yoo, H. Kim, and D-Y. Kim, "Effect of SiO_2 and TiO_2 Addition on the Exaggerated Grain Growth of $BaTiO_3$," *J. Eur. Ceram. Soc.*, **17** 805-11 (1997)

20 P. R. Rios, "Abnormal Grain Growth Development From Uniform Grain Size Distributions Due to a Mobility Advantage," *Scripta Materialia.*, **38** [9] 1359-64 (1998)

21 M. Hillert, "On the Theory of Normal and Abnormal Grain Growth," *Acta Metall.*, **13** 227-38 (1965)

22 F. Lee and K. J. Bowman, "Texture Development via Grain Rotation in β-Silicon Nitride," *J. Am. Ceram. Soc.*, **77** [4] 947-53 (1994)

23 D. F. K. Hennings, R. Janssen, and P. J. L. Reynen, "Control of Liquid-Phase-Enhanced Discontinuous Grain Growth in Barium Titanate," *J. Am. Ceram. Soc.*, **70** [1] 23-27 (1987)

24 A. F. Shimanskij, M. Drofenik, D. Kolar, "Subsolidus Grain Growth in Donor Doped Barium Titanate," *J. Mat. Sci.*, **29** [23] 6301-5 (1994)

25 M. Fukuhara, C-Y Huang, A. S. Bhalla, R. E. Newnham, "Grain Orientation and Electrical Properties of $Sr_2Nb_2O_7$ Ceramics," *J. Mater. Sci.*, vol. **26** 61(1991)

26 P.A. Fuierer, "Grain Oriented Perovskite Layer Structure Ceramics for High Temperature Piezoelectric Applications," Ph.D. Thesis, The Pennsylvania State University, University Park, PA (1991)

27 NIH Image, v. 1.56, by W. Rasband, National Institute of Health, USA.

28 V. Prasadarao, U. Selvaraj, S. Komarneni, and A.S. Bhalla, "Sol-Gel Synthesis of Strontium Pyroniobate and Calcium Pyroniobate," *J. Am. Ceram. Soc.*, **75** [10] 2697-701 (1992)

29 P. P. Leshchenko, A. V. Shevchenko, L. N. Lykova, L. M. Kovba, and E. A. Ippolitova, "The System SrO-Nb_2O_5," *Russ. J. Inorg. Chem.*, **18** [7] 1202-05 (1982)

30 Y. Neiman, I. P. Zapasskaya, A. L. Podkorytov, and V. M. Zhukovskii, "The Macro-Mechanism of the Solid-phase Reactions of Alkaline Earth Metal Carbonates and Oxides with Niobium(V) and Molybdenum(VI) Oxides," *Russ. J. Inorg. Chem.*, **28** [9] 1259-63 (1983)

31 N. Hotta, M. Hasegawa, H. Maeda, and S. Matsuo, "Solid State Reaction between Nb_2O_5 and CaO," *Yogyo-Kyokai-Shi*, **89** [1] 9-13 (1981)

32 W. Dressler, H-J. Kleebe, M. J. Hoffmann, M. Ruhle, and G. Petzow, "Model Experiments Concerning Abnormal Grain Growth in Silicon Nitride," *J. Eur. Ceram. Soc.*, **10** 3-14 (1990)

33 Z. K. Huang, D. S. Yan, T. Y. Tien, and I. W. Chen, "Phase Relationships in the La_2O_3-SrO-Nb_2O_5 System," *Mater. Lett.*, **11** [8,9] 286-90 (1991)

Chapter 4

TEXTURE DEVELOPMENT IN $Sr_2Nb_2O_7$ BY TEMPLATED GRAIN GROWTH

4.1 INTRODUCTION

Traditional ceramic processing techniques result in microstructures which exhibit physical properties governed by ∞∞m symmetry. This leads to averaging in the properties. In general, each grain in the polycrystalline sample has a crystallographic orientation different from that of its neighbors. Thus, grain orientations are randomly distributed in relation to an arbitrarily chosen frame of reference. This random distribution results in an averaging of properties in all directions, often leading to isotropic properties even in materials that possess strongly anisotropic properties in the single crystal form. In contrast, preferred orientation of grains along particular crystallographic directions results in the development of texture. Textured ceramics can exhibit anisotropic physical properties which are typical of single crystals.[1-5] Therefore, enhanced and anisotropic electrical, magnetic, optical, and structural properties can be achieved in a polycrystalline body with desirable texture.

Two types of texture can be obtained in polycrystalline materials depending on the degree of constraint imposed on the crystallographic orientation of the grains.[6,7]

(i) *Fiber or Wire Texture:* Polycrystalline bodies in which the same crystallographic direction in all or most of the grains is parallel to a common direction in the sample exhibit fiber texture. These samples possess rotational symmetry about the direction of texture, and hence can exhibit two principal values for physical properties.

(ii) *Sheet Texture:* Polycrystalline bodies in which most crystallites are oriented with a particular crystallographic plane parallel to a common plane in the sample, and the same crystallographic direction in that crystallographic plane of most of the grains is parallel to a common direction in the sample, exhibit sheet texture. In the ideal case the sample possesses 3-dimensional texture, and hence exhibits the property anisotropy of a single crystal of the same composition.

Textured ceramics have been produced by a variety of techniques including hot-pressing,[8] tape casting,[9] extrusion,[10] or magnetic alignment[11] of anisotropically shaped crystallites followed by densification, and crystallization from eutectic melts (melt texturing).[12] More recently, templated grain growth (TGG) has been investigated as a means of obtaining textured ceramics.[13-15] However, sheet texture in ceramics has not been achieved by employing any of the above-mentioned techniques. Previous work on textured $Sr_2Nb_2O_7$ was based on hot forging,[16] which is expensive and unsuitable for production of a large number of samples. In this study we discuss the use of pressureless templated grain growth in achieving fiber texture in $Sr_2Nb_2O_7$, and the formation of sheet texture in $(Sr,La)_2Nb_2O_7$ by a modification of the TGG process. TGG refers to the growth of one or many large, oriented, single-crystal "template" particles in a dense, fine-grained matrix by suitable heat treatment which leads to an increase in the textured volume fraction of the ceramic.

Single crystal particles have been oriented by many different techniques based on the application of (i) a shear field on a slurry containing anisotropic templates such as during tape casting[9] or extrusion,[17] (ii) a magnetic field to orient anisotropically shaped ferrite particles,[11] (iii) the application of an electric field on a dispersion containing particles with a dipole moment,[18] or (iv) uniaxial pressing of anisotropic particles.[19] In this study, tape casting was chosen to impart orientation to the template particles for TGG.

The template particle size used for TGG is governed by a number of factors. The template particles must be large and anisotropically shaped so that they can be oriented in the shear field produced under the moving doctor blade during tape casting. They should not hinder densification of the matrix by forming percolated clusters either locally or across the sample dimensions for the chosen concentration of template particles. The templates must be large enough to initiate oriented grain growth in a dense matrix. Based on previous studies, use of templates in the size range 5-50 μm has resulted in successful development of texture by TGG.[13-15]

Besides obtaining samples with oriented template particles, the other technological challenge in TGG is the determination of conditions favorable for the growth of the templates at the expense of the matrix. In order to overcome this challenge, it is necessary to understand grain growth in the system of interest. Based on previous TGG experiments in SiC,[14] Si_3N_4,[13] and Al_2O_3,[15] a few common principles important for TGG can be established. The requirements include anisotropic crystal growth rates, epitaxial match between the templates and the matrix, high mobility of the template-matrix grain interface, avoidance of nucleation of exaggerated grain growth in the matrix, a large driving force for template growth, and rapid rates of template growth. Previous TGG studies have attributed texture development to anisotropic grain growth.[13-15]

However, some researchers have suggested exaggerated grain growth as the reason for growth of a few very large grains in a fine matrix.[20,21] Moreover, most TGG studies to date have depended on the presence of a large quantity (>1 vol%) of a liquid phase to enhance grain growth. However, in the case of $Sr_2Nb_2O_7$, a large amount of liquid phase (formed by 5 mol% excess niobium) leads to uncontrolled matrix growth as discussed in the preceding chapter. In this study, the lower limits for the amount of liquid phase required for successful TGG in $Sr_2Nb_2O_7$ are established by studying the effect of small variations in the Nb/Sr ratio on template growth.

The ability to tailor the shape of $Sr_2Nb_2O_7$ template particles in the form of orthorhombic blades can be fully exploited to maximize property anisotropy by inducing sheet texture. The predictions based on Jeffrey's equations[22,23] for the motion and orientation of whisker-like and plate-like particles under shear fields were used to develop a gated doctor blade arrangement as discussed in section 4.3.2.2. The set-up was used to orient the large rectangular face of the templates parallel to the surface of the cast tape, and the long edge of most of the blades along the direction of casting. This enabled the production of sheet texture in $(Sr,La)_2Nb_2O_7$ by TGG.

The effect of various processing parameters such as template size, concentration, temperature, and time on texture development in $Sr_2Nb_2O_7$ samples with fiber texture is first described. The factors influencing grain growth in La-doped samples from Chapter 3 are combined with the results of fiber texture studies to investigate the development of sheet texture in $(Sr,La)_2Nb_2O_7$ as a function of template morphology and orientation technique. Grain growth kinetics for minimum amount of excess niobium, and development of texture in La-doped $Sr_2Nb_2O_7$ were also studied.

4.2 EXPERIMENTAL PROCEDURE

4.2.1 Fiber Texture in $Sr_2Nb_2O_7$

Equiaxed solid-state reacted powder with an average particle size of ~0.6 μm was used as the matrix powder. The process for the production of this powder is described in detail in Chapter 3. Template particles of two different sizes (i) 2 μm x 1 μm x 0.2 μm and (ii) 5-15 μm x 2 μm x 0.2 μm were used for TGG. The procedure for the synthesis of template particles is described in detail in Chapter 2. The initial amount of template particles used was either 5 vol% or10 vol%.

A mixture of template particles and strontium niobate powder was dispersed in an azeotropic mixture of ethanol and 2-butanone with a commercial dispersant (KD-1, ICI). The tape casting formulation was based on an acrylic binder (Acryloid B-7, Rohm Haas) and a mixture of butyl benzene phthalate and polyethylene glycol plasticizers. The slurry was cast under a blade opening of 250-500 μm at a blade velocity of 7-9 cm/s. After drying at room temperature, 10-100 layers of tape were stacked and laminated under a load of 0.3-0.5 MPa at 70°C. The binder was removed from the green laminate by heating to 600°C at 3°C/min. The samples were then sintered at various temperature-time conditions.

The densification behavior was determined by measuring densities at room temperature by the Archimedes technique. Microstructural evolution was tracked by scanning electron microscopy (SEM). Grain growth data were determined by analyzing these micrographs. For stereological measurements, samples were first polished with 0.1

µm diamond paste and then annealed at 100-200°C below the sintering temperature. SEM micrographs with 250-1000 grains from 2-5 random cross-sections were used for stereological measurements. Grain size statistics were computed using the NIH image analysis software.[24] The area, major and minor axes of inscribed ellipses, and angle of the major axis from the vertical were measured in sections parallel to the axis of fiber texture. The degree of texture was evaluated by calculating Lotgering factors[25] for the (0k0) peaks because the [0k0] direction was found to be the direction of fiber texture in $Sr_2Nb_2O_7$.

4.2.2 Sheet Texture in $(Sr,La)_2Nb_2O_7$

Coprecipitated La-doped powder with an average particle size of 0.5 µm was used as the matrix powder for TGG of $(Sr,La)_2Nb_2O_7$ (process described in Chapter 3). $Sr_2Nb_2O_7$ template particles in the 20-50 µm x 3-5 µm x 0.2-0.5 µm (**a** x **c** x **b**) range were used for this study. The matrix powder was dispersed in 2-propanol by milling for 12 h with a commercial dispersant (KD-2). The binder plus plasticizer system (Ferro B7407 was then added to the suspension, and the slurry was milled for 6 h. The template particles were separately dispersed in 2-propanol by mild ultrasonication for 3 minutes followed by stirring in a beaker for 1 h. After the matrix powder was milled it was stirred in a beaker.

The suspension of template particles was slowly added to the matrix powder slurry while stirring. The slurry was stirred for up to 6 h to adjust the amount of solvent

(2-propanol) by evaporation at room temperature to attain a solids loading of ~30-35 vol%. The slurry was then cast at 7-9 cm/s under a gated doctor blade. The blade opening was 300-500 μm. The gates were formed by sewing needles of 0.5 mm diameter spaced 1 mm apart before the doctor blade. The gates provide the shear field required to orient the length of the templates along the casting direction. The dried tape was stacked (200-500 layers) and laminated at room temperature at (500 g on 1.5 cm^2) for 5 minutes. Binder burnout was performed by heating to 250°C at 2°C/min and holding for 1 h, heating to 350°C at 2°C/min and holding for 1 h, and heating at 3°C/min to 600°C and holding for 1 h.

The amount of liquid phase formed during TGG was adjusted by varying the Nb to (Sr+La) molar ratio. Stoichiometric (Sr+La:Nb=1) coprecipitated powder was used in all cases. The excess niobium was supplied in the form of niobium oxalate. The addition of niobium oxalate was carried out after binder burnout to prevent binder-oxalate ion interactions which cause coagulation of the binder. The laminate was impregnated with solutions of niobium oxalate of different concentrations to obtain ppm level compositional variations in the Nb/(Sr+La) molar ratio. The laminates were then heated at 3°C/min to 500°C to convert the niobium oxalate to an amorphous Nb_2O_5 on the surface of the grains.

Stereological analysis of grain growth was carried out according to the procedure described in the previous section on fiber texture. Stereological analysis was carried out on three orthogonal planes normal to the *a*, *b*, and *c* crystallographic directions. The *b*-axis is normal to the casting plane, and the *c*-plane was normal to the casting direction.

The shape of the grown templates can be approximated to a thin, rectangular plate. This implies that grain dimensions of templates obtained from 2-D sections parallel to the casting plane would closely approximate the true dimensions along the *a* and *c*-directions.

4.3 RESULTS AND DISCUSSION

4.3.1 Fiber Texture in $Sr_2Nb_2O_7$

4.3.1.1 Effect of Template Particle Size

Figure 4.1 shows micrographs of two different sizes of template particles used for TGG and the matrix powder produced by solid state reaction. The anisotropic, faceted morphology of the templates and the equiaxed shape of the starting matrix powder are clearly evident. Green samples containing 10 vol% of oriented small templates and samples with 10 vol% large templates were sintered at 1450°C for 1 h to densities above 95%. The microstructures of the sintered edge perpendicular to the tape cast surface are shown in Figure 4.2. A comparison of these microstructures shows that the smaller templates do not generate the high degree of texture that results from the use of larger template particles. Another notable feature of the microstructure generated by the use of small template particles is the comparable size of the matrix grains. This indicates that the coarsening of the matrix grains reduces the driving force for the growth of smaller template particles. The driving force for anisotropic grain growth is due to the surface

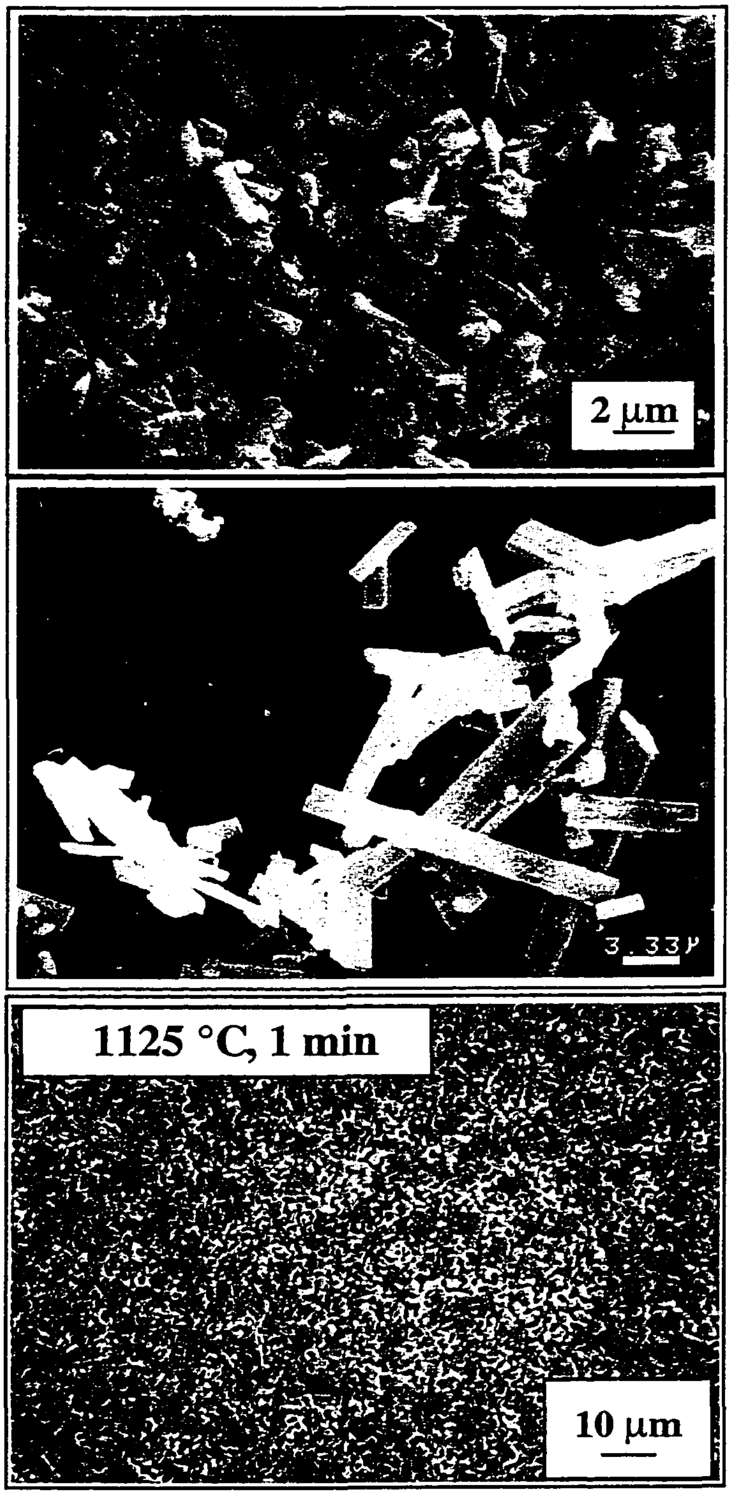

Figure 4.1 Micrographs of (a) small templates, (b) large templates, (c) sintered matrix powder

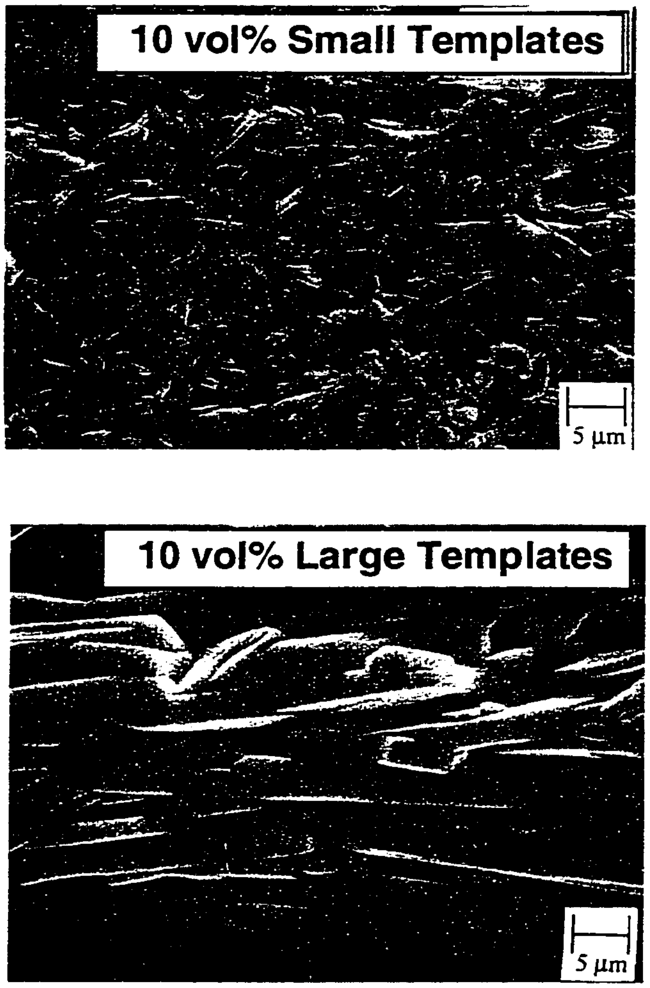

Figure 4.2 Effect of template size on degree of texture. SEM micrographs of edges perpendicular to cast plane sintered at 1450°C

energy difference of different planes, and is considerably diminished as the matrix grains start to facet at long hold times at high temperature. Therefore, the relative size of the template particles with respect to the matrix grains is one key to the success of the TGG approach. As the fast growing direction of the templates is perpendicular to the thickness, the area of the face of the templates must be larger than the matrix size to dominate grain growth in the matrix. The smaller templates have a face area of only about 5-10 μm^2 compared to the matrix grain area of ~4 μm^2. The larger templates had a face area of about an order of magnitude larger than that of the matrix grains, and hence are more successful in producing texture.

4.3.1.2 Effect of Template Concentration

The effect of initial template concentration on microstructural development was studied to determine the minimum volume fraction of templates that is required to develop texture in $Sr_2Nb_2O_7$. Microstructures developed from 5 vol% and 10 vol% initial template concentrations sintered at 1450°C for 1 h are compared in Figure 4.3. It can be seen that the degree of texture is much stronger in the samples with 10 vol% templates. Although some texture is developed in the 5 vol% samples, the template particles don't grow and consume a large part of the matrix prior to the growth of matrix grains to sizes comparable to that of template particles. Hence, the minimum initial template concentration required for TGG of $Sr_2Nb_2O_7$ is between 5 and 10 vol% which is significantly higher than the 1-2 vol% reported for TGG of SiC.[14] The higher initial

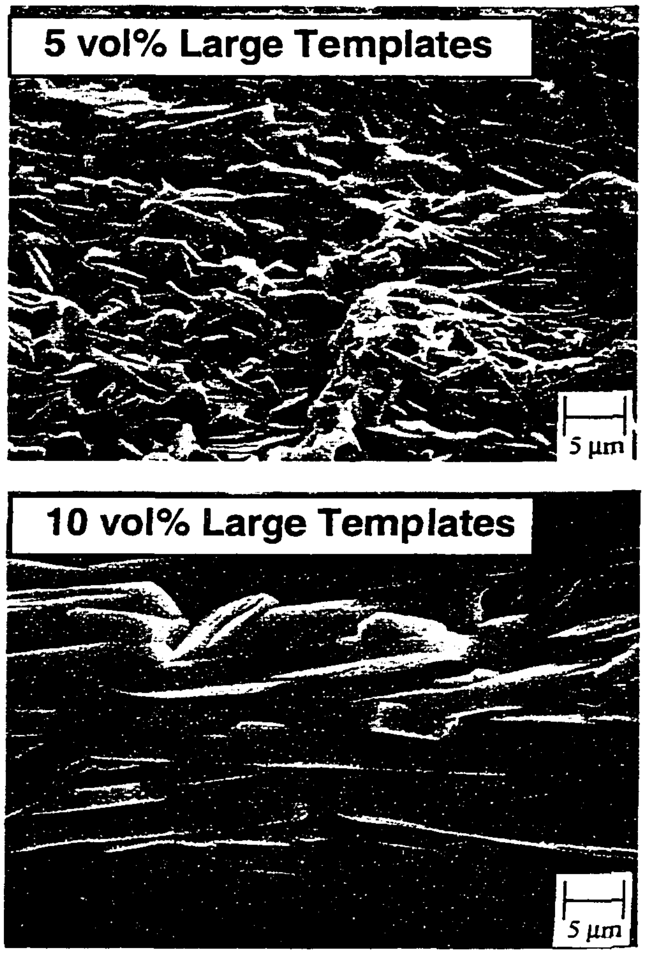

Figure 4.3 Effect of template volume fraction on degree of texture. SEM micrographs of edges perpendicular to cast plane sintered at 1450°C and 1550°C

template concentration requirement is most probably the result of a relatively faster growing matrix in the case of $Sr_2Nb_2O_7$ and differences in other processing parameters.

4.3.1.3 Densification Behavior

The shrinkage during sintering in three orthogonal directions was studied using a thermomechanical analyzer. The data were obtained on samples of equal thicknesses. The shrinkage rate is faster in the thickness direction (along the *b*-axis) and results in net shrinkage which is twice that observed in the other two directions in the plane of casting as seen in Figure 4.4. Sintered densities were measured by the Archimedes technique. The densification behavior is summarized in Figure 4.5. TGG samples with a high degree of grain orientation and densities >97% were obtained at 1400°C. This demonstrates the ability to generate dense, grain-oriented $Sr_2Nb_2O_7$ by a pressureless technique. The highest density,~98%, was obtained in samples that were sintered for 2 h at 1550°C. Thus, the use of 10 vol% initial templates does not prevent the achievement of high density in spite of constrained shrinkage in the casting plane due to the presence of large platy templates.

Reduction in sintered density was observed with increasing sintering time at 1550°C. The decrease was observed after a maximum of ~98% was reached at 1550°C. This decrease might be due to the stresses generated by impinging anisotropic grains during grain growth. Reduction in final density after attaining densities >95% was also reported by Fukuhara et al.[26] for randomly oriented $Sr_2Nb_2O_7$ ceramics.

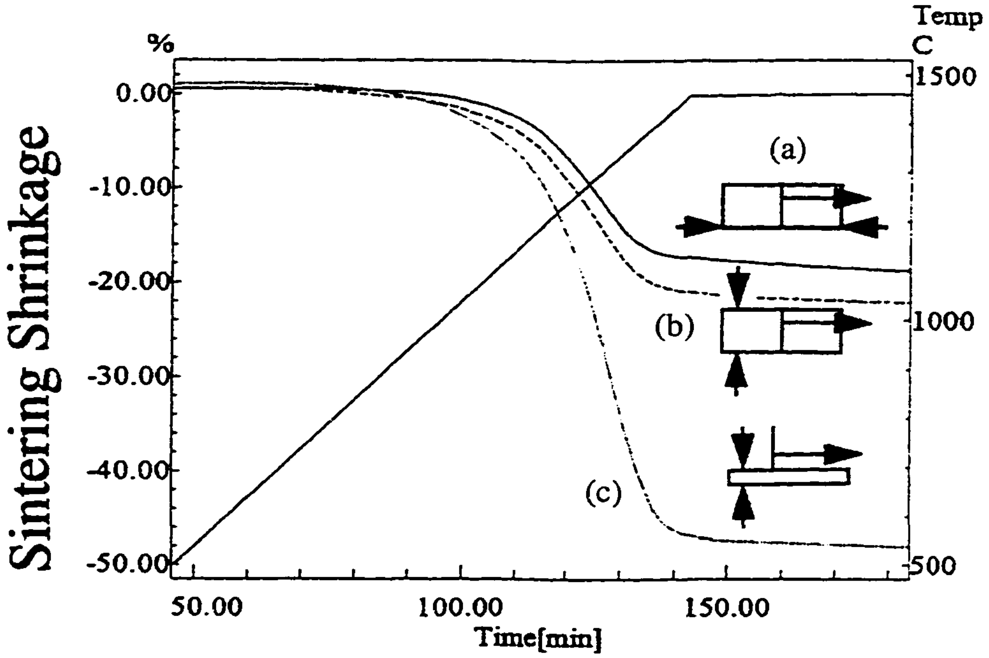

Figure 4.4 Sintering shrinkage along three orthogonal directions in TGG samples measured by a thermomechanical analyzer (a) along casting direction, (b) perpendicular to casting direction and tape thickness, and (c) along tape thickness

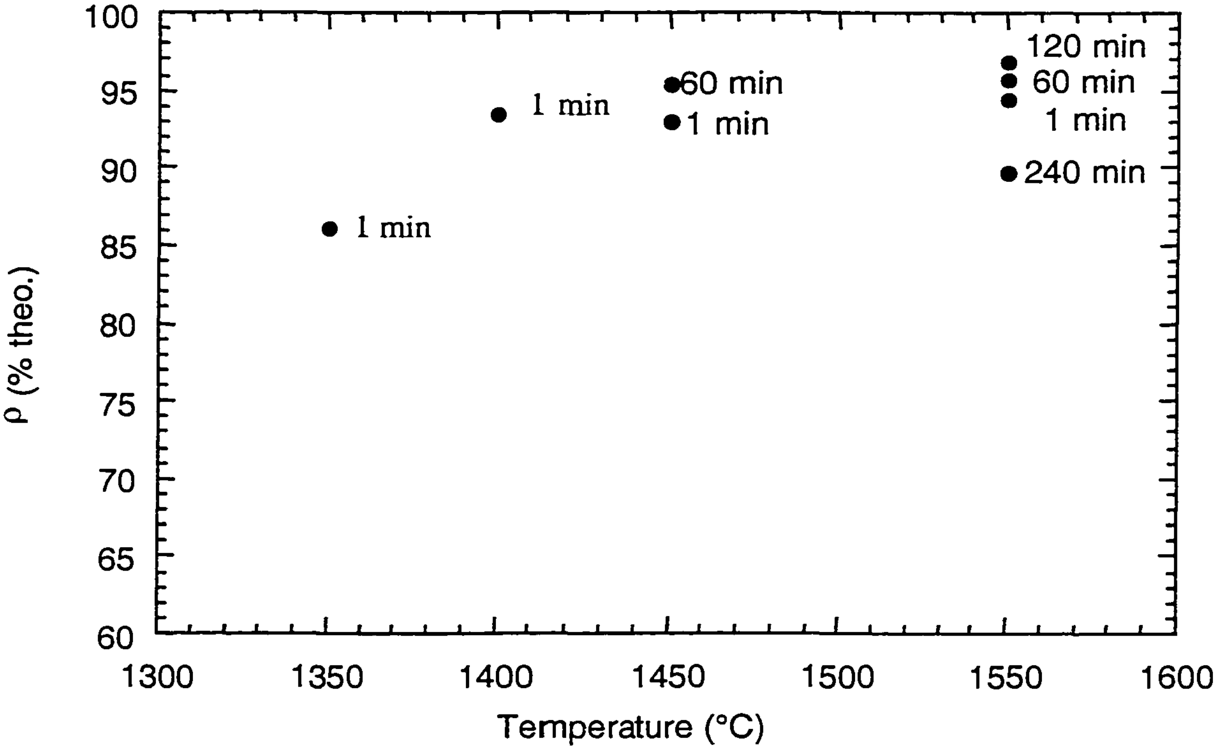

Figure 4.5 Densification behavior of TGG samples containing 10 vol% of initial large templates

4.3.1.4 Grain Growth and Texture Evolution During TGG of $Sr_2Nb_2O_7$ with Fiber Texture

Grain growth in TGG samples of $Sr_2Nb_2O_7$ containing 10 vol% initial templates was studied by microstructural characterization, and the degree of texture was followed by calculating the Lotgering factor for the crystallographic *b*-direction from X-ray diffraction measurements.

Figure 4.6 shows SEM micrographs of sintered edges perpendicular to the tapecast plane at 1450°C and 1550°C. The orientation and anisotropy of grains is clearly seen in the micrographs. The grain size in these samples was characterized by the major and minor axes of the inscribed ellipse within each anisotropic grain. Average lengths of major and minor axes measured from microstructures sintered for 1 h at 1300°C, 1450°C, and 1550°C are shown in Figure 4.7a. The bars indicate one standard deviation to each side of the average value of the distribution. This gives a measure of the breadth of the grain size distribution in the sintered microstructure. The change in grain dimensions at 1450°C from 1 min to 1 h is shown in Figure 4.7b. The microstructure at 1300°C contains several smaller matrix grains and is representative of the grain size distribution prior to the onset of template growth.

Template growth in both the length and thickness directions increases with increasing temperature. The rate of lengthening seems to be faster than the rate of thickening with both increasing time and increasing temperature. Drawing a conclusion about the relative growth rates by comparing average values of grain dimensions provides an inaccurate picture of the process. Figure 4.8 shows the change in aspect ratio with sintering temperature. The initial dimensional ratio of template particles is 1:5:20

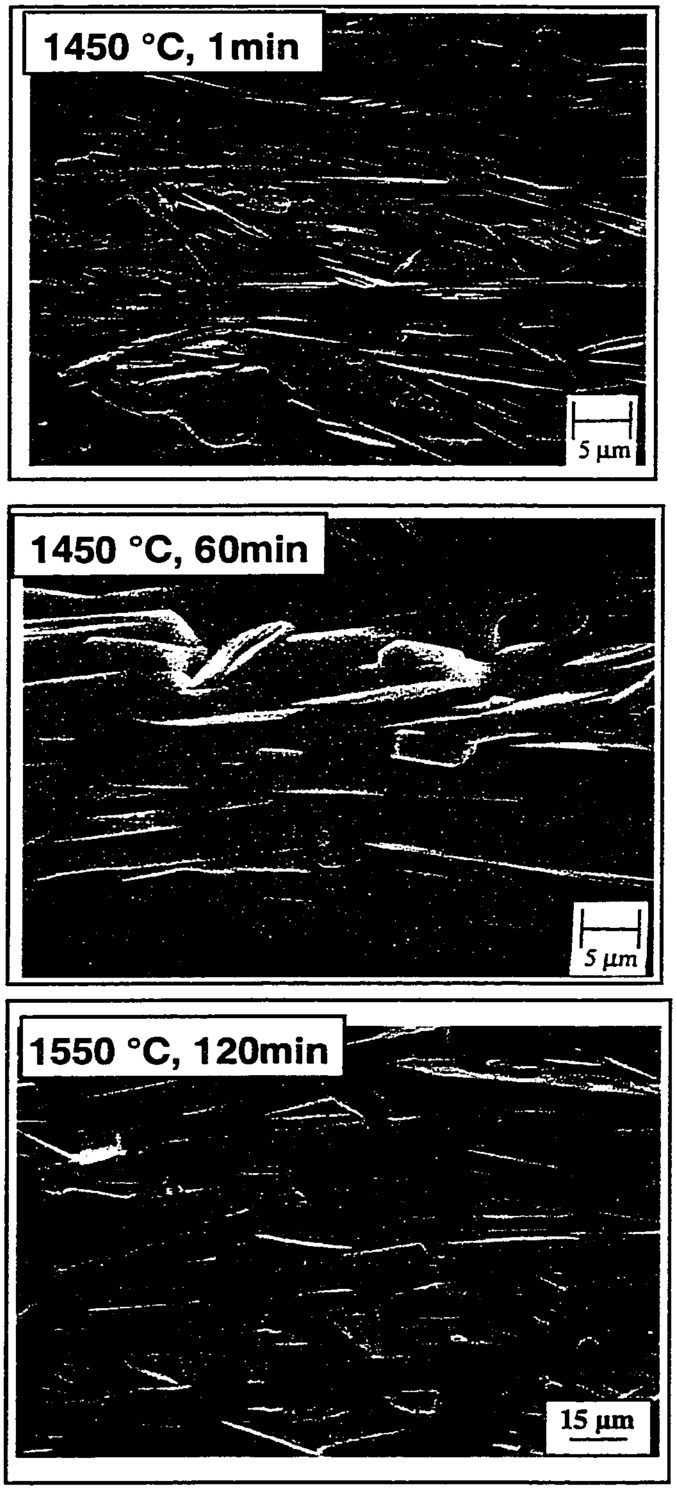

Figure 4.6 SEM micrographs of edges perpendicular to cast plane sintered at 1450°C and 1550°C

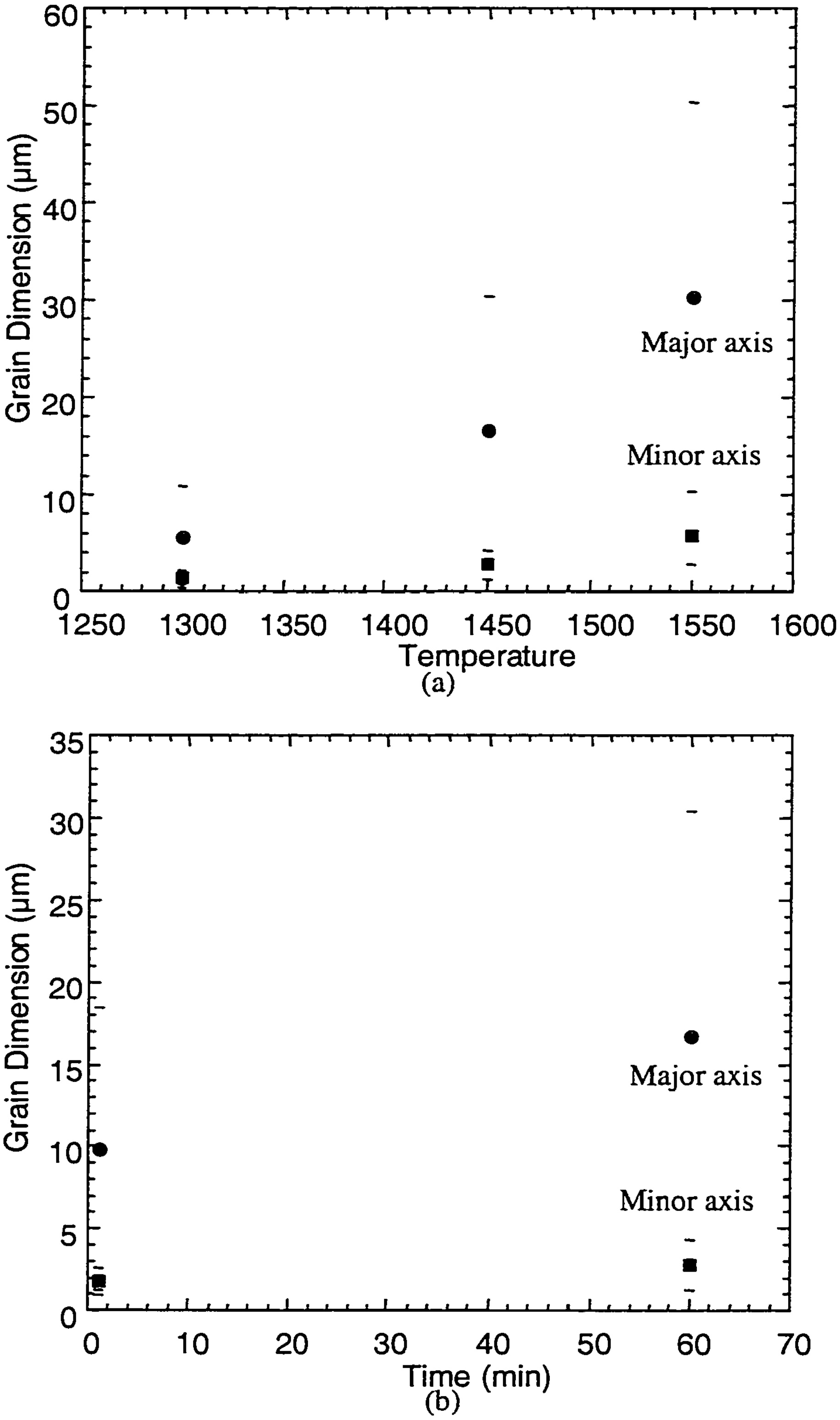

Figure 4.7 (a) Change in grain dimension with temperature, (b) Change in grain dimension at 1450°C with time

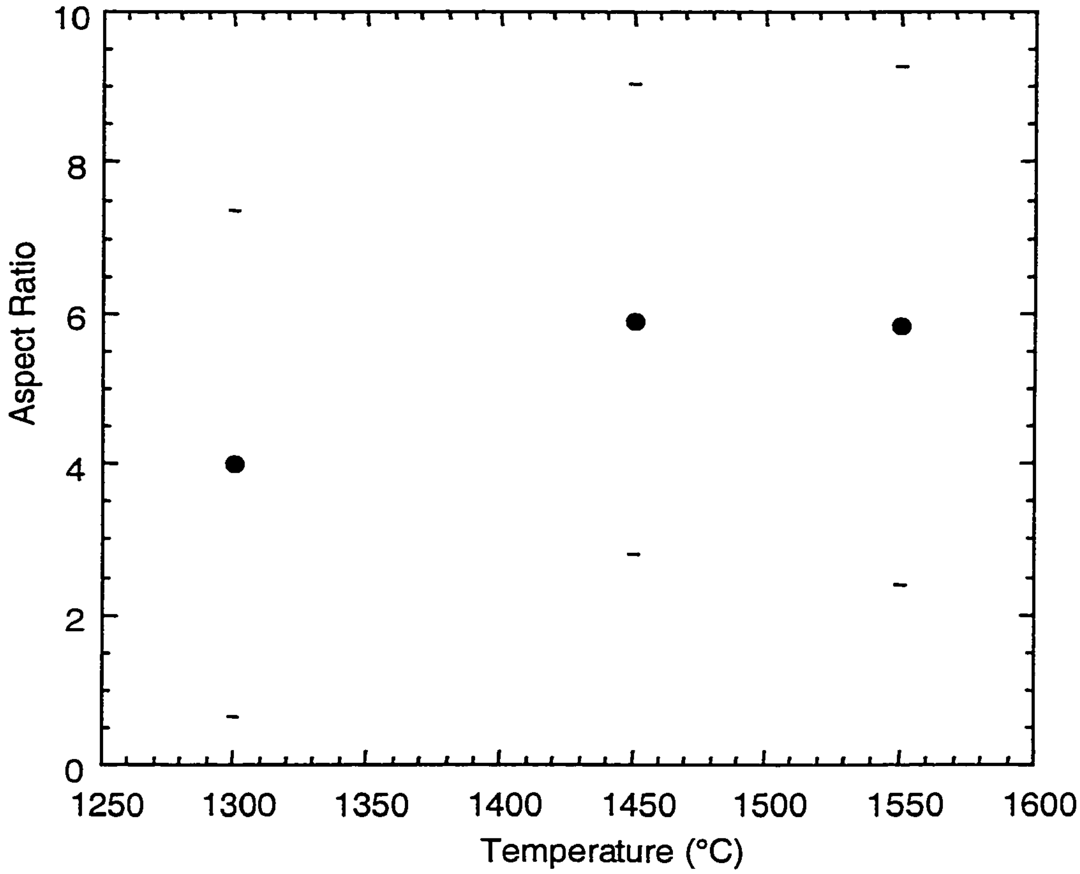

Figure 4.8 Change in aspect ratio with temperature for samples sintered for 1h.

(thickness :width: length). In 2D cross sections parallel to the axis of fiber texture, the initial aspect ratio at 1300°C measured for all anisotropic grains in the microstructure was ~4. The initial aspect ratio is greatly underestimated due to the presence of a large number of lower aspect ratio matrix grains at 1300°C. An increase in aspect ratio from ~4 at 1300°C to ~6 at 1450°C is followed by a drop to ~5.8 for sintering times of 1 h. The initial increase in aspect ratios results from the faster lengthening of template grains which are surrounded by smaller matrix grains. As shown earlier, the microstructure at 1450°C is almost entirely composed of large anisotropic grains. Once this stage is reached, the lengthening of large grains is constrained by other impinging large grains. Impingement does not affect thickening to the same extent, and this leads to a reduction in aspect ratio. The average aspect ratios in samples sintered for 1 min, 1 h at 1450°C, and 1 h at 1550°C are 6.02, 5.92, and 5.84, respectively. These values are representative of the average aspect ratio (of over 200 grains) defined by the ratio of the average length of the rectangular section of a grain that would be intersected by a plane parallel to the *b*-axis and the thickness of the grains along the *b*-axis. No stereological correction factors were applied to the measurements. Only the thickness value (minor axis) is representative of the true grain dimension. The significance of the measured major axis is only for comparative purposes. Therefore, the usefulness of the above exercise is only the development of a qualitative understanding of the effect of various processing parameters on microstructural texture development.

It was not possible to determine the grain growth mechanism in undoped, fiber textured, $Sr_2Nb_2O_7$ due to the potential for the presence of impurity phases in solid state reacted powder and the resulting difficulty in controlling the process parameters such as liquid phase formation, amount, and distribution. These factors have a determining influence on grain growth rates. The broadening trend in the grain size distribution, and the potential for formation of a liquid phase in the $SrO\text{-}Nb_2O_5$ system with increasing temperature and time indicates the strong possibility of exaggerated grain growth. This is contrary to observations in cases of normal grain growth, where grain size distributions are shifted to larger size but are self similar.[27]

The TGG samples are expected to have fiber texture along the crystallographic *b*-axis direction (laminate thickness direction). A comparison of the X-ray diffraction patterns obtained from the face, and the cross-section in the thickness direction shows a marked difference in the relative peak heights of the (0k0) peaks in the pattern as shown in Figure 4.9. The Lotgering factor was calculated to quantify the degree of texture. X-ray diffraction peak intensities from planes normal to the fiber texture direction in an oriented sample are compared to those obtained for the same set of planes in a random sample. The Lotgering factor is normalized so that a random sample would have a factor of zero, and a perfectly oriented sample (single crystal-like) would have a factor of 1.[25]

$$\text{Lotgering factor, } f = \frac{(p - p_o)}{(1 - p_o)},$$

$$\text{where } p = \frac{\Sigma I_{(0k0)}}{\Sigma I_{(hkl)}} \text{ for sample of interest,}$$

$$\text{and } p_o = \frac{\Sigma I_{(0k0)}^{random}}{\Sigma I_{(hkl)}^{random}} \text{ for sample with randomly oriented grains}$$

Calculated values of Lotgering factors are plotted in Figure 4.10 for different sintering conditions for TGG samples containing 5 and 10 vol% of small template particles, and

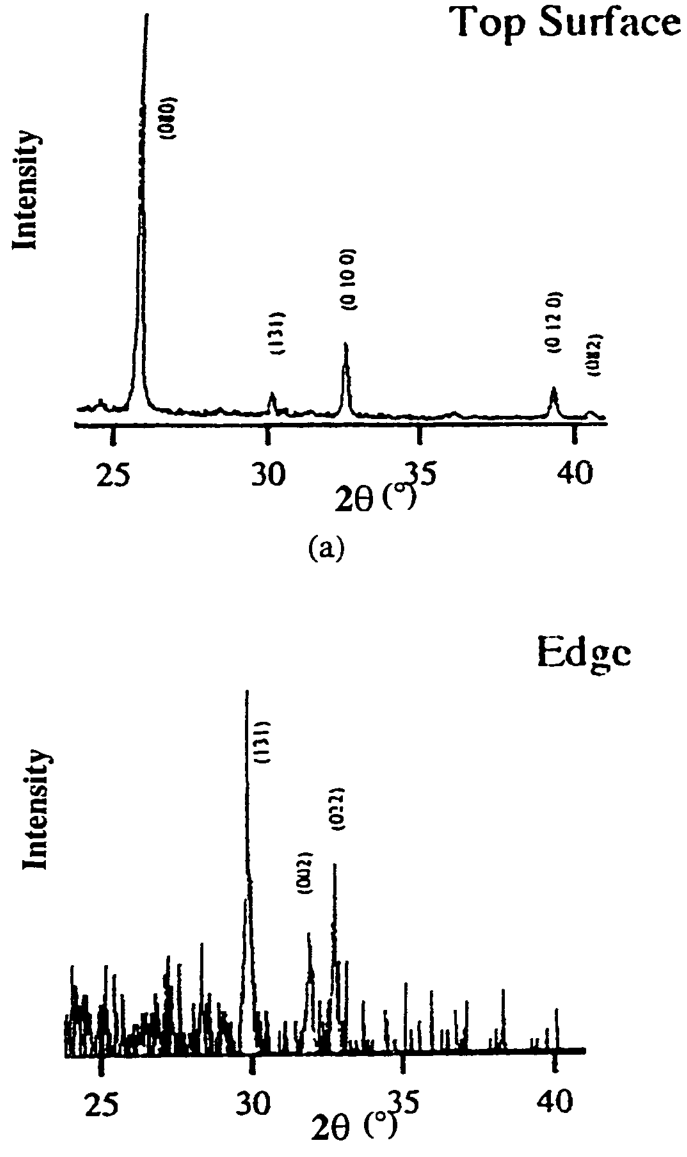

(a)

(b)

Figure 4.9 X-ray diffraction patterns from (a) Top surface, (b) Edge

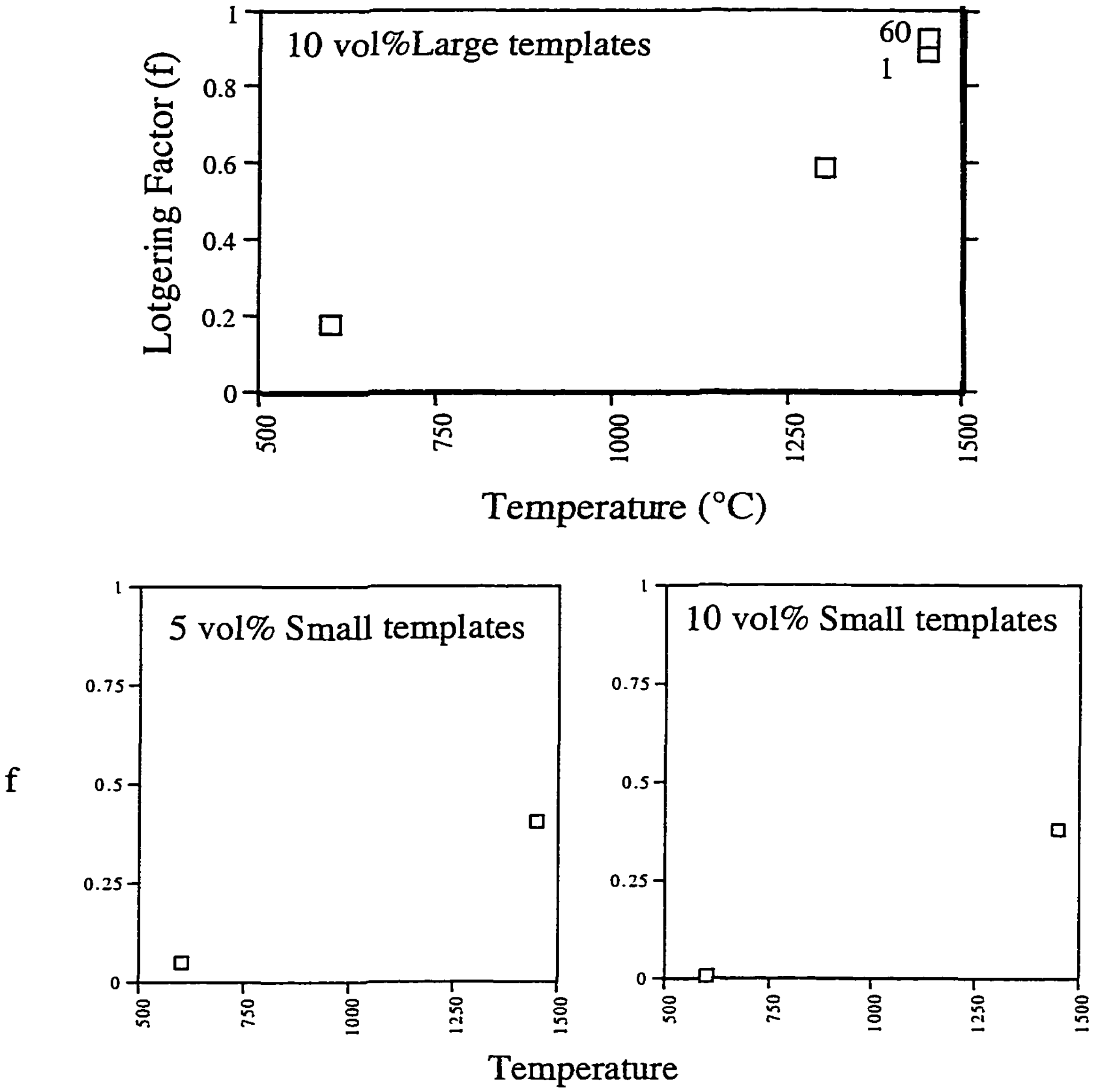

Figure 4.10 Calculated Lotgering factors for fiber textured samples

10 vol% large template particles initially. The inability to generate texture by using small template particles is demonstrated again in this data. The high degrees of grain orientation seen in the SEM micrographs are translated to high degrees of crystallographic fiber texture as determined by their Lotgering factors. Confirmation of fiber texture by pole figure measurement and the physical property measurements are discussed in Chapter 5.

4.3.2 Sheet Texture in $(Sr_{0.9}La_{0.1})_2Nb_2O_7$

Sheet textured samples were fabricated by TGG using coprecipitated 2 mol% La-doped $Sr_2Nb_2O_7$ powder. The $Sr_2Nb_2O_7$ template particles were synthesized in KCl using $SrCO_3$ and large $SrNb_2O_6$ crystals synthesized in $SrCl_2$ as the niobium source as described in section 2.3.5.

4.3.2.1 Template Morphology and Sheet Texture

The template particles used in this section are shown in Figure 4.11. These particles have a long rectangular face and a thickness which is much shorter than the breadth of the particles. Hartman and Perdok[28] proposed that growth occurs preferentially in directions along uninterrupted series of strong bonds. The directions in which one can find continuous, rigid bonding in $Sr_2Nb_2O_7$ are coincident with the

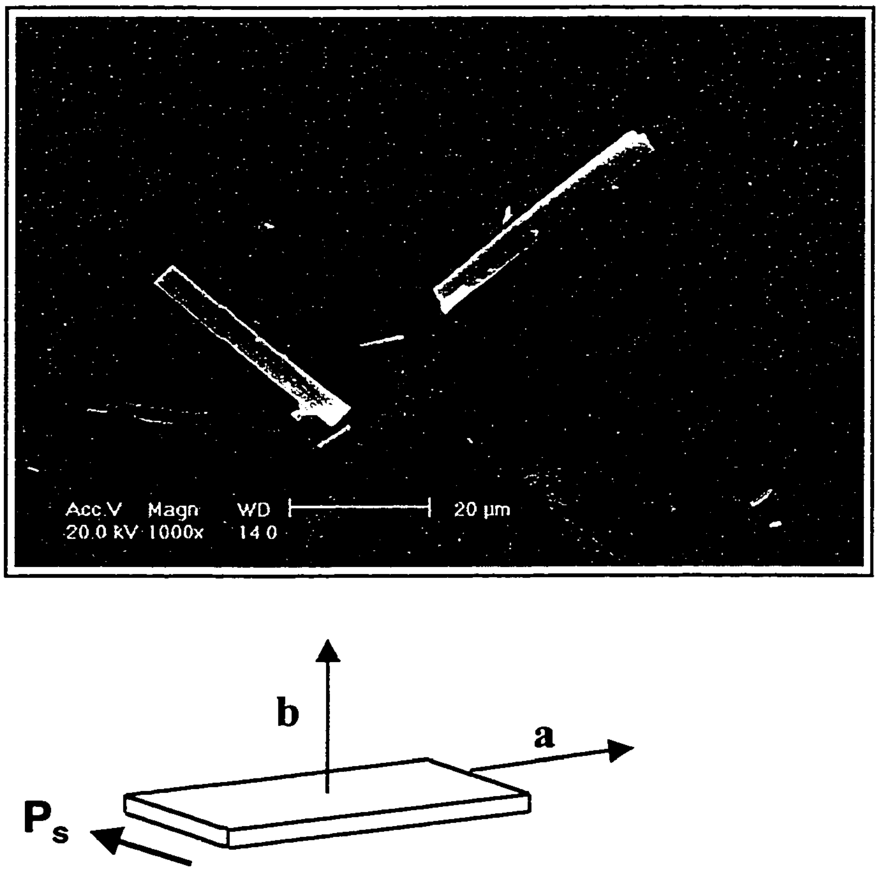

Figure 4.11 Template particles used to produce sheet texture and relation to crystal structure

crystallographic *a* and *c*-axes. The Nb-O bonds along the *b*-axis are discontinuous. Hence one would expect the growth to be slowest in the *b*-direction. X-ray diffraction of plate-like or blade-like particles of $Sr_2Nb_2O_7$ indicates that the shortest dimension is along the *b*-axis. This evidence is further corroborated by the enhancement of the (0k0) peaks in the X-ray diffraction pattern of a plane parallel to the casting plane in grain-oriented samples. The length of the blade like particles is along the *a*-axis and the width of the face is along the *c*-axis as the shape of the blade like $SrNb_2O_6$ precursor particles influences the morphology of $Sr_2Nb_2O_7$ templates synthesized in KCl. Therefore, it is extremely difficult to devise a technique to achieve fiber texture along the *c*-axis using flux grown, rectangular blade-shaped $Sr_2Nb_2O_7$ templates. A low degree of orientation along the polarization axis (*c*-axis) defeats the purpose of using texture to improve piezoelectric properties in $Sr_2Nb_2O_7$. However, samples with sheet texture (3-dimensional texture) would exhibit a high degree of orientation along the *c*-axis.

4.3.2.2 Orientation of Template Particles for Sheet Texture

Production of sheet texture in $(Sr,La)_2Nb_2O_7$ requires the orientation of blade-like template particles with their long-axis along the tape casting direction and their largest rectangular face parallel to the tape casting plane. The orientation described above would make the *b*-planes of all templates parallel to each other and the tape cast surface, and make a particular direction (*a*-direction) in the oriented *b*-plane of all templates parallel to a common direction (casting direction), thereby satisfying the conditions for sheet texture.

A number of experimental studies have proved the ability of orienting plate-shaped particles using the shear field developed under the doctor blade during tape casting. Numerous theoretical treatments[22,23] based on Jeffery's equations for dynamic motion of particles in fluid flow have been used to describe orientation in flow systems subjected to various shear fields. These equations have been used to describe orientation of rods and discs in simple shear conditions such as couette flow, and have been modified to describe orientation developed in more complex flows.[29-32]

Orientation of rod-shaped particles will be discussed first, to develop the argument for orientation of blade-shaped template particles.

For a rod-shaped particle of unit length in a liquid under zero shear, the liquid molecules are expected to frequently collide with the rod at very short time intervals. These collisions impart a random motion through very small angles before subsequent collisions. This motion is referred to as the diffusional reorientation. The rotational motion of such a rod under shear is described by the following differential equation:[33]

$$\frac{\partial c(r,t)}{\partial t} + \frac{\dot{\gamma}\sin\theta}{2} \bullet \frac{\partial c(r,t)}{d\phi} = \Theta\nabla^2 c(r,t) \qquad (1)$$

where c(r,t) is the concentration of rods whose axis is described by the unit vector **r** in spherical coordinates (r,θ, ϕ), and $\dot{\gamma}$ is the shear rate. The steady state solution is a rod which rotates with a period T,

$$T = \frac{2\pi}{\dot{\gamma}}(\rho + \frac{1}{\rho})$$

where ρ is the aspect ratio of the rod (ρ=b/a). Although the differential equation (1) cannot be solved analytically for the orientation distribution as a function of time, it does highlight the importance of two processes leading to particle rotation. These are the diffusion constant Θ and the shear rate $\dot{\gamma}$. The relative importance of these two processes is described by the rotational Peclet number, Pe_r,

$$Pe_r = \frac{\dot{\gamma}}{\Theta}$$

When $Pe_r \rightarrow \infty$, diffusion is negligible and the particle rotates towards a direction of preferential orientation as shown in Figure 4.12, and when $Pe_r \rightarrow 0$, Brownian motion causes all orientations to have the same probability. Therefore, a large Peclet number would result in orientation of the rods along the direction of shear. This treatment has been extended by Perrin[34] to oblate and prolate ellipsoids. Since a prolate ellipsoid is a closer approximation to the template particles used in this study than a rod or an oblate ellipsoid, the following equation is used to approximate the diffusion coefficient Θ,

$$\Theta = \frac{3k_BT}{16\pi\eta a^3}\{\frac{(2-\rho^2)G(\rho)/\rho^{\frac{2}{3}}-1}{(1-\rho^4)}\},$$

where η is the solution viscosity and G(ρ) is defined as:

$$G(\rho) = \rho^{\frac{2}{3}}(1-\rho^2)^{\frac{-1}{2}}\ln\{\frac{1+(1-\rho^2)^{\frac{1}{2}}}{\rho}\}$$

Using the value of Θ based on template particle dimensions, and the average shear rate during tape casting, we can calculate the approximate Peclet number during casting. The effect of matrix particles on Θ is neglected in this treatment. During conventional tape

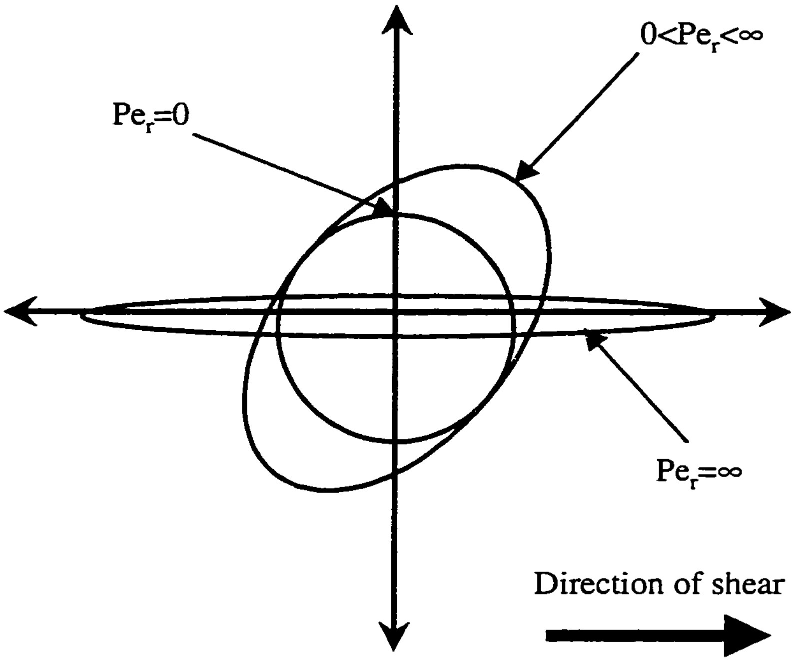

Figure 4.12 Schematic of the steady state solution of the rotary convective diffusion equation for ellipsoids of revolution showing the orientation probability along direction of shear rate.

casting, the shear field is applied only in the narrow gap in the vertical plane below the doctor blade, which results in large shear rates and large Peclet numbers. By using a narrow blade opening, a high viscosity slurry, templates with large aspect ratios, and high casting velocities, Peclet numbers large enough to orient particles with their thin dimension along the tape thickness can be produced. This is sufficient for producing fiber texture using platelets and rods. A slurry having a viscosity of 20 mPas^{-1} under the doctor blade, template particle size of 20 μm with an aspect ratio of 5-10 (length to width), casting speed of 9 cm/s, and a blade gap of 300 μm were used to calculate Peclet numbers during tape casting of TGG samples. The Peclet number for TGG conditions used in this study is $5.1 \times 10^{10} - 2.4 \times 10^{11}$ for an average shear rate of 150 s^{-1}.

However, in the plane of casting, due to the large distance (5-10 cm) between the walls of the moving reservoir across the width of the cast tape, there is a large region of plug flow where the shear rate is zero. Therefore, in any section parallel to the casting plane, the shear rate is nearly zero across the width of the tape. This results in a Peclet number of ~0 for particle motion in the casting plane, which means that the particles don't experience any couple that would result in preferential orientation along the casting direction.

One way to produce a shear field in the casting plane is to provide a set of closely spaced narrow openings with evenly spaced rods or needles along the long edge of the doctor blade as shown in Figure 4.13. In this study, needles of 0.5 mm diameter were spaced ~1.0 mm apart for the "gated" tape casting set up. This results in an average shear rate of ~50 to 75 s^{-1} while the slurry is under the doctor blade during casting, and the relatively high viscosity immediately after the doctor blade allows just enough flow for

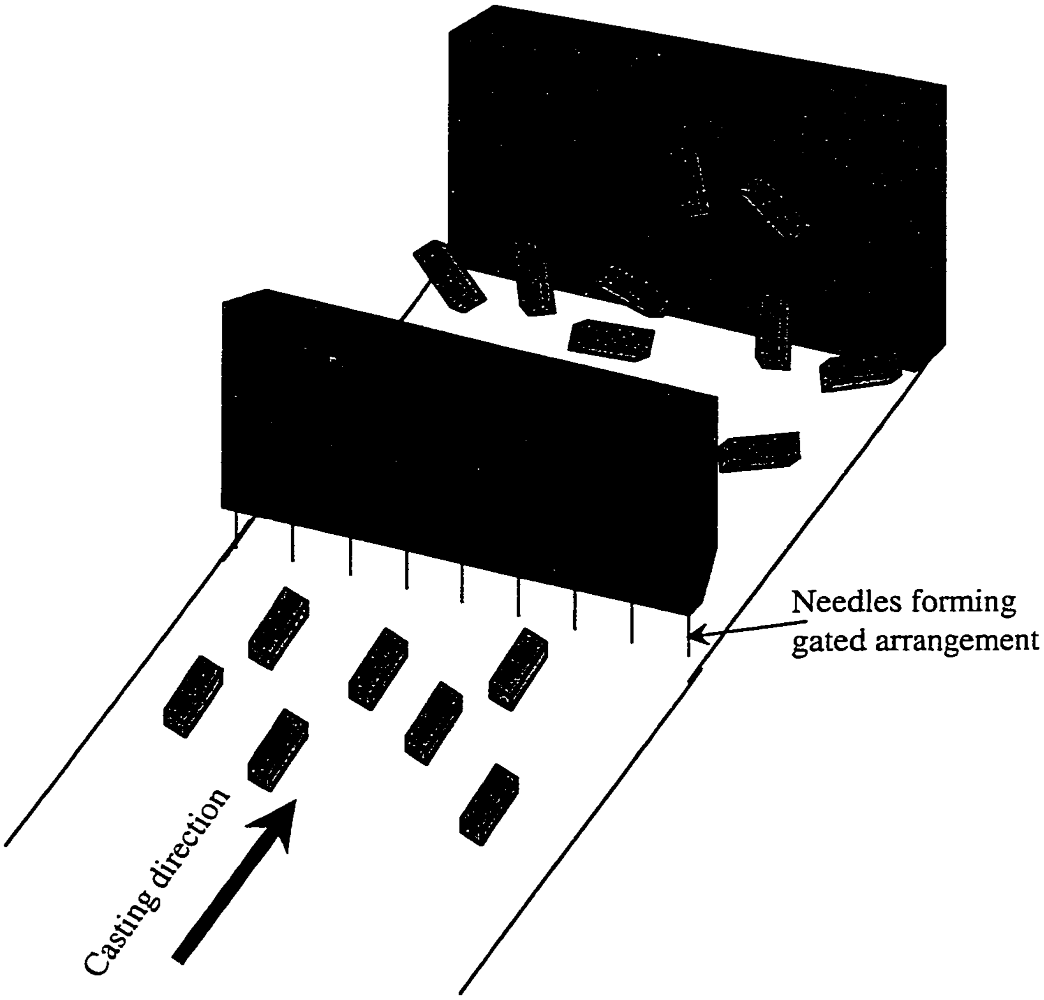

Figure 4.13 Use of gated tape casting arrangement for obtaining sheet texture

leveling of the tape due to the surface tension of the cast surface. Based on the template aspect ratio, slurry viscosity behavior, and spacing between the needles, a Peclet number of ~1.6×10^{10}-7.4×10^{10} was calculated for the flow under the doctor blade in the horizontal plane. The high Peclet number shows the possibility of using such an approach to align rods and blade-shaped templates by the gated tape casting technique. The orientation of the *b*-planes of the templates parallel to the casting plane is most likely a result of gravitational force on rotating particles during tape casting and the effect of uniaxial lamination. The effect of these processes was not included in the qualitative treatment presented above.

The above description is a qualitative description based on well developed theoretical equations. The applicability of this analysis depends on a number of other factors such as matrix powder-template interaction, template-template interactions, and other tape casting process parameters. Experimental verification of the accuracy of the predicted numbers is beyond the scope of this study. However, the usefulness of such a treatment has been demonstrated in Albers-Werk and Ring's study[35] on the orientation of mica particles during dip-coating, and numerous studies on the orientation of short fibers during the extrusion of short fiber composites.[30,31]

The orientation produced during tape casting must be preserved during uniaxial lamination. 200-500 layers of dry tape (~150 μm thick) were stacked and preheated to ~60°C in an oven. Lamination was carried out at extremely low loads of 500 g on an initial area of ~ 6.25 cm^2. The lamination resulted in very minimal spreading of the laminate surface. This process was found to be suitable for producing thick laminates with sheet texture.

Slurries of 80 vol% AKP-50, fine alumina powder, and 20 vol% of $PbNb_2O_6$ rod shaped particles, with solids loading of ~30-35 vol%, were cast under the conditions used for TGG of $(Sr,La)_2Nb_2O_7$ to experimentally determine the feasibility of using gated tape casting for producing alignment along the long axis of templates. The samples were sintered at 1250°C for 1 h to promote sintering of the templates and the matrix prior to sectioning the sample for SEM observation. A section parallel to the cast surface produced by gated tape casting is shown in Figure 4.14 . The orientation of the rod-shaped particles is seen in the tapes produced by gated tape casting.

4.3.2.3 Effect of Excess Niobium on Grain Growth in $(Sr_{0.99}La_{0.01})_2Nb_2O_7$

As discussed in Chapter 3, the amount and distribution of liquid phase can affect the rate and extent of template growth. If template growth is due to dissolution at a matrix grain, diffusion through a liquid phase, and reprecipitation on the growing grain, then controlling the amount of liquid phase is important to control template growth. If diffusion through the liquid layer is rate-controlling, a thinner layer would result in a steeper concentration gradient and faster kinetics of mass transport.[36] Therefore, the amount of excess niobium at the grain boundaries must be reduced to obtain faster growth rates. Another reason to minimize the amount of excess niobium is to avoid degradation of electrical properties due to niobium rich oxides at the grain boundaries.

TGG samples with 10 vol% initial templates and small excess amounts of Nb (in ~ 5-1000 ppm range) were sintered at 1350°C and 1450°C. The *c*-direction edges of samples sintered at 1450°C for 1 h with different amounts of excess niobium are shown

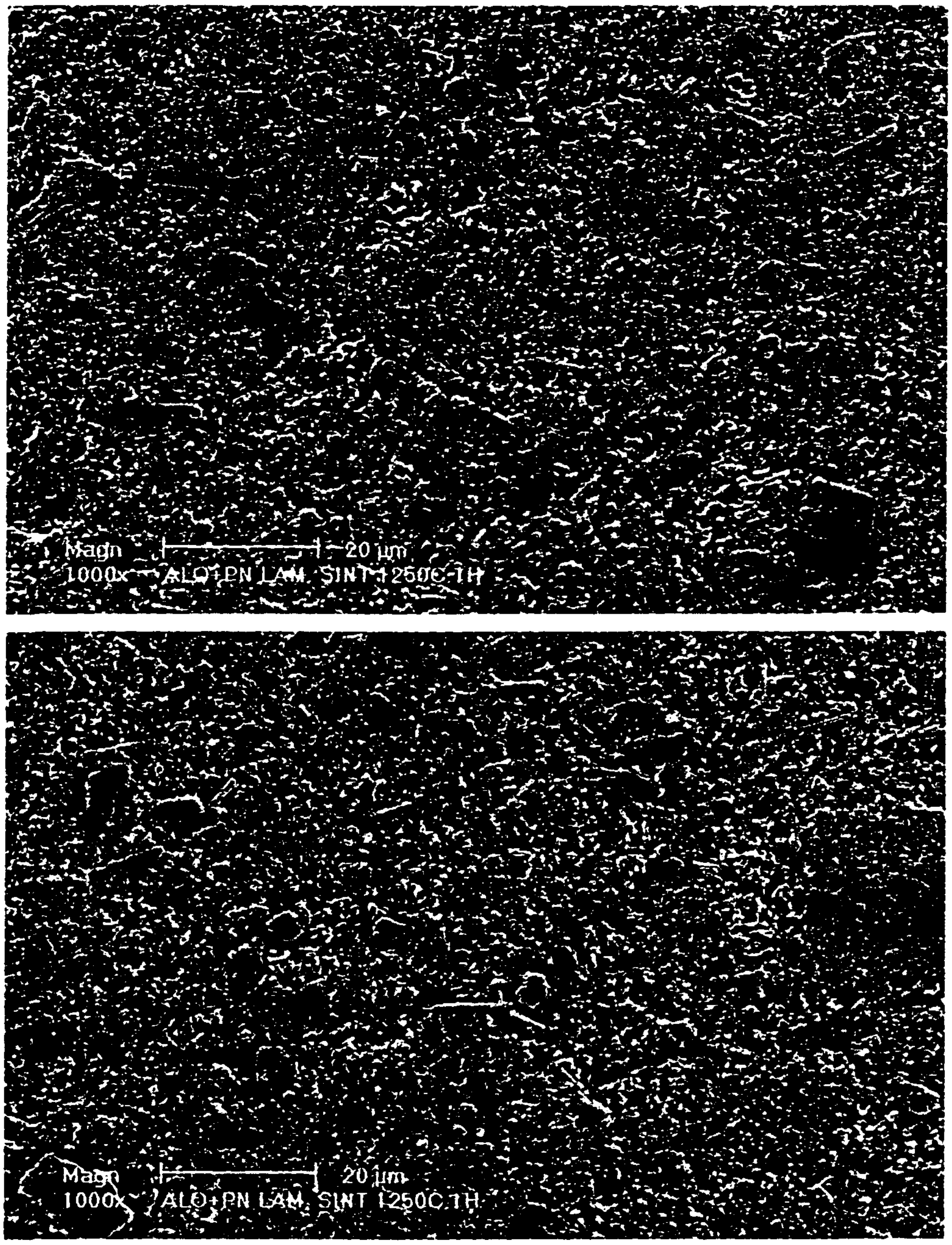

Figure 4.14 Two SEM micrographs of different areas on a plane parallel to the casting plane, showing $PbNb_2O_6$ templates oriented along the casting direction in an alumina matrix by gated tapecasting.

in Figure 4.15. One of the noteworthy features of these microstructures is the absence of impingement among the large grains. This allows us to observe the growth prior to any change due to impingement.

The average grain area of large grains, presumably templates, is shown in Figure 4.16. The average grain area increases with increasing niobium concentration. This is contrary to the expectation that a lower amount of liquid phase would result in thinner liquid layers and higher growth rates. One possible reason for this anomaly might be that the liquid formation is a result of a reaction, and at such low amounts of excess niobium, the distribution might not result in a continuous film. A similar increase in growth of alumina grains in the presence of ppm-levels of impurities was observed by Baik et al.[19] The larger grains result in a larger area fraction of large anisotropic grains as shown in Figure 4.17.

In order to detect the contribution of exaggerated grain growth in the matrix grains leading to large anisotropic grains, the number density of large (>15 μm) anisotropic grains was tracked at 1350°C and 1450°C with increasing niobium concentration. The results are plotted in Figure 4.18. The nearly constant number density of large grains implies that the coarsening of matrix grains does not contribute to the population of large grains. This is also validated by the SEM micrographs which show very few grains which are not aligned in the expected direction.

The average grain dimensions (major and minor axis of inscribed ellipses) obtained in microstructures sintered at 1350°C and 1450°C for 1 h with different amounts of excess niobium are presented in Figure 4.19. The breadth of the distributions is indicated by a spread of one standard deviation to each side of the average. Although the

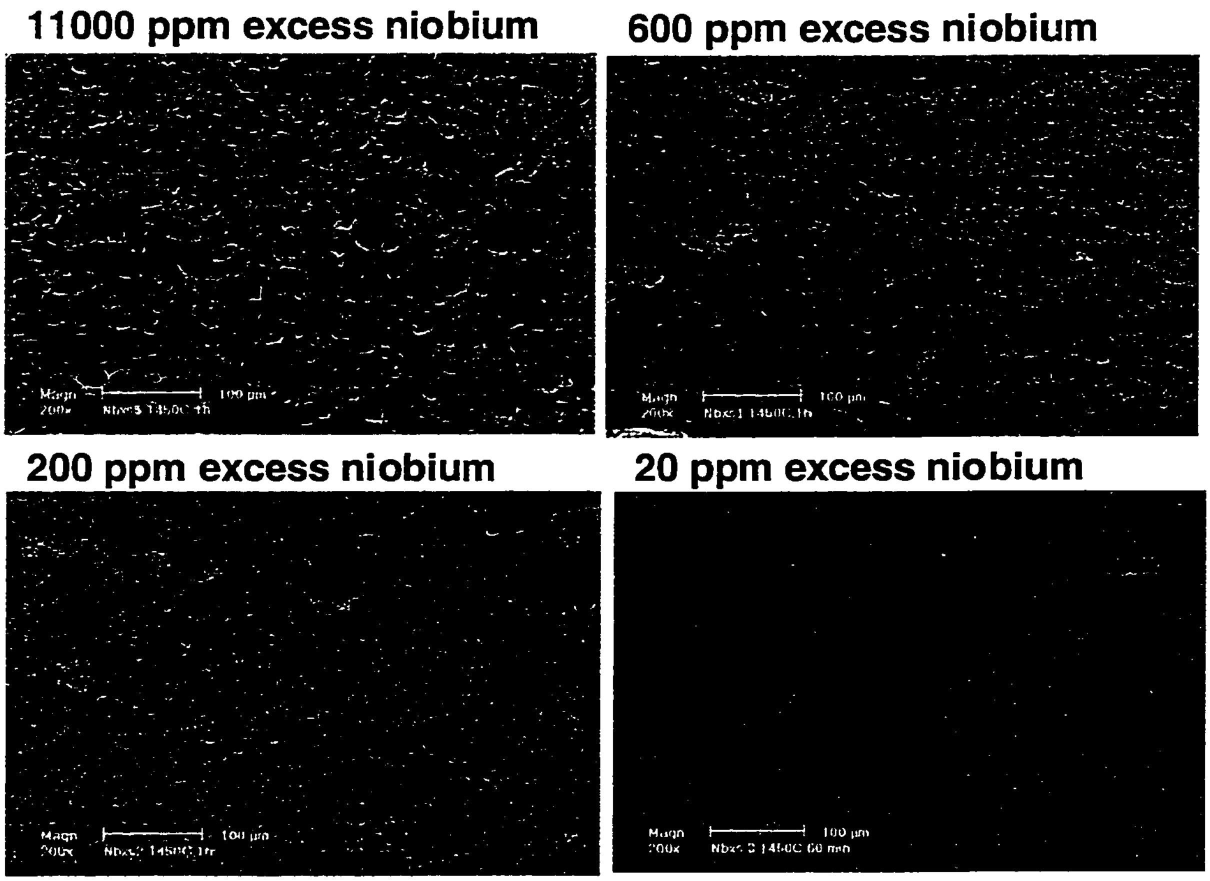

Figure 4.15. SEM micrographs of c-planes for TGG samples sintered at 1450°C for 1h (10 vol% initial templates) as a function of excess niobium

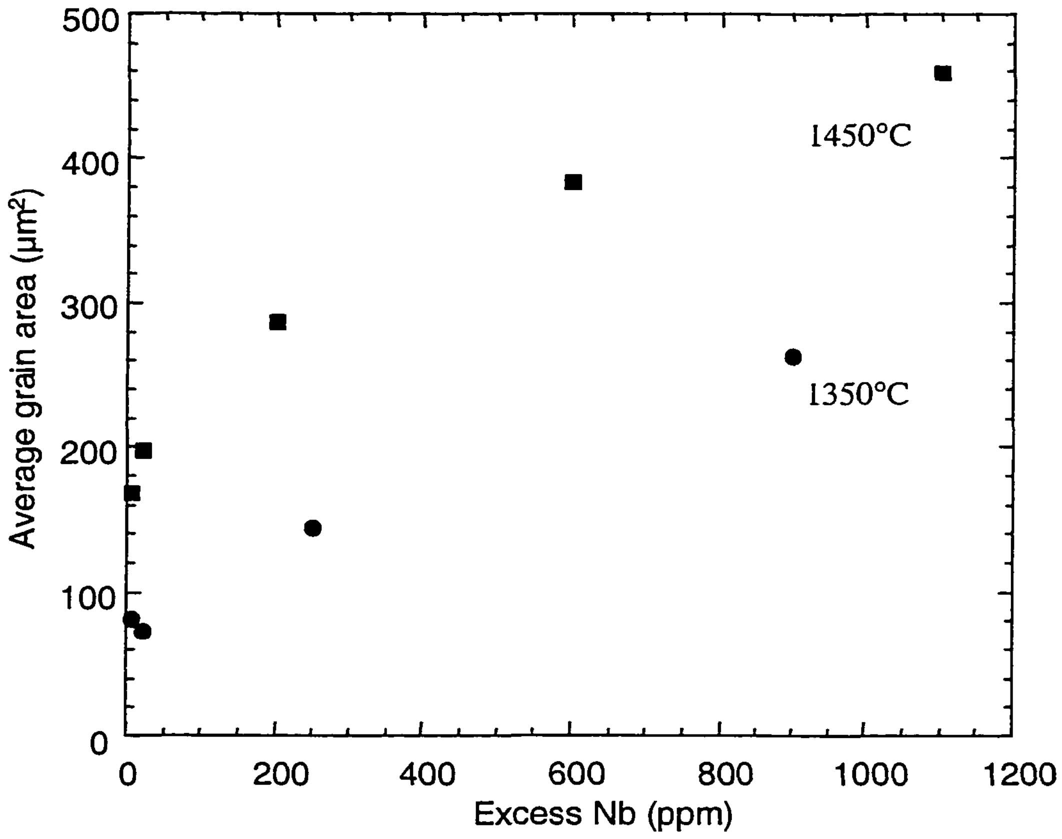

Figure 4.16 Average area occupied by a template grain as a function of excess niobium (10 vol% initial templates)

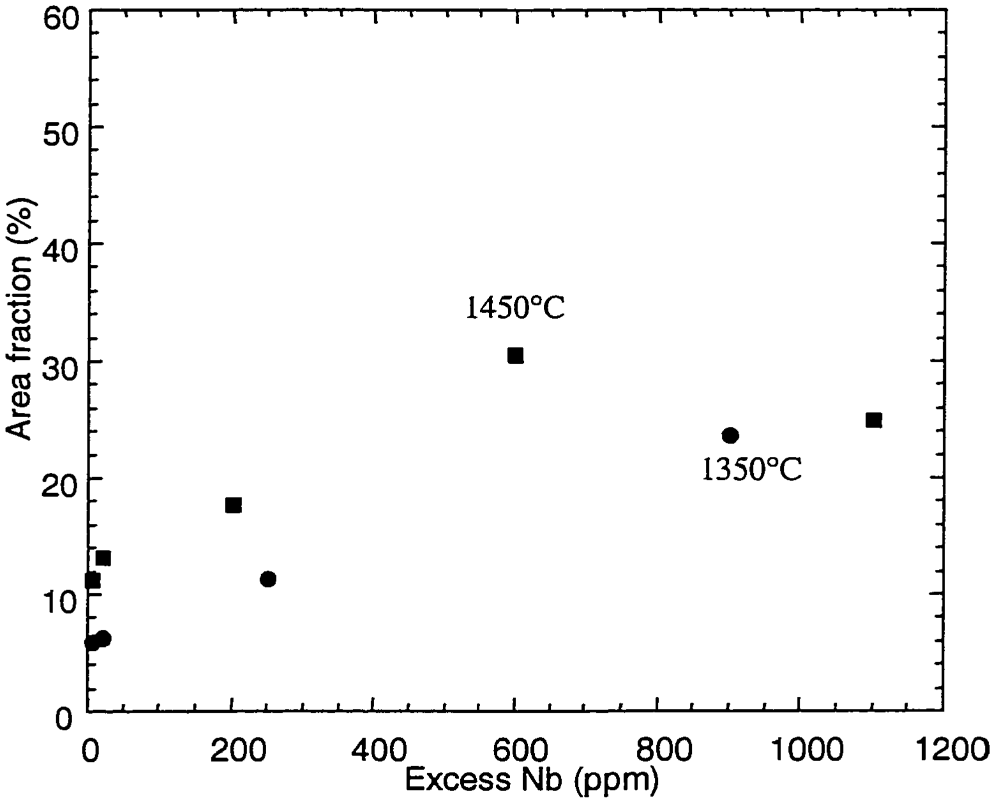

Figure 4.17 Area fraction occupied by a template grain as a function of excess niobium (10 vol% initial templates)

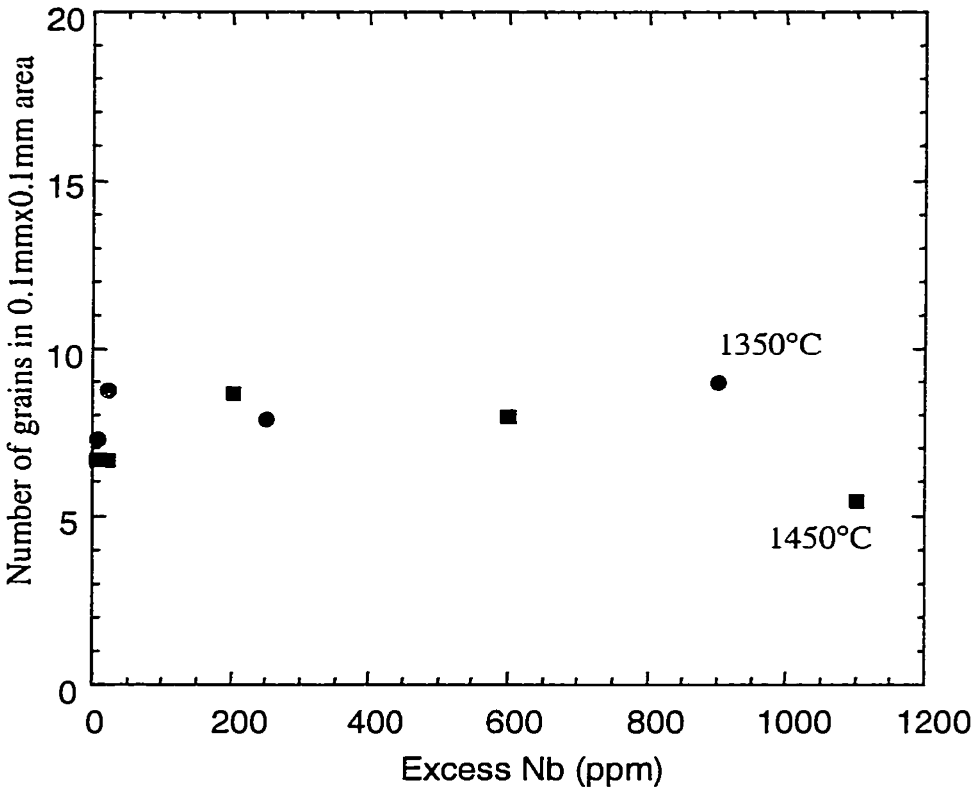

Figure 4.18 Number density of template grain (N/0.1 mm x 0.1 mm) as a function of excess niobium (10 vol% initial templates)

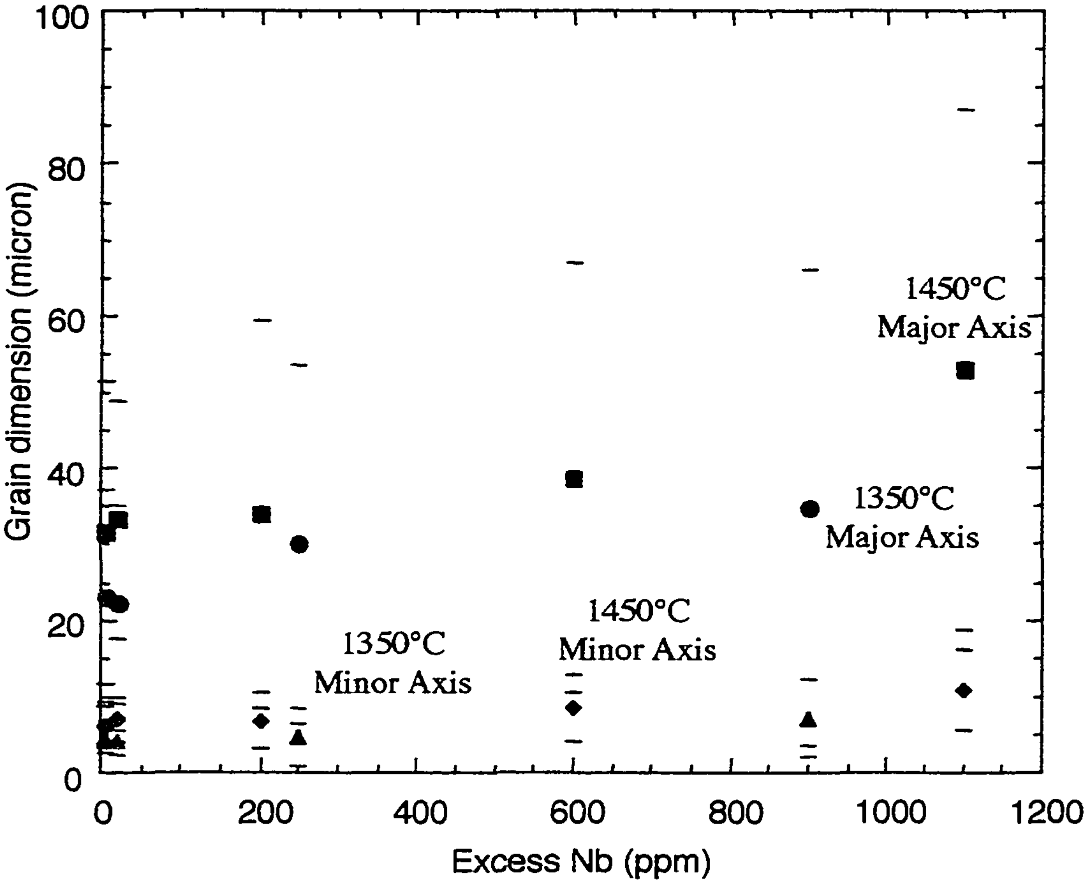

Figure 4.19 Average grain dimensions of template grains as a function of excess niobium (10 vol% initial templates)

maximum grain size was observed to be well over 100 μm, the average value reaches a maximum of ~50-60 μm for 1200 ppm of niobium at 1450°C. Figure 4.20 shows the aspect ratios obtained as a function of excess niobium. The aspect ratios show a slight increase with increasing excess niobium and then level off around ~6 for higher amounts. On the basis of these observations, excess niobium in the 500-1000 ppm range was chosen to fabricate TGG samples with sheet texture.

4.3.2.4 Grain Growth Kinetics for Sheet Textured $(Sr_{0.99}La_{0.01})_2Nb_2O_7$ Ceramics

Grain growth was studied as a function of time at 1450°C in samples containing 1000 ppm excess niobium oxide and 10 vol% initial templates. Microstructures of sample sections parallel to the *c*-plane and sections parallel to the *b*-plane sintered at 1450°C for 1, 10, 30, and 60 minutes were analyzed. Typical microstructures are shown in Figure 4.21. Sheet texture of large anisotropic grains can be seen in these microstructures.

Stereological measurements of template size distributions were made to determine the average grain growth rates along the *a*, *b*, and *c*-directions. Sintering conditions at which template grains and matrix grains could be differentiated were used for template growth kinetics. This was necessary to obtain true template dimensions and growth rates along different crystallographic axes. Template particles with major axes longer than 15 μm were included in the data used to calculate template size and orientation statistics as the average matrix grain size was 5-10 μm. The major and minor axes of an inscribed ellipse, grain area, the angle between the major axis and the *b*-direction in the *c*-plane,

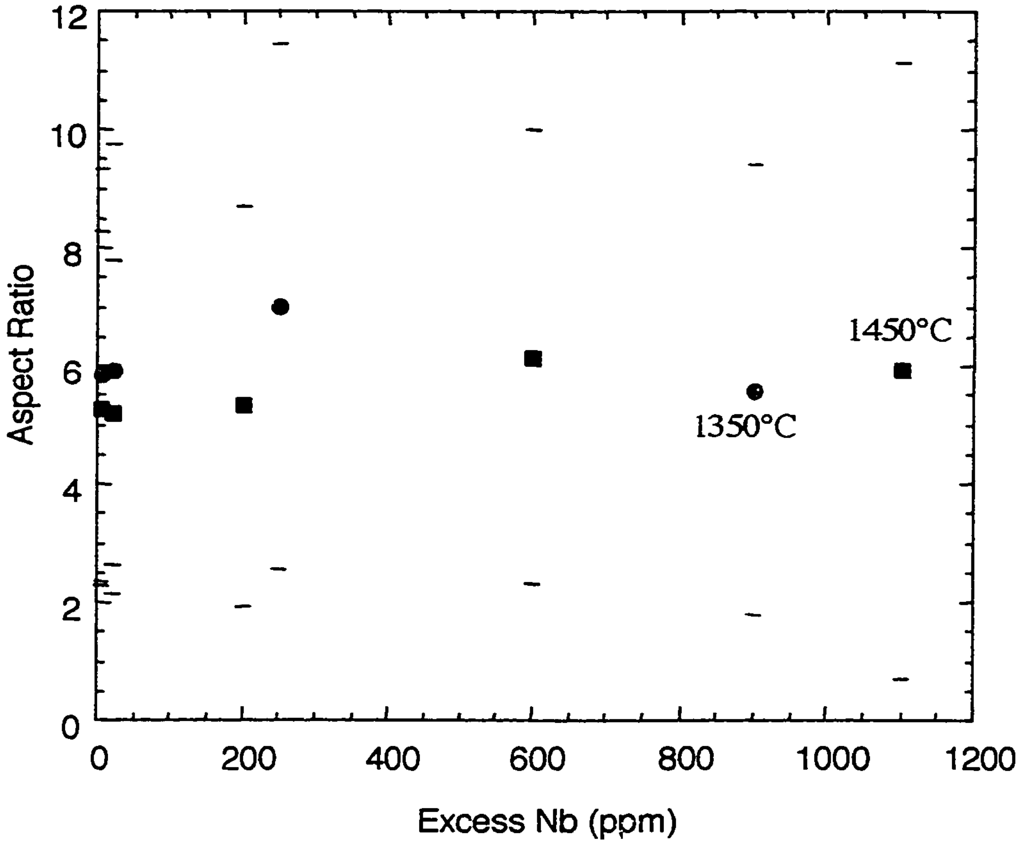

Figure 4.20 Average aspect ratios of template grains as a function of excess niobium (10 vol% initial templates)

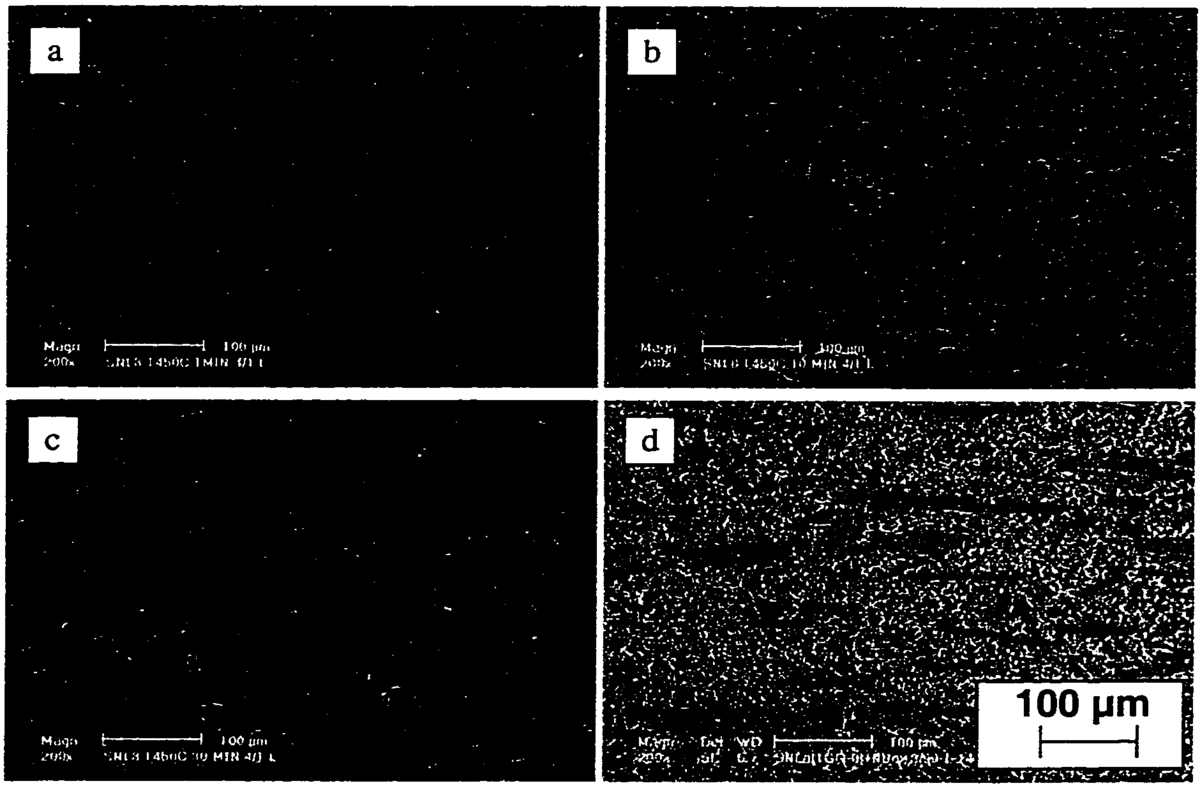

Figure 4.21 (I) SEM micrographs of sintered microstructures parallel to the c-plane sintered at 1450°C for (a) 1 min, (b) 10 min, (c) for 30 min, (d) for 60 min

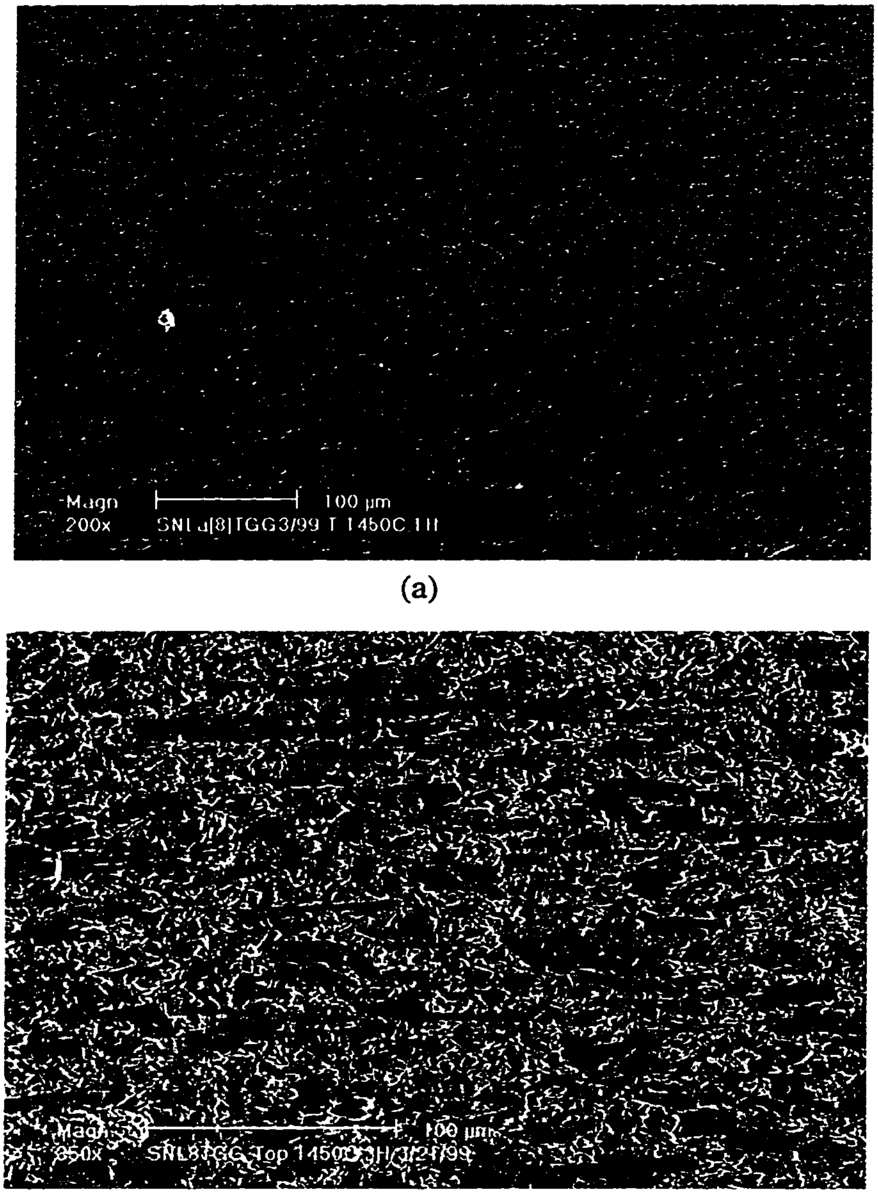

(a)

(b)

Figure 4.21 (II) SEM micrographs of sintered microstructures parallel to the b-plane sintered at 1450°C for (a) 1 h and (b) 2 h and the angle between the major axis and the *c*-direction in the *b*-plane were measured by NIH image software for all large grains. The data are shown in Figure 4.22. Figure 4.22b shows the angular distribution of template orientations. The above-mentioned angles and the corresponding area fractions were measured over 5° intervals. For a template particle that has attained the ideal orientation during gated tape casting, the angles would be 90° in both the *b* and *c*-planes. The plot (Figure 4.22b) shows the distributions at 1 min and 60 min for both number percent and area percent. The similarity of the distributions is maintained with time. This implies that there is no reorientation or rotation of template particles. Another feature of these distributions is the sharp peak around 90° in two planes of projection perpendicular to each other. In the third plane, the *a*-plane, it is difficult to separate the template grains from the matrix grains as they have similar cross sections. However, at conditions which lead to high degrees of textured volume fraction, such as 1500°C, 4 h, the angle distribution for oriented grains in the *a*-plane 4 h revealed a similar distribution centered around 90° with respect to the *b*-direction. This implies that the particles are well oriented in all three directions, and sections parallel to their *a*,*b*, and *c*-planes yield true values of *a*,*b*, and *c* -grain dimensions.

The dimensions along different axes are plotted in Figure 4.23. The values for average grain dimension along the *a*-axis, obtained from the *b* and *c*-planes is approximately the same, further confirming the sheet texture in these samples. The values of grain dimension along *b* and *c*-directions were obtained from the *c* and *b*-planes respectively. The breadth of the distribution of these dimensions is represented by the upper and lower bounds (one standard deviation from the average to each side). The

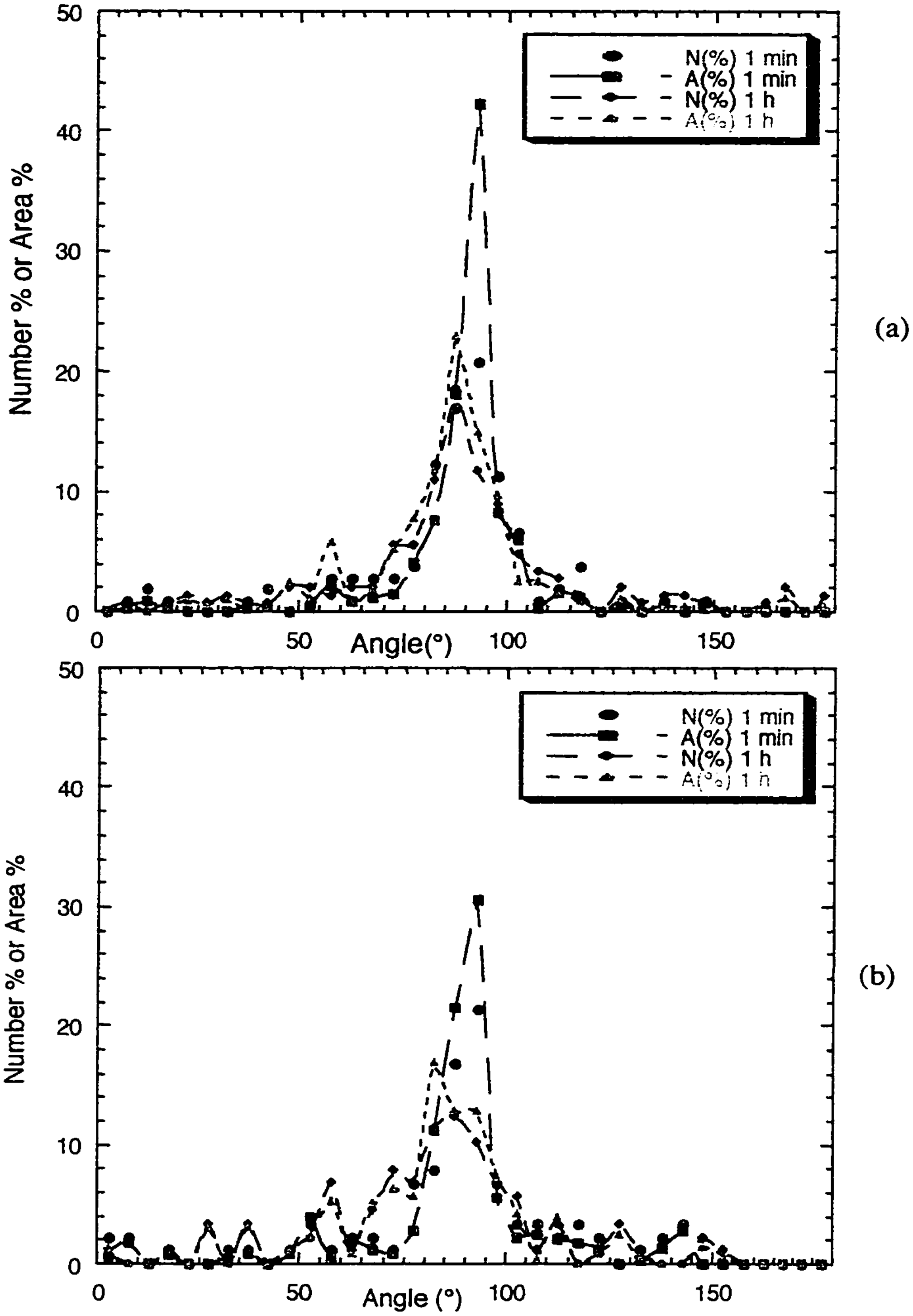

Figure 4.22 $(Sr,La)_2Nb_2O_7$ TGG samples (10 vol% initial templates) sintered at 1450°C. Number and area fraction as a function of angle from the b-axis in the (a) c-plane and (b) a-plane. N(%) and A(%) refer to the number percentage and area perccentage of grains at a particular angle.

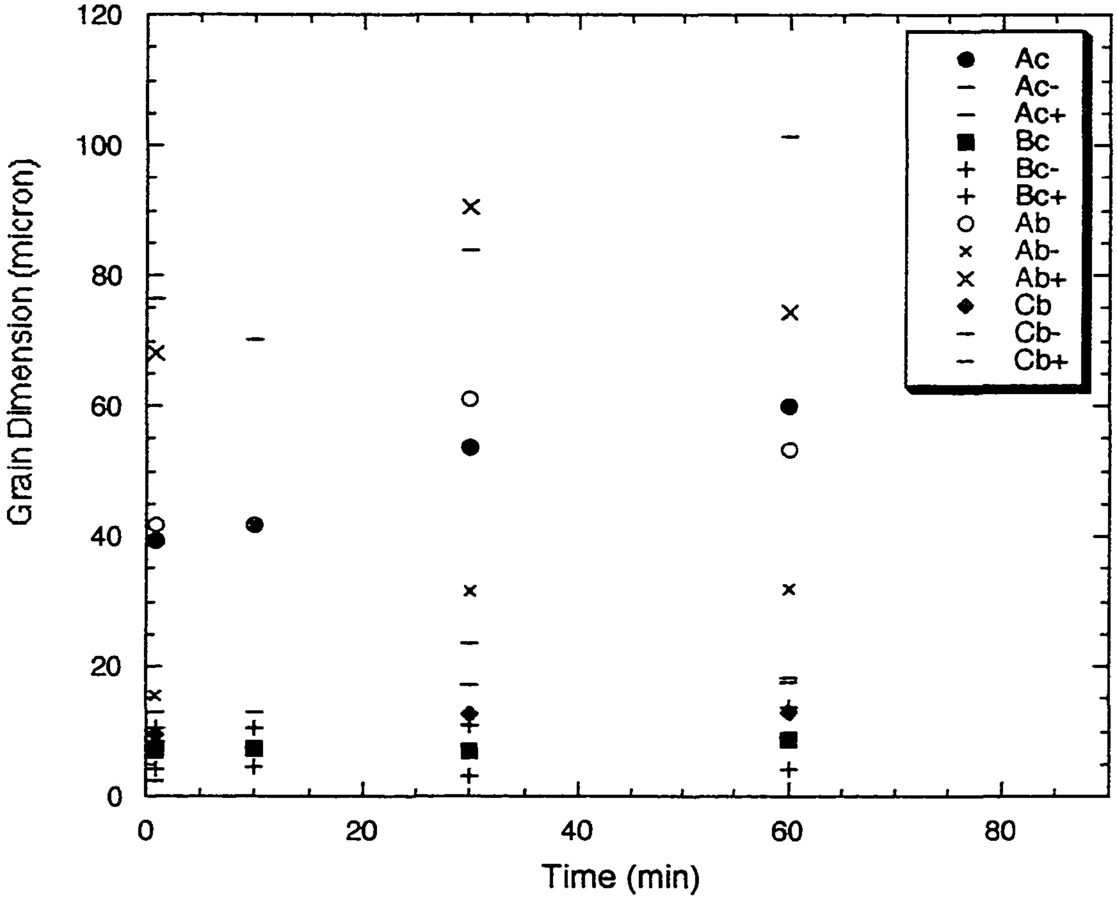

Figure 4.23 $(Sr,La)_2Nb_2O_7$ TGG samples (10 vol% initial templates) sintered at 1450°C. Ac: average grain dimension along a-direction from c-plane, Ab: average grain dimension along a-direction from b-plane, Bc: average grain dimension along b-direction from c-plane, Cb: average grain dimension along c-direction from b-plane. The respective upper and lower bounds are also plotted (for example Ac+ and Ac- refer to the bounds on Ac).

average values of grain dimensions were used to plot the aspect ratios (a/b, a/c, and c/b) as a function of time at 1450°C in Figure 4.24. From this plot, the increasing trend in a/b indicates that the growth rate along the *a*-direction is the fastest and that along the *b*-direction is the slowest. Figure 4.25 shows the number density of large templates in the b and *c*-planes. The number density does not change significantly. This means that the matrix grains do not grow to a large size and dominate the grain growth process. The area fraction occupied by the templates increases to about 25-30% from about 12% in 1 h (Figure 4.26). The matrix is consumed to a greater extent at 1500°C, 4 h or after ~8 h at 1450°C. The microstructures of a sample sintered at 1450°C, 1 h in Figure 4.27, shows the developing sheet texture. The X-ray diffraction patterns from the planes parallel to *a*,*b*, and *c*-crystallographic planes, sintered at 1500°C for 4 h, are shown in Figure 4.28. The enhancement of the 200, 080, and 002 peaks respectively, is another measure of the sheet texture in these samples.

4.4 CONCLUSIONS

Several processing factors have an effect on the texture development in $Sr_2Nb_2O_7$ ceramics. The template size relative to the matrix grain size and concentration were found to have a strong effect on the success of TGG. For $Sr_2Nb_2O_7$, 10 vol% initial templates were found to be effective. Template morphology determines the nature of the fiber texture and the possibility of producing sheet texture. Blade-like $Sr_2Nb_2O_7$ templates can be oriented to achieve sheet texture by the gated tape casting technique described in this study. Another processing factor, the amount of excess niobium,

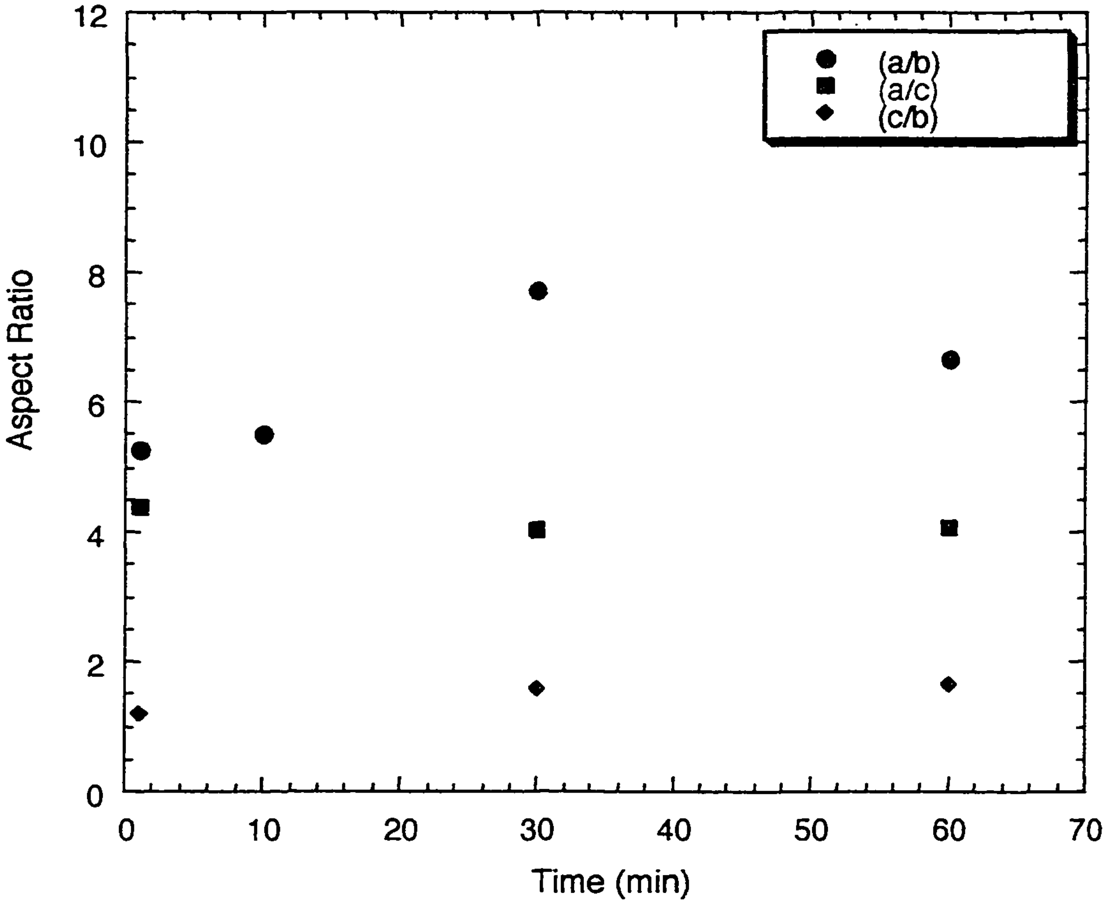

Figure 4.24 $(Sr,La)_2Nb_2O_7$ TGG samples (10 vol% initial templates) sintered at 1450°C. Aspect ratios for combinations of average a, b, and c-dimensions as a function of time

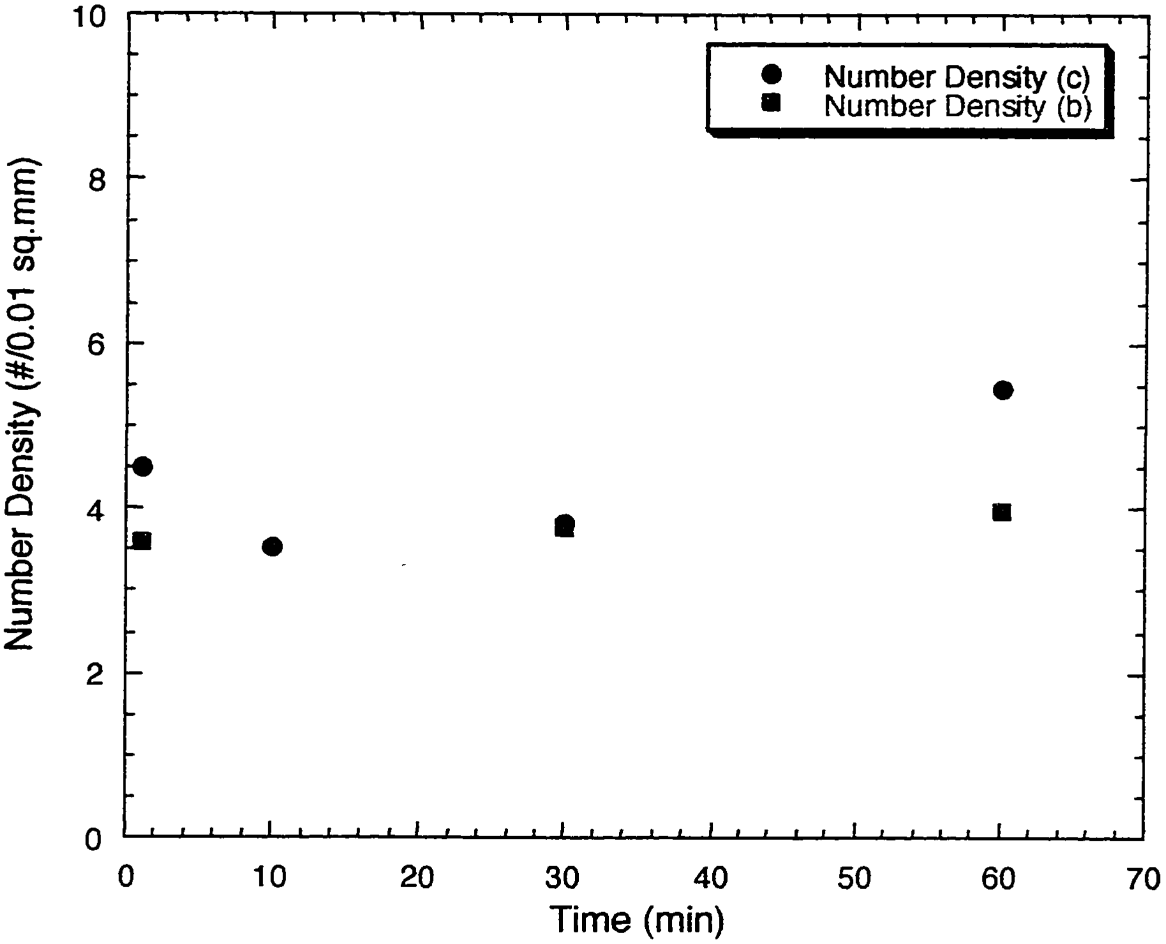

Figure 4.25 $(Sr,La)_2Nb_2O_7$ TGG samples (10 vol% initial templates) sintered at 1450°C. Number density as a function of time for c and b-planes

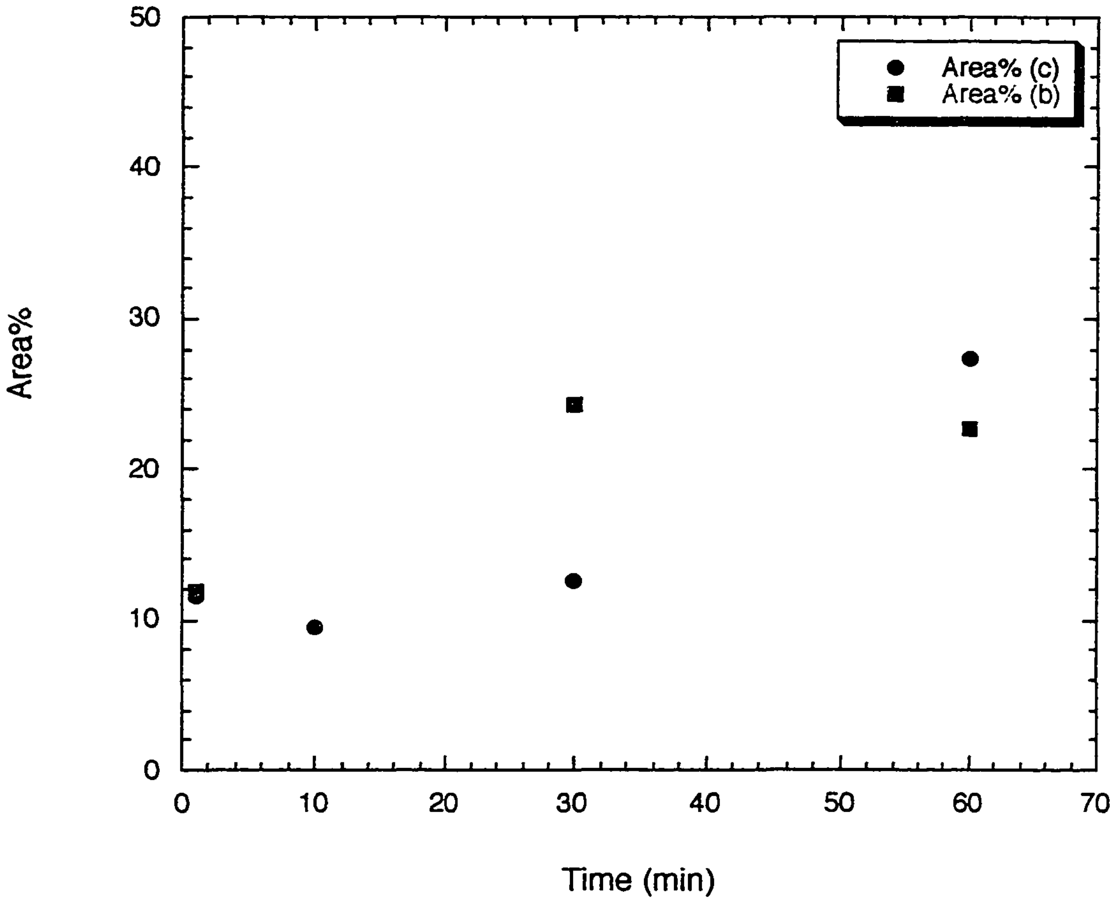

Figure 4.26 $(Sr,La)_2Nb_2O_7$ TGG samples (10 vol% initial templates) sintered at 1450°C. Area percent occupied by templates as a function of time for c and b-planes

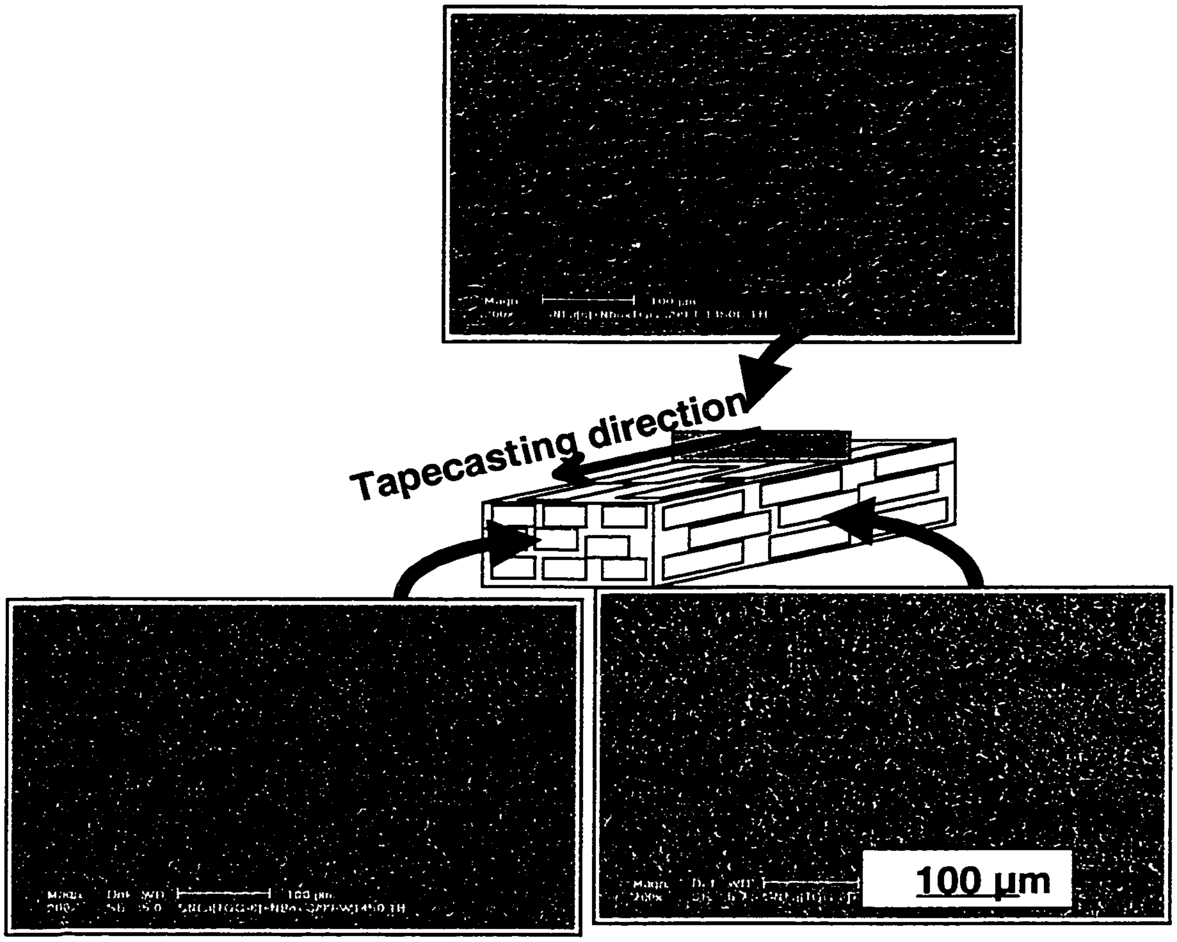

Figure 4.27 SEM micrographs of a, b, and c-planes for TGG samples sintered at 1450°C for 1 h (10 vol% initial templates) showing sheet texture

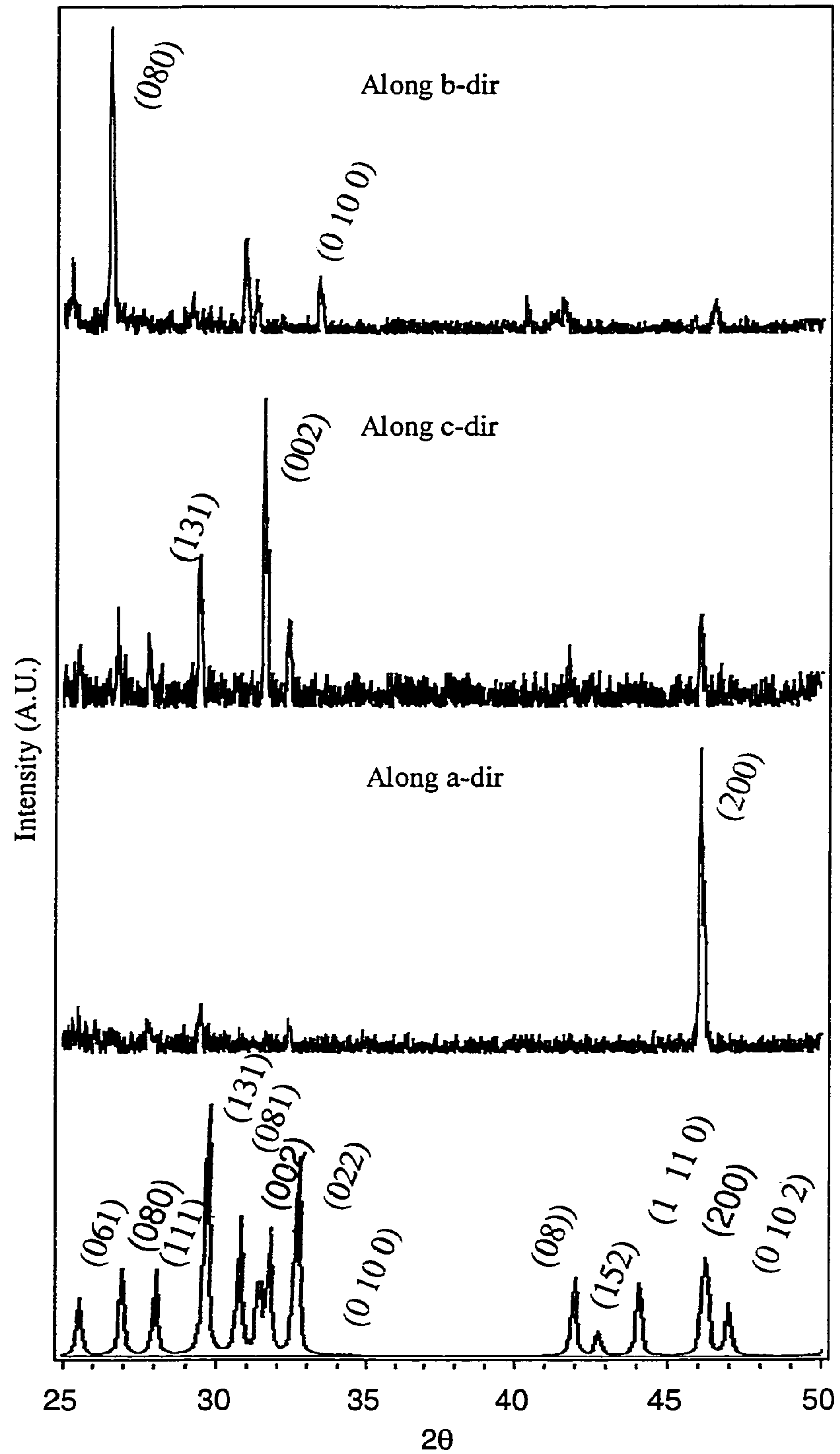

Figure 4.28. XRD patterns from a, b, and c-planes for TGG samples sintered at 1500°C for 4h (10 vol% initial templates) showing sheet texture

determines the amount of liquid formed and the extent of template growth. Template growth in this system has the characteristics of exaggerated grain growth. However, TGG can be used to obtain high degrees of texture in $Sr_2Nb_2O_7$.

4.5 REFERENCES

1 H. Igarashi, K. Matsunaga, T. Taniai, and K. Okazaki, "Dielectric and Piezoelectric Properties of Grain-Oriented $PbBi_2Nb_2O_9$ Ceramics," *Am. Ceram. Soc. Bull.*, **57** [9] 815-17 1978

2 K. Nagata, Y. Kawatani, and K. Okazaki, "Anisotropies of Hot-Pressed Transparent (Pb, Ba, La) Nb_2O_6 Ceramics," *Jap. J. Appl. Phys.*, **22** [9] 1353-56 (1983)

3 Y. Inoue, T. Kimura, T. Yamaguchi, K. Nagata, and K. Okazaki, "Grain Orientation and Electrical Properties of Hot-Pressed Bismuth Titanate Ceramics," *Yogyo-Kyokai-Shi*, **92** [7] 416-19 (1984)

4 T. Takenaka and K. Sakata, "Electrical Properties of Grain-Oriented Ferroelectric Ceramics in Some Lanthanum Modified Layer-Structure Oxides," *Ferroelectrics*, **38** 769-72 (1981)

5 H. Igarashi, M. Fujii, K. Nagata, and K. Okazaki, "Mechanical Properties of Grain Oriented Piezo-Ceramics with Bismuth-Layer and Tungsten-Bronze Structures," *Ferroelectrics*, **49** 189-94 (1983)

6 H. J. Bunge and C. Esling, Eds., Quantitative Texture Analysis, DGM Informationsgesellschaft m.b.H., Verlag, Germany (1981)

7 B. D. Cullity, Elements of X-ray Diffraction, 2nd Ed., Addison-Wesley Publ. Co., Inc., Reading, MA (1978)

8 K. Nagata and K. Okazaki, "One-Directional Grain-Oriented Lead Metaniobate Ceramics," *Jap. J. Appl. Phys.*, **24** [7] 812-14 (1985)

9 H. Watanabe, T. Kimura, and T. Yamaguchi, "Particle Orientation during Tape Casting in the Fabrication of Grain-Oriented Bismuth Titanate," *J. Am. Ceram. Soc.*, **72** [2] 289-93 (1989)

10 M. Wu and G. L. Messing, "Fabrication of Oriented SiC-Whisker-Reinforced Mullite Matrix Composites by Tape Casting," *J. Am. Ceram. Soc.*, **77** [10] 2586-92 (1994)

11 K. Sumiya, S. Watani, F. Hayama, K. Nakamae, and T. Matsumoto, "The Orientation of Magnetic Particles for High Density Recording," *J. Magnetism and Magnetic Mater.*, **2** (1983)

12 R. Gopalan, A. K. Singh, T. Rajasekharan, G. Rangarajan, and U. V. Varadaraju, "Pole Figure Studies in Melt Grown Y-Ba-Cu-O Samples," *J. Mater. Sci. Lett.*, **14** 1043-45 (1995)

13 K. Hirao, T. Nagaoka, M. E. Brito, and S. Kanzaki, "Microstructure Control of Silicon Nitride by Seeding with Rodlike β-Si_3N_4 Particles," *J. Am. Ceram. Soc.*, **77** [7] 1857-62 (1994)

14 M. J. Sacks, G. W. Scheiffele, and G. A. Staab, "Fabrication of Textured Silicon Carbide via Seeded Anisotropic Grain Growth," *J. Am. Ceram. Soc.*, **79** [6] 1611-16 (1996)

15 M. M. Seabaugh, I. H. Kerscht, and G. L. Messing, "Texture Development by Templated Grain Growth in Liquid-Phase-Sintered α-Alumina," *J. Am. Ceram. Soc.*, **80** [5] 1181-88 (1997)

16 P. A. Fuierer, "Grain Oriented Perovskite Layer Structure Ceramics For High Temperature Piezoelectric Applications," Ph.D. Thesis, Pennsylvania State University (1991)

17 C. G. Kang and S. S. Kang, "Effect of Extrusion on Fiber Orientation and Breakage of Aluminar Short Fiber Composites," *J. Composite Mater.*, **28** [2] 155-66 (1994)

18 Y. V. Pridatchenko and Z. V. Pasechnik, "Flow of Dilute Suspensions of Deformable Ellipsoidal Particles in the Presence of an Applied Electric Field, Unsteady Orientation of Particles," *Fluid Mech. Sov. Res.*, **3-4** (1991)

19 E. Suvaci, M. M. Seabaugh and G. L. Messing, "Reaction-Based Processing of Textured Alumina by Templated Grain Growth," *J. Eur. Ceram. Soc.*, (1999) in press

20 S. I. Bae and S. Baik, "Determination of Critical Concentrations of Silica and/or Calcia for Abnormal Grain Growth in Alumina," *J. Am. Ceram. Soc.*, **76** [4] 1065-67 (1993)

21 J. D. Powers and A. M. Glaeser, "Grain Boundary Migration in Ceramics," *Interface Sci.*, **6** 23-39 (1998)

22 N. C. Gay, "The Motion of Rigid Particles Embedded in a Viscous Fluid During Pure Shear Deformation of the Fluid," *Tectonophysics*, **5** [2] 81-88 (1968)

23 E. Anczurowski and S. G. Mason, "The Kinetics of Flowing Dispersions III. Equilibrium Orientations of Rods and Discs (Experimental)," *J. Coll. Inter. Sci.*, **23** 533-46 (1967)

24 NIH Image, v. 1.56, by W. Rasband, National Institute of Health, USA.

25 F. K. Lotgering, "Topotactical Reactions with Ferrimagnetic Oxides Having Hexagonal Crystal Structures-I," *J. Inorg. Nucl. Chem.*, **9** 113 (1959)

26 M. Fukuhara, C-Y Huang, A. S. Bhalla, and R. E. Newnham, "Grain Orientation and Electrical Properties of $Sr_2Nb_2O_7$ Ceramics," *J. Mat. Sci.*, **26** 61-66 (1991)

27 M. Hillert, "On the Theory of Normal and Abnormal Grain Growth," *Acta Metall.*, **13** 227-38 (1965)

28 P. Hartman and W. G. Perdok, "On the Relations between Structure and Morphology of Crystals. I," *Acta Cryst.*, **8** 49-51 (1955)

29 M. L. Becraft and A. B. Metzner, "The Rheology, Fiber Orientation, and Processing Behavior of Fiber-filled Fluids," *J. Rheol.*, **36** [1] 143-74 (1992)

30 R. Shanker, J. W. Gillespie, and S. I. Guceri, "On the Effect of Nonhomogeneous Flow Fields on the Orientation Distribution and Rheology of Fiber Suspensions," *Poly. Engg. Sci.*, **31** [3] 161-71 (1991)

31 S. Akbar and M. C. Altan, "On the Solution of Fiber Orientation in Two-Dimensional Homogeneous Flows," *Poly. Engg. Sci.*, **32** [12] 810-22 (1992)

32 M. C. Altan, S. Subbiah, S. I. Guceri, and R. B. Pipes, "Numerical Prediction of Three-Diemnsional Fiber Orientation in Hele-Shaw Flows," *Poly. Engg. Sci.*, **30** [14] 848-59 (1990)

33 T. A. Ring, Fundamentals of Ceramic Powder Processing and Synthesis, Academic Press, New York (1996)

34 J. Perrin, Brownian Motion and Molecular Reality, Taylor and Francis, London (1910)

35 M. L. Albers-Werk and T. A. Rings, "Dip Coating of Anisotropic Platelets," unpublished manuscript

36 D. F. K. Hennings, R. Janssen, and P. J. L. Reynen, "Control of Liquid-Phase-Enhanced Discontinuous Grain Growth in Barium Titanate," *J. Am. Ceram. Soc.*, **70** [1] 23-27 (1987)

Chapter 5

TEXTURE AND PROPERTY ANISOTROPY IN $Sr_2Nb_2O_7$

5.1 INTRODUCTION

For single crystals, anisotropy in physical properties depends on the symmetry elements that describe the periodic structure and the chemistry of the material.[1,2] Along similar lines, texture in polycrystalline ceramics can be described with the same symmetry elements that are used to describe crystal symmetry. The symmetry of polycrystal assemblies such as ceramics are described by Curie groups.[3,4] Therefore, anisotropy in physical properties in ceramics can be predicted on the basis of their macroscopic symmetry or Curie group.

In this chapter, the expected orientation of grains developed by templated grain growth (TGG) is used to predict the symmetry of the ceramic. The symmetry relations are further used to predict the directional dependence of the dielectric constant in a textured sample. The measured properties are also compared to the expected values. This helps determine the single-crystal nature of TGG samples in the $Sr_2Nb_2O_7$ system.

5.2 BACKGROUND

5.2.1 Pole Figure Measurement

Pole figure measurement is a convenient diffraction technique which can be used to collect orientation distribution information from a large number of crystallites at the same time.[5-7] The sample is examined in 3-D space to determine the relative intensity for a particular hkl pole as a function of sample orientation. The pole density can be determined by X-ray, electron, or neutron diffraction using a monochromatic beam. The source and the detector are moved in a coordinated manner to satisfy the Bragg condition for diffraction by the hkl peak of interest at all times. The sample is rotated about two orthogonal axes to obtain pole density information from an entire hemisphere or a region of interest. The positions of high pole densities can be used to determine the presence and nature of texture. The information can be plotted as a stereographic projection with the intensities plotted as contours or represented by the height above the projection plane. The pole figure for a single crystal resembles the stereographic projection for the set of hkl planes of interest.

5.2.2 Symmetry of Single-Crystal $Sr_2Nb_2O_7$

As discussed in Chapter 1, the paraelectric to ferroelectric phase transition at 1342°C results in a change in symmetry from a paraelectric mmm to a ferroelectric orthorhombic mm2 point group.[8] The formation of an incommensurate phase at 215°C results in a slight shift in atomic positions, but the overall symmetry can be approximated to mm2. Due to the development of a polarization component along the *b*-axis at -156°C, the symmetry changes from mm2 to m. The symmetry elements and their relation to the crystal structure and polarization are shown in Figure 5.1.

The calculated stereographic projections for some of the planes of interest in the $Sr_2Nb_2O_7$ system are shown in Figure 5.2 (a-c). The projections were calculated using Ca.R.Ine,[9] a software for crystal structure manipulations. The stereographic projections are extremely useful in determining the pole of interest in texture evaluation.

5.2.3 Symmetry of Fiber Texture

TGG samples possessing fiber texture belong to the Curie group ∞/mm. The grain orientation in the microstructures and the relation to the symmetry elements is shown in Figure 5.3. This particular Curie group is similar to the 6/mmm point group for hexagonal crystals as far as tensor property matrix relations determined by applying Neumann's law are concerned.[10]

Based on X-ray diffraction data presented in Chapter 4, the sample shows fiber texture with the fiber axis parallel to the crystallographic *b*-direction. Therefore pole figure measurements of the 080 pole were measured for the plane parallel to the plane of tape casting.

The centrosymmetric nature of the Curie group makes second rank tensor matrices symmetric, with only non-zero diagonal elements. Another constraint is that two of the three principal values (diagonal elements) are equal. A second rank tensor matrix describes properties such as thermal expansion, dielectric constant, and electrical

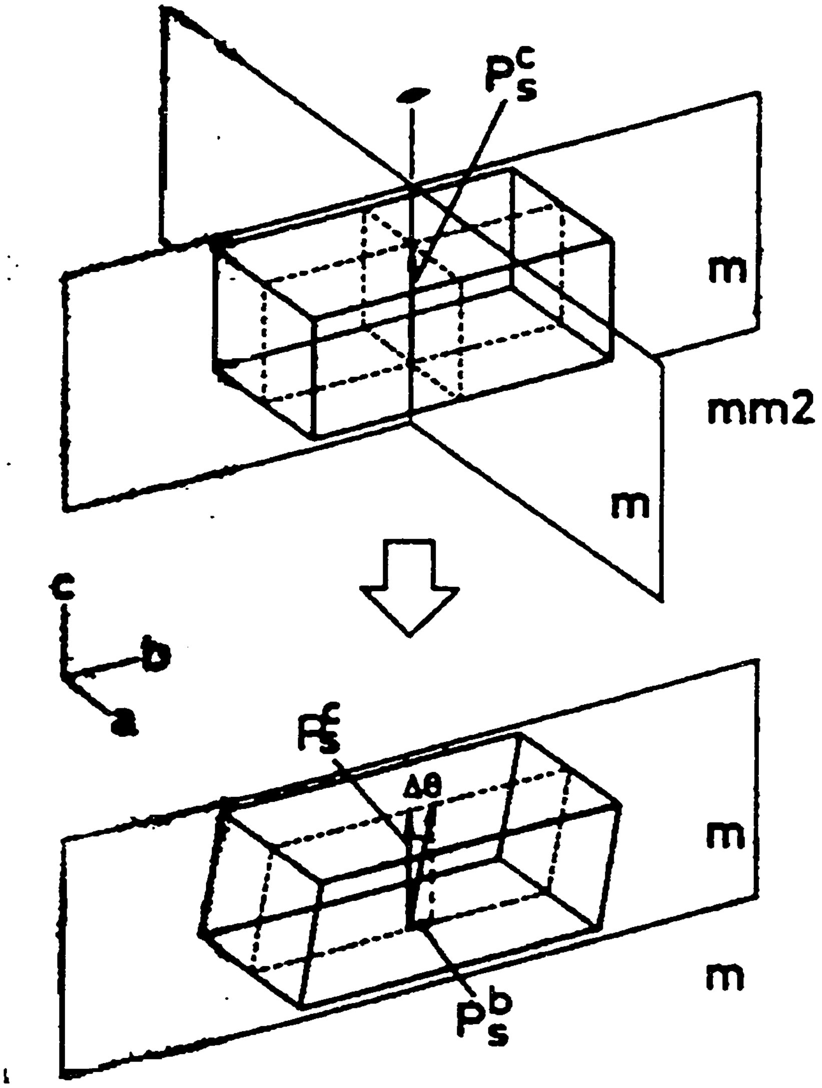

Figure 5.1 Symmetry elements and their relation to crystallographic directions for single crystal $Sr_2Nb_2O_7$. The ferroelectric mm2 point group is reduced to point group m at -156°C due to the small b-component of polarization [9].

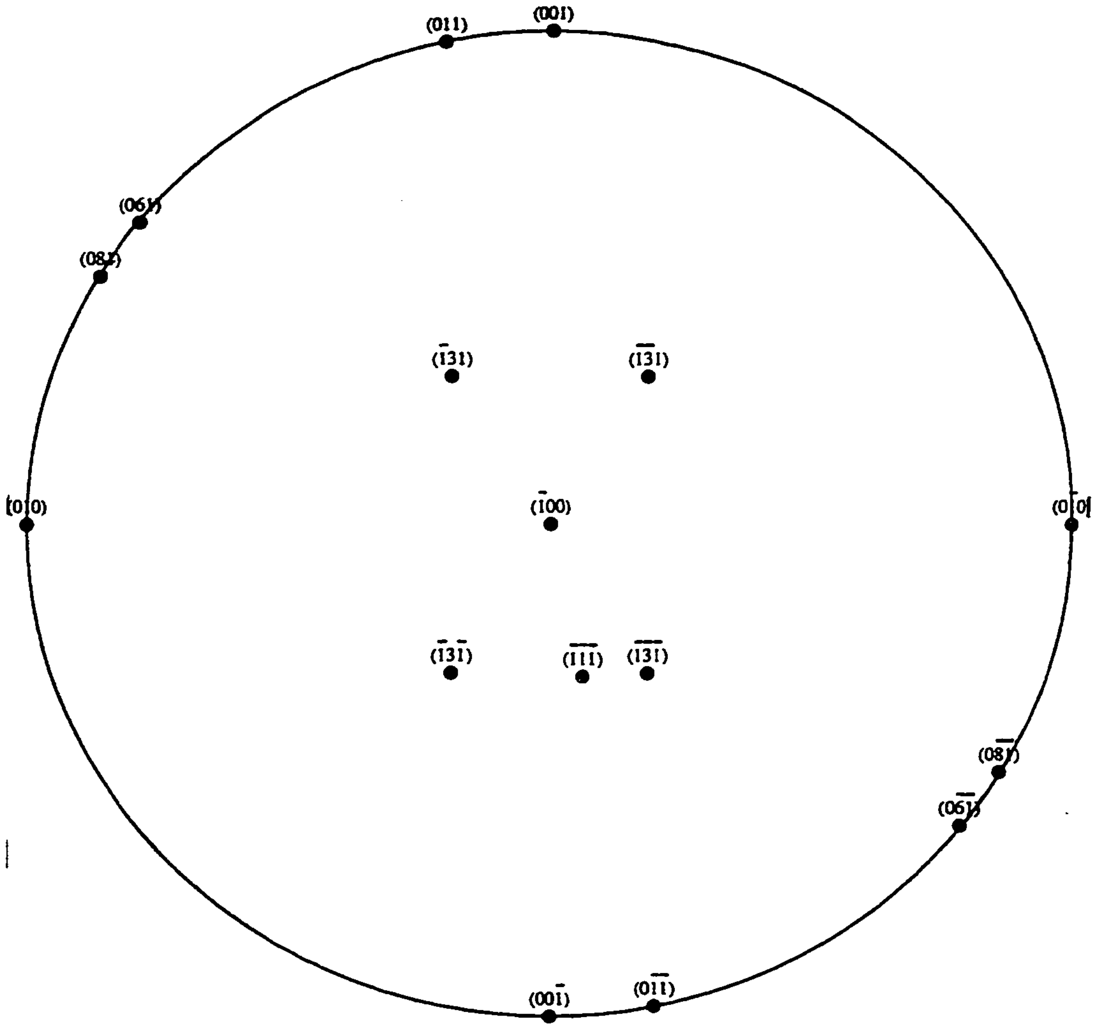

Figure 5.2 (a) Stereographic projection of orthorhombic $Sr_2Nb_2O_7$ (point group mm2) on the a-plane

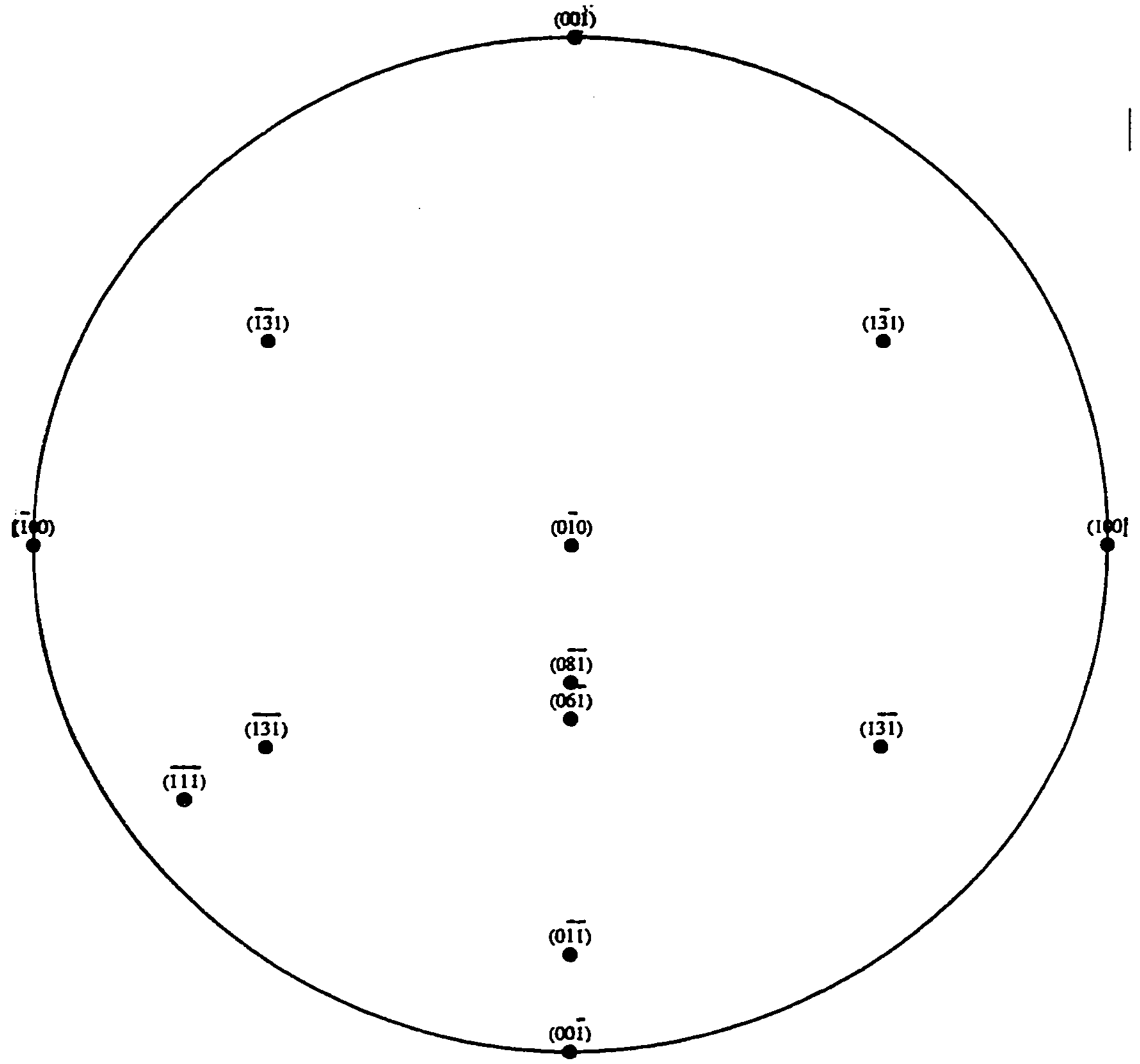

Figure 5.2 (b) Stereographic projection of orthorhombic $Sr_2Nb_2O_7$ (point group mm2) on the b-plane

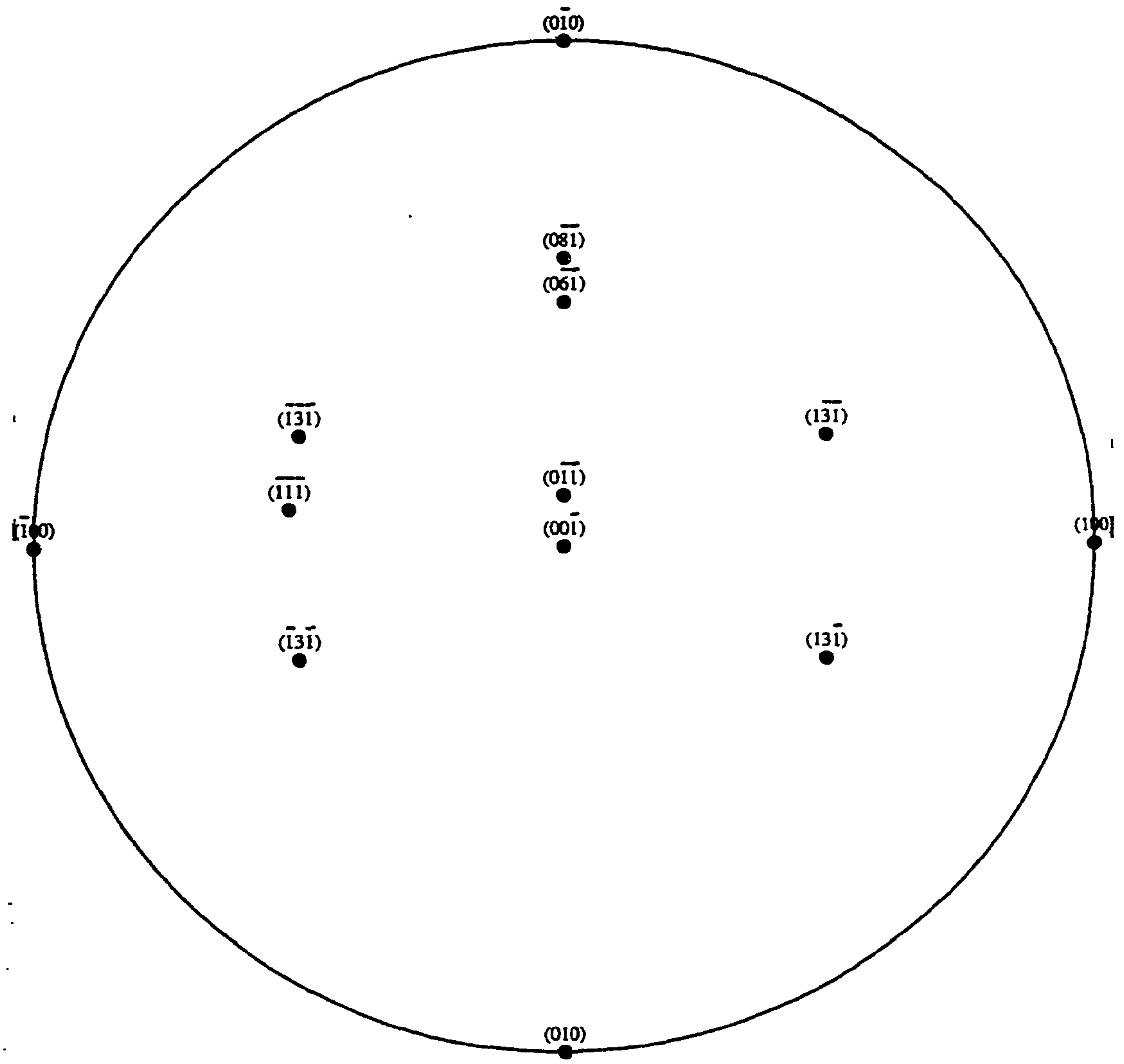

Figure 5.2 (c) Stereographic projection of orthorhombic $Sr_2Nb_2O_7$ (point group mm2) on the c-plane

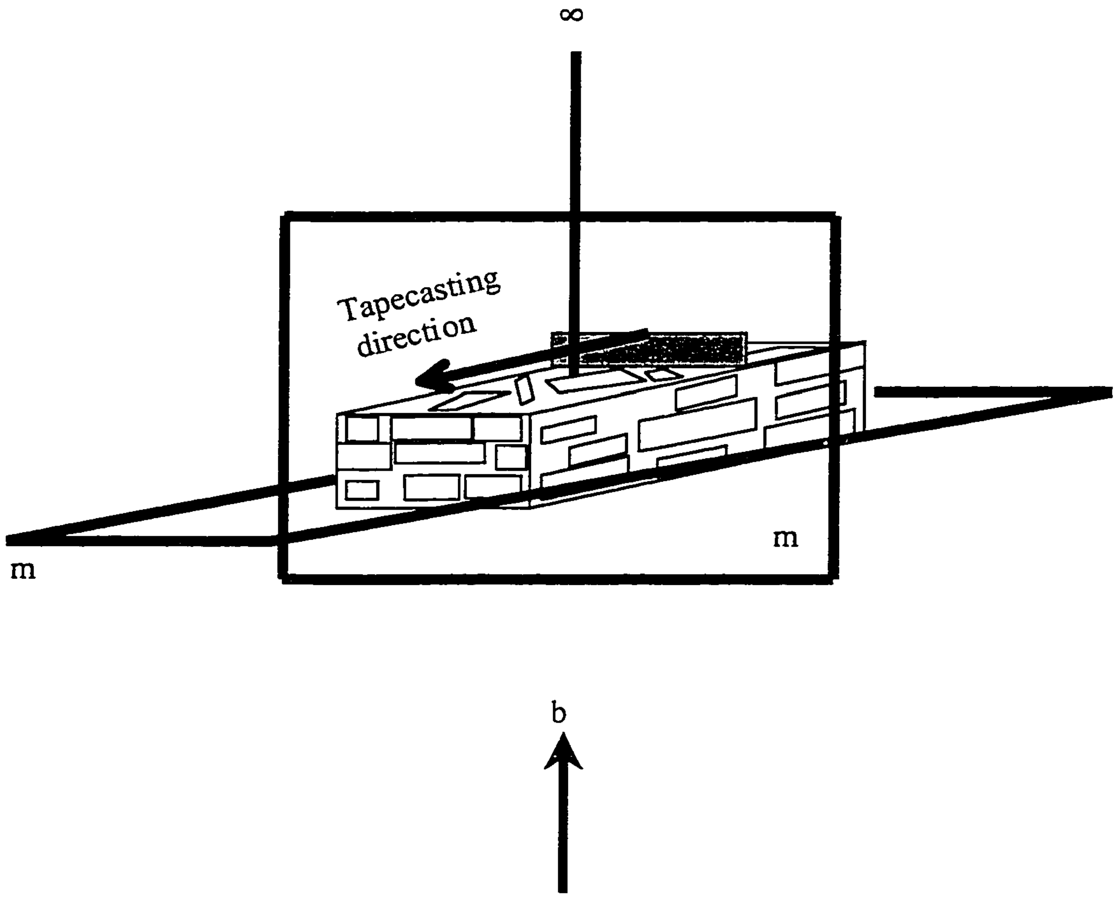

Figure 5.3 Symmetry elements and their relation to crystallographic directions and microstructure for $Sr_2Nb_2O_7$ TGG samples with fiber texture. The mirror symmetry element perpendicular to the b-axis is lost in the process of poling along the c-direction.

resistivity.

The degree of fiber texture in TGG samples can thus be evaluated by measuring second rank tensor properties along the fiber axis, and any direction perpendicular to it in the sample. The property matrix can be expected to be:

$$\begin{pmatrix} A_P & 0 & 0 \\ 0 & A_P & 0 \\ 0 & 0 & A_f \end{pmatrix},$$

where A_f and A_P are the property values along the fiber direction and the direction perpendicular to the fiber axis, respectively. As the fiber direction is along the *b*-axis, the value of A_f should approximate the single-crystal value along crystallographic *b*-axis, and A_P should be approximately the average of the single crystal values along a and *c*-axes to account for the in-plane randomness. Therefore the matrix describing dielectric constants (K) for TGG samples should be,

$$\mathrm{K} = \begin{pmatrix} 60.5 & 0 & 0 \\ 0 & 60.5 & 0 \\ 0 & 0 & 43 \end{pmatrix}, \text{(at 1 MHz measured at room temperature)}$$

5.2.4 Symmetry of Sheet Texture

TGG samples with sheet texture have the symmetry of the point group mm2, which is the same as that of a single crystal of $Sr_2Nb_2O_7$. Thus, the anisotropy in physical properties should show the same trends as single crystals. Figure 5.4 shows the relation between the microstructural texture and the symmetry elements for $Sr_2Nb_2O_7$ samples with sheet texture.

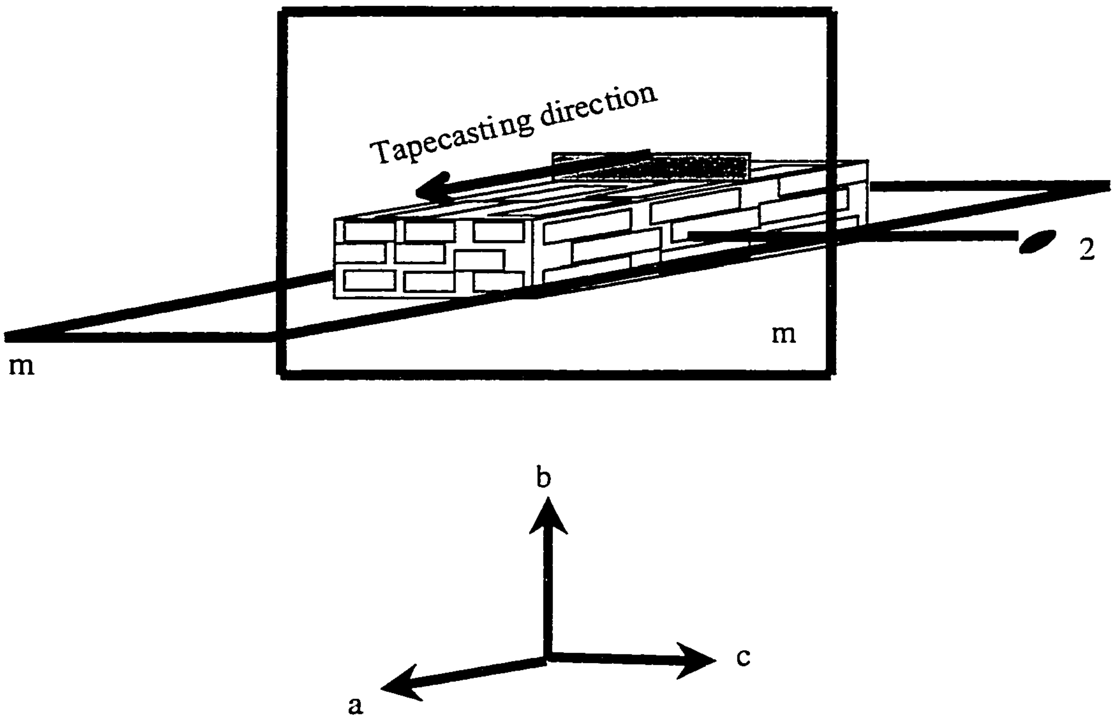

Figure 5.4 Symmetry elements and their relation to crystallographic directions and microstructure for $Sr_2Nb_2O_7$ TGG samples with sheet texture.

Measuring the 080 pole density distribution from the top surface (parallel to the tape casting plane) would only confirm the presence of fiber texture about the *b*-axis. Measurement of the 200 and 002 poles from this surface can be expected to produce no regions of high density. Similarly, the 080, 200, and 002 pole densities can be measured from three mutually orthogonal planes, and the nature of texture can be determined.

On examining the stereographic projections for a single crystal in Figure 5.2, it can be seen that the 131 family of poles lies at four distinct orientations for a projection along the principal crystallographic axes. The 131 plane is also at an angle to the a, b, and *c*-planes. A sample with no texture (randomly oriented) would produce the same pole density at all orientations. A sample with fiber texture would produce a ring-shaped region of higher 131 pole density at the Φ value predicted in the stereographic projection. The ring shape is a result of in-plane randomness. However, a sample with sheet texture would exhibit four distinct peaks at the predicted orientations for the 131 poles in the stereographic projection. Hence, a single 131 pole figure measurement can yield information about the presence or lack of sheet texture in $Sr_2Nb_2O_7$.

If the samples possess perfect (single crystal) sheet texture, the second rank tensor for dielectric constant can be expected to be,

$$K = \begin{pmatrix} 75 & 0 & 0 \\ 0 & 43 & 0 \\ 0 & 0 & 46 \end{pmatrix}, \text{(at 1 MHz measured at room temperature)}^{11}$$

Measurements of higher rank tensor properties such as piezoelectricity were also attempted to ascertain the single-crystal nature and potential use as high temperature piezoelectrics.

5.3 EXPERIMENTAL PROCEDURE

5.3.1 Pole Figure Measurement

A Phillips four circle diffractometer was used to collect pole figure data. First, the Bragg condition for the pole of interest was determined by a θ-2θ scan. The sources and detector are then fixed in relative 2θ throughout the measurement. The notation for the angles used in the discussion are shown in Figure 5.5. Samples of circular geometry (~1 cm^2 area) were used to avoid producing anisotropy artifacts in the Ω scan due to different areas of illumination as a result of beam defocusing at high values of Φ. The pole figure data from a random sample was used to normalize the data collected from textured samples for defocussing and beam spreading as a function of Φ. The randomly oriented sample was made by cold isostatic pressing a pellet of $(Sr,La)_2Nb_2O_7$ at 275 MPa. Φ was measured from the vertical about an axis along the incident beam from 0° to 90° in increments of 3°. For each value of Φ, the sample face was rotated one complete rotation in plane in increments of 10° (Ω scan). The collection time was set at 5 s at each orientation. The 080, 002, 200, and 131 poles were measured for different sample surfaces. The data was plotted as contour plots and by three-dimensional representations to help identify the pole positions visually.

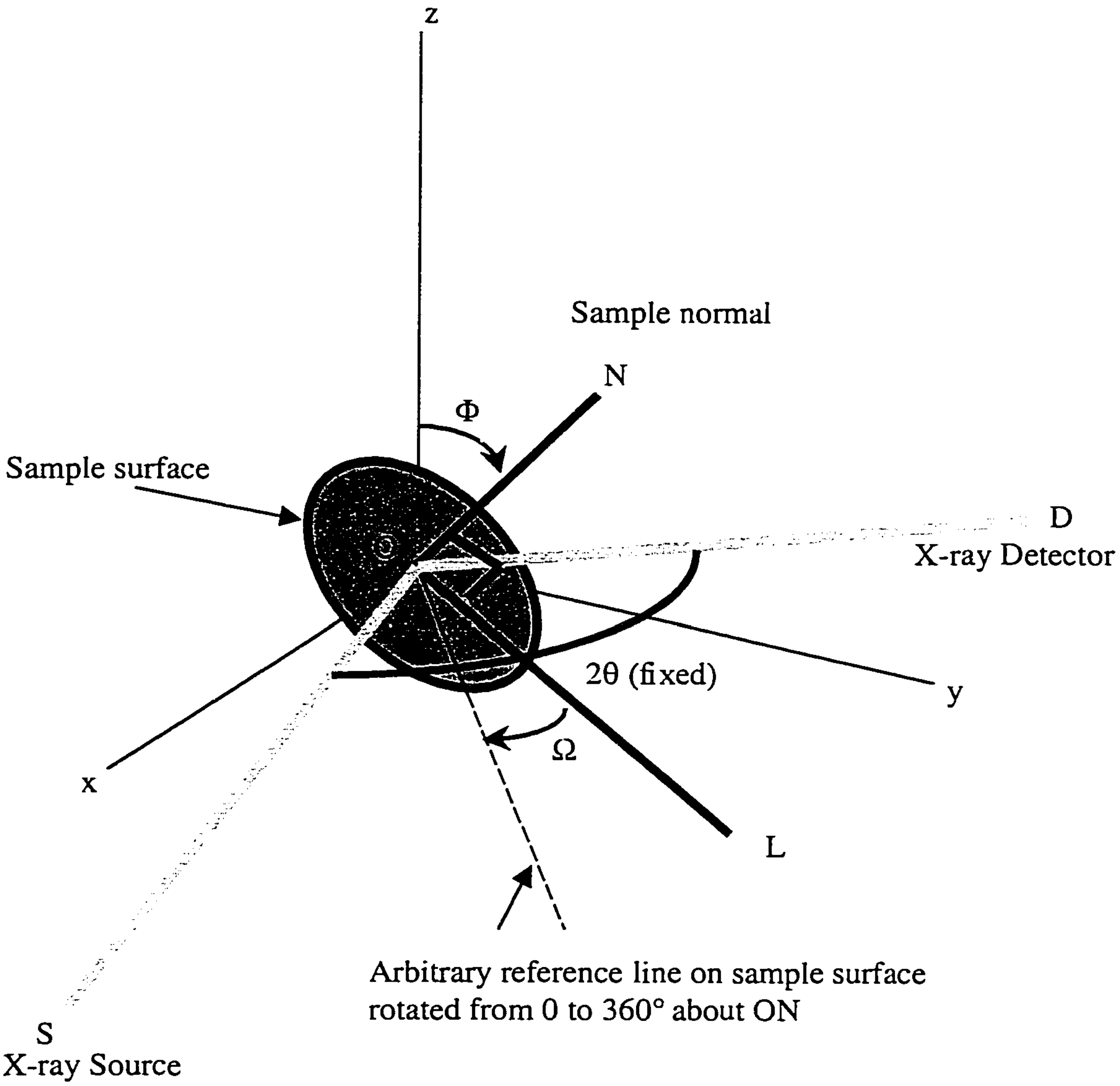

Figure 5.5 Schematic of sample surface orientation and its relation to the X-ray source and detectors at an angle 2θ. The lines SO and OD lie in the xy plane and the line OL lies in the yz plane

5.3.2 Dielectric Constant Measurement

Dielectric properties of TGG samples with both fiber texture and sheet texture were measured. Parallel sample surfaces were polished using a final grit of 1 μm diamond paste. Samples were cleaned with water and acetone, and dried. Sputtered platinum was used as the electrode surface on both faces. Capacitance and loss measurements from ~-175°C to 440°C were made using an HP4192A LCR bridge and an Euro 808 oven. A 1V signal was used to measure the dielectric properties of samples with 35 - 150 pF capacitance at 10 KHz, 100 KHz, and 1 MHz. The dielectric constant was calculated based on the geometry of the specimen.

5.4 RESULTS AND DISCUSSION

5.4.1 Pole Figures

As discussed earlier, the 080, 131, and 002 poles were analyzed by 4-circle X-ray diffraction of different sample cuts to obtain information about the texture in TGG samples. Figure 5.6 shows the 080 pole intensity obtained from a random sample. The 3D representation does not show any strong peaks, indicating that the 080 pole density is relatively uniform in all directions indicating a random orientation of grains. This is also seen from the relatively flat contour map in Figure 5.6b. The random orientation distribution of grains leads to a random distribution of 080 planes with respect to the sample normal. This means that the probability of finding 080 planes is roughly the same at all angles. There is a slight decrease in intensity at high Φ. This is due to spreading or defocusing of the incident beam on the surface of the sample at high angles from the

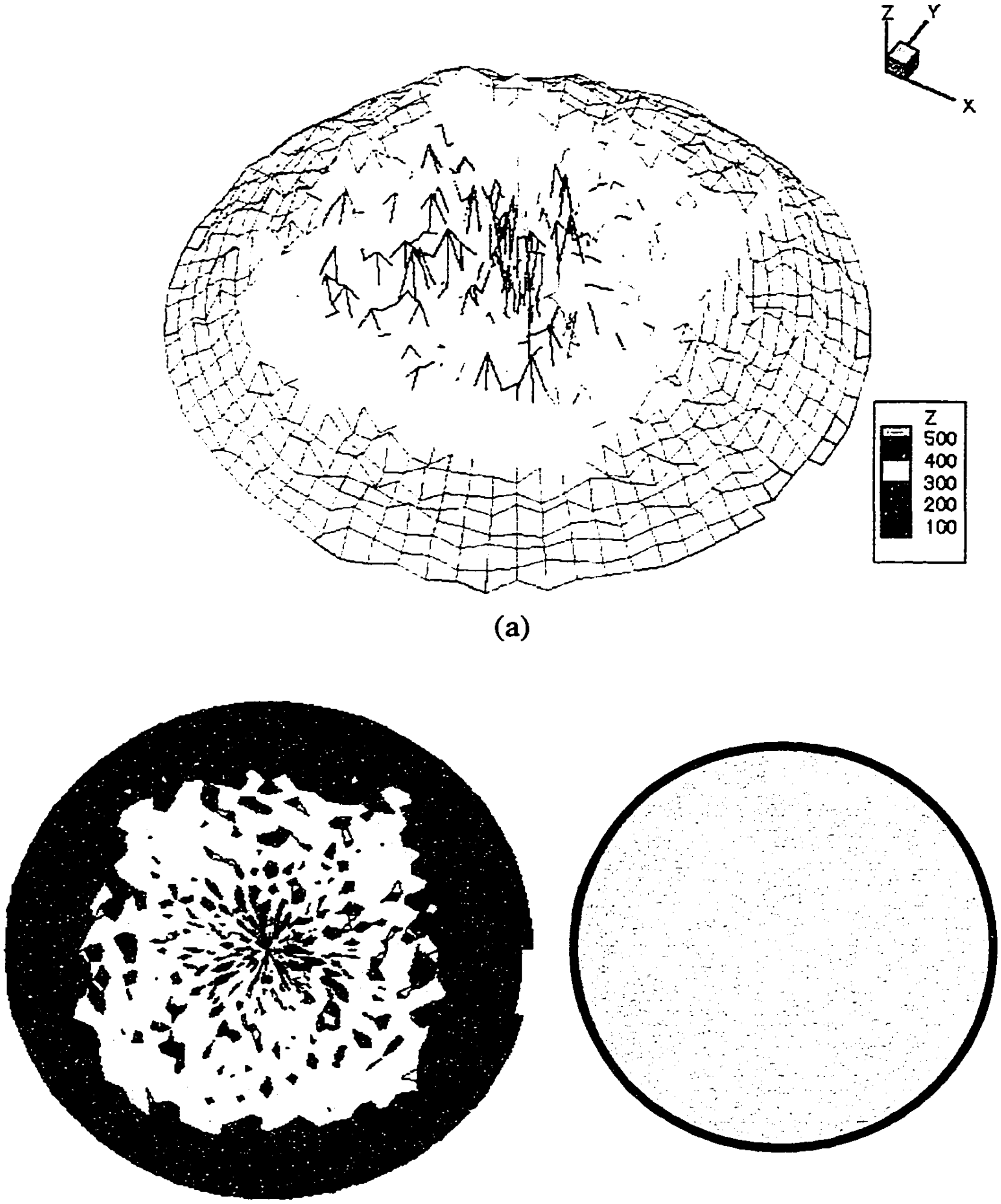

(a)

(b)

(c)

Figure 5.6 Pole figure from a surface containing randomly oriented $(Sr,La)_2Nb_2O_7$ showing 080 pole intensity (a) 3D representation, (b) Contour plot of intensities as a function of Ω, (c) Position of 080 spots in stereographic projection on random plane.

vertical. Thus the data for TGG samples are also expected to show a slight reduction in intensity as we move out radially from the center of the projection (Φ=0).

Figure 5.7 shows the pole figure for the 080 pole obtained from the top surface of a $(Sr,La)_2Nb_2O_7$ sample, sintered at 1500°C for 4 h, possessing sheet texture. The direction of doctor blade motion during tape casting is along the *a*-direction. The strong peak at Φ=0° points to strong fiber texture about the *b*-axis. The position of the peak coincides with the calculated position of the 080 spot in the stereographic projection along the crystallographic *b*-direction. The full width of the 080 peak at half of maximum intensity (FWHM) is ~25° along the *a*-direction, and ~15° along the *c*-direction, implying that the templates are better oriented with respect to the tape casting direction as compared to a direction perpendicular to the casting direction in the plane of casting. The random sample has a FWHM which is ~180°.

The 131 pole density obtained from the top surface is plotted in Figure 5.8. Four spots are expected as shown in Figure 5.8c. The pole figure data was collected from Φ=0° to 72°. The contour plot of the X-ray intensity from 131 planes shows two spots which are fairly distinct and two other which seem to be slightly suppressed. This could be due to a slight inclination of the top surface with respect to the true crystallographic *b*-plane.

Pole figure data collected for the 080 pole alone does not prove the presence of sheet texture. The 080 pole can only provide evidence for fiber texture along the *b*-axis. However, the 131 plane, being at an angle to all three crystallographic axes, provides information about grain orientation with respect to all three planes. The presence of sheet texture can be deduced from the agreement of 131 pole peak intensity positions in the

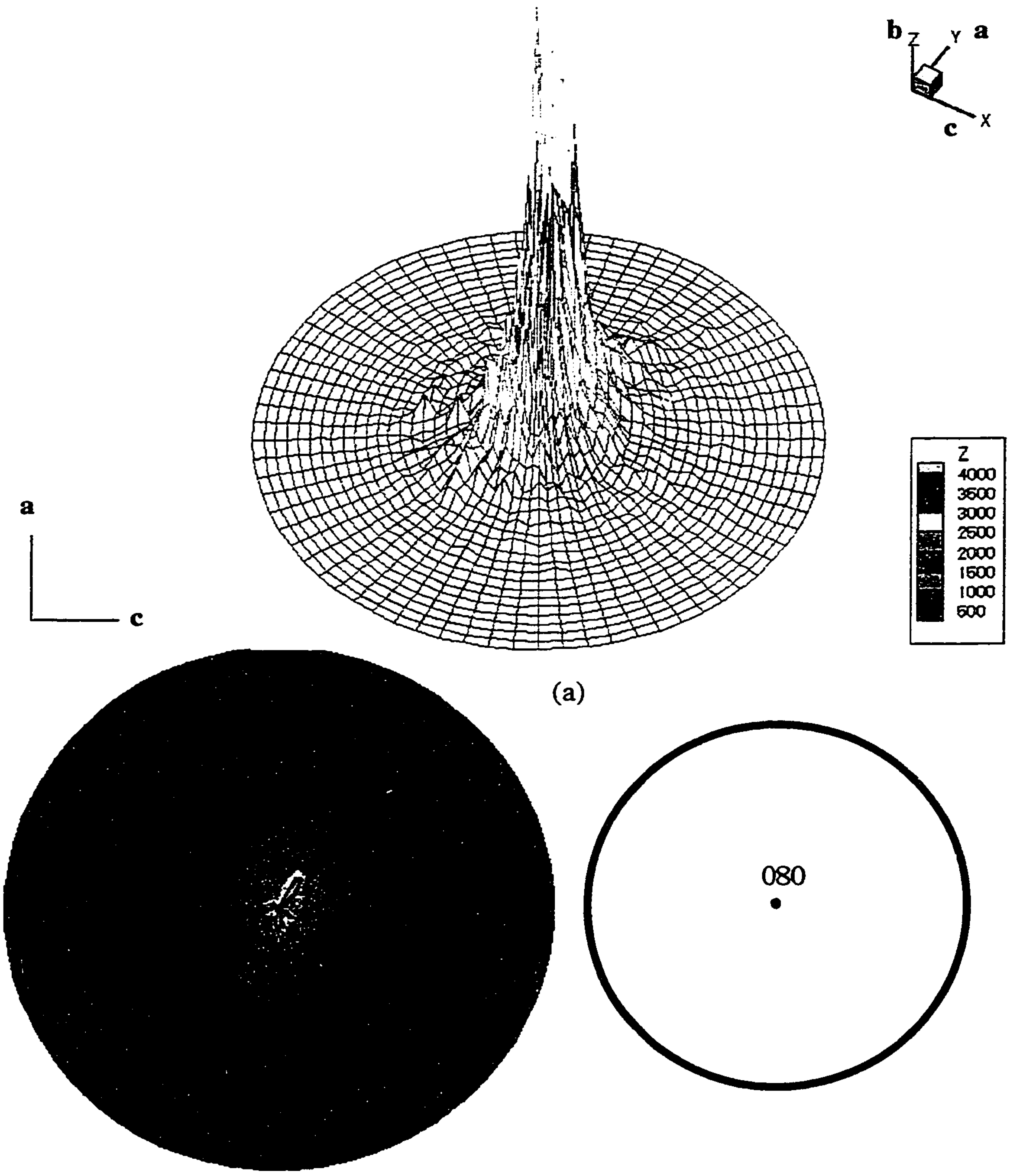

(a)

(b) (c)

Figure 5.7 Pole figure from the top surface of $(Sr,La)_2Nb_2O_7$ TGG sample (sheet texture) showing 080 pole intensity (a) 3D representation, (b) Contour plot of intensities as a function of Ω, (c) Calculated positions of 080 spots in stereographic projection on a-c plane.

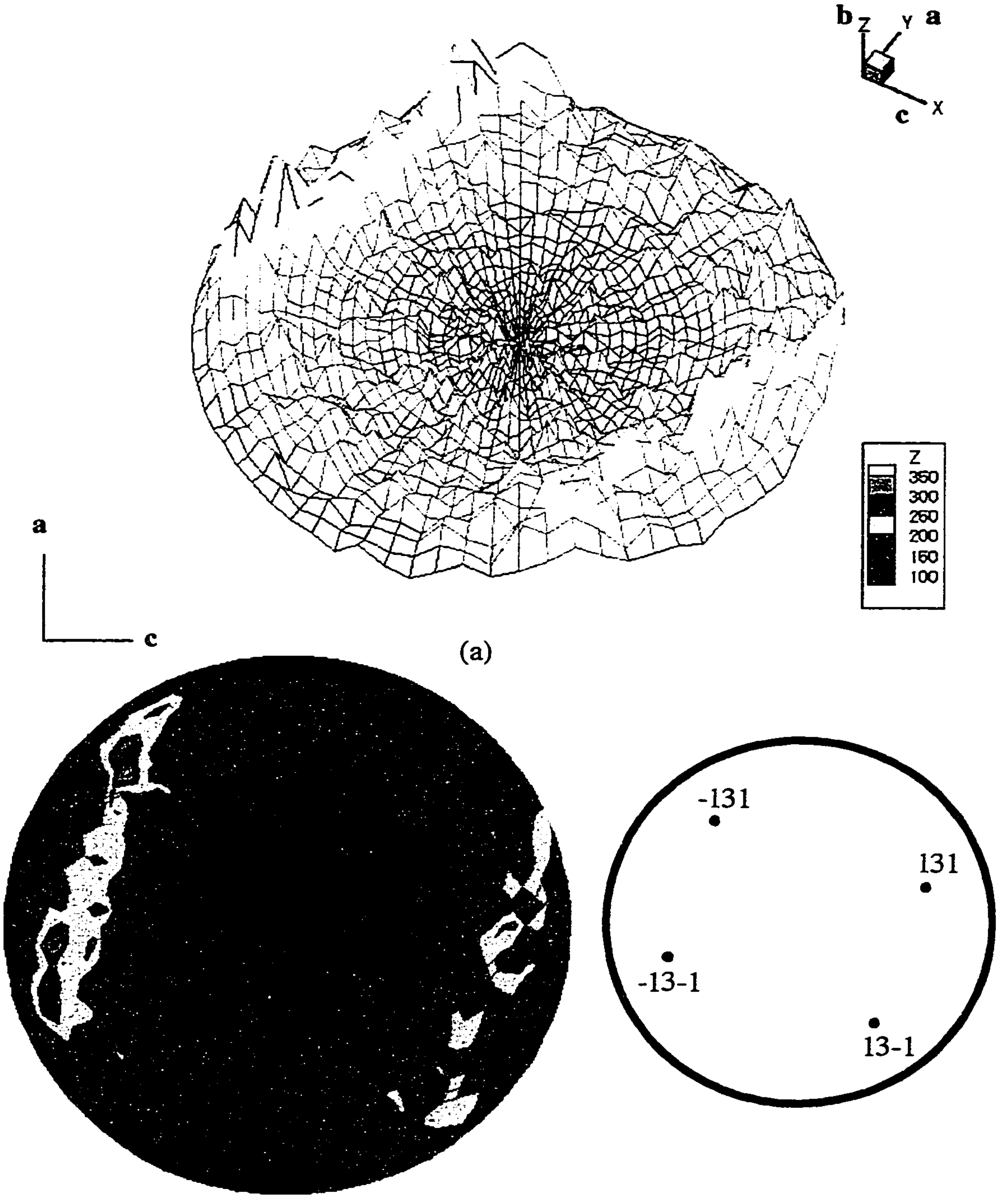

(a)

(b) (c)

Figure 5.8 Pole figure from the top surface of $(Sr,La)_2Nb_2O_7$ TGG sample (sheet texture) showing 131 pole intensity (a) 3D representation, (b) Contour plot of intensities as a function of Ω, (c) Calculated positions of 131 spots in stereographic projection on a-c plane.

contour map shown in Figure 5.8b and in the calculated stereographic projection in Figure 5.8c. The broad and relatively weak peaks indicate that the sheet texture is not very strong in this sample. This could be due to a misorientation of the polished surface with respect to the crystallographic *b*-plane.

A cut parallel to the plane along the casting direction and perpendicular to the cast plane (c-plane) was also used to obtain pole figure information from a sheet textured TGG sample sintered at 1500°C for 4 h. Figures 5.9, 5.10, and 5.11 show the 080, 002, and 131 pole figures, respectively. The data were obtained from a *c*-plane oriented with the casting direction along $\Omega=90°$. Figures 5.9b and c show the experimentally determined 080 peak positions and the calculated 080 positions on the *c*-plane. The scan was conducted from $\Phi=0$ to 81°. A single spike was observed at $\Phi=0°$. The most probable reason for such a sharp spike is the presence of one or a very few large grains which are oriented with their *b*-plane parallel to the sample *c*-plane. This grain could be the result of the growth of a misoriented template or exaggerated grain growth in the matrix. There are two other regions where 080 peaks seems to be developing. These are at $\Omega=0°$, 180° at Φ-> 90°. This is in agreement with the expected positions of 080 poles in the stereographic projection (Figure 5.9c).

Figure 5.10 shows the pole figure for the 002 pole. The sharp peak (FWHM ~ 20°) at $\Phi=0$ is expected due to the orientation of the sample parallel to the *c*-plane. There is a split in this peak, which is probably due to misoriented templates or due to diffraction of the 081 planes. The 002 and 081 peaks are very close to each other in the θ-2θ scan. The FWHM of this peak is ~ 20°.

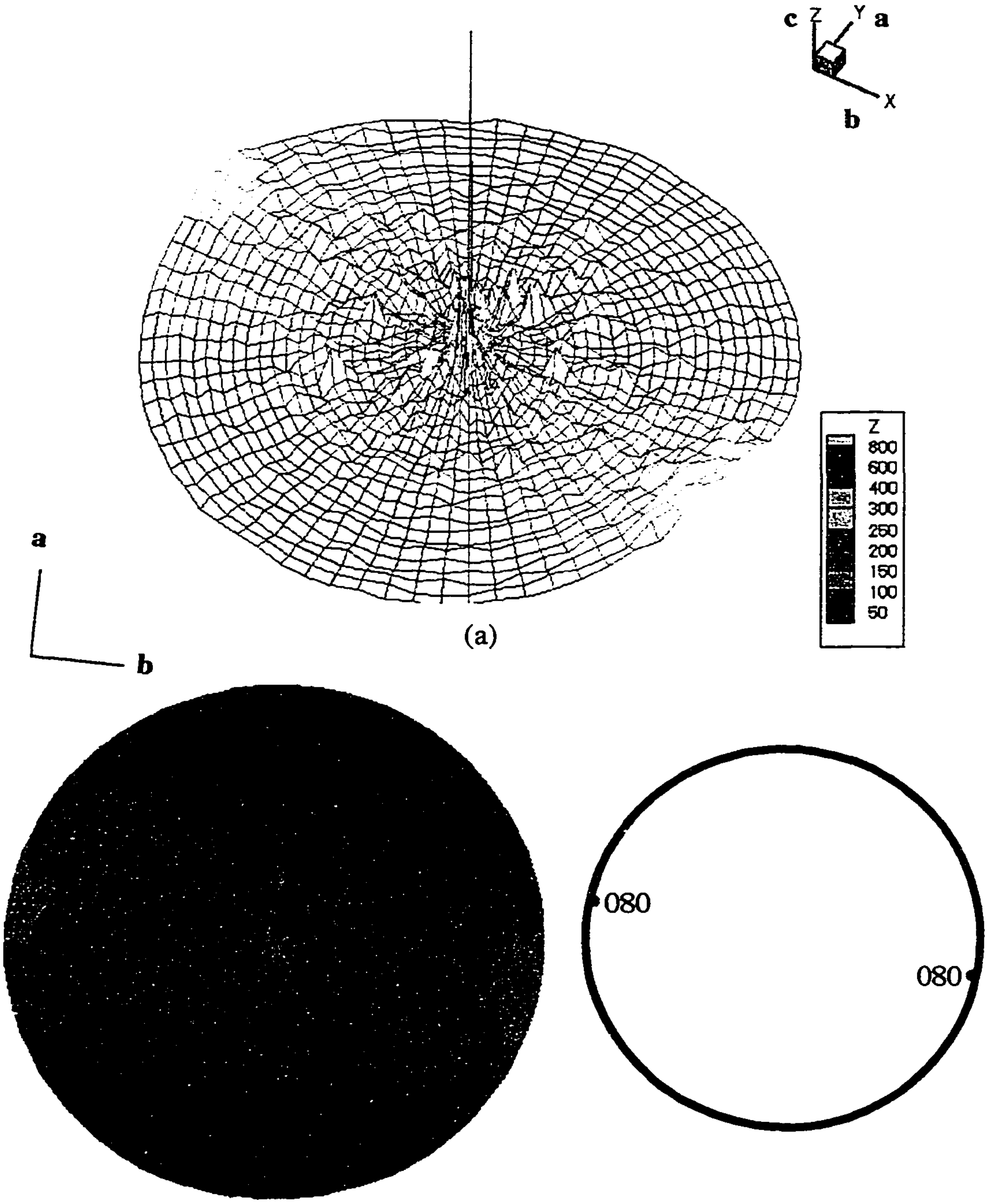

(a)

(b) (c)

Figure 5.9 Pole figure from the "c" edge of $(Sr,La)_2Nb_2O_7$ TGG sample (sheet texture) showing 080 pole intensity (a) 3D representation, (b) Contour plot of intensities as a function of Ω, (c) Calculated positions of 080 spots in stereographic projection on a-b plane.

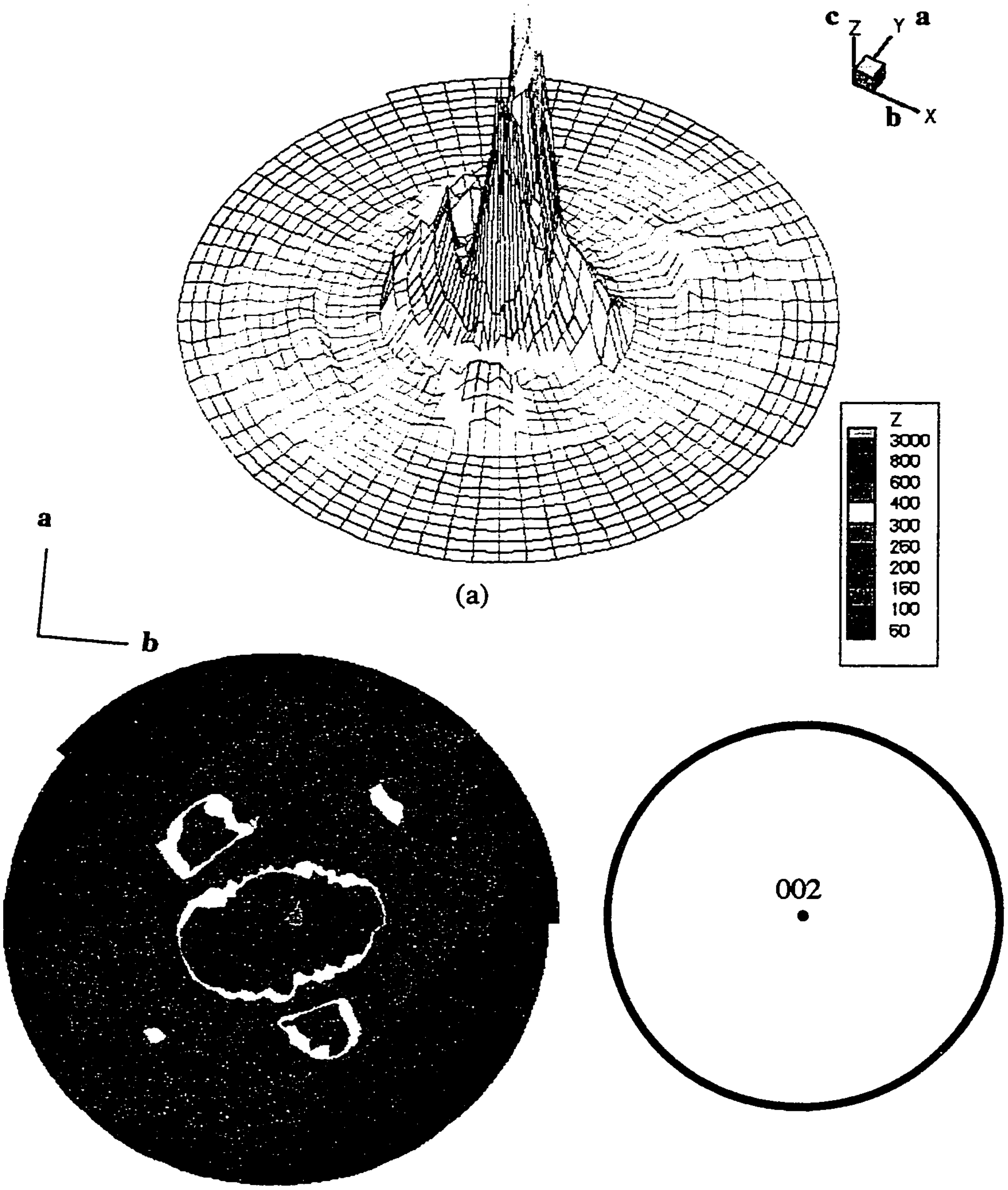

(a)

(b) (c)

Figure 5.10 Pole figure from the "c" edge of $(Sr,La)_2Nb_2O_7$ TGG sample (sheet texture) showing 002 pole intensity (a) 3D representation, (b) Contour plot of intensities as a function of Ω, (c) Calculated positions of 002 spots in stereographic projection on a-b plane.

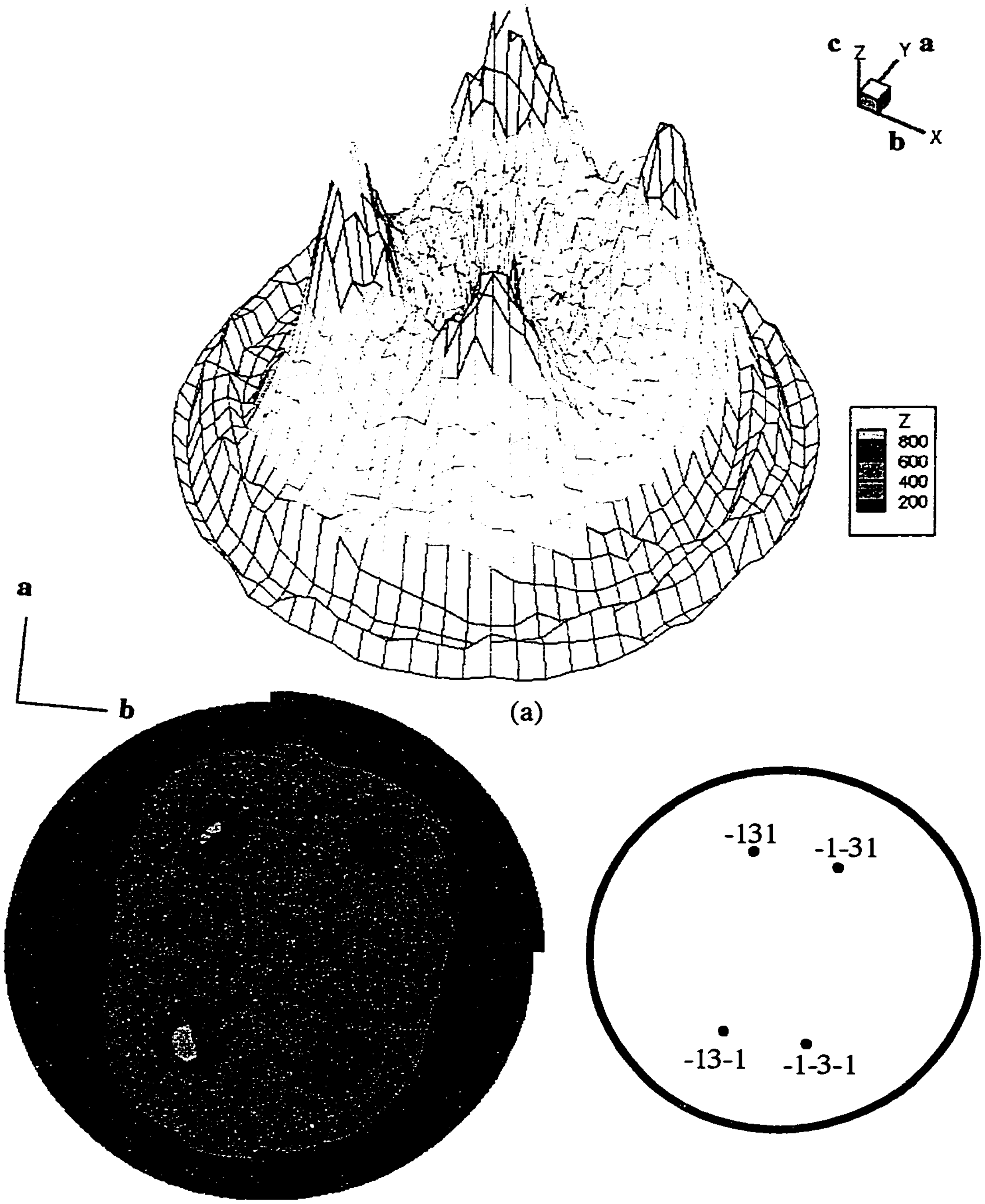

(a)

(b) (c)

Figure 5.11 Pole figure from the "c" edge of $(Sr,La)_2Nb_2O_7$ TGG sample (sheet texture) showing 131 pole intensity (a) 3D representation, (b) Contour plot of intensities as a function of Ω, (c) Calculated positions of 131 spots in stereographic projection on a-b plane.

Figure 5.11 shows 131 pole figure data. The four distinct peaks at positions coinciding with the calculated 131 poles in the stereographic projection conclusively prove the presence of sheet texture in $(Sr,La)_2Nb_2O_7$ TGG samples. The FWHM is ~30° in the arc joining the maxima of the 4 peaks as compared to 90° for a random sample.

Based on the above discussion a single 131 pole figure from any cut in the sample which is not parallel to the 131 plane can be used to determine the degree of sheet texture in $(Sr,La)_2Nb_2O_7$ samples.

5.4.2 Dielectric Properties

Dielectric constant and loss were measured as a function of temperature, sample orientation, and signal frequency. The variations in dielectric constant with temperature (25°C to 400°C) and sample orientation measured at 1 MHz are shown in Figure 5.12 for fiber textured samples. The anisotropy in the measured dielectric constants for samples with fiber texture, sintered at 1550°C for 2 h, verifies the fiber texture along *b*-axis.

As seen from Figure 5.12, $Sr_2Nb_2O_7$ samples possessing fiber texture show two distinct dielectric constants as a function of temperature. At room temperature, the dielectric constant along the *b*-direction is ~48, and in a perpendicular direction it is ~ 52 (at 1 MHz). The value along the *b*-axis is slightly higher than the value of 43 for a single crystal, and the value in the *a-c* plane is lower than the average of the *a* and *c*-direction values (60.5).

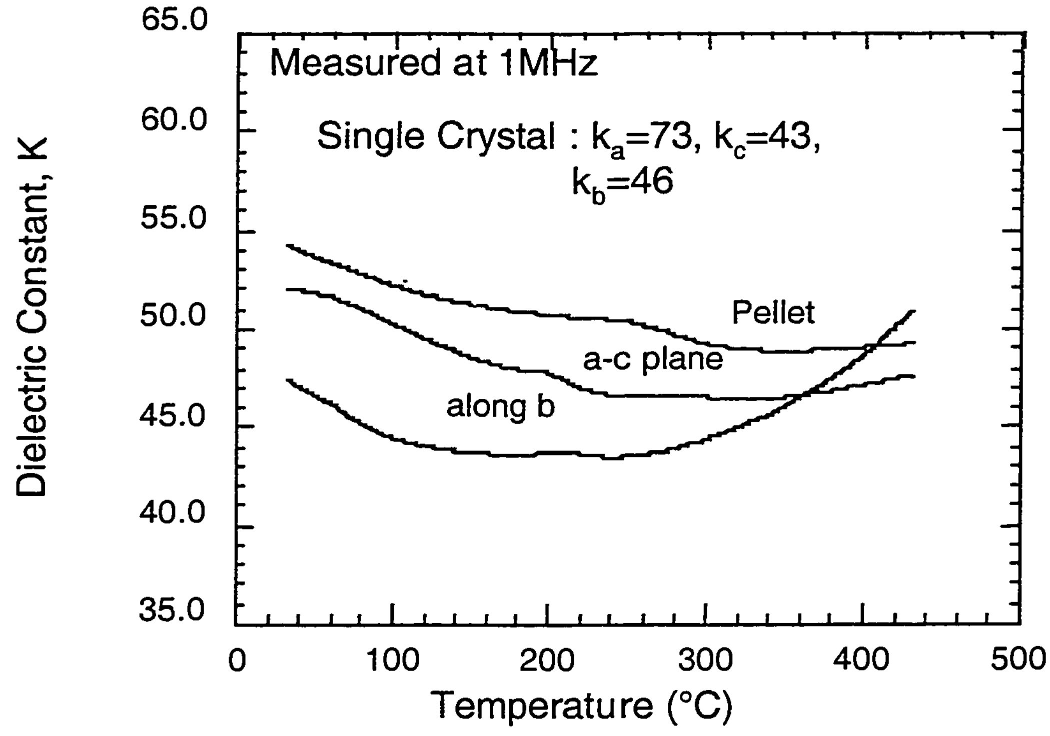

Figure 5.12 Dielectric constant as a function of temperature for a fiber textured sample sintered at 1550°C for 2 h in different directions

For sheet textured TGG samples sintered at 1500°C for 4 h, the sample orientation (direction of measurement) is the crystallographic axis for which maximum intensity was observed in the X-ray diffraction pattern.

The sample can be imagined to be made of many discrete volume fractions having single crystal dielectric constant, $K'_{11}(\theta,\phi)$ for (θ,ϕ), the crystallographic orientation of the particular volume element with respect to the sample axes. Each discrete element is assumed to be in parallel with the rest. Therefore the expected dielectric constant can be calculated as the sum of K'_{11} over all the volume elements.

Although ϕ can be determined from the stereological analysis of angles made by the major axes of each grain intersected by the top surface, θ cannot be determined directly. However, θ can be determined trignometrically if both θ_1 and θ_2, the angles made by the major axes with reference axes in the a and *c*-planes, are known simultaneously. The schematic for the above described angles and their relation to the sample geometry and crystallographic axes is shown in Figure 5.13a.

As the specific orientation of each and every grain is unavailable, the angle distribution curves shown in Figure 5.13b were used to approximate the probabilities, $P(\theta_1)$, $P(\theta_2)$, and $P(\phi)$, that a certain volume fraction of the material has an orientation θ_1, θ_2, and ϕ. The grains with this orientation make an angle θ_1 with the *a*-axis in the section parallel to the *c*-plane, an angle θ_2 with the *c*-axis in the section parallel to the *a*-plane, and an angle ϕ with the *a*-direction in the section parallel to the *b*-plane. The volume fraction that has an orientation $(\theta_1, \theta_2, \phi)$ is the product of the three individual probability functions that describe volume distribution as a function of angle (Figure 5.13b). The

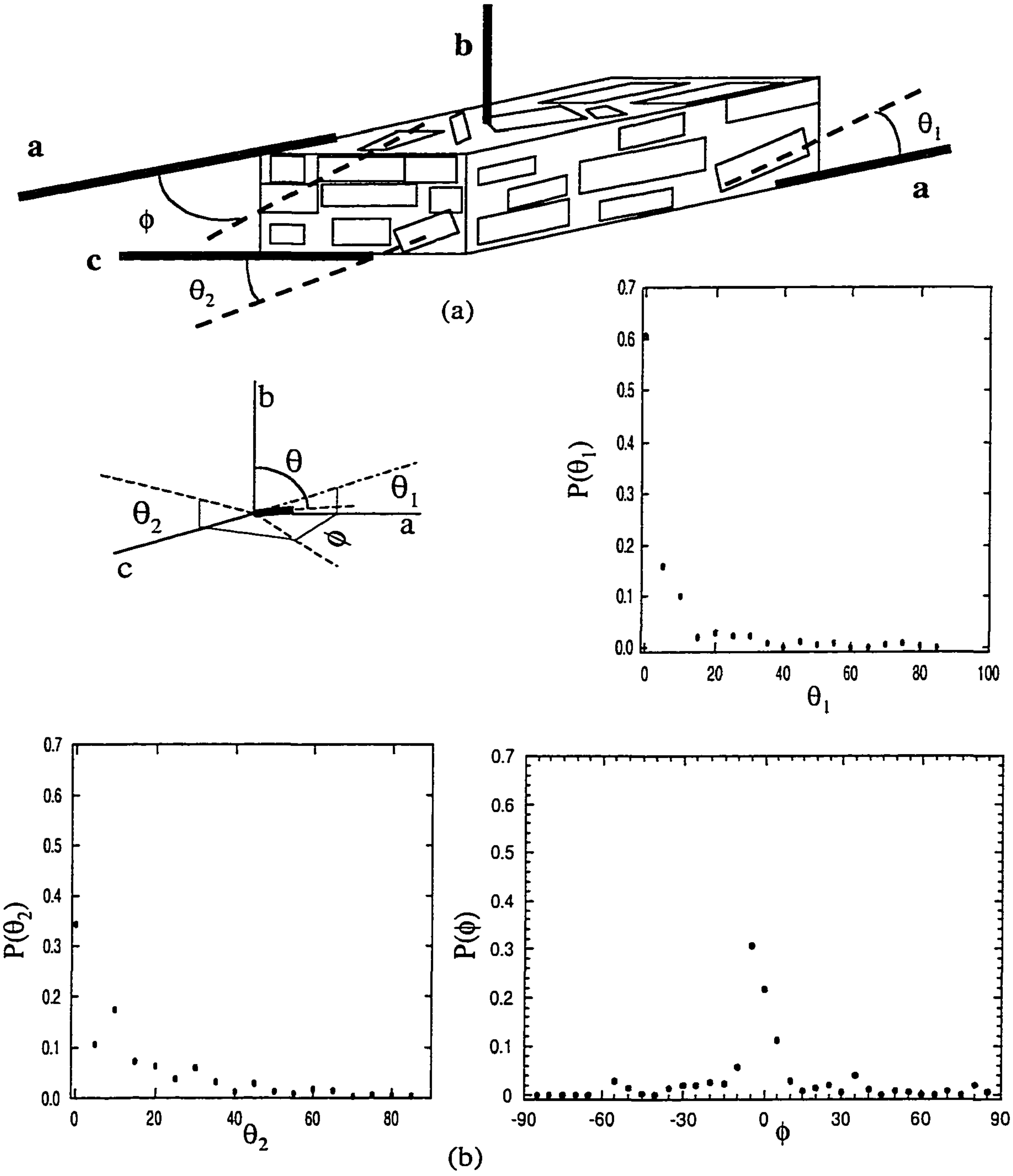

Figure 5.13 (a) Relation of stereologically measured angles and crystallographic directions, (b) Orientation distribution functions, $P(\theta_1)$, $P(\theta_2)$, and $P(\phi)$

true value of θ, as shown in Figure 5.13, can be expressed in terms of the measured θ_1 and θ_2 by the following equation.

$$\cos^2\theta = \left(1 + \frac{\tan^2\theta_1 + \tan^2\theta_2}{\tan^2\theta_1 \cdot \tan^2\theta_2}\right)^{-1} \qquad (1)$$

The value of $\cos^2\theta$ and $\sin^2\theta$ can be substituted in equation 2 to obtain the contribution of the volume fraction of the material oriented at $(\theta_1, \theta_2, \phi)$.

$$P(\theta_1,\theta_2,\phi)\cdot K'_{11} = [K_3\cos^2\theta + \sin^2\theta\cdot(K_1\cos^2\phi + K_2\sin^2\phi)]\cdot P(\theta_1)\cdot P(\theta_2)\cdot P(\phi) \qquad \ldots(2)$$

Based on such an approach, the dielectric constants at room temperature, measured at 1 MHz, were calculated to be 71, 46, and 47 along a, b, and *c*-directions of the sample (roughly parallel to the a, b, and c crystallographic directions), respectively.

Figure 5.14 shows the dielectric behavior of sheet textured TGG samples of $(Sr,La)_2Nb_2O_7$ sintered at 1500°C for 4 h. The dielectric properties were measured in the temperature range of -150°C to 450°C at 1 MHz. The dielectric constant follows the measured trends for single crystals shown in Chapter 1 (Figure 1.6). The room temperature values in the *a*,*b*, and *c* directions for TGG samples were 68, 45, and 49, respectively. These values are in reasonable agreement with the predicted values within experimental errors. While some of the anisotropy may be a consequence of different distributions of the grain boundary phase in the three perpendicular directions, the good

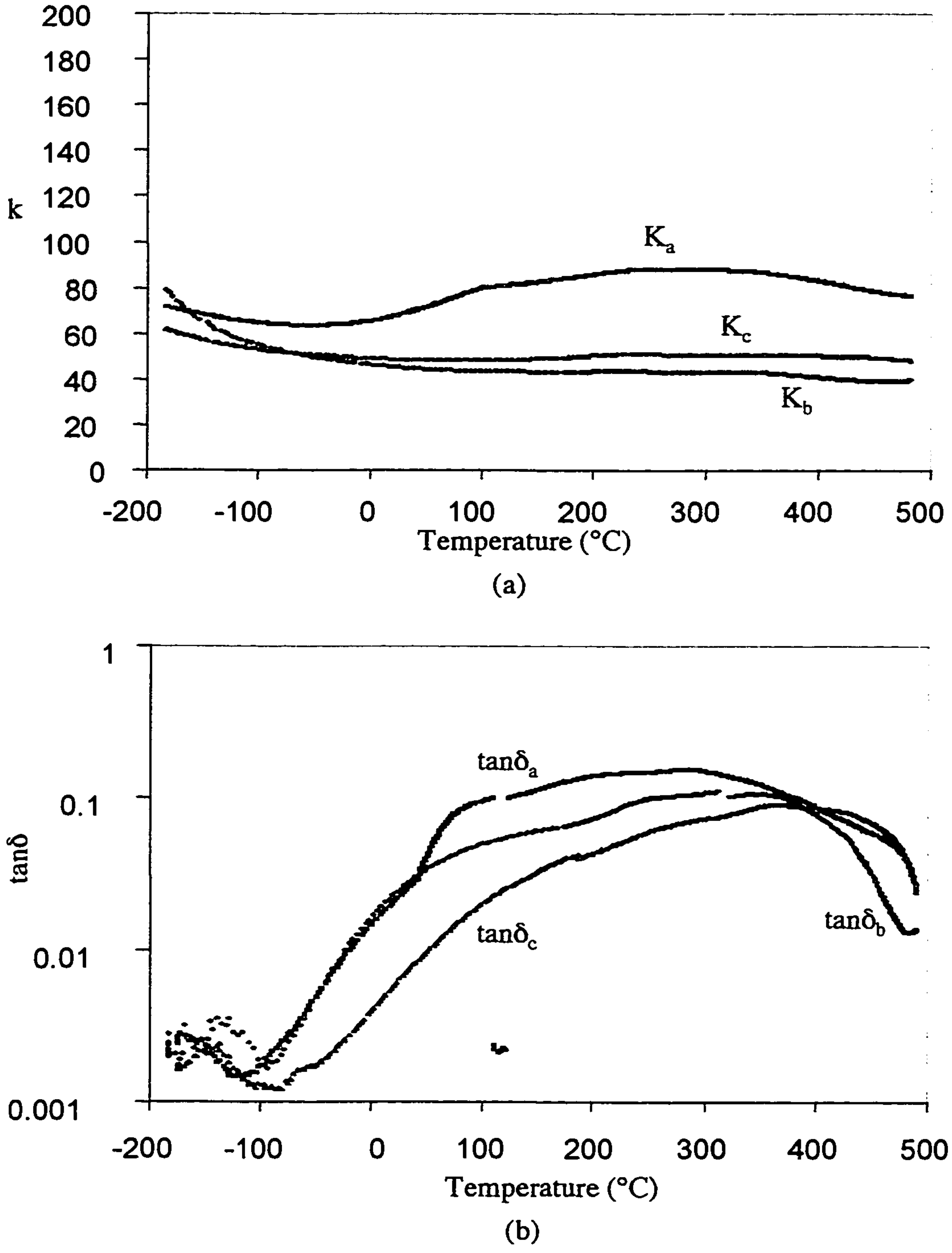

Figure 5.14 Dielectric properties of sheet textured $(Sr,La)_2Nb_2O_7$ samples sintered at 1500°C for 4 h at 1 MHz as a function of temperature and direction (a) dielectric constant and (b) dielectric loss

agreement between the X-ray determined texture distributions and the permittivities suggests that crystallographic texture contributes, at least in part, to the observed anisotropy. Once again, this underscores the effect of texture on physical properties. The observed anisotropy also implies that the templates were able to grow to produce a volume fraction of textured material close to unity at 1500°C for 4 h. Another feature of the dielectric behavior is the trend in the *b*-direction dielectric constant. The *b*-direction constant remains lower than the *c*-direction constant at temperatures >25°C, and starts rising as the temperature approaches -156°C. The dielectric constant in the *b*-direction for single crystals shows similar behavior with a peak at -156°C due to the phase transition that results in a small component of P_s along the *b*-direction. This rise is not as marked in the *a* and *c*-direction dielectric constants for the sheet-textured TGG samples. This could be due to the nearly constant, low permittivity contribution of grain boundary phases. Further low temperature measurements of dielectric constant would help elucidate the contribution, if any, of the grain boundaries to the measured dielectric constant. Identification of the grain boundary phase and its distribution, and incorporating this data will help increase the accuracy of the model for predicting dielectric constants of textured $(Sr_{0.99}La_{0.01})_2Nb_2O_7$ ceramics. The dielectric loss is plotted as a function of temperature in Figure 5.14b.

5.4.3 Poling

The poling of sheet textured samples along the direction of spontaneous polarization (c-direction) was attempted. Pt-electroded samples were used for this study.

The samples underwent electrical breakdown at 70-100 kV/cm at ~150°C and did not exhibit piezoelectric coefficients that could be measured by a d_{33} meter. Alternately, samples electroded with fired Pt paste electrodes were subjected to fields of ~0.4 kV/cm as they were cooled from 1400°C through the Curie temperature (1342°C). This approach was also unsuccessful in poling textured $Sr_2Nb_2O_7$ obtained by TGG.

5.5 CONCLUSIONS

Morphological or microstructural texture in $Sr_2Nb_2O_7$ ceramics results in crystallographic texture. Pole figure measurements give a better idea about the degree of fiber or sheet texture. Measurement of a single 131 pole figure on any one of the a, b, or *c*-planes is sufficient to detect sheet texture. Texture affects other properties such as dielectric constant of the textured ceramic. Another result of this investigation is the development of a method to estimate the dielectric constant of textured ceramics based on stereologically determined orientation distributions.

5.6 REFERENCES

1 J. F. Nye, Physical Properties of Crystals, Their Representation by Tensors and Matrices, Oxford University Press, Inc., New York (1985)

2 R. E. Newnham, Structure-Property Relations, Springer Verlag, New York (1975)

3 L. Fuentes and O. Raymond, "Texture, Piezoelectricity and Ferroelectricity," *Textures and Microstructures*, **23** 221-36 (1995)

4 H. J. Bunge, "Textures in Non-metallic Materials," *Textures and Microstructures*, **14-18** 283-326 (1991)

5 H. J. Bunge and C. Esling, Eds., Quantitative Texture Analysis, DGM Informationsgesellschaft m.b.H., Verlag, Germany (1981)

6 P. R. Morris and R. E. Hook, "Comparison of Incomplete Pole-Figure Methods for Surfaces Perpendicular to Rolling, Transverse and Normal Directions," *Textures and Microstructures*, **19** 75-80 (1992)

7 R. Gopalan, A. K. Singh, T. Rajasekharan, G. Rangarajan, and U. V. Varadaraju, "Pole Figure Studies in Melt Grown Y-Ba-Cu-O Samples," *J. Mater. Sci. Lett.*, **14** 1043-45 (1995)

8 Y. Akishige, M. Kobayashi, K. Ohi and E. Sawaguchi, "Dielectric and Ferroelectric Properties in the Low Temperature Phase of Strontium Niobate," *J. Phys. Soc. Jpn.*, **55** [7] 2270-77 (1986)

9 Ca.R.Ine Crystallography, V 3.0, Divergent SA

10 P.A. Fuierer, "Grain Oriented Perovskite Layer Structure Ceramics for High Temperature Piezoelectric Applications," Ph.D. Thesis, The Pennsylvania State University, University Park, PA (1991)

11 S. Nanamatsu, M. Kimura, and T. Kawamura, "Crystallographic and Dielectric Properties of Ferroelectric $A_2B_2O_7$ (A=Sr, B=Ta, Nb) Crystals and Their Solid Solutions," *J. Phys. Soc. Jpn*, **38** [3] 81 (1975)

Chapter 6

TEMPLATED GRAIN GROWTH OF $PbNb_2O_6$ CERAMICS

6.1 INTRODUCTION

Templated grain growth can be used to produce texture in other ferroelectric ceramics. Based on the work on $Sr_2Nb_2O_7$ and other TGG systems the important elements required for successful TGG are:

- availability of large (5-50 μm), anisotropic template particles,
- availability of fine matrix powder,
- formation of a liquid phase which promotes growth of template grains, and
- a method of orienting template particles in the green body.

$PbNb_2O_6$ with a Curie temperature of 570°C and its reported ability to resist depoling to 550°C makes it another candidate for high temperature applications.[1] It belongs to the tungsten bronze family of compounds. The anisotropic crystal structure is capable of accommodating a number of cations in solid solution.[2-5] The synthesis, TGG, and properties of textured $PbNb_2O_6$ are discussed in this Chapter.

6.2 BACKGROUND

Ferroelectricity in lead metaniobate was discovered by Goodman[6] in 1953. The paraelectric phase is tetragonal and has corner-shared octahedra as shown in Figure 6.1. This structure can be chemically represented by the formula, $[A1(A2)_2C_2][B1(B2)_4]O_{15}$,

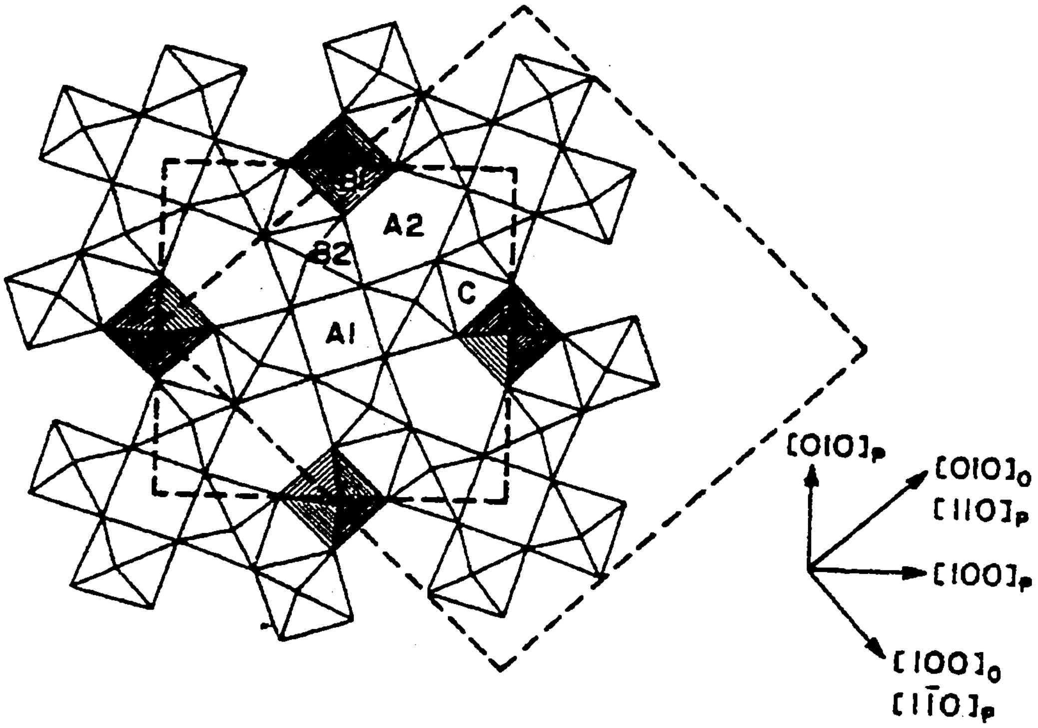

Figure 6.1 Crystal structure of paraelectric phase of $PbNb_2O_6$ [3]

where combinations of larger monovalent ions such as K^+, Na^+, Rb^+, divalent Pb^{2+}, Ba^{2+}, Sr^{2+}, Ca^{2+}, and trivalent La^{3+}, Eu^{3+}, Gd^{3+} occupy the square and pentagonal tunnels, A1, and A2 sites. Triangular tunnels or C-sites in the structure can be occupied only by very small ions such as Li^+. The octahedral B1 and B2 sites can be occupied by Nb^{5+}, Ta^{5+}, Ti^{4+}, and Zr^{4+}. In lead metaniobate, $PbNb_2O_6$, the replacement of Pb by other divalent ions reduces the Curie temperature.[1] The effect of adding or substituting various ions in lead metaniobate is shown in Figure 6.2. Lead metaniobate also forms a morphotropic phase boundary with $BaNb_2O_6$ as shown in Figure 6.3.[2] This system is of interest for the following reasons. Francombe[7] and Neurgaonkar[8] have reported large piezoelectric coefficients near the morphotropic boundary. In the low Ba, orthorhombic compositions, the spontaneous polarization, P_s, is along 4 perpendicular directions which are orthogonal to the c-axis. In the high Ba-tetragonal phase, the direction of P_s switches and is along the c-axis.

The commonly observed morphology of $PbNb_2O_6$ is acicular with the needle-axis along the c-direction.[9,10] Large, needle-shaped single crystal particles of lead metaniobate have been synthesized by molten salt synthesis. These particles can be aligned along their long axis to obtain fiber texture along the c-axis by extrusion, double hot-forging,[9,11] or with the c-axis oriented in one plane by tape casting.[10] In the orthorhombic phase, like in most ferroelectrics, the polarization direction is perpendicular to the direction of possible fiber orientation that can be achieved using the morphological anisotropy. However, the high Ba (>0.4) tetragonal phase is one of the few exceptions in which the polarization direction coincides with the direction of possible orientation of anisotropic particles (needles in the case of $PbNb_2O_6$). Grain-orientation or texture has

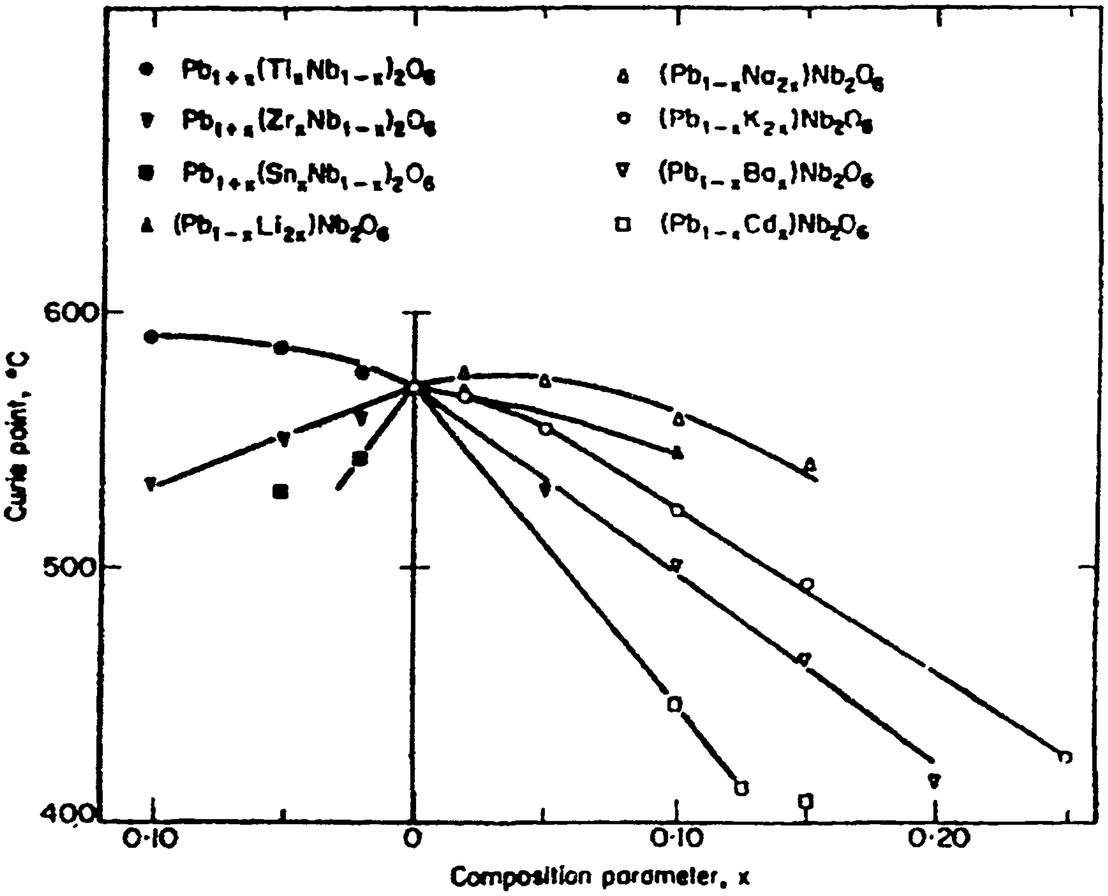

Figure 6.2 Curie temperature as a function of composition for various $PbNb_2O_6$ solid solutions [1]

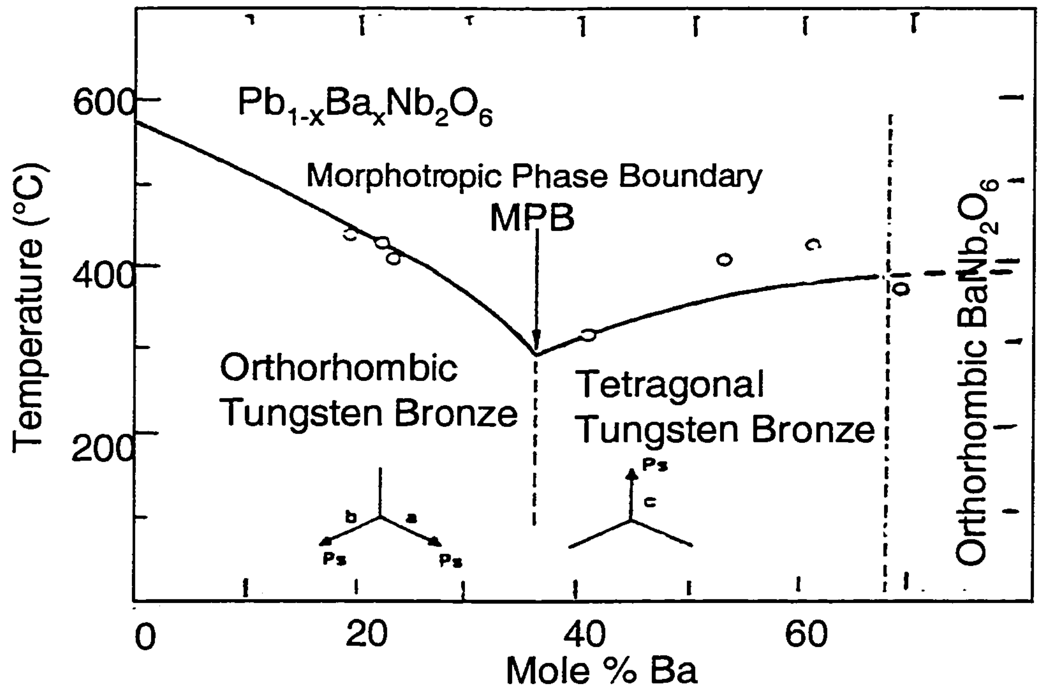

Figure 6.3 $PbNb_2O_6$- $BaNb_2O_6$ binary system showing the morphotropic phase boundary [2]

been demonstrated to increase the piezoelectric coefficients in lead metaniobate compositions.[8,10,12] The highest values for piezoelectric coefficients were obtained in microstructures which had needle shaped particles oriented along the c-axis. These microstructures were obtained by an expensive double hot-forging technique. Gated tape casting is a less expensive alternative that can be used to generate alignment of needles along the long axis, and TGG can be used to produce high volume fractions of textured material. This provides the motivation for the study of TGG in lead metaniobate.

There are several processing challenges that have to be overcome to fabricate dense lead metaniobate. Lead metaniobate transforms from a low temperature non-ferroelectric rhombohedral form to a high-temperature tetragonal form at about 1150°C. The tetragonal form can be quenched in by cooling rapidly from a temperature >1250°C as the transformation from tetragonal to rhombohedral is very slow. The quenched-in tetragonal phase transforms to an orthorhombic, ferroelectric form at ~570°C.[13] Several researchers have reported that the fabrication of dense lead metaniobate is very difficult. Kimura et al.[13] have shown that during heating, the transformation from rhombohedral to tetragonal enhances grain growth and retards densification. If the phase transformation takes place after significant densification has occurred in the rhombohedral form, large anisotropic grains with intra-grain porosity were observed to reduce the sintered density. On the other hand, if the phase transformation takes place prior to densification, high final densities can be obtained. The use of orthorhombic starting powder or lowering the rhombohedral to tetragonal transformation temperature are also beneficial to densification of the tetragonal phase at high temperatures. Potassium doped lead metaniobate, $Pb_2KNb_6O_{15}$ (PKN), was found to have a stable orthorhombic form at room temperature even when the cooling rate from the high temperature tetragonal form is slow.[4] Ba substitution of Pb was found to lower the rhombohedral to tetragonal transformation temperature. Molten salt synthesis in KCl leads to the formation of PKN and PBKN particles,[12] therefore, PKN and PBKN compositions were selected for this study.

6.3 EXPERIMENTAL PROCEDURE

Compositions used in this study were orthorhombic $Pb_2KNb_5O_{15}$, $(Pb,K)_{0.7}Ba_{0.3}Nb_2O_6$ (MPB composition), and tetragonal $(Pb,K)_{0.4}Ba_{0.6}Nb_2O_6$. Template particles were synthesized by molten salt synthesis in KCl. Stoichiometric mixtures of PbO, Nb_2O_5 and $BaCO_3$ were milled in 2-propanol for 12 h in a vibratory mill. KCl was added to the milled and dried mixture in a 2:1 weight ratio and lightly ground in a mortar and pestle. The mixture was reacted in the molten KCl at 1050, 1150, 1200, and 1250°C for 4h. The single crystal particles were separated by washing the solidified mass with deionized water 4-8 times.

Matrix powder was synthesized by reacting stoichiometric mixtures of $PbCO_3$, Nb_2O_5, $BaCO_3$, and K_2CO_3 ball-milled in 2-propanol for 24 h at 1200C for 2h. The calcined powder was vibratory-milled for 12 h in 2-propanol and dried. X-ray diffraction of both the template particles and the matrix powder showed the absence of rhombohedral phase peaks.

20 vol% templates and 80 vol% matrix powder were used to form the tape casting slurry. The slurry preparation and casting process described in Chapter 4 for sheet

textured $(Sr,La)_2Nb_2O_7$ was followed. After binder burnout, the samples were sintered at 1250°C-1350°C for 30 min to 6 h.

The microstructure of TGG samples was observed by SEM and the phase and texture were determined by X-ray diffraction. The dielectric constant and loss were measured as a function of temperature. The samples were poled using a FLUKE Model 4210 high voltage power supply. The samples were heated to 160°C, and a field of 40-70 kV/cm was applied for 30 min. The samples were cooled under field to below 50°C. The piezoelectric coefficient, d_{33}, was determined by using a model ZJ-2 piezo-meter.

6.4 RESULTS AND DISCUSSION

6.4.1 Synthesis of Template Particles

The SEM micrographs of template particles used for TGG are shown in Figure 6.4. These particles were synthesized from mixtures containing 67 wt% KCl. Increasing Ba content was found to inhibit the growth of large template particles. Therefore, higher temperatures (>1200°C) were required to form templates with length >10 μm which could be used for TGG. Higher synthesis temperatures led to higher amounts of Pb-loss. Initial excess PbO in the 2-4 wt% range was found to compensate Pb-loss in the templates during synthesis. Figure 6.5 shows the evolution in template particle size and morphology with temperature at the morphotropic phase boundary. Particles synthesized at 1050°C appeared to be clusters of slender rod shaped particles which had aggregated together. This was observed to be the case for all compositions. Higher temperatures

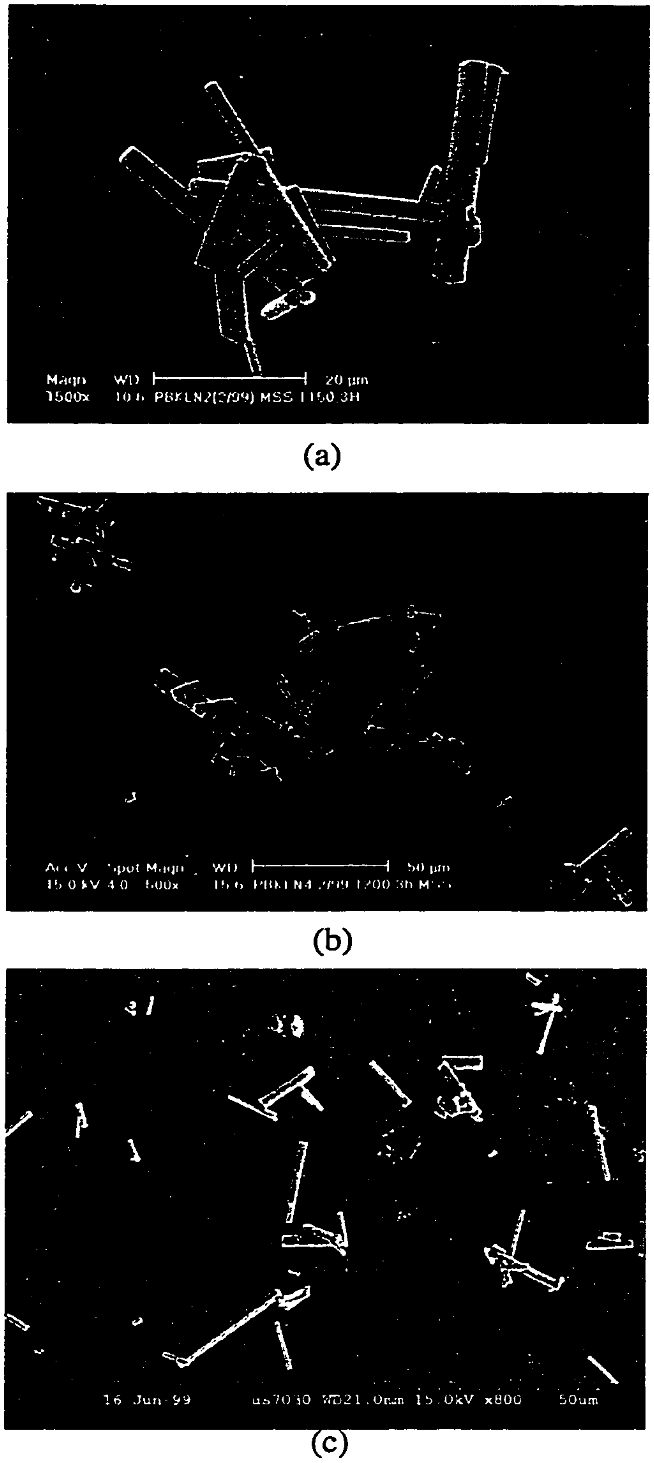

(a)

(b)

(c)

Figure 6.4 Template particles synthesized by molten salt synthesis in KCl (a) $Pb_2KNb_5O_{15}$, (b) $(Pb,K)_{0.7}Ba_{0.3}Nb_2O_6$, and (c) $(Pb,K)_{0.4}Ba_{0.6}Nb_2O_6$

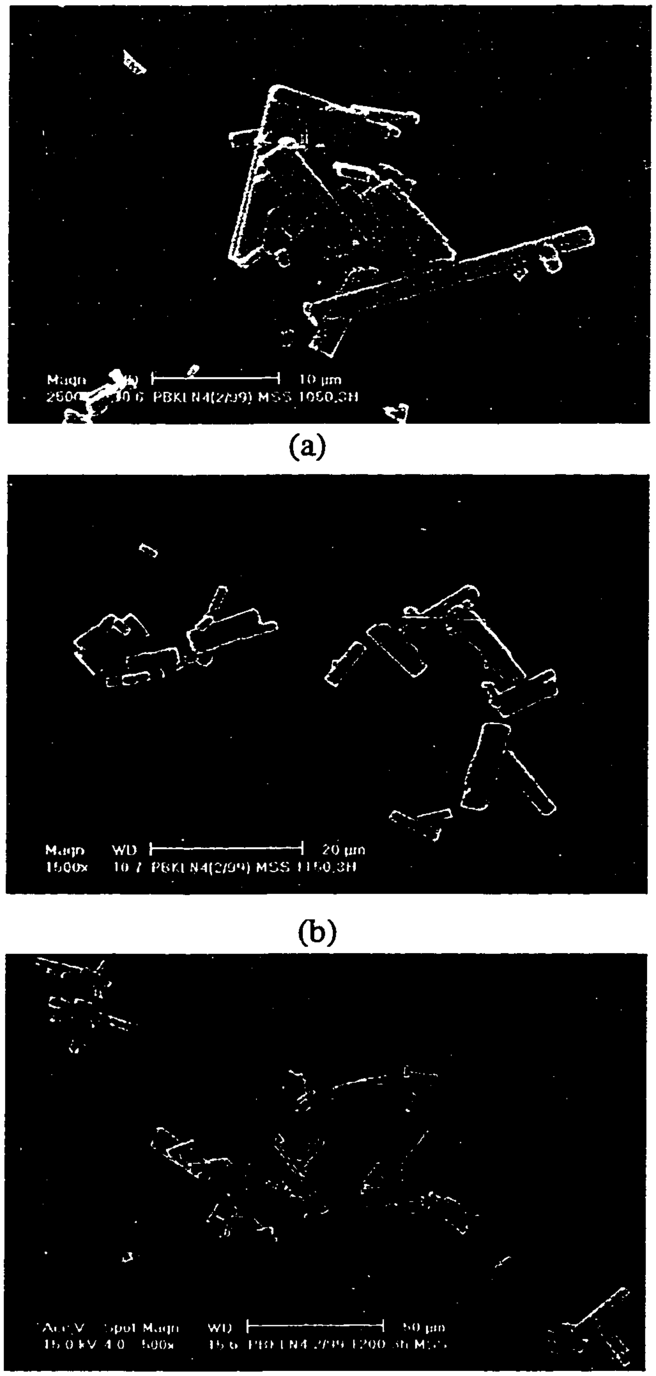

(a)

(b)

(c)

Figure 6.5 $(Pb,K)_{0.7}Ba_{0.3}Nb_2O_6$ template particles synthesized by molten salt synthesis in mixtures containing 67 wt% KCl (a) 1050°C, 3h (b)1150°C, 3h, and (c) 1200°C, 3h lead to the formation of well developed single crystal particles with a cylindrical morphology. Template particle lengths for the MPB composition grew from ~8-10 μm at 1050°C for 3 h to 10-15 μm at 1150°C for 3h to 20-40 μm at 1200°C for 3h. In contrast to the study by Nagata et al.,[12] Ba-rich $PbNb_2O_6$ templates in the 20-50 μm were synthesized by determining the optimum reaction temperature for each composition. Therefore, tetragonal, potassium doped $(Pb,K)_{0.4}Ba_{0.6}Nb_2O_6$ template particles suitable for TGG (in the 20-50 μm size range) were synthesized at 1250°C for 4h as shown in Figure 6.4c.

6.4.2 Densification of Matrix Powder

As reported previously, increasing the amount of Ba leads to slower densification and grain growth.[13] Figure 6.6 shows the microstructures obtained by sintering pellets of the calcined matrix powder of the MPB composition with 5 mol% excess PbO. Dense microstructures (>96%) were obtained by sintering at >1250°C for 3 h. This was found to be the case for all compositions. The previously reported densification problems were not encountered due to the use of orthorhombic or tetragonal starting powder, which did not contain any X-ray detectable rhombohedral phase.

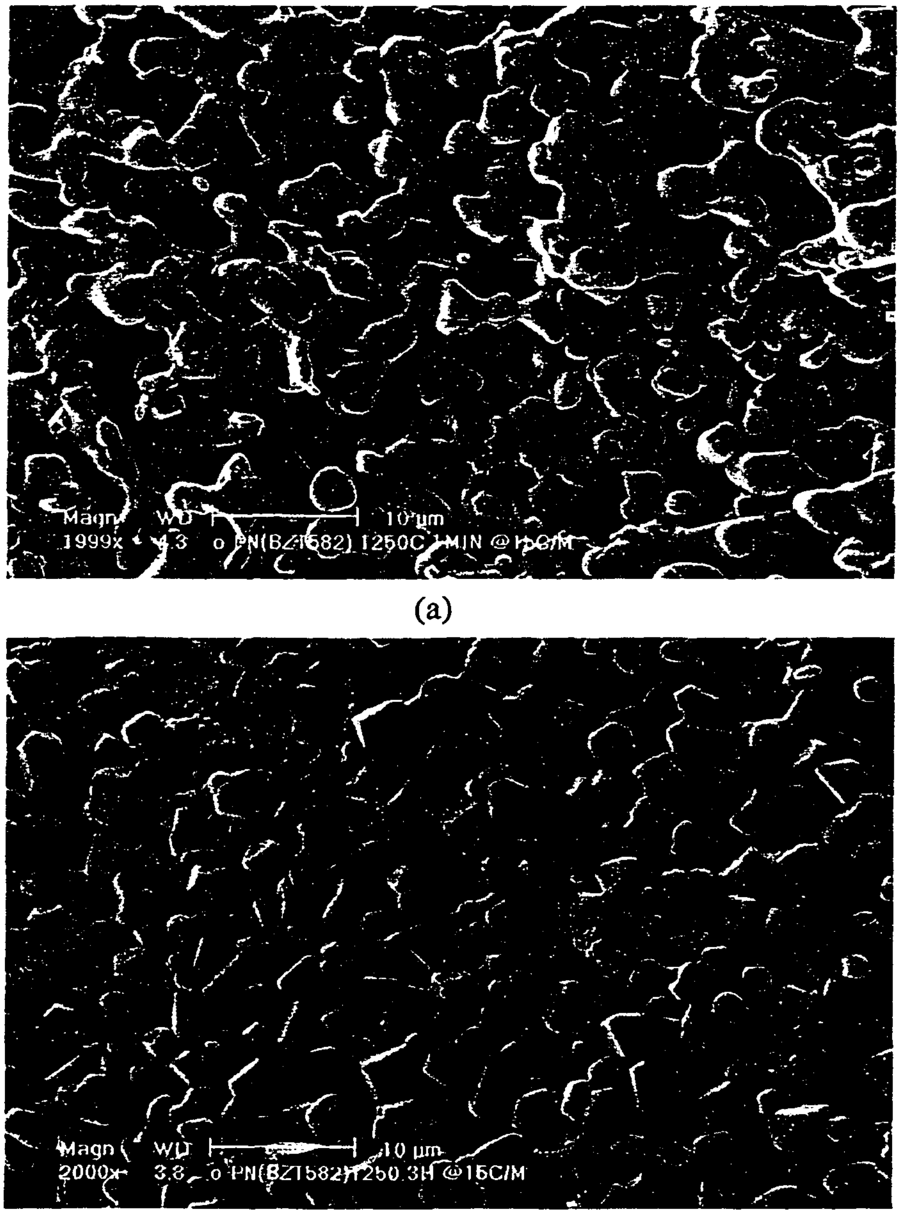

(a)

(b)

Figure 6.6 $(Pb,K)_{0.3}Ba_{0.7}Nb_2O_6$ matrix powder sintered at 1250°C for (a) 1 min, (b) 3 h

6.4.3 Templated Grain Growth

After binder burnout, TGG samples were sintered at 1250°C-1350°C. Figure 6.7 shows the microstructure of $Pb_2KNb_5O_{15}$ samples containing 20 vol% templates sintered at 1270°C for 2 h. The orientation and growth of large template grains can be clearly seen in the SEM micrographs. Long blade-like grains were observed in the SEM micrographs of sections parallel to the tape cast plane, and a number of equiaxed grain-sections and a few anisotropic grains are observed in sections parallel to the top suface. Although some alignment of rod-like templates is obvious from the top surface, the texture is mostly random in the a-b plane. For the highest Ba content compositions used in this study, $(Pb,K)_{0.4}Ba_{0.6}Nb_2O_6$, higher sintering temperatures were required for texture development. In order to promote template growth at higher temperatures, 8 mol% excess PbO and 37.5 vol% of initial templates were used, and the samples were surrounded by loose matrix powder of the same composition during sintering to minimize lead-loss. SEM micrographs of sections sintered at 1320°C for 2 h are shown in Figure 6.8. In these micrographs, orientation of growing templates along the casting direction is seen. The need for higher temperatures and longer times for pressureless TGG is a disadvantage for texturing Ba-rich compositions.

The X-ray diffraction patterns obtained for textured $Pb_2KNb_5O_{15}$ samples confirms the development of texture as shown in Figure 6.9. The X-ray diffraction patterns obtained from the top surface show an increase in the (hk0) peaks and an attenuation of the (hkl) peak intensities for $l \neq 1$. This implies that the rod-shaped grains are preferentially oriented in the plane parallel to the top surface (casting plane).

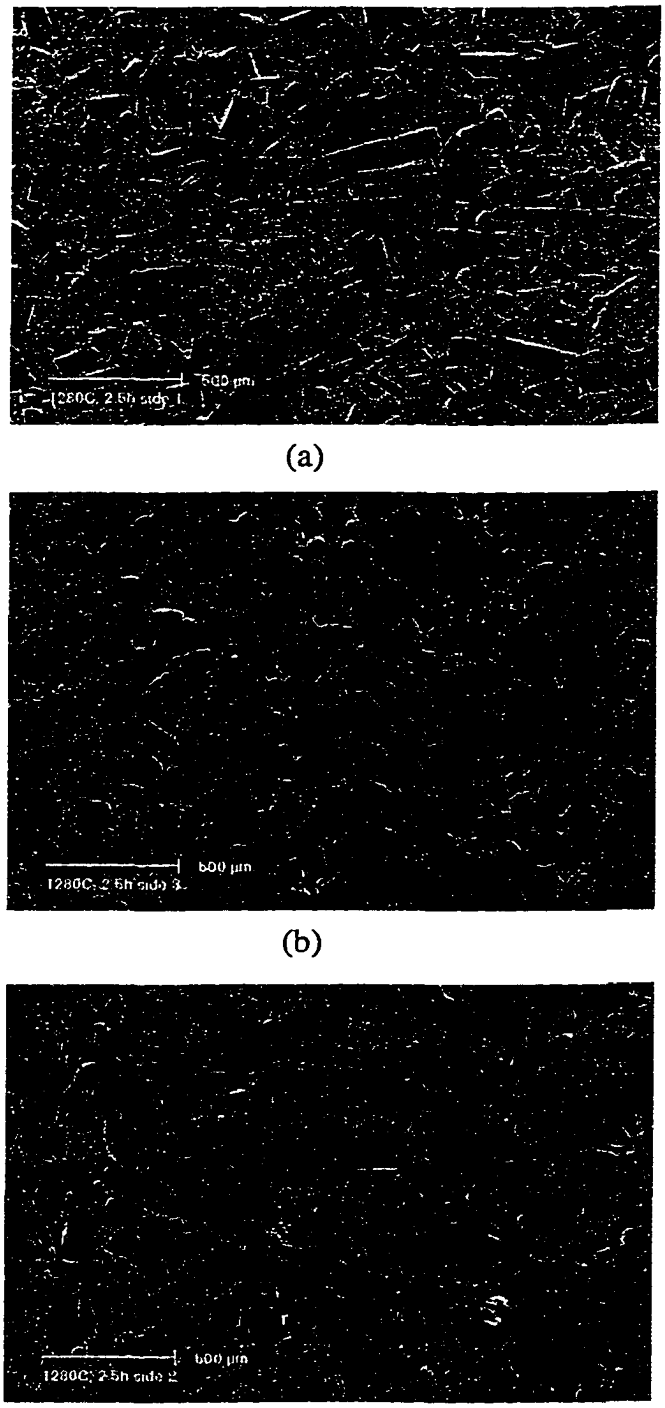

(c)

Figure 6.7 SEM micrographs of $Pb_2KNb_5O_{15}$ TGG samples sintered at 1270°C for 2 h. (a) top surface, (b) edge perpendicular to tape casting direction, and (c) edge parallel to tape casting direction and perpendicular to casting plane

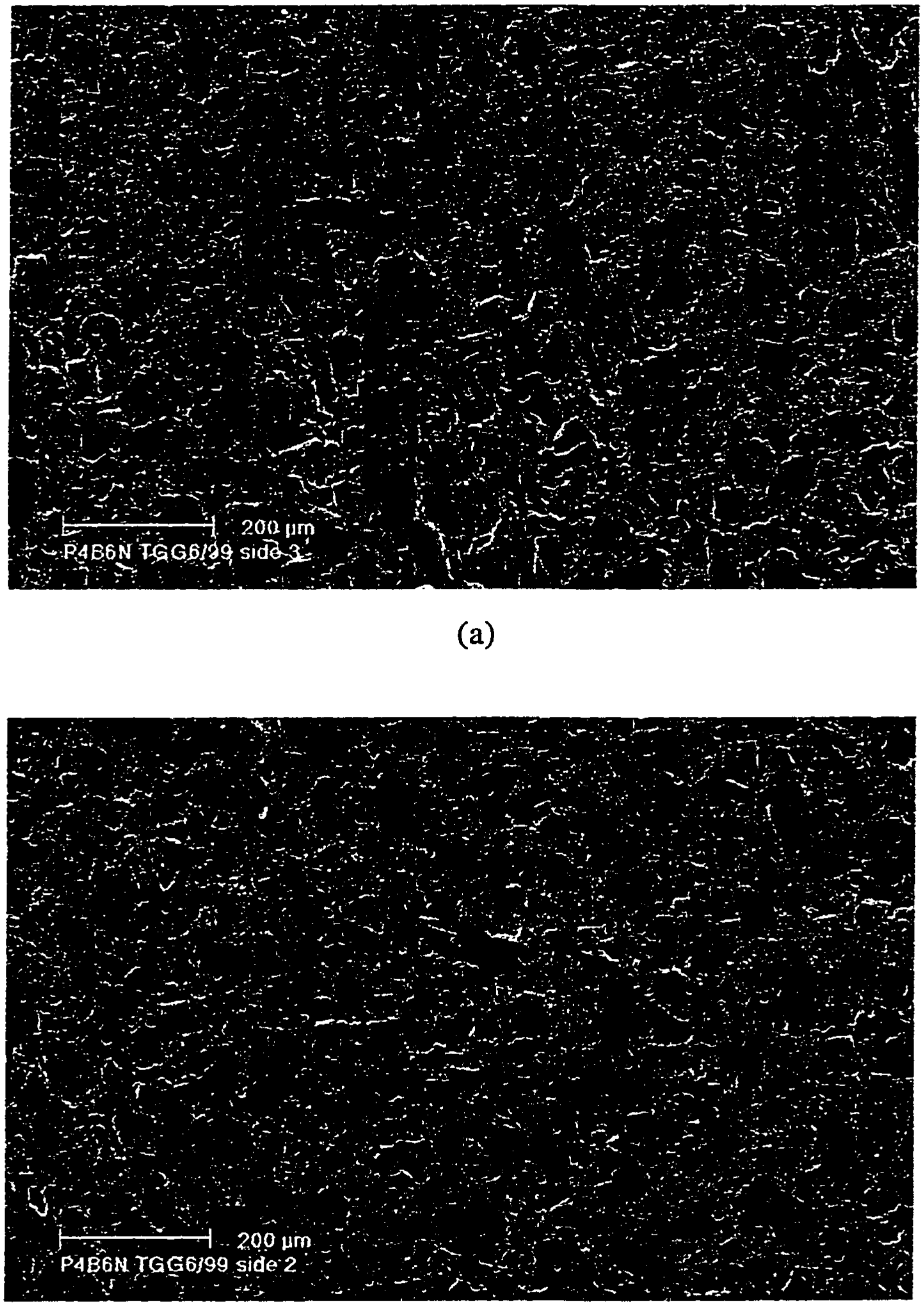

(a)

(b)

Figure 6.8 $(Pb,K)_{0.4}Ba_{0.6}Nb_2O_6$ TGG samples sintered at 1320°C, 2 h. SEM micrographs of (a) plane perpendicular to the tape casting plane, and parallel to the casting direction, and (b) plane perpendicular to casting direction

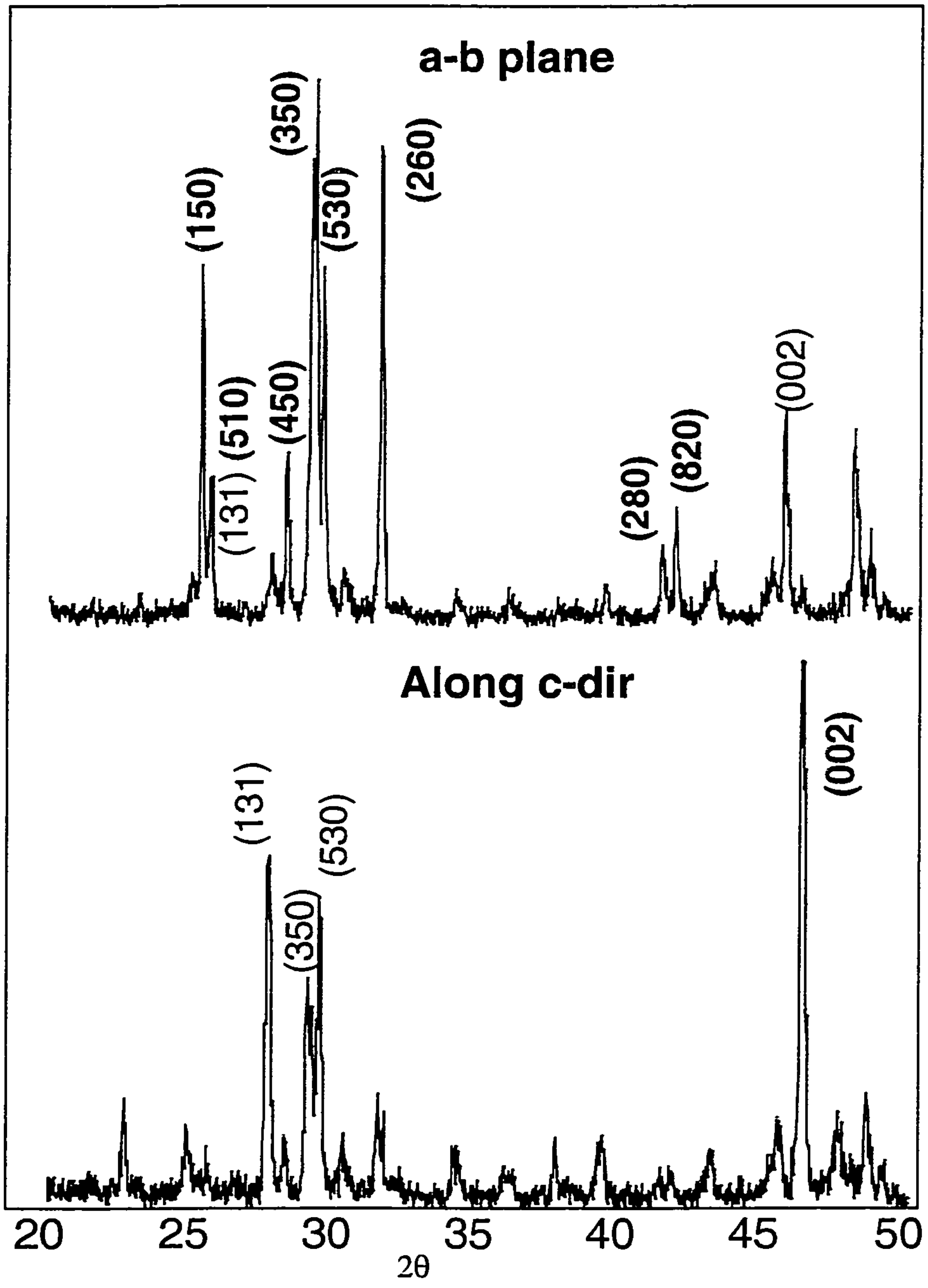

Figure 6.9 X-ray diffraction patterns from top surface (a-b plane) and c-plane for $Pb_2KNb_5O_{15}$ sintered at 1270°C for 2 h, showing orientation of the a-b plane parallel to the top surface.

6.4.4 Electrical Properties

Figure 6.10 shows the dielectric properties for $Pb_2KNb_5O_{15}$ and $(Pb,K)_{0.4}Ba_{0.6}Nb_2O_6$ as a function of temperature. The room temperature values of dielectric constant measured at 1 MHz are 360 and 460 in the tape casting plane and the tape thickness directions, respectively. A peak value of ~3100 was observed in the dielectric constant at ~400°C. The position of this peak suggests that the Curie temperature was considerably lowered due to the addition of potassium to lead metaniobate. The observed anisotropy in dielectric constant is in agreement with previously reported values.[10]

Texture produced by TGG was reported to increase the piezoelectric constant, d_{33}, in certain directions.[8-12] Randomly oriented samples and textured samples (in tape thickness direction) were poled under a field of 40-70 kV/cm at 160°C for 30 min in an oil bath. The samples were cooled to 50°C under field. The randomly oriented samples possessed a d_{33} of 85-90 pC/N. The textured samples showed an enhancement due to grain orientation. These samples showed a d_{33} of 120 pC/N which is in close agreement with the observation of Granahan et al.[10]

6.5 CONCLUSIONS

Texture development in lead niobate ceramics can be achieved by the TGG approach. Molten salt approach was successfully used to obtain long rod-like templates of various compositions which were found to be suitable for TGG. Excess PbO was required to enhance template growth. The microstructural texture was confirmed in both

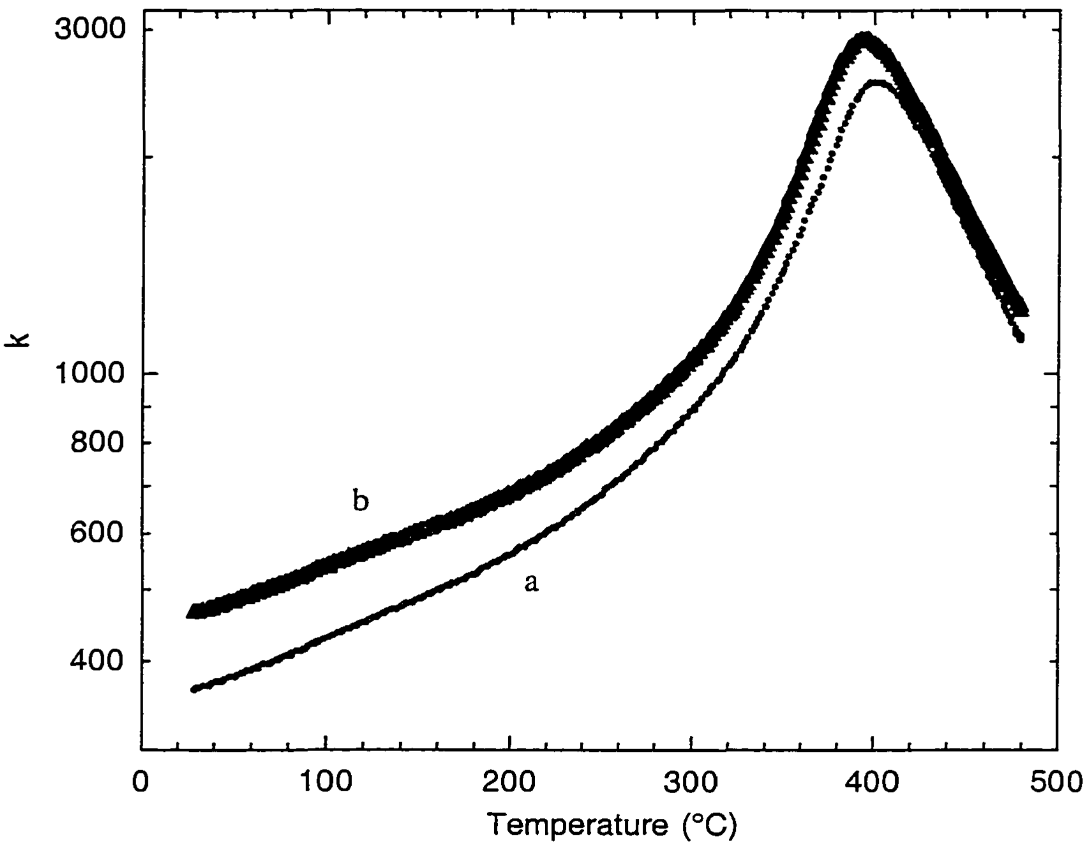

Figure 6.10 Dielectric constant as a function of temperature (measured at 1 MHz). (a) In the tape casting plane and (b) Perpendicular to tape casting plane. The dielectric constant is plotted on logarithmic scale

X-ray analysis and by the anisotropy in dielectric constant. PKN samples were successfully poled, and a d_{33} of 120 pC/N was obtained in the direction of tape thickness.

6.6 REFERENCES

1 B. Jaffe, W. R. Cook, and H. Jaffe, Piezoelectric Ceramics, Academic Press, London (1971)

2 J. R. Oliver and R. R. Neurgaonkar, "Ferroelectric Properties of Tungsten Bronze Morphotropic Phase Boundary Systems," *J. Am. Ceram. Soc.*, **72** [2] 202-11 (1989)

3 C. A. Randall, R. Guo, A. S. Bhalla, and L. E. Cross, "Microstructure-Property Relations in Tungsten Bronze Lead Barium Niobate, $Pb_{1-x}Ba_xNb_2O_6$," *J. Mater. Res.*, **6** [8] 1720-28 (1991)

4 R. R. Neurgaonkar, J. R. Oliver, and W. K. Cory, "Structural and Dielectric Properties of the Phase $Pb_{1-2x}K_xM_x{}^{3+}Nb_2O_6$, M = La or Bi," *Mat. Res. Bull.*, **18** 735-41 (1981)

5 E. C. Subbarao and J. Hrizo, "Solid Solutions Based on Ferroelectric $PbNb_2O_6$," *J. Am. Ceram. Soc.*, **45** [11] 528-531 (1962)

6 G. Goodman, "Ferroelectric Properties of Lead Metaniobate," *J. Am. Ceram. Soc.*, **36** [11] 368-72 (1953)

7 M. H. Francombe, "The Relation Between Structure and Ferroelectricity in Lead Barium and Barium Strontium Niobates," *Acta Cryst.*, **13** 131-40 (1960)

8 R. R. Neurgaonkar, J. R. Oliver, and J. G. Nelson, "Piezoelectric and Ferroelectric Properties of La-Modified and Unmodified Tungsten Bronze $Pb_{0.6}Ba_{0.4}Nb_2O_6$ Dense Ceramics," *Mat. Res. Bull.*, **26** 771-77 (1991)

9 K. Nagata and K. Okazaki, "One-Directional Grain-Oriented Lead Metaniobate Ceramics,". *Jap. J. Appl. Phys.*, **24** [7] 812-14 (1985)

10 M. Granahan, M. Holmes, W. A. Schulze, and R. E. Newnham, "Grain-Oriented $PbNb_2O_6$ Ceramics," *Comm. Am. Ceram. Soc.*, **64** [4] C68-69 (1981)

11 Y. Inoue, T. Kimura, T. Yamaguchi, K. Nagata, and K. Okazaki, " Grain Orientation and Electrical Properties of Hot-Pressed Bismuth Titanate Ceramics," *Yogyo-Kyokai-Shi*, **92** [7] 416-19 (1984)

12 K. Nagata, Y. Uchida, K. Okazaki, and H-D. Nam, "Electrical Properties of Grain-Oriented Ba and La Modified Lead Niobate Ceramics from Molten Salt Synthesized Powders," *Jpn. J. Appl. Phys.*, **24** 100-2 (1989)

13 T. Kimura, Y. Kuroda, H. S. Lee, "Effect of Phase Transformation on the Sintering of Lead Barium Metaniobate Solid Solutions," *J. Am. Ceram. Soc.*, **79** [3] 609-12 (1996)

Chapter 7

SUMMARY AND FUTURE WORK

7.1 SUMMARY

7.1.1 Template Particle Synthesis

A method for synthesizing anisotropic faceted single crystal particles of $Sr_2Nb_2O_7$ was developed. The process takes advantage of the differences in the solubility of precursors in a molten salt. It was shown that plate-like faceted particles in 1-5 μm size range grow on Nb_2O_5 or Nb-source particles in alkali halide melts because Nb_2O_5 and Nb-source particles have limited solubility. Thus, the size of the growing particles depends on the size of the precursor particles. Large single crystal particles form in $SrCl_2$ melts because the Sr-metal-oxides have higher solubility in $SrCl_2$ melts than in alkali halide melts.

The shape of $Sr_2Nb_2O_7$ can be regulated by adjusting the relative solubilities in a two-step process. Large, blade-shaped $SrNb_2O_6$ particles crystallized from mixtures of $SrCl_2$ and Nb_2O_5 were used as the Nb-source for reactions with $SrCO_3$ in KCl melts. Thus 10-15 μm $Sr_2Nb_2O_6$ particles yield 10-50 μm long, blade-shaped templates of $Sr_2Nb_2O_7$. The morphology of the template particles is controlled by the morphology of the $SrNb_2O_6$ particles with the large rectangular face of the particles being perpendicular to the crystallographic b-direction and the length of the particles along the a-direction.

7.1.2 Synthesis of Fine $Sr_2Nb_2O_7$ Powder

A low cost process was developed to synthesize sub-micron, narrow size distribution, equiaxed particles that are chemically homogeneous, and phase pure. Although, sol-gel synthesized powder was shown to have the best starting powder characteristics, the problem of strong agglomeration and the cost of the precursors, especially for Nb, precludes its use for the synthesis of large amounts of fine powder.

Powders were obtained by solid state reaction of milled stoichiometric mixtures of $SrCO_3$ and Nb_2O_5, or coprecipitated strontium oxalate and hydrated niobium oxide. Calcination of reactants packed in large area beds of low height in low-walled crucibles at 1050°C to 1100°C for 2 h resulted in complete formation of $Sr_2Nb_2O_7$ phase. Milling the calcined powder yielded equiaxed powder with a sub-micron particle size distribution. The coprecipitation scheme was amenable to homogeneous additions of dopants. Another advantage of the coprecipitated powder was the suppression of exaggerated grain growth due to better chemical homogeneity. Therefore, milled, coprecipitated La-doped powder was used for TGG of samples with sheet texture.

7.1.3 Anisotropic Grain Growth

A number of factors such as crystal structure, stoichiometry, formation of liquids, temperature, and temperature profile promote anisotropic grain growth. It was determined that a small excess of niobium at grain boundaries resulted in the formation of a liquid phase between 1300°C and 1350°C leading to accelerated grain growth.

La-doping was found to be beneficial in increasing high temperature a.c. resistivity in agreement with earlier studies. However, lanthanum suppressed grain growth in $Sr_2Nb_2O_7$ ceramics because of either a solute drag mechanism, or because lanthanum oxide-rich phase on the grain boundaries retards the mobility of the grain boundaries.

By coating the surface of stoichiometric $(Sr,La)_2Nb_2O_7$ particles with excess niobium, conditions favorable for anisotropic grain growth were created.

7.1.4 Fiber Texture by Templated Grain Growth of $Sr_2Nb_2O_7$

Fiber texture in $Sr_2Nb_2O_7$ was induced by TGG by using a sub-micron matrix powder, and relatively large template particles (5-15 μm). Oriented, faceted templates with a face area of 2 μm x 2 μm were found to be unsuitable because matrix grain growth resulted in a large population of matrix grains of a comparable size under the sintering conditions used.

The initial volume fraction of template particles has a strong effect on the volume fraction of textured material. The use of 5 vol% of initial templates did not result in very highly textured microstructures. However, the use of 10 vol% of initial templates resulted in microstructures with very high volume fractions of textured material. Lotgering factor measurements along the b-direction verified the high degree of texture in the microstructures.

7.1.5 Sheet Texture in $(Sr,La)_2Nb_2O_7$ by TGG

Although fiber texture along the b-axis was obtained in $Sr_2Nb_2O_7$, the formation of fiber texture along the c-axis or sheet texture is the most desirable form of crystallographic texture in $Sr_2Nb_2O_7$ ceramics from the point of view of enhancing piezoelectric properties.

A gated tape casting arrangement was developed to orient blade-shaped templates with their large rectangular faces (perpendicular to the b-axis) parallel to the casting plane and the length (parallel to a-axis) along the casting direction. High viscosity, high shear rate (small blade opening and a high casting rate), and the use of closely spaced "needles" promote the development of sheet texture.

The minimum amount of liquid phase required for growth of templates was found to be about 200 ppm of excess niobium. 500-1000 ppm excess niobium was used for production of sheet texture. Texture was developed by growing templates as the number of large grains per unit area remained nearly constant, suggesting that exaggerated grain growth in the matrix does not contribute to the population of large grains. Measurement of the angle distribution of the major axes of large grains from orthogonal faces of the sintered sample revealed that the degree of sheet texture is strong. Therefore, the grain dimensions measured from 2D sections orthogonal to each other and parallel to the texture directions are a good approximation of the true grain dimensions. Growth rates along different axes were found to be anisotropic.

X-ray diffraction patterns from different faces of the sintered sample confirm the crystallographic sheet texture in these samples.

7.1.6 Pole Figure Measurement of Sheet Texture

Pole figure measurements were found to be very useful in determining the presence of sheet texture in the samples. A single pole figure measurement of the 131 pole from any of the three orthogonal sample faces gives enough information to confirm the presence of sheet texture in $Sr_2Nb_2O_7$.

7.1.7 Anisotropic Properties of Textured $Sr_2Nb_2O_7$

Stereologically determined orientation distributions from three orthogonal sections along the crystallographic axes can be used to obtain a function that describes the volume fraction as a function of orientation. By using the calculated dielectric constant for different orientations of a single crystal, we can obtain the dielectric constant of each volume element of a textured sample. The overall dielectric constant of the textured sample can then be calculated. Measured dielectric properties showed the expected anisotropy due to texture in the ceramic samples at room temperature. While some of the anisotropy may be a consequence of different distributions of the grain boundary phase in the three perpendicular directions, the good agreement between the X-ray determined texture distributions and the permittivities suggests that crystallographic texture contributes, at least in part, to the observed anisotropy. The observed degree of anisotropy also suggests that the volume fraction of textured material obtained at 1500°C for 4 h was close to unity. The dielectric constant agrees reasonably well with the calculated dielectric constant. The effect of texture on properties was observed in both fiber-textured and sheet-textured samples.

7.1.8 Templated Grain Growth of $PbNb_2O_6$ Ceramics

The principles of templated grain growth identified by the study of texture development in $Sr_2Nb_2O_7$ can be directly applied to the $PbNb_2O_6$ system. Template synthesis, sintering, and grain growth in orthorhombic tungsten bronze, tetragonal tungsten bronze, and morphotropic phase boundary compositions in the $(Pb,K)Nb_2O_6$-$BaNb_2O_6$ system were studied.

Large template particles of all the compositions can be successfully synthesized by molten salt synthesis in KCl. 5-7 mol% excess PbO was used as the liquid phase to promote grain growth during sintering. Template growth resulted in texture in these ceramics. The texture is reflected in the X-ray diffraction patterns obtained from different sintered faces, and the measured dielectric constants. A room temperature d_{33} value of 120 pC/N was measured for poled TGG samples, perpendicular to the cast plane, of $(Pb,K)Nb_2O_6$ as compared to 90 pC/N for randomly oriented ceramic samples.

7.2 FUTURE WORK

7.2.1 Template Particles

The two step molten salt synthesis approach used to prepare $Sr_2Nb_2O_7$ templates can be used to synthesize single crystal particles of other materials. This approach is suitable for regulating both the size and morphology of the powders. More studies need to be conducted to generalize this approach to other technologically useful compositions and materials. TEM studies can help determine if there is an epitaxial relation between the precursor particles (Nb-rich phase) and the template particles. The reaction sequence and solubility of various compounds in the $SrO-Nb_2O_5$ system in $SrCl_2$ melts need to be investigated further to be able to crystallize small crystals of $Sr_2Nb_2O_7$ from $SrCl_2$ melts.

7.2.2 Templated Grain Growth

In spite of the number of TGG studies on a variety of materials, certain scientific aspects of this process remain unclear. Whether the cause of template growth is a result of surface energy anisotropy, equilibrium solubility anisotropy, or anisotropic liquid wetting behavior needs to be established conclusively. This requires a combination of TEM investigations and processing studies. Template grain growth cannot be conclusively attributed to any of the above factors without an extensive study of the microscopic causes for anisotropic growth. Studies on the growth of single crystals in a matrix of fine powder suggest that the causes for template growth and single crystal growth are identical, and that would be a good starting point for future studies.[1,2]

An epitaxial match between the templates and the matrix material has been identified as one of the requirements for TGG. Determining the degree of lattice mismatch that can be tolerated during TGG has several uses. The use of template particles of one material to texture another opens several potential opportunities. It is not always possible to synthesize template particles of a desired composition or shape. In such cases, small volume fractions of templates of a different material can still be used to obtain texture. Thus, plate shaped templates of PLS compounds can be used to template a number of perovskite and perovskite-like materials.

The presence of a liquid phase has been reported to cause anisotropic grain growth in a number of ceramic systems. To date, all reports of TGG have used a liquid phase to facilitate anisotropic grain growth. The requirement of a liquid phase may prove to be a limitation for a number of dielectric, electromechanical, and thermo-mechanical applications, unless a transient liquid phase is used for TGG. It is not known yet whether TGG in the solid state is possible. Although there are a few reports of rapid anisotropic grain growth in solid state systems,[3] the possibility of trace amounts of liquid phase forming due to stoichiometric variations or extrinsic impurities has not been conclusively eliminated. The connection between the presence of a liquid phase and rapid anisotropic grain growth needs to be proved or disproved by TEM studies of grain growth in a single component system of extremely high purity.

Techniques and analytical equations for the quantification of sheet texture need to be optimized for $Sr_2Nb_2O_7$ and other PLS compounds. This is a prerequisite for developing models to predict the properties of textured ceramics based on the properties of single crystals.

Technologically, the TGG process can be used to form polycrystalline materials with controlled texture distributions. As it is possible to produce both sheet texture and fiber texture in tape cast layers, all possible combinations of macroscopic orientation distributions can be produced by controlling the relative orientation of layers in the laminated green body and adding dicing, stacking, and relamination steps to the process. This can prove to be advantage over single crystals for certain applications.

7.2.3 Piezoelectricity in $Sr_2Nb_2O_7$

Although orientation along the polar axis (c-axis) was developed by producing sheet texture in $Sr_2Nb_2O_7$ ceramics, piezoelectricity was not detected due to the inability to pole the ceramic. High temperature poling experiments were limited by the field that could be applied. Further experiments on pulse poling or corona poling at high temperatures might be more successful. The measurement of piezoelectric properties in these samples would make the TGG technique valuable for the production of high temperature vibration sensors based on $Sr_2Nb_2O_7$. Another alternative is to reduce the Curie temperature to enable poling at lower temperatures. Addition of tantalum has been demonstrated to lower the Curie temperature to 500-1000°C in previous studies.[4] However, tantalum substitution severely retards grain growth and densification in $Sr_2Nb_2O_7$. An alternative dopant which is compatible with the requirements of TGG and which can reduce the Curie temperature needs to identified.

The inability to pole textured samples even under fields of 70-100 kV/cm at 150-200°C can possibly be overcome by high temperature poling. One of the requirements for high temperature poling is a high resistivity at high temperatures. Recent work on bismuth layer structure compounds has shown that increasing the resistivity by fabricating a fine-grained ceramic was beneficial to high temperature piezoelectric properties.[5] The fine grains have a lower surface area fraction of the typical platy facet of anisotropically grown bismuth layer compounds which exhibits high conductivity. Since there is some indication that $Sr_2Nb_2O_7$ also shows higher conductivity in the a-c plane than along the b-direction,[6] based on the fine-grained bismuth titanate work, one way to achieve high temperature piezoelectricity in $Sr_2Nb_2O_7$ is by curbing anisotropic grain growth and producing highly insulating, very fine-grained microstructures. Another option might be to form insulating grain boundary phases around oriented, anisotropically grown grains. Therefore a study of the electrical resistivity and breakdown strengths of textured $Sr_2Nb_2O_7$ ceramics with different dopants and additives is an important step towards successful high temperature poling. Understanding the conduction and loss mechanisms in ceramic $Sr_2Nb_2O_7$ is also important to the overall goal of enhancing resistivity to obtain piezoelectricity at high temperatures for sensing applications, and to prevent depoling during operation. Contributions to the dielectric loss are expected due to ion migration, d.c. conductivity losses, ion jump and domain/dipole relaxation losses. It will be important to establish a connection between the defect chemistry of the system and the conductivity in order to establish the conduction mechanism. Conductivity in $Sr_2Nb_2O_7$ has been reported to be p-type by Fuierer.[6] P-type conductivity in $Sr_2Nb_2O_7$ could be due to the presence of oxygen interstitials, O_i'', in the relatively open PLS structure, metal ion vacancies on the Sr or Nb sites, V_{Sr}'' or V_{Nb}''''', K_{Sr}' from potassium impurities from the molten salt synthesis, or the presence of reduced niobium in the 4+ state, Nb_{Nb}'. Experiments to determine conductivity as a function of oxygen partial pressure can help determine which of the above defects are responsible for conduction. If the conductivity increases with increasing oxygen partial pressure, oxygen interstitials would be the most likely cause. On the other hand, if conductivity drops with increasing oxygen partial pressure, $[Nb_{Nb}']$ or K_{Sr}' might control the concentration of holes, and hence the conductivity. If the conductivity remains unchanged with change in oxygen partial pressure, the conductivity is most likely governed by metal vacancy concentration. Preliminary oxygen annealing experiments showed an increase in resistivity, suggesting that the presence of reduced Nb or potassium impurities from molten salt synthesis are the most likely causes for conductivity. However, a systematic study is required to determine the role of defect chemistry on conductivity. Examining the anisotropy of the resistivity in textured samples would also be important. As conduction is a thermally activated process, determining the activation energies for conduction would help determine the primary cause for breakdown at various poling temperatures.

The slight structural instability at the incommensurate-commensurate phase transitions may be exploited for enhancing poling efficiency. The transition temperature can be raised above 215°C by irradiation to cause defects or by determining a suitable dopant. Poling can then be attempted at higher temperatures around the transition temperature to enhance poling efficiency.

The low temperature transition at -156°C might also be a candidate for poling as there is a structural instability associated with it that can be exploited for enhancing poling efficiency. Poling experiments along the b-direction and the c-direction at -156°C would determine the feasibility of such an approach.

As the piezoelectric properties of $Sr_2Nb_2O_7$ ceramics are relatively weak, resonance techniques must be employed to measure piezoelectric properties in poled samples. Resonance measurements require samples of various geometries. This requires the optimization of the lamination and binder burnout processes to fabricate laminates with several hundred stacked layers.

7.2.4 Piezoelectricity in Other Materials

Other phases in the SrO-Nb_2O_5 system have not been thoroughly investigated. Textured samples produced by TGG can be used to investigate these compositions for interesting and useful physical properties if it is difficult to obtain single crystals.

TGG can be used to texture various compositions in the $PbNb_2O_6$-$BaNb_2O_6$ binary system. Based on earlier reports,[7,8] high piezoelectric constants can be obtained near the morphotropic phase boundary. Electromechanical characterization of textured samples of this composition needs to be completed. The effect of substitutions on the ability of lead metaniobate to resist depoling must also be investigated.

TGG of other PLS compounds and piezoelectric ceramics with anisotropic crystal structures might yield ceramic piezoelectrics with enhanced properties. TGG can also be applied to cubic perovskites by using anisotropically shaped templates of materials with perovskite-related crystal structure having a heteroepitaxial relation to the cubic perovskite. This may be one way to produce textured lead magnesium niobate-lead titanate and lead zirconate titanate for piezoelectric applications.

7.3 REFERENCES

1. J. Rodel and A. M. Glaeser, "Anisotropy of Grain Growth in Alumina," *J. Am. Ceram. Soc.*, **73** [11] 3292-301 (1990)

2. M. M. Seabaugh, "Texture Development in Liquid Phase Sintered Alpha Alumina via Anisotropic Template Growth," PhD. Thesis, The Pennsylvania State University, University Park, PA (1998)

3. J. D. Powers and A. M. Glaeser, "Grain Boundary Migration in Ceramics," *Interface Sci.*, **6** 23-39 (1998)

4. S. Nanamatsu, M. Kimura, and T. Kawamura, "Crystallographic and Dielectric Properties of Ferroelectric $A_2B_2O_7$ (A=Sr, B=Ta,Nb) Crystals and Their Solid Solutions," *J. Phys. Soc. Jpn.*, **38** [3] 81 (1975)

5. H. S. Shulman, M. Testorf, D. Damjanovic, and N. Setter, "Microstructure, Electrical Conductivity, and Piezoelectric Properties of Bismuth Titanate," ," *J. Am. Ceram. Soc.*, **79** [12] 3124-8 (1996)

6. P. A. Fuierer, "Grain Oriented Perovskite Layer Structure Ceramics for High Temperature Piezoelectric Applications," PhD. Thesis, The Pennsylvania State University, University Park, PA (1991)

7 M. H. Francombe, "The Relation Between Structure and Ferroelectricity in Lead Barium and Barium Strontium Niobates," *Acta Cryst.*, **13** 131-40 (1960)

8. R. R. Neurgaonkar, J. R. Oliver, and J. G. Nelson, "Piezoelectric and Ferroelectric Properties of La-Modified and Unmodified Tungsten Bronze $Pb_{0.6}Ba_{0.4}Nb_2O_6$ Dense Ceramics," *Mat. Res. Bull.*, **26** 771-77 (1991)

VITA

Bhaskar Brahmaroutu

Bhaskar Brahmaroutu was born December 19, 1971 in India. He graduated from Atomic Energy Junior College in 1989. He then obtained his B. Tech in Metallurgical Engineering at the Indian Institute of Technology, Bombay in 1994. After graduation from IIT Bombay, Mr. Brahmaroutu joined the graduate program in Materials Science and Engineering at the Pennsylvania State University in August 1994. He has since been working towards his Ph.D. He has accepted an offer to work in the Phosphors and Coatings division of General Electric Lighting, Cleveland.